Molecular Dynamics Study of Context Dependent Structural and Dynamical Properties of Water in Heterogenous Environments and Water Mediated Self-Assembly Processes

Thesis submitted to AcSIR for the Award of the Degree of

DOCTOR OF PHILOSOPHY

In

Chemical Sciences

By

Vrushali Ravindra Hande

Registration No.: 10CC17J26030

Under the guidance of

Dr. Sarika Bhattacharyya   **Dr. Suman Chakrabarty**
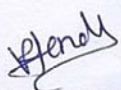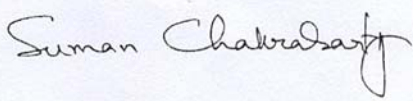
(Supervisor)   **(Co-supervisor)**

CSIR–National Chemical Laboratory, Pune, India

Certificate

This is to certify that the work incorporated in this Ph.D. thesis entitled "**Molecular dynamics study of context dependent structural and dynamical properties of water in heterogenous environments and water mediated self-assembly processes**" submitted by **Ms. Vrushali Ravindra Hande** to Academy of Scientific and Innovative Research (AcSIR) in fulfillment of the requirements for the award of the Degree of **Doctor of Philosophy in Chemical Sciences**, embodies original research work under our supervision/guidance. We further certify that this work has not been submitted to any other University or Institution in part or full for the award of any degree or diploma. Research material obtained from other sources has been duly acknowledged in the thesis. Any text, illustration, table etc., used in the thesis from other sources, have been duly cited and acknowledged.

It is also certified that this work done by the student, under my supervision, is plagiarism free.

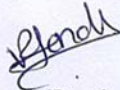|		
------------------------------	------------------------------	------------------------------
Vrushali Ravindra Hande	**Dr. Sarika Bhattacharyya**	**Dr. Suman Chakrabarty**
(Student)	(Supervisor)	(Co-supervisor)
CSIR-NCL, Pune	CSIR-NCL, Pune	SNBNCBS, Kolkata

Date: 16/3/2020

Place: CSIR-NCL, Pune

Declaration

I hereby declare that the thesis entitled "**Molecular dynamics study of context dependent structural and dynamical properties of water in heterogenous environments and water mediated self-assembly processes**" submitted for the degree of Doctor of Philosophy in Chemical Sciences to the Academy of Scientific & Innovative Research (AcSIR), has been carried out by me at the Physical and Material Chemistry Division of CSIR-National Chemical Laboratory, Pune under the supervision of Dr. Sarika Bhattacharyya and Dr. Suman Chakrabarty. Such material as has been obtained by other sources has been duly acknowledged in the thesis. The work is original and has not been submitted in part or full by me for any other degree or diploma to any other Institution or University.

Date: 16/3/2020

Place: CSIR-NCL, Pune

Vrushali Ravindra Hande

(Ph.D. candidate)

Abstract

Water is responsible for regulating and controlling the biological functions and structures of proteins. In the protein folding problem, hydrophobic interactions and hydration plays a vital role. Considering the essential aspects of hydrophobic hydration, understanding of the fundamental properties of water will provide insights in such biological problems. Though water being a very simple dipolar solvent molecule, it has strong context dependent nature. Therefore, in the present thesis, using molecular dynamics simulation technique, we have examined thoroughly the structure and dynamics of water in different contexts such as around non-polar spherical solutes and flexible polymers, in spherical AOT reverse micelle and water-in-oil (isooctane) confinement, and near bilayers with different types of charge distribution on the head groups (anionic, zwitterionic and hydrophobic). Subsequently, we have explored the structural and conformational dynamics of peptide CXCR1 in AOT reverse micelle confinement. We have also studied the morphology and dynamics of the self-assembly of mixed surfactant (SDS+CAPB) systems at hydrate forming thermodynamic conditions in the presence and absence of methane.

Size-dependent structural order-disorder crossover have been revealed for the spherical hydrophobes in water. An analogous behavior has been ascertained between bulk water with temperature variation and hydration shell water around hydrophobes with size variation. For the water near a complex heterogeneous (having different patches of curvatures) polymeric surfaces, a strong solute-solvent coupling has been demonstrated. In such kinds of surfaces, water always finds the highest curvature region of the surface to wrap around so as to maximize the hydrogen bonded interactions.

Since, water under confinement is known to exhibit widely divergent properties as compared to bulk water. In order to dissect the relative role of confinement versus interaction with charged interface, we have compared between a model water-in-oil nanodroplet (confined water) and AOT reverse micelle. We have demonstrated that water in the core region (far from the interface) in the hydrophilic confinement shows considerable deviations from the bulk water compared to hydrophobic confinement, where

the perturbation is restricted to the interfacial region. Therefore, the structural and dynamical perturbation in reverse micelles can be attributed to the electrostatic interactions between the water and hydrophilic surfaces rather than only the effect of confinement. The translational dynamics (diffusion) gets significantly affected due to the pure confinement effect. Nevertheless, the water perturbation length scale highly depends on the property under investigation. Local translational ordering e.g. density gets perturbed least as compared to local and global orientational ordering of water. The work has been extended to planar surfaces with varying charge distribution, namely anionic, zwitterionic and hydrophobic surfaces. The water perturbation has been decreased compared to spherical confinement of reverse micelle systems.

Furthermore, the effect of the hydration size of AOT reverse micelle on the structural and conformational dynamics of the CXCR1 peptide under confinement has been investigated. We have shown that the peptide has strong surface binding affinity and has enhanced translational dynamics of peptide with increase in the hydration size of reverse micelle. Finally, from the mixed surfactant SDS+CAPB system, we have commented on the aggregation kinetics and morphologies of the aggregates. We have also investigated the structural features including packing of the surfactant molecules in the aggregates. Our analyses also indicate that there exist at least three distinct timescales of relaxation in the mixed surfactant systems. In the context of the effect of such mixed surfactant systems on the methane hydrate growth kinetics, we have observed that the presence of methane molecules significantly alter the structure and dynamics of these aggregates and renders them more fluid-like.

Acknowledgement

I am blessed to have the constant support and encouragement of several people during my Ph.D. tenure without which it would not have completed.

First of all, I would like to express my deep and sincere gratitude to my research supervisor, Dr. Sarika Bhattacharyya and Dr. Suman Chakrabarty. I would like to thank Dr. Sarika Bhattacharyya for her constant support, care and encouragement in ensuring that my research work continued smoothly without any official hassle. I am extremely thankful to Dr. Suman for giving me an opportunity to work with him and providing me his invaluable guidance and support throughout my tenure. He has guided me through the methodology to carry out research as well as to present the research works as clearly as possible. It was a great privilege and honor to work and study under his guidance.

I am grateful for the opportunities to work in collaboration with Dr. Rajnish Kumar and Dr. Sudip Roy. I am thankful to them for funding me in my early research period (Project-assistantship). I would like to express my sincere gratitude to the members of my Doctoral Advisory Committee (DAC): Dr. K. Krishnamoorthy, Dr. Sayan Bagchi, and Dr. Durba Sengupta for giving insightful comments and encouragement as well as evaluating my research progress from time to time. I am also very grateful to Dr. Debashree Ghosh for her valuable suggestions and comments during my work presentations. I would like to thank my coursework instructors: Dr. Kumar Vanka, Dr. Sayan Bagchi, Dr. Suman Chakrabarty, Dr. Debashree Ghosh, Dr. Neelanjana Sengupta, Dr. Sarika Bhattacharyya, Dr. Leelavati Naralikar, Dr. T. G. Ajithkumar, Dr. Guruswamy Kumaraswamy, Dr. J. Nithyanandhan for teaching me. I thank the former and present CSIR-NCL directors, Dr. Sourav Pal and Dr. Ashwini Kumar Nangia; departmental heads of Physical Chemistry Division, Dr. Anil Kumar and Dr. P. A. Joy, for providing the necessary research infrastructure and allowing me to carry out research. I would like to extend my sincere thanks to all the NCL administration departments; Student Academic Office (SAO), AcSIR office at CSIR-NCL, accounts and bill section, ERP sections, store and purchase sections for doing the necessary administrative work. I acknowledge CSIR for providing me with Senior Research Fellowship (CSIR-SRF).

List of Publications

1. Structural order of water molecules around hydrophobic solutes: Length scale dependence and solute-solvent coupling. **Vrushali R. Hande** and Suman Chakrabarty, J. Phys. Chem. B 119, 11346 (2015). doi: 10.1021/acs.jpcb.5b03449

2. Exploration of the presence of bulk-like water in AOT reverse micelles and water-in-oil nanodroplets: Role of charged interface, confinement size and water properties. **Vrushali R. Hande** and Suman Chakrabarty,Phys. Chem. Chem. Phys., 18, 21767-21779 (2016). doi: 10.1039/C6CP04378J

3. Effect of sodium dodecyl sulfate surfactant on methane hydrate formation: a molecular dynamics study. Nilesh Choudhary, **Vrushali R. Hande,** Sudip Roy, Suman Chakrabarty and Rajnish Kumar, J. Phys. Chem. B, 122, 6536(2018). doi:10.1021/acs.jpcb.8b02285

4. Analogous behavior of hydration shell water around hydrophobes of varying size and bulk water with varying temperature and a study of hydrophobic chain length-independent behavior of water around alcohols. **Vrushali R. Hande** and Suman Chakrabarty. (*Manuscript under submission*)

5. Structural characterization of aggregates into crystal or micelle in Sodium dodecyl sulfate and Cocoamidopropylbetaine mixtures at methane hydrate formation conditions. **Vrushali R. Hande**, Nilesh Choudhary, Suman Chakrabarty, and Rajnish Kumar. (*Manuscript under submission*)

6. Structure and dynamics of interfacial water: Effect of surface charges, specific interactions, and distance dependence. **Vrushali R. Hande** and Suman Chakrabarty. (*Manuscript under submission*)

7. Structure and dynamics of the N-terminal domain of chemokine receptor CXCR1 in AOT reverse micelles: Effect of hydration. **Vrushali R. Hande** and Suman Chakrabarty. (*Manuscript under submission*)

Contents

x

List of Figures

List of Tables

Chapter 1: Introduction

Water is the most precious gift to the life on Earth and is essential for the survival. It helps to accomplish specific metabolic functions and regulates our body temperature. It is inorganic, colorless, tasteless and odorless chemical substance required for numerous industrial processes and in agribusiness. The optimal strength and directionality of hydrogen bonding in water give rise to several anomalies. For example, while most solid materials expand on melting, density of ice increases on melting and density maximum appears at 4^0C.[1] It has unusually high melting[2], boiling[3] and critical[4] point, high surface tension[5], high viscosity,[6] and many others.[7–16]

The strength of hydrogen bond in liquid water is about 5.0 kcal/mol.[17] It has an optimal value for carrying out biomolecular processes that are essential for sustaining life on Earth.[18] Since the lifetime of the hydrogen bonds in bulk water is very short (~10 ps)[19], the hydrogen bond breaking and reforming process is constantly ongoing in bulk water.[20] The hydrogen bond present in liquid water can be shorter, longer, straighter, weaker, stronger, or bent.[21,22] The straight hydrogen bonds are stronger among all, where O-H of one water and O atom of nearby molecule are in straight line and O-O distance is less than 3 A^0.[22] On the other hand, because of such networks of hydrogen bonds, bulk water at any instant have tetrahedral symmetry in it with mesh like arrangements.[23,24] Each water molecule can form on an average four hydrogen bonds, arranged tetrahedrally around the central water molecule.

1.1 Context dependent nature of water: Interfacial and confined water

Although being a very simple triatomic dipolar molecule, it has a characteristic feature of getting adjusted to the surface present nearby. During which water may have notable modification in the hydrogen bonding network and tetrahedral symmetry and dynamics.[9,25] It behaves quite differently in different contexts such as near ions of varying sizes, hydrophilic molecules, hydrophobic molecules, near proteins, bilayers as well as in confinements e.g. in reverse micelles or protein grooves, in hydropobic cavities.[26–31] Based on the proximal surface, water can be either interfacial water or confined water.[27,32,33] Interfacial water is the one which is in touch with the surfaces and having an ability to exchange with the bulk water, for example near lipid bilayers.[34] In contrast, confined water is the one which have difficulties in exchanging with bulk water, it has

rotational as well as translational restrictions due to geometric confinement, for example in reverse micelle.[35,36]

1.1.1 Hydrophobicity and hydrophilicity

The term "hydrophobic effect" was first coined by Charles Tanford[37]. Hydrophobicity is an important phenomenon from the industrial point of view, since these are used in coating, film stability, adhesion, wetting, coagulation and mineral floatation and many more.[38] In general, hydrophobicity or hydrophobic effect is defined as the propensity of aggregation of nonpolar molecules in water resulting in phase separation on a large scale.[31] The word hydrophobic literally mean "water fearing". The nonpolar molecules separate out from the water phase to lower the contact area with water. In terms of thermodynamics, the free energy of transferring a hydrophobic molecule from vacuum to water is positive, whereas it is negative for hydrophilic molecules. Hydrophilic molecules have capacity to make ionic or hydrogen bonding with water or polar particles through electrostatic interactions. These features of water are important for the evolution of life. Hydrophobic interactions play a crucial role in folding of proteins, as well as in formation of lipid bilayer, cell membranes and self-assembly of surfactants in various shapes.[31,39,40]

1.1.2 Macroscopic quantities to define hydrophobicity

Macroscopically, hydrophobicity can be quantified using partition coefficient, solubility and contact angle.

1.1.2.1 Partition coefficient

The partition coefficient or distribution coefficient is the ratio of solute in organic phase and water phase.[41] The logarithm of this value is used to obtain the hydrophobicity. The partition coefficient can be measured experimentally by number of ways such as HPLC[42], electrochemical method[43] and pH-metric techniques[44] etc.

1.1.2.2 Solubility

Solubility can also be used to predict hydrophobicity of solutes. Commonly, the low solubility of hydrophobic groups increases the tendency of its separation from water to a great extent.[45] Generally used and accurate method for measuring the solubility is through equilibration of a suspension, followed by calculation of the solution composition.[46] The method requires sampling followed by separation to eliminate the solids and measurement of the concentration using for

example, a gravimetric, spectroscopic or a chromatographic methods. However, this Equilibrium Concentration (EqC) method[46] is tough and time taking. Two other methods are easily available: Solvent Addition (SA) and Temperature Variation (TV) methods[47], in which respectively the composition of the suspension and the temperature of the suspension are gradually changed until all crystals are dissolved.

1.1.2.3 Contact angle

Contact angle is conventionally used method to quantify hydrophobicity of a planar surface. It can be defined as the angle measured at a point where solid-liquid–vapor interface meets.[48] A unique equilibrium contact angle exists for the given solid, liquid, and vapor system at a precise thermodynamic condition. If the liquid scans the entire surface, the contact angle would be 0°. Usually, contact angle lesser than 90° indicates hydrophilic material and greater than that denotes hydrophobic material.[49] Some materials with highly porous surface called super-hydrophobic material exceeds contact angle 150°.[50] There are different experimental methods to measure contact angle such as pendant drop method, static and dynamic sessile drop method, and Washburn's equation capillary rise method etc.[51]

1.1.3 Microscopic quantities to define hydrophobicity

The exact quantity to define hydrophobicity on molecular scale is not available. Many definitions of the hydrophobicity exist in the literature, focusing on the hydrophobic aggregation due to solvent depletion around hydrophobes, entropic and enthalpic origin of size-dependent hydrophobicity, orientational preferences of hydration shell water, and so on.[52–56] Therefore, on microscopic scale defining hydrophobicity by only by one quantity seems difficult. Hydrophobic interactions are always inseparable with its hydration. Density depletion/increase relies upon the molecular size of hydrophobic solute. Since, protein folding arises because of the hydrophobic interactions, where water also plays a remarkable role in the conformational changes of protein.[57] Therefore, hydration shell water can be used as probe to predict hydrophobicity. Besides significant change in the first hydration shell structure and orientation, some studies report that second shell of the hydrophobes also gets influenced by presence of the surfaces.[58] Some useful order parameters to quantify local hydration shell structure can be listed here; (i) Radial Distribution Function (RDF) of solute-water[59] to examine the local density of the hydration shell by directly analyzing the population of water in the solvation shells, (ii) the distance and angle

dependent tetrahedral order parameter[60] (Q) to probe the tetrahedrality of water structure in the first solvation shell (iii) orientational order parameters[58] measures the orientational preferences of the second hydration shell around central water molecule (iv) number of hydrogen bonds[61] made by hydration shell water and (v) reorientational dynamics[62] of hydration shell water which uses time autocorrelation functions to extract the timescales of relaxations of the water dipolar vector and (vi) translational dynamics[63] of hydration shell water to account for the nature of diffusivity of water near solute surfaces using well-known mean squared displacement (MSD) measure. These are the few and routinely used parameters that are quite sensitive towards surface hydrophobicity. Other than these parameters, the size dependent solvation free energies can be used for any signatures of hydrophobicity.[64,65] At small length scales (less than 1 nm) of solute, it linearly varies with the excluded volume.[64] Whereas, for the solutes of size larger than 1 nm, or for assemblies of small solutes it linearly scales with surface area of that excluded volume.[66–68] Stanley and coworkers[69] introduced a tetrahedral entropy of water based on the local water structure around hydrophobes. Furthermore, number of hydrophobic contacts by using contact map analysis can also give hydrophobicity.[70] The "average area buried upon folding" in the protein core can also be a measure of hydrophobicity.[71] The hydrophobicity scales of amino acids can also be used as primary tool to predict hydrophobicity.[72]

The hydrophobic hydration has been extensively studied by Ben-Amotz and coworkers in recent years.[73–79] They use Raman scattering measurements with multivariate curve resolution (Raman-MCR) technique to probe first hydration shell of the hydrophobic parts of alcohols. Recent IR study measures the extended hydrogen bonded structure near noble gases to study hydrophobic hydration.[61] However, choosing pure hydrophobic model experimentally is challenging and probing only first solvation shell is tough task as well. Garde et al.[80] did molecular simulation studies of materials with varying their chemistry from –CF3, -CH3 to –OH, -CONH2, to generate realistic hydrophobic to hydrophilic surfaces, respectively. They have shown that the water density in the proximity of weakly hydrophobic surface (-CF3) is either bulk-like or greater than that and is the poor measure of hydrophobicity. On the other hand, the possibility of cavity formation or the binding free energy of hydrophobes with the interfaces provides a better quantitative measure which can also correlate with the macroscopic wetting parameter such as contact angle and is the excellent signature of hydrophobicity.[80]

1.2 Interfacial water

1.2.1   Hydrophilic molecules and surfaces

For the ionic bodies, the attractive and repulsive forces emerge between ions and water, ions and surfaces, surfaces and water.[81–84] The ion-induced change in solubility is the classical example of these interactions.[26] The Hofmeister ranked ions on ability of their salting-in (denaturation) and salting-out (precipitation) effects can be given as $CO_3^{2-} > SO_4^{2-} > S_2O_3^{2-} > H_2PO_4^{2-} > OH^- > F^- > HCO_2^- > CH_3COO^- > Cl^- > Br^- > NO_3^- > I^- > ClO_4^- > SCN^-$.[85] Anions present on the R.H.S. of the Cl^- are known for the salting-in effect of the protein i.e. favorable for the open state of protein also known as structure maker or kosmotropes. They make strong binding with water than water-water binding in the solution and thus water will be less active towards protein which helps protein to maintain its folded/native state more stable. While anions present on the L.H.S of the Cl^- are known for the salting-out effect of the protein i.e. favorable for the folded/collapsed state of it; also known as structure breakers or chaotropes. They interact weakly with water than water-water interaction in the solution. An impressive amount of experimental[86–90] as well as computational[30,82,91–93] studies are devoted to study the water properties in ion-hydration. While among the cations for a given anion can be given as: $(CH_3)_4N^+ > (CH_3)_2NH_2^+ > K^+ \sim Na^+ > Cs^+ > Li^+ > NH_4^+ > Mg_2^+ > Ca_2^+ >> C(NH_2)_3^+$.[85] Basically, the low charge ions are structure-breakers and highly charged ions are structure makers.[94] However, there can be reversals of ions to both the series of anions and cations.[84,85,95,96] Hofmeister series pertains to ions near macromolecular surface such as protein, polymers, biological membrane surfaces. There would be already some orientational and structural ordering due to these surfaces and therefore, in such cases, the pure effect of ions cannot be straightly associated to an isotropic dilute solutions.[84,85]

Surprisingly, MD simulation of hydrophilic hydroxylated silica surface shows that residence time of water in first hydration shell is insensitive to the hydrophilicity of surface.[97] The structural perturbation of water continues upto 1 nm from the surface and have strongest perturbation near surface. However, perturbation of diffusion rates and orientational relaxation of water is comparatively less.[97] On the other hand, translational and orientational relaxation dynamics of the interfacial water near DMPC lipid bilayer found to be slowed down considerably compared to bulk water.[98,99] Water translational motion is sub-diffusive or non-diffusive near this bilayer. Coupling between interfacial water and lipid hydrophilic head groups contribute largely to the alteration in

the dynamical behavior of water.[100] The interfacial water hydrogen bonded to the lipid head group moieties contribute to the lowering of dynamics.[98]

1.2.2   Hydrophobic surfaces

Hydrophobicity is responsible for the very low solubility of nonpolar molecules in water. Many theories have contributed to the understanding of hydrophobic hydration on microscopic scales such as Configurational entropy expansions[101], Pratt-Chandler integral-equation theory [56], Scaled-particle theory[102–104], and theories based on cavity-size distributions[55,105,106], information theory[45,105], perturbation theory[107], density fluctuations[108] and many other. [69,109,110]

1.2.2.1   Small solutes

Nonpolar solute does not form hydrogen bond with water and introduces excluded volume in the system. Chandler and coworkers[68] predicted the size dependent order-disorder crossover around the hydrophobic solute. When the size of the solute particle is less than a nanometer, water can maintain the hydrogen bonding network around the solute. In fact, it is previously stated that, water has an enhanced structuring around small non-polar solutes.[111] This was first observed in 1945 by Frank and Evans and termed as "iceberg" model[112], and later Kauzmann[113] proposed "entropic" origin of these hydrophobic attractions as depicted in Figure 1.1 (a and b). To create a space for a nonpolar solute, hydrogen bonded network must be broken. However, it should be accomplished without losing hydrogen bonds to avoid enthalpic penalty. To achieve this, water molecules rearrange around the hydrophobes in somewhat systematic way to construct that microscopic cage around it[94] as shown in Figure 1.1 (a).

These cages were referred as "iceberg" cages, because they seem like nonpolar solute is enclosed in an ice-like water shell. These are pseudo crystalline cages similar to those found in gas hydrates.[114] In gas hydrates (Figure 1.2), the cavities are formed by the strong and long lasting hydrogen-bonded network arranged in pentagonal fashion around the guest molecules instead of the hexagonal rings of the ice.[115] As Kauzmann stated, the cost of building such reasonably well-defined structure around hydrophobe is to loose rotational and translational freedom which results in the entropy decrease. When two such "caged" hydrophobes come together, the "structured" water around them is returned to the bulk state (as shown in Figure 1.1 (b)), resulting into an increase in entropy.[94]

However, in strict sense clathrate-like water structure around hydrophobes has not been observed at ambient thermodynamic conditions and debate is still ongoing on this topic.[61,62,116–121] Infact, Laage and Hynes[121] have shown that structuring is not required for entropy reduction and it is due to excluded volume. Ultimately, this results into the lower solubility values of small non-polar solutes in water. The entropy cost and resultant solubility can be compared directly to the properties of bulk water, e.g. radial distribution function. However, the possibility of aggregation of small hydrophobic groups is very less in water at low concentrations.[122]
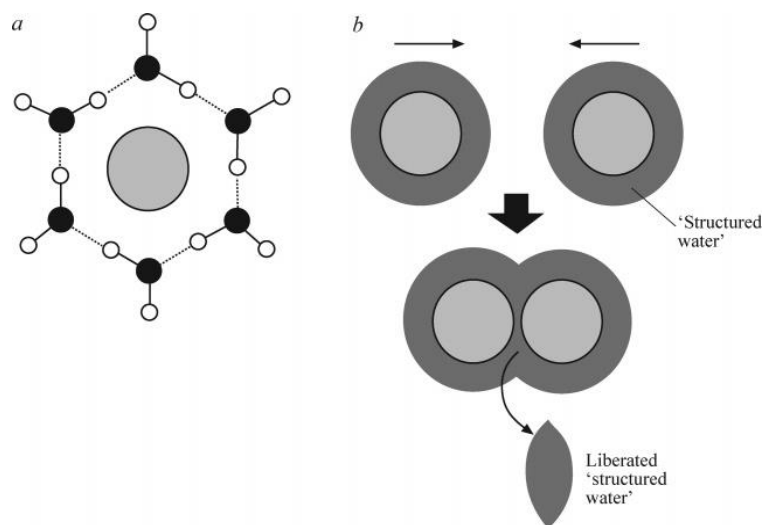
Figure 1.**1**: **(**a**)** Hydration of nonpolar solute depicting **"Iceberg"** model **(**b**)** Kauzmann**'**s portrayal of the attraction between nonpolar solutes**.** Schematics is reproduced from Chem**.** Rev**.** **2008**, 108 **(**1**),** 74–108**.**
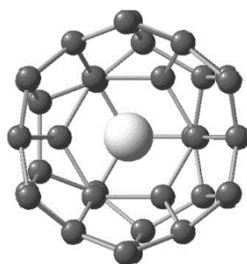
Figure 1.**2**: Structural representation of gas hydrate**.** Gray color represents the water oxygen and white is guest gas molecule**.**

In 1977, Pratt and Chandler[56] addressed the two possibilities of two non-polar species in water, whether they are stable when separated by a single file of water or will they come into contact with one other? The first condition is the solvent-separated minimum and second is the contact minimum. And later on it has been found out that, when two non-polar solutes are small, they preferably stay in solvent-separated state, while larger sized non-polar solutes come in contact.[123] This is depicted in Figure 1.3 (a), the RDF for the three different sizes, 0.7, 1.5 and 2.0 nm, and Figure 1.3 (b), depicts the solvent separated pair of hydrophobes and contact between them for the larger size. The stronger peaks in the pair distribution functions ascertain the above hypothesis.[124]
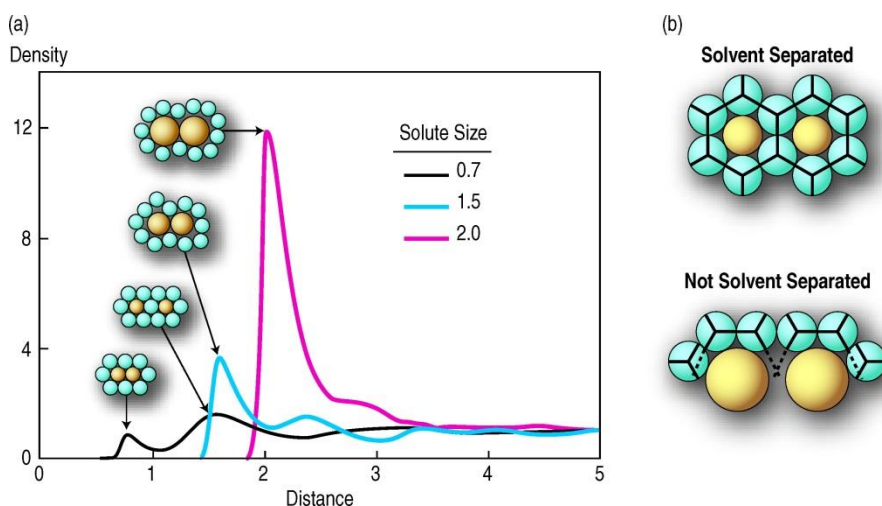
Figure 1.3: **(**a**)** RDF of solute-solute for different solute sizes**. (**b**)** Solvent separated minimum; and contact minimum**.** Schematics is reproduced from Annu**.** Rev**.** Biophys**.** Biomol**.** Struct**. 2005**, 34, 173–199.

1.2.2.2   Large solutes and surfaces

As the radius of spherical nonpolar solute increases beyond 1 nm, it becomes even more challenging for first-shell waters to maintain its hydrogen bonds due to geometrical restrictions imposed by the adjacent solute surface.[124] In this scenario, water forms a vapor-liquid interface to lower the surface free energy described by the higher entropy of the first hydration shell.[125,126] As proposed by Stillinger[102], the resulting energetic effect can encourage drying. Drying near extended hydrophobic surfaces such as the two parallel plates leads to the strong attractions between pair of such surfaces; these are the solvent-induced interactions.[68] Several studies report that these attractive interactions persist even if they are separated by distance greater than 10

nm.[49,122] But, this theory does not account for the changes in the orientational order of water and bond angle correlations.[126] Two oblate hydrophobic plates, when come in contact within a characteristic critical distance D_c, spontaneous drying occurs which is important in the protein aggregation and folding. Uniformly charged solutes strongly reduce this hydrophobic attraction, which results in total repulsive force at sufficiently high charge and a substantial asymmetry between cationic and anionic solute pairs occurs, the former experiences a lesser hydrophobic attraction.[52] While the situation becomes more complicated when solutes have distinct arrangements of charges.[52]

Attractive interaction between hydrophobic solutes is associated with surface dewetting which occurs below a critical inter-particle separation, D_c.[127] where, D_c is given by the Kelvin's equation[122]

$$D_c = \frac{2(\gamma_{wl} - \gamma_{wv})}{\rho \Delta \mu} \tag{1.1}$$

where ρ is the liquid number density, $\Delta \mu$ is the difference in chemical potential of the liquid from liquid/gas coexistence value, γ is the interfacial tension, and subscripts w, l, and v denote the walls and the intervening liquid or vapor phase, respectively. For strongly hydrophobic solutes, at ambient conditions, with the bulk pressure P_b=1 atm, and $\rho \Delta \mu \sim P_b$, the distance D_c below which the vapor phase is favored is of the order of 100 nm.[127]

Berard et al.[128] did the first simulation of two repulsive walls to show drying transition. Enormous amount of literature reports on hydrophobic hydration of planar and spherical confinement.[129–131]As mentioned above, for the extended solute surfaces, solvent density near to it, is depleted relative to the bulk water density.[52,130,132] This density depletion quite often termed as dewetting/cavitation/capillary action/bubble formation between two hydrophobic plates.[108,132,133] Wolde et al.[133] developed a model that accounts for these large length scale effects induced by surfaces. The cavitation occurs via gas bubble formation of critical size between the plates through density fluctuations and later develops a vapor layer suggesting that liquid to vapor transition is a nucleation driven process with formation critical vapor nucleus. The transition path sampling of cavity formation between two hydrophobic plates is nicely demonstrated by Bolhuis and Chandler.[134]

The distance dependent exponential decrease of the attractive long-range forces between hydrophobic plates in water is characterized as the hydrophobic force law (HFL).[135] Molecular dynamics (MD) simulations done by Berry and coworkers[136] and Bagchi and coworkers[135] found that the microscopic origin of the attraction is governed by the orientations of water around them, rather than conventional density-dependence of hydrophobic attraction. Schematics in Figure 1.4 displays the domains of the polarized water around hydrophobes and induced dipoles on the hydrophobic solute surfaces. Bagchi and coworkers[135] have concluded that the attraction between the hydrophobic rods at large separation distance arises mainly because of a destructive interference of the orientations of water molecules present in between them. Hydrophobic aggregation initiates in such a way that the non-polar particles surrounded by the water coating approaches each other due to electrostatic forces. The precursor regime arises before the entropy rise due to freeing those structured water to bulk. van der Waals attractive interaction then takes over and dries out contact area between the hydrophobes. Therefore, the density alone cannot serve as the quantitative measure of hydrophobicity. Zhang et al. [137] did a MD simulation of hydrophobic plates investigated the dielectric response of the confined liquid as a function of the distance. They observed that dipolar fluctuations are altered to large distances nearly tens of nanometers as well as strong directional anisotropies have been noticed in the dielectric relaxation.
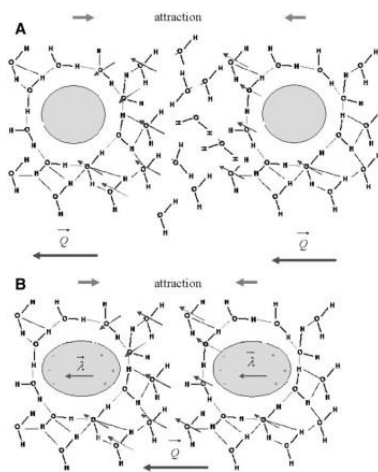
Figure 1.4: Schematics of polarized water domains initiates long‑range attraction between hydrophobes **(**a**)** and induced dipoles on the hydrophobic solute surfaces **(**b**).** Schematics is reproduced from Biophysical Journal, **2007**, 92**(**2**)** 373–378**)**

1.2.2.3 Chemical and geometrical heterogeneity of surfaces

A recent MD simulation explores the connection among microscopic (surface atomic polarity) and mesoscopic (liquid drop contact angle) characteristics of water on silica surface.[138] The results show that tuning the polarity as well as topography of the surface act in concert with the non-uniform distribution of charge can modify hydrophobicity significantly and would be extreme when substantial surface polarity is present. First hydration shell structure around solute i.e. orientation and packing is subtle to the geometry and chemistry of solute–water interactions.[139] Indeed, a variety of phenomena such as salt effects on protein stability and solubility, salting-in and salting-out of hydrophobic solutes, the well-known Hofmeister effects, and selectivity of ion channels, highlight the significance of charge density dependent solvation of ionic solutes. [84,139,140] Further, the chemistry of these substances also influences the hydrophobicity.[80] The water structure also strongly depends on the surface topography including shallow or deep concave grooves, convex patches, and planar surfaces.[141] Recently, Altabet and Debenedetti[142] proposed a theory which accounts for the material flexibility in deriving the critical drying distance (D_c) between the plates having flexibility. The proposed equation is given by the sum of drying distance for perfectly rigid confining substances and an additional term which accounts for the flexibility of substance.

1.3 Confined water

The confined water on nanometer length scales required for the biological molecular machines to designing of self-assembling nanoscale materials and performance of fuel cells.[143] Perhaps the most straightforward outcome of nano-confinement of water is the development of different phase behavior.[143] Confined water has several drastically different properties as compared to bulk water. Few examples discussed here are confined water in carbon nanotubes, reverse micelles, and biological water channels.

1.3.1 Carbon Nanotubes

The one dimensional water channel inside single walled carbon nanotubes (SWCNTs) can be considered a good model for nano-confinement. Water confined within such CNTs shows anomalous behaviors such as formation of specific ice phases[144–146], and an unusually high water permeability.[147,148] The disorder-to-order transformation of the ice-like phases can be purely

attained via modification the radii/size of the CNTs.[144,149] Confined water molecules in thin CNTs are organized in a one layer and display solid like structuring at 298K due to strong hydrogen bonding between neighboring molecules.[146] The faster water transport through CNTs is attributed to the strong modifications of hydrogen bonded networks and low friction flow of monolayer of water through it.[150] But the origin of the ultrafast water flow is still remained in debate.[150] Some of the reports illustrates that the origin of this extraordinary water permeability is due to curvature-induced effects[32] and smoothness[147] of the CNTs. Free water OH bonds directing to the wall of tube and the reduced intermolecular hydrogen bonding in water results into the increased flow rates in CNTs.[147,151] Interestingly, water inside CNTs have highly anisotropic orientational dynamics. Dipolar orientation of water is quite slow of the order of several nanoscale and HH vector orientation is ultrafast ~150fs, 10 times faster than bulk water.[146] In fact, rough hydrophilic surfaces does not show the enhancement in the water transport unlike CNTs.[147,152] Such systems are used as a model systems for the biological channels to mimic the rapid water flow through aquaporin or proton conduction through protein pump and enzymes, as well as in designing nanofluidics and molecular filtration devices or fuel cells.[147,150,153] Other than the fast transportation of water through nanotubes, recent study reports the anisotropy in the dielectric properties of water along the axial and perpendicular directions, they approach the bulk behavior in opposite manner.[154]

1.3.2 Water in channels of biological membrane: Aquaporins

Biological cellular channels serve as chemically selective gatekeepers with protein walls that permit enormously rapid transportation water and ions.[148] Aquaporins (AQP); the integral membrane proteins acting as channels through which small solute and water transportation through membrane takes place. In mammalian cells, above 10 isoforms (AQP0-AQP10) are found. They are present in several kinds of tissues and cells such as in blood vessels, eye, ear, intestine, kidney proximal tubules, kidney collecting ducts and so on.[155] Experimentally measured time to transmit one water molecule through AQP1 is 10 ns and conformational changes of protein affects water over a significantly larger timescales.[156] While the MD simulations of AQP0 suggest that the low permeability of water through it is to maintain the mechanical stability of junction.[157] The total free energy map of water transport through AQP4 has been elucidated through MD simulations.[158] MD simulations have also contributed to the understanding on high degree of

selectivity and efficiency in water or glycerol passage, while managing the exclusion of ions, specially H^+ ions, at the same time.[158,159] Nevertheless, a molecular picture of the impact of both the protein's electric field and desolvation effects on the barrier still remain elusive. [158,160,161]

1.3.3   Water in reverse micelles

Reverse micelles (RMs) are versatile models for the crowded systems, many important bio-chemical reaction takes place in such environment e.g. membranous organelles, the interior of macromolecular chaperones, and extracellular spaces.[162] It is a spherical system having water nanopool confined in monolayer of surfactant in oil environment. The confinement size in the reverse micelles are often characterized by the water loading ratio $w_0 = [H_2O]/[Surfactant]$.[163] The most commonly used surfactant for the studies is AOT (aerosol-OT) surfactant; an anionic surfactant.[163–168] Examples of other neutral surfactants forming RMs are diethylene glycol monodecyl ether, Igepal, etc. and cationic surfactants e.g. CTAB.[167,169–171] Water in such confinement have drastically different properties than bulk water.[172] The water inside the RMs is generally divided into two regions, namely interfacial/bound water and free/bulk water.[173] The free water is expected to gradually recover its bulk properties as the size of water nanopool increases.[173] Interfacial water has exceptionally slow dynamics compared to bulk water in respect to both reorientation as well as translational dynamics.[174] However, in purely hydrophobic confinement, changes in the water dynamics is modest or faster than bulk.[175] In spherical confinement, the dielectric behavior of water is also altered with the confinement size.[176]

1.4 Biological water

Water exhibits different properties when present nearby biomolecular surfaces, such as near proteins, in the grooves of DNA, lipid bilayers, in cells etc.[37,98,99,177–179] The unique characteristics it exhibits near these surfaces makes water different and is widely termed as "biological water".[180] The modification in the hydrogen bonding network near biological surfaces occurs, the extended network of it can be lost either fully or partially in certain situations. [180] The water molecules can be organized locally and can have different structural patterns than bulk water. The biological water can be classified in two categories: "free" and "bound" water molecules.[179] The bound water molecules have stronger interaction and hydrogen bonding with the charged/polar moieties present in the biological surfaces. While many free water molecules behave like bulk water;

weakly bound or partially free. The dynamics of the biological water also covers a wide range of time; a faster (like bulk water) and slower dynamics because of bound water molecules.[179] NMR studies show residence times in the diverse range of 300-500 ps,[181] 10-200 ps,[182] and of the order of 10 ns[183] shown through dielectric relaxation experiments. Given the chemical heterogeneity present on the surfaces, water density also differs at those patches.[59] However, Martin and Matyushov[184] argued the idea of special distinction of "biological water". They suggest that density fluctuation dynamics of hydration shells reveal the coupling of solute-solvent dynamics and should not be distinctly characterized as "biological water." Density fluctuation parameter does not influence as much as the orientation properties of water by the presence of nearby protein/charged interface.[185] Depending on the properties under consideration, the water orientational structure perturbed by the protein continues almost up to 3 to 5 hydration shells.[184]

1.5 Role of water in different processes

Water is essential in driving many processes, some of them are discussed in the next subsections.

1.5.1   Protein folding and stability

Proteins are made up of around 20 different alpha-amino-acids and have diverse functional groups such as aromatic, carboxylic, amide, thiol, hydroxyl and so on. It achieves a characteristic 3D folded structure under normal temperature, pH, and ionic strength conditions.[186] It exists in different structural varieties such as primary (amino-acid sequence), secondary (structural elements such as alpha helix, β sheets), tertiary and quaternary structures. Hydrogen bonds and hydrophobic interactions in water are major contributors to protein structure and stability.[186,187] This hydrophobic effect acts a basis for the mechanism of the characteristics folded 3D structure of protein.[186] Therefore, the protein in oversimplified manner is a "polymer micelle" where hydrophobic residues are buried inside and hydrophilic residues are exposed to water.[94] Some studies reveal that protein folding is a two stage process; in the first stage the protein is partially hydrated in the collapsed interior core and in the second stage, the residual water slowly expelled from that core.[94] But, some water molecules still remain in the core, forms a strong hydrogen bonds to the peptide. Sometimes during the process of folding, water molecules gets "frozen" as an element of the secondary structure and not as an lubricant.[18,94]

The thermodynamic analysis of folding $\rightleftharpoons$ unfolding process gives the measure of protein stability. [186] In such analysis, the entropy and enthalpy changes are considered. The folding free energy can be expressed as $\Delta G = \Delta G_{folded} - \Delta G_{unfolded}$ between the folded and unfolded conformation. It can be elaborately written as

$$\Delta G = \Delta H_{chain} + \Delta H_{solvent} - T(\Delta S_{chain} + \Delta S_{solvent}) \tag{1.2}$$

where enthalpic change is $\Delta H = \Delta H_{folded} - \Delta H_{unfolded}$ and entropic change is $\Delta S = \Delta S_{folded} - \Delta S_{unfolded}$. It provides a qualitative analysis of thermodynamics of protein folding process. Rocha et al.[186] have given the detailed analytical solutions in their paper. At normal temperature, the entropy of both polar and non-polar groups are negative which indicates that ordering is created in water environment.[188] The entropy of the non-polar residues increases with an increase in temperature which shows their less ability of water ordering at higher temperature; allows an easy dynamics of water molecules. In contrast, for the polar residues, entropy decreases with increasing temperature. This results in ordered water molecules than a bulk water with the increase in temperature around hydrophilic residues. On the other hand, the enthalpy changes in transferring hydrophilic groups from protein interior to aqueous medium at lower temperature is positive and negative at higher temperature.[189]. At lower temperature, the water is structurally more ordered, breakdown of such structure as well as polar interactions within protein results in positive change in enthalpy. While transferring non-polar residues from protein core to aqueous medium is negative below 298K and positive above.[189,190] In conclusion, the protein stability is directly tied to the structural ordering and hydrogen bonding of water molecules around polar and non-polar groups.

1.5.2 Enzyme activity

Enzymes are the substances known as biological catalyst, that lowers the activation energy of the biological reaction without changing itself and hence alters the kinetics of the reactions. They have high affinity for the transition state of the reaction. Enzyme requires a certain amount of bound water to perform the function fully as well as to maintain their natural conformation.[191–194] At the protein active site, bound water will play more than structural role: it can act as nucleophile or a proton, thus it can be a reagent in biological reactions.[94] Generation of larger polarizability at the protein active site due to electrostatic interactions in water reduces activation energy of proton

or electron transfer.[195] Both of these processes are further facilitated by the structured water which connects electron donor to electron acceptor or proton donor to proton acceptor. This transfer is faster when linking water molecules have stronger hydrogen bonding. And this hydrogen bonded network of water plays a catalytic role in oxidation of water such as in spinach photosystem II. [196] Local ordered water structures and water wires formed by hydrogen bonding those are proton conductors, sometimes affected by the binding by different ions e.g. Cl^-/H^+. [197,198] Water also helps enzymes in back and forth displacement of the products as well as substrate from the active sites.[199]

1.5.3   Bound water: drug binding affinity

In general, water hydrogen-bonds gets reorganized/displaced in the drug binding process to the target protein.[94,200,201] The loosely expressed idea is that the water molecule having "unfavorable" thermodynamic signature compared to bulk is displaced by ligand with extra strong binding affinity than displacing a water molecule with "favorable" signature.[202,203] Huang et al.[204] in their recent study have shown the role of water and water-mediated interactions in blocking unfavorable binding sites and in stabilizing the binding modes of maltotriose. Water typically helps in molecular recognition and association process.[205,206] However, the thermodynamic role of water in ligand-binding to the receptor is still not fully understood.[206] Baron et al.[206]   shown thermodynamically how water plays a role in the cavity-ligand recognition by taking into account enthalpic and entropic contributions of bound water. The comparative radii of the binding cavity and the binding ligand helps in determining the thermodynamics as well as kinetics of the hydrophobic cavity-ligand binding system.[207] The binding energy can be ascribed to the change in free energy due to the rupture, formation and reorganization of the network of hydrogen bonds in association of two hydrophobic groups.[208] Hydrophobic ligand groups assist removing of water molecules from the binding pockets (before ligand binding) because of a decrease in the interference of previously bound water with the protein's internal hydrogen bonding and enhanced bulk hydrogen bonding.[209] Nevertheless, efficiency of ligand binding is also influenced by characteristic dynamics of hydration.[200] In the enzyme-inhibitor complex of barnase-barnstar, interfacial water exhibits glassy relaxation dynamics at the tightly bound complex even at room temperature.[210] The smaller size, good polarity and good conformational stability of water in combination with directionality and interaction strengths altogether assures decent fit while recollecting the flexibility and easiness of reversibility. The driving force for binding not only

depends on the interaction of the biomolecules with one another but also on energetic cost of crucial water removal and its displacement as well as on the energy gain for the succeeding microscopic reorganization of solvation shell.[57,208,211]

1.5.4   Self-assembly processes of amphiphilic molecules

Molecular self-assembly is a multidisciplinary field of research ranging from nanomaterials to biological and chemical application.[212,213] The self-assembly is repetitive association of building blocks to form highly ordered 3D structures.[212] The wide variety of structures they form can be micelles, vesicles, nano-fibrils, bilayers, and lamellae.[27,39,78,214] The amphiphiles can be surfactants, lipids, proteins or polymers as well.[212,213] Water-mediated hydrophobic interactions between the hydrophobic groups, hydrogen bonding and electrostatic interactions between the peptide backbones or amphiphiles and with water are the major driving forces for the self-assembly process.[215–217] The macroscopic or mesoscopic structures thus formed are water soluble and have applications in detergent, emulsifiers, and cosmetics etc.[214] In the primitive sense, this concept was described by the hydrophobic interactions between the hydrophobic groups of the side-chain groups or biomolecules, to stick to each other, so that the exposure to the solvent is minimized such as during protein folding and micelle formation.[217] Hydrogen bonding in the peptide backbone drives the longitudinal packing of peptide monomers to form β sheets. In the recent experimental and MD studies, it has been shown that in the confinement peptide has tendency to form secondary structures with increasing the hydration size of water pool of reverse micelles.[218,219] Lipids and surfactants are perhaps the simplest amphiphilic molecules which forms various structures in aqueous medium such as bilayers, vesicles, micelles and so on. Whereas, peptide and proteins are complex amphiphilic molecules, gives rise to various folded structure in water.[212]

1.6 Thesis organization

As discussed so far, water is the backbone of life. Although being a small molecule, the understanding of water properties is still lacking. Therefore, this thesis explores mainly the context dependent nature of water in various model systems. The work is further extended to understand the structure and conformational dynamics of the CXCR1 peptide in AOT RM confinement and

self-assembly process of SDS surfactant under methane hydrate formation conditions. The thesis is organized into nine chapters mentioned below;

Chapter 1, covers the general introduction of water in various contexts, molecular level aspects and its research significance.

Chapter 2, presents the methodology which is used in this thesis.

Chapter 3, discusses structural order and vibrational dynamics of water molecules around spherical hydrophobic solutes.

Chapter 4, demonstrates structural order and vibrational dynamics of water molecules around flexible, rigid polymers and alcohol molecules.

Chapter 5, explores the bulk like water and perturbation length-scale of water properties in the hydrophobic and hydrophilic confinement of water-in-oil (W/O) and AOT reverse micelle systems with increasing the hydration size of water pool.

Chapter 6, describes the structural, dynamical properties and perturbation length-scale of water near bilayers (roughly planar surfaces) of differently charged surfaces with special attention on orientational relaxation dynamics.

Chapter 7, explores the conformational dynamics of the CXCR1 peptide under AOT reverse micelle confinement with increasing the hydration size of water pool.

Chapter 8, sheds light on morphology and dynamics of SDS surfactants under methane hydrate forming conditions emphasizing on the effect of CAPB co-surfactant and methane absorption.

Chapter 9, summarizes the work presented and propose future directions on the topic of water using MD simulation.

1.7 References

(1)   Stokely, K.; Mazza, M. G.; Stanley, H. E.; Franzese, G. **2008**.

(2)   Golecki, I.; Jaccard, C. *J. Phys. C Solid State Phys.* **1978**, *11* (20), 4229–4237.

(3)   Preston-Thomas, H. *Metrologia* **1990**, *27* (1), 3–10.

(4)   Herrig, S.; Thol, M.; Harvey, A. H.; Lemmon, E. W. *J. Phys. Chem. Ref. Data* **2018**, *47* (4), 043102.

(5)   Xiong, X. M.; Chen, L.; Zuo, W. L.; Li, L. F.; Yang, Y. Bin; Pang, Z. Y.; Zhang, J. X. *Chinese Phys. Lett.* **2014**, *31* (7), 076801.

(6)   Ni, K.; Fang, H.; Yu, Z.; Fan, Z. *J. Mol. Liq.* **2019**, *278*, 234–238.

(7)   Guildner, L. A.; Johnson, D. P.; Jones, F. E. *Vapor Pressure of Water at Its Triple Point*; 1976.

(8)   Goncharuk, V. V.; Orekhova, E. A.; Skil'skaya, M. D.; Kavitskaya, A. A. *J. Water Chem. Technol.* **2015**, *37* (3), 103–107.

(9)   Zhao, L.; Ma, K.; Yang, Z. *Int. J. Mol. Sci.* **2015**, *16* (12), 8454–8489.

(10)   Vasisht, V. V.; Mathew, J.; Sengupta, S.; Sastry, S. *J. Chem. Phys.* **2014**, *141* (12), 124501.

(11)   Zhigang Liu; Kim, A. K. *J. Fire Prot. Eng.* **1999**, *10* (3), 32–50.

(12)   Pallares, G.; El Mekki Azouzi, M.; González, M. A.; Aragones, J. L.; Abascal, J. L. F.; Valeriani, C.; Caupin, F. *Proc. Natl. Acad. Sci. U. S. A.* **2014**, *111* (22), 7936–7941.

(13)   Wirgin, A. **2017**.

(14)   Stanley, H. E.; Buldyreva, S. V.; Canpolat, M.; Meyer, M.; Mishima, O.; Sadr-Lahijany, M. R.; Scala, A.; Starr, F. W. *Phys. A Stat. Mech. its Appl.* **1998**, *257* (1–4), 213–232.

(15)   Stanley, H. E.; Kumar, P.; Xu, L.; Yan, Z.; Mazza, M. G.; Buldyrev, S. V.; Chen, S. H.; Mallamace, F. *Phys. A Stat. Mech. its Appl.* **2007**, *386* (2), 729–743.

(16)   Chaplin, M. F. *Biophys. Chem.* **2000**, *83* (3), 211–221.

(17)   Suresh, S. J.; Naik, V. M. *J. Chem. Phys.* **2000**, *113* (21), 9727–9732.

(18)   Levy, Y.; Onuchic, J. N. *Proceedings of the National Academy of Sciences of the United States of America*. National Academy of Sciences March 9, 2004, pp 3325–3326.

(19) *Biophysics: A Physiological Approach - Patrick F. Dillon - Google Books*.

(20) Liu, J.; He, X.; Zhang, J. Z. H.; Qi, L. W. *Chem. Sci.* **2018**, *9* (8), 2065–2073.

(21) Sripa, P.; Tongraar, A.; Kerdcharoen, T. *J. Mol. Liq.* **2017**, *248*, 271–277.

(22) Pethes, I.; Pusztai, L. *J. Mol. Liq.* **2015**, *212*, 111–116.

(23) Ruberto, S.; Reutzsch, J.; Weigand, B. *Int. Commun. Heat Mass Transf.* **2016**, *77*, 190–194.

(24) Chen, B.; Ivanov, I.; Klein, M. L.; Parrinello, M. *Phys. Rev. Lett.* **2003**, *91* (21), 215503.

(25) Layfield, J. P.; Troya, D. *J. Phys. Chem. B* **2011**, *115* (16), 4662–4670.

(26) Kim, J. S.; Wu, Z.; Morrow, A. R.; Yethiraj, A.; Yethiraj, A. *J. Phys. Chem. B* **2012**, *116* (39), 12007–12013.

(27) Zhao, W.; Moilanen, D. E.; Fenn, E. E.; Fayer, M. D. *J. Am. Chem. Soc.* **2008**, *130* (42), 13927–13937.

(28) Patra, A.; Luong, T. Q.; Mitra, R. K.; Havenith, M. *Phys. Chem. Chem. Phys.* **2014**, *16* (25), 12875–12883.

(29) Mountain, R. D.; Thirumalai, D. *Proc. Natl. Acad. Sci. U.S.A* **1998**, *95*, 8436–8440.

(30) Dewan, S.; Carnevale, V.; Bankura, A.; Eftekhari-Bafrooei, A.; Fiorin, G.; Klein, M. L.; Borguet, E. **2014**, *30*, 8065.

(31) Garde, S. *Nature* **2015**, *517* (7534), 277–279.

(32) Falk, K.; Sedlmeier, F.; Joly, L.; Netz, R. R.; Bocquet, L.; Lpmcn, †. **2010**.

(33) Sarkar, N.; Das, K.; Datta, A.; Das, S.; Bhattacharyya, K. *Solvation Dynamics of Coumarin 480 in Reverse Micelles. Slow Relaxation of Water Molecules*; 1996.

(34) Pal, S. K.; Peon, J.; Bagchi, B.; Zewail, A. H. *J. Phys. Chem. B* **2002**, *106* (48), 12376–12395.

(35)   Zulauf, M.; Eicke, H. F. *J. Phys. Chem.* **1979**, *83* (4), 480–486.

(36)   Fayer, M. D.; Levinger, N. E. *Annu. Rev. Anal. Chem.* **2010**, *3* (1), 89–107.

(37)   Tanford, C. *Science* **1978**, *200* (4345), 1012–1018.

(38)   Olga I.Vinogradova. *J. Colloid Interface Sci.* **1995**, *169* (2), 306–312.

(39)   Ling, S.; Kaplan, D. L.; Buehler, M. J. *Nat. Rev. Mater.* **2018**, *3* (4), 1–15.

(40)   Israelachvili, J. N.; Mitchell, D. J.; Ninham, B. W. *J. Chem. Soc. Faraday Trans. 2* **1976**, *72* (0), 1525.

(41)   JEPSON, G. W.; BLACK, R. K.; MCCAFFERTY, J. D.; MAHLE, D. A.; GEARHART, J. M. *Toxicol. Sci.* **1994**, *22* (4), 519–524.

(42)   Coskun, O. *North. Clin. Istanbul* **2016**, *3* (2), 156.

(43)   Bard, a; Faulkner, L. *Russ. J. Electrochem.* **2002**, *38* (12), 1505–1506.

(44)   Jennings, P. A.; Mullen, C. A.; Roy, M. In *Encyclopedia of Life Sciences*; John Wiley & Sons, Ltd: Chichester, UK, 2010.

(45)   G. Hummer, *; S. Garde; A. E. García; M. E. Paulaitis, † and; Pratt, L. R. *J. Phys. Chem. B* **1998**, *102* (51), 10469–10482.

(46)   Takács-Novák, K.; Urac, M.; Horváth, P.; Völgyi, G.; Anderson, B. D.; Avdeef, A. *Eur. J. Pharm. Sci.* **2017**, *106*, 133–141.

(47)   Reus, M. A.; Li, P. W.; Guguta, C.; Kramer, H. J. M.; Ter Horst, J. H. *Solubility: Importance, Measurements and Applications*.

(48)   Dwivedi, C.; Pandey, I.; Pandey, H.; Ramteke, P. W.; Pandey, A. C.; Mishra, S. B.; Patil, S. In *Nano- and Microscale Drug Delivery Systems: Design and Fabrication*; Elsevier, 2017; pp 147–164.

(49)   Hua, L.; Zangi, R.; Berne, B. J. *J. Phys. Chem. C* **2009**, *113* (13), 5244–5253.

(50)   Shirtcliffe, N. J.; McHale, G.; Atherton, S.; Newton, M. I. *Advances in Colloid and*

Interface Science. Elsevier December 15, 2010, pp 124–138.

(51)   Bikerman, J. *Ind. Eng. Chem. Anal. Ed.* **1941**, *13* (6), 443–444.

(52)   Dzubiella, J.; Hansen, J.-P. *J. Chem. Phys.* **2004**, *121* (11), 5514–5530.

(53)   Banerjee, S.; Singh, R. S.; Bagchi, B. *J. Chem. Phys.* **2015**, *142* (13).

(54)   Despa, F.; Berry, R. S. *Biophys. J.* **2007**, *92* (2), 373–378.

(55)   Pohorille, A.; Pratt, L. R. *J . Am. Chem. SOC* **1990**, *112*, 5066–5074.

(56)   Pratt, L. R.; Chandler, D. *J. Chem. Phys.* **1977**, *67* (8), 3683–3704.

(57)   Lim, V. I.; Curran, J. F.; Garber, M. B. *J. Theor. Biol.* **2012**, *301*, 42–48.

(58)   Bandyopadhyay, D.; Choudhury, N. *J. Chem. Phys.* **2012**, *136* (22), 224505.

(59)   Merzel, F.; Smith, J. C. *Is the First Hydration Shell of Lysozyme of Higher Density than Bulk Water?*; 2002; Vol. 16.

(60)   Errington, J. R.; Debenedetti, P. G. *Nature* **2001**, *409* (6818), 318–321.

(61)   Grdadolnik, J.; Merzel, F.; Avbelj, F. **2017**, *114* (2).

(62)   Galamba, N. *J. Phys. Chem. B* **2013**, *117* (7), 2153–2159.

(63)   Rani, P.; Biswas, P. *J. Phys. Chem. B* **2015**, *119* (42), 13262–13270.

(64)   Lum, K.; Chandler, D.; Weeks, J. D. *J. Phys. Chem. B* **1999**, *103* (22), 4570–4577.

(65)   Li, I. T. S.; Walker, G. C. *Proc. Natl. Acad. Sci. U. S. A.* **2011**, *108* (40), 16527–16532.

(66)   Huang, D. M.; Chandler, D. *Proc. Natl. Acad. Sci.* **2000**, *97* (15), 8324–8327.

(67)   David M. Huang and; David Chandler. *J. Phys. Chem. B* **2002**, *106* (8), 2047–2053.

(68)   Chandler, D. *Nature* **2005**, *437* (7059), 640–647.

(69)   Kumar, P.; Buldyrev, S. V.; Stanley, H. E. *Proc. Natl. Acad. Sci. U. S. A.* **2009**, *106* (52), 22130–22134.

(70)   Rajapandian, M.; Rao Konda, S.; Krishnamoorthy, S.; J.; M. R.; Rao, S. *Prediction of Hydrophobic Core Using Contact Map and Minimal Connected Dominating Set Chemical Graph Theory View Project Pre A* Algebra View Project Prediction of Hydrophobic Core Using Contact Map and Minimal Connected Dominating Set*; 2015; Vol. 13.

(71)   Dyson, H. J.; Wright, P. E.; Scheraga, H. A. *Proc. Natl. Acad. Sci. U. S. A.* **2006**, *103* (35), 13057–13061.

(72)   Bull, H. B.; Breese, K. *Arch. Biochem. Biophys.* **1974**, *161* (2), 665–670.

(73)   Davis, J. G.; Gierszal, K. P.; Wang, P.; Ben-Amotz, D. *Nature* **2012**, *491* (7425), 582–585.

(74)   Perera, P. N.; Fega, K. R.; Lawrence, C.; Sundstrom, E. J.; Tomlinson-Phillips, J.; Ben-Amotz, D. *Proc. Natl. Acad. Sci. U. S. A.* **2009**, *106* (30), 12230–12234.

(75)   Davis, J. G.; Rankin, B. M.; Gierszal, K. P.; Ben-Amotz, D. *Nat. Chem.* **2013**, *5* (9), 796–802.

(76)   Wilcox, D. S.; Rankin, B. M.; Ben-Amotz, D. *Faraday Discuss.* **2013**, *167* (0), 177.

(77)   Rankin, B. M.; Ben-Amotz, D.; van der Post, S. T.; Bakker, H. J. *J. Phys. Chem. Lett.* **2015**, *6* (4), 688–692.

(78)   Long, J. A.; Rankin, B. M.; Ben-Amotz, D. *J. Am. Chem. Soc.* **2015**, *137* (33), 10809–10815.

(79)   Ben-Amotz, D. *J. Phys. Chem. Lett.* **2015**, *6* (9), 1696–1701.

(80)   Godawat, R.; Jamadagni, S. N.; Garde, S. *Proc. Natl. Acad. Sci. U. S. A.* **2009**, *106* (36), 15119–15124.

(81)   Rajamani, S.; Truskett, T. M.; Garde, S. *Proc. Natl. Acad. Sci. U. S. A.* **2005**, *102* (27), 9475–9480.

(82)   Jungwirth, P.; Tobias, D. J. *Chem. Rev.* **2006**, *106* (4), 1259–1281.

(83)   Song, J.; Kang, T. H.; Kim, M. W.; Han, S. *Physical Chemistry Chemical Physics*. Royal

Society of Chemistry April 7, 2015, pp 8306–8322.

(84) Parsegian, V. A. *Nature* **1995**, *378* (6555), 335–336.

(85) Marcus, Y. *Chem. Rev.* **2009**, *109* (3), 1346–1370.

(86) Tian, C. S.; Shen, Y. R. *Proc. Natl. Acad. Sci. U. S. A.* **2009**, *106* (36), 15148–15153.

(87) Perera, P. N.; Browder, B.; Ben-Amotz, D. *J. Phys. Chem. B* **2009**, *113* (7), 1805–1809.

(88) Tauber, M. J.; Mathies, R. A. *J. Am. Chem. Soc.* **2003**, *125* (5), 1394–1402.

(89) Mondal, J. A.; Nihonyanagi, S.; Yamaguchi, S.; Tahara, T. *J. Am. Chem. Soc.* **2012**, *134* (18), 7842–7850.

(90) Mondal, J. A.; Nihonyanagi, S.; Yamaguchi, S.; Tahara, T. *J. Am. Chem. Soc.* **2010**, *132* (31), 10656–10657.

(91) Vazdar, M.; Uhlig, F.; Jungwirth, P. *J. Phys. Chem. Lett.* **2012**, *3* (15), 2021–2024.

(92) De, T. K.; Maitra, A. *Adv. Colloid Interface Sci.* **1995**, *59* (C), 95–193.

(93) Wernersson, E.; Jungwirth, P. *J. Chem. Theory Comput.* **2010**, *6* (10), 3233–3240.

(94) Ball, P. *Chem. Rev.* **2008**, *108* (1), 74–108.

(95) Salis, A.; Cristina Pinna, M.; Bilaničová, D.; Monduzzi, M.; Nostro, P. Lo; Ninham, B. W. *J. Phys. Chem. B* **2006**, *110* (6), 2949–2956.

(96) Salomäki, M.; Tervasmäki, P.; Areva, S.; Kankare, J. *Langmuir* **2004**, *20* (9), 3679–3683.

(97) Lee, S. H.; Rossky, P. J. *The Journal of Chemical Physics*. American Institute of Physics February 15, 1994, pp 3334–3345.

(98) Srivastava, A.; Debnath, A. *J. Chem. Phys.* **2018**, *148* (9), 094901.

(99) Srivastava, A.; Malik, S.; Debnath, A. *Chem. Phys.* **2019**, *525*.

(100) Srivastava, A.; Karmakar, S.; Debnath, A. **2018**.

(101) Lazaridis, T.; Paulaitis, M. E. *J. Phys. Chem* **1992**, *96*, 3841–3855.

(102) Stillinger, F. H. *J. Solution Chem.* **1973**, *23* (2).

(103) Reiss, H. John Wiley & Sons, Inc.; pp 1–84.

(104) Pierotti, R. A. *Chem. Rev.* **1976**, *76* (6), 717–726.

(105) Hummer, G.; Garde, S.; Garcia, A. E.; Pohorillet, A.; Pratr, L. R.; Chandler, D. *JBiophysics* **1996**, *93*, 8951–8955.

(106) Garde, S.; Hummer, G.; García, A. E.; Paulaitis, M. E.; Pratt, L. R. *Phys. Rev. Lett.* **1996**, *77* (24), 4966–4968.

(107) Hummer, G.; Garde, S. *Phys. Rev. Lett.* **1998**, *80* (19), 4193–4196.

(108) Chandler, D. *Phys. Rev. E* **1993**, *48* (4), 2898–2905.

(109) Truskett, T. M.; Debenedetti, P. G.; Torquato, S. *J. Chem. Phys.* **2001**, *114* (5), 2401–2418.

(110) Ashbaugh, H. S.; Truskett, T. M.; Debenedetti, P. G. *J. Chem. Phys.* **2002**, *116* (7), 2907–2921.

(111) Blokzijl, W.; Engberts, J. B. F. N. *Angew. Chemie Int. Ed. English* **1993**, *32* (11), 1545–1579.

(112) Frank, H. S.; Evans, M. W. *J. Chem. Phys.* **1945**, *13* (11), 507–532.

(113) W. Kauzmann. *Adv. Protein Chem.* **1959**, *14*, 1–63.

(114) Choudhary, N.; Kushwaha, O. S.; Bhattacharjee, G.; Chakrabarty, S.; Kumar, R. *Energy Procedia* **2017**, *105*, 5026–5033.

(115) Kumar, A.; Bhattacharjee, G.; Kulkarni, B. D.; Kumar, R. *Ind. Eng. Chem. Res.* **2015**, *54* (49), 12217–12232.

(116) Head-Gordon, T.; Stillinger, H. *Is Water Structure around Hydrophobic Groups Clathrate-like? Communicated by Frank*; 1995; Vol. 92.

(117) Head-Gordon, T.; Sorenson, J. M.; Pertsemlidis, A.; Glaeser, R. M. *Differences in Hydration Structure Near Hydrophobic and Hydrophilic Amino Acids*; 1997; Vol. 73.

(118) Titantah, J. T.; Karttunen, M. *J. Am. Chem. Soc.* **2012**, *134* (22), 9362–9368.

(119) Choudhary, N.; Das, S.; Roy, S.; Kumar, R. *Fuel* **2016**, *186*, 613–622.

(120) Stirnemann, G.; Rossky, P. J.; Hynes, J. T.; Laage, D. *Faraday Discuss.* **2010**, *146*, 263–281; discussion 283-98, 395–401.

(121) Laage, D.; Stirnemann, G.; Hynes, J. T. *J. Phys. Chem. B* **2009**, *113* (8), 2428–2435.

(122) Lum, K.; Chandler, D.; Weeks, J. D. *J. Phys. Chem. B* **1999**, *103* (22), 4570–4577.

(123) Hribar, B.; Southall, N. T.; Vlachy, V.; Dill, K. A. *J. Am. Chem. Soc.* **2002**, *124* (41), 12302–12311.

(124) Dill, K. A.; Truskett, T. M.; Vlachy, V.; Hribar-Lee, B. *Annu. Rev. Biophys. Biomol. Struct.* **2005**, *34* (1), 173–199.

(125) Willard, A. P.; Chandler, D. *J. Chem. Phys.* **2014**, *141* (18), 18C519.

(126) Berne, B. J.; Weeks, J. D.; Zhou, R. *Annu. Rev. Phys. Chem.* **2009**, *60* (1), 85–103.

(127) Bratko, D.; Curtis, R. A.; Blanch, H. W.; Prausnitz, J. M. *J. Chem. Phys.* **2001**, *115* (8), 3873–3877.

(128) Bérard, D. R.; Attard, P.; Patey, G. N. *J. Chem. Phys.* **1993**, *98* (9), 7236–7244.

(129) Xuhui Huang, ‡; Ruhong Zhou, ‡, § and; Bruce J. Berne*, ‡, §. *J. Phys. Chem. B* **2005**, *109* (8), 3546–3552.

(130) Huang, X.; Margulis, C. J.; Berne, B. J. *Proc. Natl. Acad. Sci. U. S. A.* **2003**, *100* (21), 11953–11958.

(131) Ben-Amotz, D. *J. Chem. Phys.* **2005**, *123* (18), 184504.

(132) Chandler, D. *Nature* **2007**, *445* (7130), 831–832.

(133) Rein ten Wolde, P.; Sun, S. X.; Chandler, D. *Phys. Rev. E* **2001**, *65* (1), 011201.

(134) Bolhuis, P. G.; Chandler, D. *J. chem. phys.* **2000**, *113* (18), 8154–8160.

(135) Banerjee, S.; Singh, R. S.; Bagchi, B. *J. Chem. Phys.* **2015**, *142* (13), 134505.

(136) Despa, F.; Berry, R. S. *Biophys. J.* **2007**, *92* (2), 373–378.

(137) Zhang, C.; Gygi, F.; Galli, G. *J. Phys. Chem. Lett.* **2013**, *4* (15), 2477–2481.

(138) Giovambattista, N.; Debenedetti, P. G.; Rossky, P. J. *Proc. Natl. Acad. Sci. U. S. A.* **2009**, *106* (36), 15181–15185.

(139) Rajamani, S.; Ghosh, T.; Garde, S. *J. Chem. Phys.* **2004**, *120* (9), 4457–4466.

(140) Collins, K. D. *Biophys. J.* **1997**, *72* (1), 65–76.

(141) Cheng, Y.-K.; Rossky, P. J. *Nature* **1998**, *392* (6677), 696–699.

(142) Altabet, Y. E.; Debenedetti, P. G. *J. Chem. Phys.* **2014**, *141* (18), 18C531.

(143) Giovambattista, N.; Rossky, P. J.; Debenedetti, P. G. *Annu. Rev. Phys. Chem.* **2012**, *63* (1), 179–200.

(144) Takaiwa, D.; Hatano, I.; Koga, K.; Tanaka, H. *Proc. Natl. Acad. Sci. U. S. A.* **2008**, *105* (1), 39–43.

(145) Koga, K.; Gao, G. T.; Tanaka, H.; Zeng, X. C. *Nature* **2001**, *412* (6849), 802–805.

(146) Chakraborty, S.; Kumar, H.; Dasgupta, C.; Maiti, P. K. *Acc. Chem. Res.* **2017**, *50* (9), 2139–2146.

(147) Joseph, S.; Aluru, N. R. *Nano Lett.* **2008**, *8* (2), 452–458.

(148) Majumder, M.; Chopra, N.; Andrews, R.; Hinds, B. J. *Nature* **2005**, *438* (7064), 44–44.

(149) Noon, W. H.; Ausman, K. D.; Smalley, R. E.; Jianpeng, M. *Chem. Phys. Lett.* **2002**, *355* (5–6), 445–448.

(150) Dalla Bernardina, S.; Paineau, E.; Brubach, J. B.; Judeinstein, P.; Rouzière, S.; Launois,

P.; Roy, P. *J. Am. Chem. Soc.* **2016**, *138* (33), 10437–10443.

(151) Gordillo, M. C.; Martí, J. *Chem. Phys. Lett.* **2000**, *329* (5–6), 341–345.

(152) Scalfi, L.; Fraux, G.; Boutin, A.; Coudert, F.-X. *Langmuir* **2018**, *34* (23), 6748–6756.

(153) Rasaiah, J. C.; Garde, S.; Hummer, G. *Annu. Rev. Phys. Chem.* **2008**, *59* (1), 713–740.

(154) Mondal, S.; Bagchi, B. *J. Phys. Chem. Lett.* **2019**, *10* (20), 6287–6292.

(155) Takata, K.; Matsuzaki, T.; Tajika, Y. *Prog. Histochem. Cytochem.* **2004**, *39* (1), 1–83.

(156) Chandy, G.; Zampighi, G. A.; Kreman, M.; Hall, J. E. *J. Membr. Biol.* **1997**, *159* (1), 29–39.

(157) Jensen, M.; Dror, R. O.; Xu, H.; Borhani, D. W.; Arkin, I. T.; Eastwood, M. P.; Shaw, D. E. *Proc. Natl. Acad. Sci. U. S. A.* **2008**, *105* (38), 14430–14435.

(158) Cui, Y.; Bastien, D. A. *Biochem. Biophys. Res. Commun.* **2011**, *412* (4), 654–659.

(159) Zeuthen, T. *Trends in Biochemical Sciences*. Elsevier February 1, 2001, pp 77–79.

(160) Hub, J. S.; Grubmüller, H.; De Groot, B. L. *Handb. Exp. Pharmacol.* **2009**, *190* (190), 57–76.

(161) Preston, G. M.; Agre, P. *Proc. Natl. Acad. Sci. U. S. A.* **1991**, *88* (24), 11110–11114.

(162) Yeung, P. S. W.; Eskici, G.; Axelsen, P. H. *Biochimica et Biophysica Acta - Biomembranes*. 2013, pp 2314–2318.

(163) Chowdhary, J.; Ladanyi, B. M. *J. Phys. Chem. B* **2009**, *113* (45), 15029–15039.

(164) Pieniazek, P. A.; Lin, Y.-S.; Chowdhary, J.; Ladanyi, B. M.; Skinner, J. L. *J. Phys. Chem. B* **2009**, *113* (45), 15017–15028.

(165) Maitra, A. *J. Phys. Chem.* **1984**, *88* (21), 5122–5125.

(166) Fujii, H.; Kawai, T.; Nishikawa, H. *Bull. Chem. Soc. Jpn.* **1979**, *52* (7), 2051–2055.

(167) Chen, J.; Xia, C.; Niu, J.; Li, S. ben. *Biochem. Biophys. Res. Commun.* **2001**, *282* (5),

1220–1223.

(168) Mohamad-Aziz, S. N.; Mishra, P.; Zularisam, A. W.; Sakinah, A. M. M. *J. Mol. Liq.* **2019**, *286*.

(169) Fenn, E. E.; Wong, D. B.; Fayer, M. D. *Proc. Natl. Acad. Sci. U. S. A.* **2009**, *106* (36), 15243–15248.

(170) Patra, A.; Luong, T. Q.; Mitra, R. K.; Havenith, M. *Phys. Chem. Chem. Phys.* **2013**, *15* (3), 930–939.

(171) Senske, M.; Xu, Y.; Bäumer, A.; Schäfer, S.; Wirtz, H.; Savolainen, J.; Weingärtner, H.; Havenith, M. *Phys. Chem. Chem. Phys.* **2018**, *20* (13), 8515–8522.

(172) Verma, P. K.; Saha, R.; Mitra, R. K.; Pal, S. K. *Soft Matter* **2010**, *6* (23), 5971–5979.

(173) Biswas, R.; Furtado, J.; Bagchi, B. *J. Chem. Phys.* **2013**, *139* (14).

(174) Moilanen, D. E.; Fenn, E. E.; Wong, D.; Fayer, M. D. *J. Chem. Phys.* **2009**, *131* (1).

(175) Laage, D.; Thompson, W. H. *J. Chem. Phys.* **2012**, *136* (4), 044513.

(176) Mondal, S.; Acharya, S.; Bagchi, B. **2019**.

(177) Metzler, R. **2018**.

(178) Khesbak, H.; Savchuk, O.; Tsushima, S.; Fahmy, K. *J. Am. Chem. Soc.* **2011**, *133* (15), 5834–5842.

(179) Bhattacharyya, S. M.; Wang, Z.-G.; Zewail, A. H. *J. Phys. Chem. B* **2003**, *107* (47), 13218–13228.

(180) Bagchi, B. *Water in Biological and Chemical Processes: From Structure and Dynamics to Function*; Cambridge University Press, 2011.

(181) Otting, G.; Liepinsh, E.; Wüthrich, K. *Science (80-.).* **1991**, *254* (5034), 974–980.

(182) Gregory, R. B. In *The Properties of Water in Foods ISOPOW 6*; Springer US, 1998; pp 57–99.

(183) Wüthrich, K.; Billeter, M.; Güntert, P.; Luginbühl, P.; Riek, R.; Wider, G. *Faraday Discuss.* **1996**, *103*, 245–253.

(184) Martin, D. R.; Matyushov, D. V. *J. Chem. Phys.* **2014**, *141* (22), 22D501.

(185) Hande, V. R.; Chakrabarty, S. *Phys. Chem. Chem. Phys.* **2016**, *18* (31), 21767–21779.

(186) Rocha, L. F. O.; Tarragó Pinto, M. E.; Caliri, A. *Brazilian J. Phys.* **2004**, *34* (1), 90–101.

(187) Papoian, G. A.; Ulander, J.; Eastwood, M. P.; Luthey-Schulten, Z.; Wolynes, P. G. *Proc. Natl. Acad. Sci. U. S. A.* **2004**, *101* (10), 3352–3357.

(188) Privalov, P. L.; Makhatadze, G. I. *J. Mol. Biol.* **1993**, *232* (2), 660–679.

(189) Makhatadze, G. I.; Privalov, P. L. *J. Mol. Biol.* **1993**, *232* (2), 639–659.

(190) Schrade, P.; Klein, H.; Egry, I.; Ademovic, Z.; Klee, D. *Journal of Colloid and Interface Science*. Academic Press Inc. February 15, 2001, pp 445–447.

(191) Rezaei, K.; Jenab, E.; Temelli, F. *Critical Reviews in Biotechnology*. October 10, 2007, pp 183–195.

(192) Kornblatt, J. A.; Kornblatt, M. J. *Int. Rev. Cytol.* **2002**, *215*, 49–50.

(193) Verma, P. K.; Rakshit, S.; Mitra, R. K.; Pal, S. K. *Biochimie* **2011**, *93* (9), 1424–1433.

(194) Pocker, Y. *C. Cell. Mol. Life Sci* **2000**, *57*.

(195) Dinpajooh, M.; Martin, D. R.; Matyushov, D. V. *Sci. Rep.* **2016**, *6* (1), 1–10.

(196) Polander, B. C.; Barry, B. A. *Proc. Natl. Acad. Sci. U. S. A.* **2012**, *109* (16), 6112–6117.

(197) Jiang, T.; Han, W.; Maduke, M.; Tajkhorshid, E. *J. Am. Chem. Soc.* **2016**, *138* (9), 3066–3075.

(198) del Val, C.; Bondar, L.; Bondar, A.-N. *J. Struct. Biol.* **2014**, *186* (1), 95–111.

(199) Decaneto, E.; Vasilevskaya, T.; Kutin, Y.; Ogata, H.; Grossman, M.; Sagi, I.; Havenith, M.; Lubitz, W.; Thiel, W.; Cox, N. *Phys. Chem. Chem. Phys.* **2017**, *19* (45), 30316–

30331.

(200) Ball, P. *Proc. Natl. Acad. Sci. U. S. A.* **2017**, *114* (51), 13327–13335.

(201) Maurer, M.; Oostenbrink, C. *Journal of Molecular Recognition.* John Wiley and Sons Ltd December 1, 2019.

(202) Cui, D.; Zhang, B. W.; Matubayasi, N.; Levy, R. M. *J. Chem. Theory Comput.* **2018**, *14* (2), 512–526.

(203) Ladbury, J. E. *Chem. Biol.* **1996**, *3* (12), 973–980.

(204) Huang, W.; Blinov, N.; Wishart, D. S.; Kovalenko, A. *J. Chem. Inf. Model.* **2015**, *55* (2), 317–328.

(205) Setny, P.; Baron, R.; McCammon, J. A. *J. Chem. Theory Comput.* **2010**, *6* (9), 2866–2871.

(206) Baron, R.; Setny, P.; Andrew McCammon, J. *J. Am. Chem. Soc.* **2010**, *132* (34), 12091–12097.

(207) Tiwary, P.; Mondal, J.; Morrone, J. A.; Berne, B. J. *Proc. Natl. Acad. Sci. U. S. A.* **2015**, *112* (39), 12015–12019.

(208) Snyder, P. W.; Lockett, M. R.; Moustakas, D. T.; Whitesides, G. M. *European Physical Journal: Special Topics.* Springer Verlag 2014, pp 853–891.

(209) Fernández, A.; Scott, L. R. *Trends Biotechnol.* **2017**, *35* (6), 490–497.

(210) Chong, S.-H.; Ham, S. *J. Phys. Chem. Lett.* **2016**, *7* (19), 3967–3972.

(211) Jana, M.; Bandyopadhyay, S. *Phys. Chem. Chem. Phys.* **2012**, *14* (18), 6628–6638.

(212) Edwards-Gayle, C. J. C.; Hamley, I. W. *Organic and Biomolecular Chemistry.* Royal Society of Chemistry July 19, 2017, pp 5867–5876.

(213) Lombardo, D.; Kiselev, M. A.; Magazù, S.; Calandra, P. *Advances in Condensed Matter Physics.* Hindawi Publishing Corporation 2015.

(214) Sammalkorpi, M.; Karttunen, M.; Haataja, M. *J. Phys. Chem. B* **2007**, *111* (40), 11722–

11733.

(215) Zhang, J.; Zhao, Y.; Han, S.; Chen, C.; Xu, H. *Science China Chemistry*. Science in China Press November 7, 2014, pp 1634–1645.

(216) Deshmukh, S. A.; Solomon, L. A.; Kamath, G.; Fry, H. C.; Sankaranarayanan, S. K. R. S. *Nat. Commun.* **2016**, *7* (1), 1–11.

(217) Ben-Naim, A. *On the Role of Water in Molecular Recognition and Self-Assembly*; 1987; Vol. 98.

(218) Kharche, S.; Joshi, M.; Sengupta, D.; Chattopadhyay, A. *Chem. Phys. Lipids* **2018**, *210*, 142–148.

(219) Chaudhuri, A.; Basu, P.; Haldar, S.; Kombrabail, M.; Krishnamoorthy, G.; Rajarathnam, K.; Chattopadhyay, A. *J. Phys. Chem. B* **2013**, *117* (5), 1225–1233.

Chapter 2: Computational Methods

Computer simulation of molecular systems has emerged as a powerful tool that can be complementary to the conventional experiments. It allows us to study a complex system at a microscopic (molecular) scale and connect to corresponding bulk property/function, which otherwise is difficult experimentally. Two major molecular simulation methods are: molecular dynamics (MD) and Monte Carlo (MC). The obvious advantage of MD over MC is that it yields dynamical properties of the system such as time-dependent responses to perturbations, spectra, rheological properties and transport properties.[1] In MD simulation, complex molecular structures are modeled with atomistic level details and the system is analyzed for various structural, dynamic, thermodynamic and mechanical properties. In this thesis, we have primarily used atomistic MD simulation to study a wide range of complex chemical systems with high degree of heterogeneity. In order to enhance the conformational sampling in certain polymeric systems, we have employed replica exchange molecular dynamics (REMD) method. A brief description of the theoretical background of these simulation methods is discussed in this chapter.

2.1 Classical molecular dynamics

Molecular dynamics simulation is the numerical method that solves classical equations of motion step-by-step. For a simple atomic system, classical Newton's equation of motion can be written as

$$\vec{f}_i = m_i \frac{\partial^2 \vec{r}_i}{\partial t^2}, i = 1,2 \dots N \tag{2.1}$$

where, m_i is the mass and $\vec{r}_i$ is the position vector of particle i in N-particles system at time t. The instantaneous force $\vec{f}_i$ acting on the particle are usually derived from a potential energy as follows,

$$\vec{f}_i = -\frac{\partial V_i}{\partial r_i} = -\nabla V_i \tag{2.2}$$

The potential V_i is the function of the position of respective particles $r^N = (r1, r2, \dots rN)$ represents the complete set of 3N atomic coordinates. Therefore, the forces acting on each particle of the system can be derived from the gradient of underlying potential energy surface. The acceleration computed from the forces can be numerically integrated to compute the velocity and

position of all particles at any time in future. Thus, we would obtain the trajectory of each particle in the phase space to analyze microscopic properties of interest about the given system.

2.1.1   Force field

The accurate potential energy surface can be computed quantum mechanically. But since those are expensive, we approximate the potential energy surfaces by pair-wise additive empirical functions called "force field". In the context of molecular modelling, force fields are the energy functions or interatomic potential that is a set of empirical parameters and functions to describe the interactions between atoms and the energy of the system as a function of the atomic coordinates. These parameters are obtained either from experiments or quantum mechanical calculations. The accuracy of the MD results is directly dependent upon the accuracy of these parameters and employed potential energy functions. A number of force fields are available depending upon the energy functional form and the strategy used for its parameterization to get results as accurate as possible. Some routinely used force fields are CHARMM,[2] OPLS,[3] AMBER,[4] and GROMOS[5]. The potential energy function generally consists of two terms: bonded and non-bonded interactions;

$$V = V_{bonded} + V_{non-bonded} \tag{2.3}$$

The bonded potential energy function can be written as,

$$V_{bonded} = V_{bonds} + V_{angles} + V_{dihedrals} \tag{2.4}$$

$$V_{bonds} = \frac{1}{2}\Sigma_{bonds} k_b(b - b_0)^2 \tag{2.5}$$

$$V_{angles} = \frac{1}{2}\Sigma_{angles} k_\theta(\theta - \theta_0)^2 \tag{2.6}$$

$$V_{dihedrals} = \Sigma_{dihedrals} k_\varphi (1 + \cos(n\varphi - \lambda)) \tag{2.7}$$

The bonded potentials include contribution from three terms; the bonds, angles and dihedrals. The bonds and angles are modelled using harmonic potential that do not allow bonds to break; dihedrals are represented as periodic cosine functions. Hence, a chemical reaction involving bond-breaking and forming cannot be studied using classical MD using harmonic bonds. The equilibrium bond length and bond angle in the above equation in equation 2.5 and 2.6 are denoted by b_0 and θ_0. Whereas, b, θ, and φ signifies the instantaneous values of them. The k_b and k_θ are

force constants for bond and angle, respectively. In equation 2.7, k_φ, n, and λ are the barrier height (energy required to rotate the central axis of the dihedral made by 4 atoms), periodicity and offset, respectively. Non-bonded potentials term in equation 2.3 has following form,

$$V_{non-bonded} = V_{van\,der\,Waals} + V_{electrostatic} \tag{2.8}$$

The van der Waals potential can be modeled by 12-6 Lennard-Jones potential which consists of attractive (dipole-dipole, dipole-induced dipole, and London interactions) and repulsive forces. And electrostatic interactions are represented by the Coulomb potential. The functional forms of them are given in following equations,

$$V_{LJ} = \sum_i^N \sum_{j=i+1}^N 4\varepsilon_{ij} \left[\left(\frac{\sigma_{ij}}{r_{ij}}\right)^{12} - \left(\frac{\sigma_{ij}}{r_{ij}}\right)^6 \right] \tag{2.9}$$

$$V_{Coulomb} = \sum_i^N \sum_{j=i+1}^N \frac{q_i q_j}{4\pi\varepsilon_0 r_{ij}} \tag{2.10}$$

In the expression for LJ potential (in equation 2.9), ε_{ij} symbolizes the strength of interactions between atoms i and j, r_{ij} is distance between them and σ_{ij} is the diameter of the particles. In Coulomb potential (in equation 2.10), q_i and q_j are the partial charges on atoms i and j, and ε_0 represents the dielectric constants in vacuum.

2.2 The MD algorithm

2.2.1 System setup

To run a MD simulation, primarily three input details are needed (i) initial coordinates, (ii) force fields and (iii) a set of instructions. The initial conformation of system of interest is placed inside the box. For the biological molecules such as protein and nucleic acids, the initial conformation can be obtained through experiments such as X-ray crystallography and NMR spectroscopic technique. Once the initial conformation of the system is obtained, it is then solvated to fill the remaining simulation box with solvent e.g. water. Selection of suitable force-field is then done for the assignment of non-bonded and bonded parameters of the atoms/particles in the system.

2.2.2 Energy minimization, equilibration and production run

With this, the system is initially energy minimized to remove any clashes between atoms and achieve at least a stable conformation for the next equilibration runs. Usually, energy minimization is accomplished using either steepest descent algorithm[6] or using conjugate gradient method.[7] After energy minimization temperature and pressure equilibrations are performed using thermostat and barostat. By using NVT and NPT equilibrations the desired temperature and pressure are achieved. During NVT, the random velocity generation is done using Maxwell-Boltzmann distribution method and the continuation run is done during NPT equilibration. Once the system is equilibrated at targeted thermodynamic conditions, it can be subsequently placed to production run to obtain the trajectory and further to analyze the data.

Initial positions of particles are the initial Cartesian coordinates as $r_i(x_i, y_i, z_i)$ and velocities $v_i(v_{xi}, v_{yi}, v_{zi})$ of particles are generated using Maxwell-Boltzmann distribution at a specific temperature using formula,

$$p(v_{xi}) = \sqrt{\frac{m_i}{2\pi k_B T}} exp\left(-\frac{m_i v_{xi}^2}{2k_B T}\right) \tag{2.11}$$

Here, distribution of each velocity component, $p(v_{xi})$ is obtained from random number generator, velocity scaling is done so that total energy would correspond to temperature T; k_B is the Boltzmann constant. After initialization, forces are calculated from the negative gradient of potentials. These forces are utilized to obtain new positions and velocity by integrating Newton's equation of motion and in this way, propagation of particles in the system is obtained. There are various integrators available such as Verlet algorithm,[8] Velocity-verlet algorithm,[9] and Leap-frog algorithm.[10] Among them a Leap-frog integrator is widely used. The new positions and velocities from forces can written as,

$$v\left(t + \frac{1}{2}\delta t\right) = v\left(t - \frac{1}{2}\delta t\right) + \frac{f(t)}{m}\delta t \tag{2.12}$$

$$r(t + \delta t) = r(t) + v\left(t + \frac{1}{2}\delta t\right)\delta t \tag{2.13}$$

Here, the position at time t and velocity at previous half time step $(t - \frac{1}{2}\delta t)$ are used to calculate the velocity at next half time step $(t + \frac{1}{2}\delta t)$. From the latter, one can calculate the positions at next integer time step $(t + \delta t)$. Thus, the velocity takes a leap over the position by half

time step, and then the position leaps over the velocity to give position at full-time step. The velocities are then approximated using following equation:

$$v(t) = \frac{1}{2}\left[v\left(t + \frac{1}{2}\delta t\right) + v\left(t - \frac{1}{2}\delta t\right)\right] \tag{2.14}$$

Here, δt is the time step used to integrate equations of motion during simulations which generally selected according to the vibrational frequency of bond. Higher time steps can be used when bonds are constrained to reduce the computational time and to increase the performance; provided it should not affect dynamics of the system significantly. Therefore, the bonds are treated as being constrained to have fixed bond length. Various bond constraint algorithms are available such as LINCS[11], RATTLE[12] and SHAKE[13].

To speed up the calculation and to truncate the total number of pair interactions, numerical approximations like cut-off schemes are useful to treat non-bonded potentials. The pairwise additive nature of non-bonded potentials almost takes computational time to perform calculation steps of square of the number of pairs ($\frac{1}{2}N(N-1)$ total pairs). Such calculations are computationally heavy to perform; therefore, this can be reduced by applying cut-off radius (r_c) around every particle. Since LJ is short-range interaction, it can be truncated beyond cut-off radius using shift or switch functions. A cutoff makes the force calculation an $O(N)$ process.[14] Long-range columbic interactions (outside cut-off) are calculated using the methods such as reaction-field[15], Ewald sum[16], PME (Particle mesh Ewald summation)[17].

2.2.3   Long range interactions

With the limited computational resources, we are bound to include only a limited number of atoms explicitly during MD simulation. Therefore, a surface or boundary of the system must be considered. As an approximation, one could assume that the explicit system is surrounded by a vacuum. With this assumption, the atoms near the surface will feel an imbalanced force that can mislead their structure from the natural structure present in the interior of a bulk system. Since we are interested in the macroscopic systems, then the surface effects are unwanted artifacts which should be eliminated.

Therefore, to deal with the problem of long range interactions, a variety of techniques are available in computer simulations of charged particles at different level of approximation.[18,19]

Here, we will discuss the Ewald summation method for the treatment of such long range interactions in periodic systems.[16] This method delivers the precise results of the electrostatic energy for the periodic system of an infinitely replicated neutral box of charged particles. Ewald method is the regular choice in complex molecular system simulations with PBC.

The Ewald potential[20] is given by

$$V'_{qd} = \frac{1}{2}\sum_{ij}^{N} \frac{1}{|\vec{r_{ij}}+\vec{r_n}|} erfc(\alpha|\vec{r_{ij}} + \vec{r_n}|) \tag{2.15}$$

$$V_{qr} = \left[\frac{1}{2\pi V}\sum_{m\neq0}^{\infty} \frac{\exp\left(-\frac{\pi^2|m|^2}{\alpha^2}\right)}{|m|^2} S(m)S(-m) - \frac{\alpha}{\sqrt{\pi}}\sum_i q_i^2\right] - V_{intra} \tag{2.16}$$

$$\text{With} \quad S(m) = \sum_i^N q_i \exp(2\pi im.\vec{r_i}) \tag{2.17}$$

$$V_{intra} = \sum_{ij-excl} q_i q_j \frac{erfc(\alpha\vec{r_{ij}})}{\vec{r_{ij}}} \tag{2.18}$$

where, $\vec{r_i}$ is the vector position of the atomic charge q_i, $\vec{r_n}$ is a vector of the direct lattice and $\vec{r_{ij}} = \vec{r_i} - \vec{r_j}$. $erfc(x) = \frac{1}{\sqrt{\pi}}\int_x^{\infty} e^{-t^2} dt$ is the complementary function, $erf(x) = 1 - erfc(x)$. m is the reciprocal lattice vector, V is the unit cell volume and α is the Ewald convergence parameter. In equation 2.15, the prime indicates the intramolecular excluded contacts are omitted. While, in equation 2.16, the V_{intra} is the intramolecular energy term between bonded pairs, which is included automatically on R.H.S. of the equation. Therefore, the summation on i and j in equation 2.15 goes over all the excluded intra-molecular contacts. For increasingly large systems, the computational cost scales with N^2 for standard Ewald summation, which is huge for everyday applications. Therefore, substitute methods those scale with a lesser power of N than standard Ewald have been suggested. Among the fastest methods, particle mesh Ewald algorithm (PME)[17] is designed for periodic systems inspired by the particle mesh method of Hockney and Eastwood.[21] Here, a multidimensional piecewise interpolation approach is used to compute the reciprocal lattice energy, V_{qr}, of Eq. 2.16, whereas the direct part, V_{qd}, is calculated straightforwardly. Choice of large values of the Ewald convergence parameter α allows because of the low computational cost of this method compared to conventional Ewald method. Accordingly, shorter cutoffs can be adopted in the direct space Ewald sum V_{qd}.

2.3 Periodic boundary conditions (PBC) and minimum image convention

MD simulations are employed to predict macroscopic properties of bulk material. However, the simulations are carried out using short box-lengths of few nanometers that contains small number of particles only, those are present near to the box surface as well. The chances that finite size and surface defects may arise. To remove such artifacts, periodic boundary conditions and minimum image conventions are routinely used during computer simulations. The periodic boundary conditions (PBC) have an advantage of representing small system as an infinite system without edges or boundary of the box. It is done in such a way that the central unit cell replicated in 3D to obtain a periodic array of simulation boxes, where each box will have its replicas in all directions. This is an excellent approach to eliminate finite size effects during simulations as shown in Figure 2.1 for 2D system. The minimum image convention is always associated with the PBC and is basically considering the nearest atom or image for the short-range forces calculation. Although, the dimension of the simulation box must also be adequate to prevent periodic artifacts due to the unphysical topology of the simulation. In a box that is too small, a large molecule may intermingle with its own image in an adjacent box, which is functionally equal to a molecule's head interacting with its own tail. This may lead to highly unphysical dynamics in large molecules, although the magnitude of the consequences and thus the appropriate box size relative to the size of the macromolecules depends on the desired accuracy, the planned length of the simulation, and the expected dynamics. Therefore, a common advice is to leave at least 1 nanometer space of solvent around the target molecules in every direction.[22]
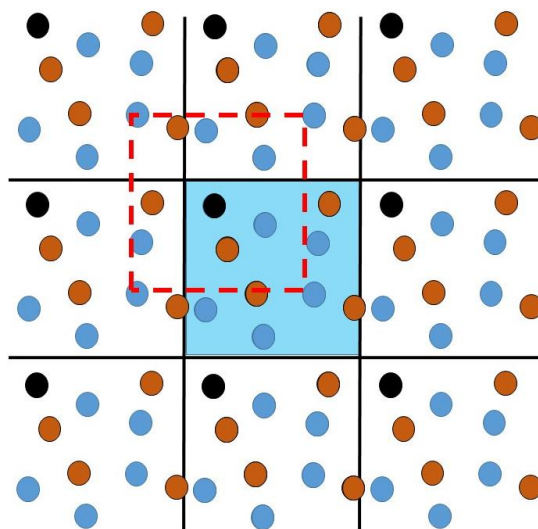
Figure 2.**1**: Schematic representation of periodic boundary conditions in a 2D space**.** Blue box represents the central simulation cell**.** Black sphere shows replicas of each atom**.** Dashed red box represents the nearest image of the black atom in central cell**.**

2.4 Thermodynamics Ensembles

A thermodynamic ensemble is a statistical ensemble that is in a statistical equilibrium. These ensembles help to achieve the main aim of gaining the thermodynamic properties of a real thermodynamic systems by deriving them from the laws of quantum and classical mechanics. There are number of thermodynamic ensemble in statistical mechanics. Three types of ensembles are mostly used in MD simulations[23]: (1) microcanonical (NVE) ensemble; where number of particles (N), volume of the simulation box (V) and energy (E) are constant, (2) canonical (NVT) ensemble; where N, V and temperature (T) are kept fixed by allowing pressure (P) and E to fluctuate, and (3) isothermal-isobaric (NPT) ensemble, where N, P and T are kept fixed and V is allowed to fluctuate. In real world, the reactions and experiments are carried out at constant temperature and pressure conditions. In molecular dynamics simulations, these conditions are maintained by coupling a given system to thermostat and barostat; the external baths. In this thesis, canonical ensemble is used to equilibrate the temperature of the system and afterwards isothermal-isobaric ensemble is used to equilibrate pressure of system and for all production runs.

2.4.1   Thermostat (Constant Temperature Simulations)

By using equipartition theorem of energy, the temperature of the system can be readily connected to the kinetic energy (KE) as below,

$$KE = \frac{1}{2}mv^2 = \frac{3}{2}Nk_BT \tag{2.19}$$

Using this KE expression, several types of thermostats have been designed to control the temperature of the system.

2.4.1.1 Velocity rescaling

Velocity rescaling[24] is a simple way to control the temperature by modification of the velocities of atoms by scaling them. This is done in such a way that the average kinetic energy of the systems matches with the system at target temperature. In this method, velocities are scaled by a factor λ,

$$\lambda = \sqrt{\frac{T_0}{T(t)}} \tag{2.20}$$

where, is T_0 the target temperature, and $T(t)$ is the instantaneous temperature before scaling.

2.4.1.2 Berendsen thermostat

The Berendsen thermostat[25] shows a proportional scaling of the velocities per time step in the algorithm with the scaling factor λ is given by

$$\lambda = \left[1 + \frac{\Delta t}{\tau_B}\left(\frac{T_0}{T(t)}\right) - 1\right]^2 \tag{2.21}$$

where Δt is the time step, T_0 is the target temperature, $T(t)$ is the instantaneous temperature and τ_B is the time constant of the Berendsen thermostat . This is reformed velocity rescaling and weak coupling thermostat. The degree of coupling to an external bath can be easily altered by varying τ_B. The limit, $\tau_B \to \infty$, represents the microcanonical ensemble.

2.4.1.3 Anderson thermostat

The Andersen thermostat[26] is the first thermostat for simulating a canonical ensemble at a fixed temperature. In this, the system is coupled to a heat bath by stochastic impulsive forces acting occasionally on randomly selected particles.[27] At each stochastic collision, the memory of the old velocity of selected particle erases and assignment of new velocity is done according to Maxwell-Boltzmann distribution at the imposed temperature. Between stochastic collisions, the N particles system progresses according to a Hamiltonian dynamic. The collision frequency (v) determines the degree of the coupling to the heat bath. The time intervals between two successive stochastic collisions is distributed as following,

$$P(v,t) = v.\exp(-vt) \tag{2.22}$$

2.4.1.4 Nosé-Hoover thermostat

This thermostat is originally designed by scientist Nosé and latter improved by Hoover. The Nosé-Hoover thermostat[28,29] incorporates an extended Lagrangian with an additional new degree of freedom and effective mass related to a fictional heat bath. The improved equations of motion of the extended system signify the evolution of both the internal and external variables in the desired ensemble. The measure of the fictitious mass ensures that thermal equilibrium is

reached efficiently. This is an effective method to simulate actual canonical ensemble with detailed fluctuations.

2.4.2   Barostat (Constant Pressure Simulations)

In the same way, as in thermostat, the system is coupled to a thermal bath; in constant pressure simulations, the system is coupled to pressure bath of target pressure. This is done by scaling the atomic coordinates and volume of the simulation box. In other words, the size and shape of the cell in NPT ensemble are rescaled to maintain an equilibrium pressure. Hence, the rate of change of pressure is given by,

$$\frac{dP}{dt} = \frac{1}{\tau_P}(P_B - P) \tag{2.23}$$

$$\lambda = 1 - \kappa \frac{\delta t}{\tau_P}(P_B - P) \tag{2.24}$$

Where, κ is the isothermal compressibility of the system given by:

$$\kappa = -\frac{1}{V}\left(\frac{\partial V}{\partial P}\right)_T \tag{2.25}$$

So, in each step, the coordinates, as well as the box lengths, are scaled by factor λ to achieve the target pressure. In this thesis, we have used Parrinello-Rahman Pressure Coupling method.[30]

2.5 Replica exchange molecular dynamics (REMD)

Sometimes the large system such as proteins, polymers and other macromolecules face the kinetic trapping in one energy minima of the potential well. To overcome from such a trapped state a normal molecular dynamics performed at constant temperature does not help. Therefore, understanding of the system details becomes difficult. Replica Exchange Molecular Dynamics (REMD)[31], one of the enhanced sampling technique can be used in such scenario. The replica exchange method was first established in the physics community to improve sampling in glassy systems[32] and has been applied to an MD simulation of protein folding later on.[31] In this method, instead of one temperature, the initial system is simulated at different temperatures at the same time unlike regular molecular dynamics simulation. Exchange between non-interacting configurations happens among various temperatures based on the metropolis criterion. This exchange of configurations permits access of higher temperature configurations to lower temperature as well and vice-versa as shown in Figure 2.2. Therefore, this exchange allows the

energetically trapped system to overcome one minimum and to explore more conformational space.
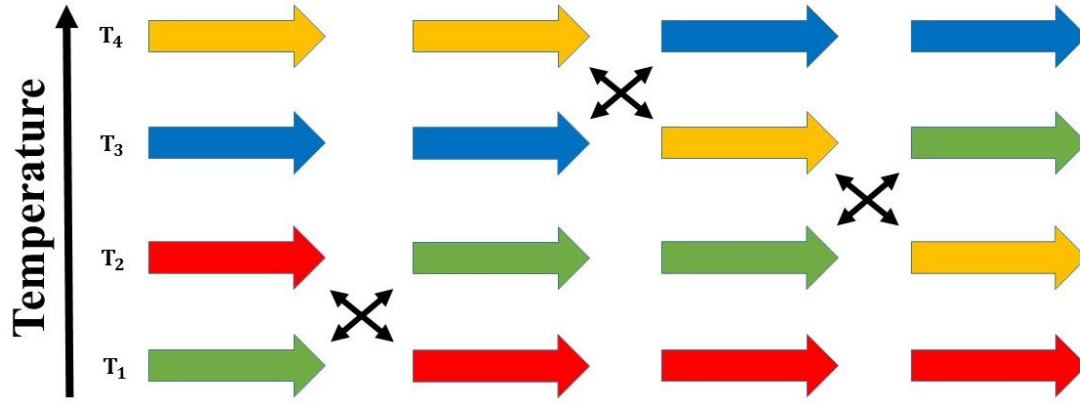
Figure 2.**2**: Representation of replica exchange molecular dynamics**.** Large colored arrows denote replicas propagating at different temperatures in MD

In REMD[33], regular MD runs are started from a set of *n* independent parallel configurations $q_0 = \{q_{1,0},\ q_{2,0} \dots q_{n,o}\}$ at temperatures $\{T_0,\ T_1 \dots T_n\}$ at time 0. A new set of configurations is obtained after a certain amount of integration time, as $q_1 = \{q_{1,1}, q_{2,1} \dots q_{,n,1}\}$. At this time, an exchange of configurations $q_{i,1}$ and $q_{j,1}$ is attempted using Metropolis criterion[23] as follows,

$$P_{accept} = min\left[1, exp\left[-\frac{1}{K_B}\left(\frac{1}{T_j} - \frac{1}{T_i}\right)\left(E(q_{i,1}) - E(q_{j,1})\right)\right]\right] \tag{2.26}$$

This acceptance probability guarantees the detailed balance condition of the overall Monte Carlo process. After repetition of these two steps an average of a thermodynamic property *A* at temperature T$_1$ is attained from an average

$$\langle A(q_1)\rangle = \lim_{n\to\infty}\frac{1}{N+1}\sum_{t=0}^{N} A(q_{1,t}) \tag{2.27}$$

This procedure is considered similar to Markov process with the use of two operators. Let us describe M as MD operator that produces the result of MD simulation with the given time step, and S as swap operator that switches two configurations with the above probability given in Eq. 2.26, a thermodynamic property can be acquired with a Markov chain $\{q_0, q_1 \dots q_n\}$ determined with

$$q_t = (SM)^t q_0 \tag{2.28}$$

Generally, exchanges between neighboring temperatures are practiced (namely, j=i+1 or j=i−1 in Eq. 2.26) to increase the acceptance ratio. Also, a number of exchanges (up to $n/2$) can be tried after every MD run. A thorough explanation of REMD method can be found in the papers of Sugita and Okamoto.[31]

In the present thesis, MD simulations and REMD simulations are done using GROMACS simulation suite.[34] It is is free and efficient MD simulation software with several acceleration and parallelization features. Some analysis reported in forthcoming chapters are performed using GROMACS inbuilt tools and other commonly used analysis parameters are self-written codes whose details are given in the next section. While the system specific parameters will be discussed in the respective chapters.

2.6 Data Analysis Methods

2.6.1 Structural order parameter

The commonly used structural order parameters are explained below;

2.6.1.1 Radial Distribution function (RDF)

"Molecular structure" of the materials represent how molecules are oriented and arranged themselves around each other in different phases. Water have a multifaceted structure that arises from hydrogen bonding interactions present in it. Because of the fact that water expands on cooling at 4^0C; a well-known density anomaly of water, the structure of it can be well given by the famous two body correlation function; Radial Distribution Function (RDF).[35] The functional form of it is as follows,

$$g(r) = \frac{N(r, r+dr)}{4\pi r^2 dr \rho} \tag{2.29}$$
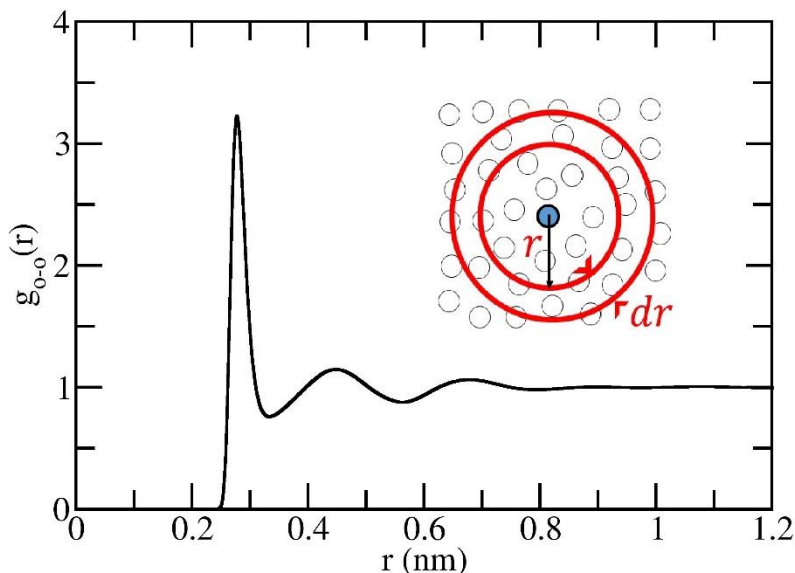
Figure 2.3: RDF of oxygen-oxygen from bulk water at 300K and inset figure represents space discretization for the calculation of RDF

where, $N(r, r + dr)$ is number of particles present within the shell of thickness dr at a distance r from the reference particle and RDF is normalized by the shell volume and bulk density ρ of the particle. Figure 2.3 represents the oxygen-oxygen RDF of bulk water at 300K and the pictorial demonstration of RDF as given inset. The oxygen-oxygen RDF at room temperature can also be found in Vega's paper.[36]

2.6.1.2 Tetrahedral order parameter (Q)

To determine the structure of water molecules with respect to its nearest four water molecules, the well-known tetrahedral order parameter (Q) given by Errington and Debendetti[37] is used,

$$Q_i = 1 - \frac{3}{8}\sum_{j=1}^{3}\sum_{k=j+1}^{4}\left(\cos\theta_{jik} + \frac{1}{3}\right)^2 \tag{2.30}$$

where, Q_i is the tetrahedral order parameter of the ith water molecule and θ_{jik} is the angle subtended on the oxygen atom of that water molecule by the each pair (given by the indices j and k) of four nearest neighbor molecules. Hence, for a perfect tetrahedral arrangement of the four neighboring water molecules around the central i[th] water molecule, Q=1, whereas for a random and uniform distribution of these angles, Q=0.

2.6.1.3 Hydrogen bond calculation

A hydrogen bond is a weak bond between two molecules formed by an electrostatic attraction between a proton (hydrogen bond donor, D) in one molecule and an electronegative atom (hydrogen bond acceptor, A) in the other. The electronegative second-row elements nitrogen(N), oxygen(O) and fluorine(F) of periodic table are particularly act as hydrogen bond acceptor. A hydrogen bond between two molecules is identified by using criterion: (i) the A−A distance between the donor and acceptor molecules should be less than 0.35 nm, and (ii) the D −A (Donor) −A (Acceptor) angle should be less than 30 degrees.

2.6.2 Dynamics order parameter

The commonly used dynamics order parameters are explained below;

2.6.2.1 Autocorrelation Function

The standard form of autocorrelation is given by,

$$C_A(t) = \frac{\langle A(t).A(0)\rangle}{\langle A(0).A(0)\rangle} \tag{2.31}$$

where A is the property of interest at time t. The angular brackets represent averaging over total number of frames and total number of atoms/molecules of interest. This function captures the timescale of relaxation of property, A. It also captures how much system remembers its previous state.

2.6.2.2 Cross correlation Function ($C_{AB}(t)$)

The cross correlation function $C_{AB}(t)$ is computed to interpret if any correlation exists between two different properties A and B at time t of the system and is obtained in following way,

$$C_{AB}(t) = \frac{\langle (A(0)-\langle A\rangle)-(B(t)-\langle B\rangle)\rangle}{\sqrt{(\langle A^2\rangle-\langle A\rangle^2)(\langle B^2\rangle-\langle B\rangle^2)}} \tag{2.32}$$

where, $C_{AB}(t)$ captures the relaxation time of the coupling between the fluctuations of the properties A(t) and B(t).

2.6.2.3 Mean square displacement (MSD)

The mean square displacement (MSD) is the measure of the average distance travelled by particle. It is given by the following equation,

$$\langle \Delta r_i(t)^2 \rangle = \langle \left(r_i(t) - r_i(0) \right)^2 \rangle \tag{2.33}$$

In this equation, $r_i(t) - r_i(0)$ is the (vector) distance traveled by the particle *i* over the time interval of t, and the vector magnitude squared is averaged (as shown by the angular brackets) over many time intervals. Frequently this quantity is averaged over all the molecules in the given system. The limiting slope of MSD at time t considered for sufficiently long time so that it should be in the linear regime, is related to the self-diffusion constant D.

$$\lim_{t \to \infty} \frac{d}{dt} \langle \Delta r_i(t)^2 \rangle = 2dD \tag{2.34}$$

where *d* is the dimension of the given space.

2.7 References

(1)   Allen, M. P. *Comput. soft matter from Synth. Polym. to proteins, Lect. notes, Nobbert Attig , Kurt Bind. , Helmut Grubmuller , Kurt Kremer* **2004**.

(2)   Klauda, J. B.; Venable, R. M.; Freites, J. A.; O'Connor, J. W.; Tobias, D. J.; Mondragon-Ramirez, C.; Vorobyov, I.; MacKerell, A. D.; Pastor, R. W. *J. Phys. Chem. B* **2010**, *114* (23), 7830–7843.

(3)   Jorgensen, W. L.; Maxwell, D. S.; Tirado-Rives, J. *J. Am. Chem. Soc.* **1996**, *118* (45), 11225–11236.

(4)   Wang, J.; Wolf, R. M.; Caldwell, J. W.; Kollman, P. A.; Case, D. A. *J. Comput. Chem.* **2004**, *25* (9), 1157–1174.

(5)   Oostenbrink, C.; Villa, A.; Mark, A. E.; Van Gunsteren, W. F. *J. Comput. Chem.* **2004**, *25* (13), 1656–1676.

(6)   Petrova, S. S.; Solov'Ev, A. D. *Hist. Math.* **1997**, *24* (4), 361–375.

(7)   Shewchuk, J. R. *An Introduction to the Conjugate Gradient Method That Even an Idiot Can Understand "*; 1994.

(8)   GrubmüLler, H.; Heller, H.; Windemuth, A.; Schulten, K. *Mol. Simul.* **1991**, *6* (1–3), 121–142.

(9)   Spreiter, Q.; Walter, M. *J. Comput. Phys.* **1999**, *152* (1), 102–119.

(10)   Van Gunsteren, W. F.; Berendsen, H. J. C. *Mol. Simul.* **1988**, *1* (3), 173–185.

(11)   Hess, B.; Bekker, H.; Berendsen, H. J. C.; Fraaije, J. G. E. M. *J. Comput. Chem.* **1997**, *18* (12), 1463–1472.

(12)   Andersen, H. C. *J. Comput. Phys.* **1983**, *52* (1), 24–34.

(13)   Krautler, V.; van Gunsteren, W. F.; Hunenberger, P. H. *J. Comput. Chem.* **2001**, *22* (5), 501–508.

(14)   Toxvaerd, S.; Dyre, J. C. *J. Chem. Phys.* **2011**, *134* (8).

(15)   Tironi, I. G.; Sperb, R.; Smith, P. E.; Van Gunsteren, W. F. *J. Chem. Phys.* **1995**, *102* (13), 5451–5459.

(16)   Toukmaji, A. Y.; Board, J. A. *Computer Physics Communications*. Elsevier 1996, pp 73–92.

(17)   Essmann, U.; Perera, L.; Berkowitz, M. L.; Darden, T.; Lee, H.; Pedersen, L. G. *J. Chem. Phys.* **1995**, *103* (19), 8577–8593.

(18)   Barker, J. A.; Watts, R. O. *Mol. Phys.* **1973**, *26* (3), 789–792.

(19)   Perram, J. W.; Petersen, H. G.; De Leeuw, S. W. *Mol. Phys.* **1988**, *65* (4), 875–893.

(20)   de Leeuw, S. W.; Perram, J. W.; Smith, E. R. *Proc. R. Soc. A Math. Phys. Eng. Sci.* **1980**, *373* (1752), 27–56.

(21)   Hockney, R. W. *Computer Simulation Using Particles*; 1988.

(22)   Norberto De Souza, O.; Ornstein, R. L. *Biophys. J.* **1997**, *72* (6), 2395–2397.

(23)   Frenkel, D.; series, B. S.-C. sciences; 2002, undefined. *dspace.library.uu.nl*.

(24)   Bussi, G.; Donadio, D.; Parrinello, M. *J. Chem. Phys.* **2007**, *126* (1).

(25)   Mudi, A.; Chakravarty, C. *Mol. Phys.* **2004**, *102* (7), 681–685.

(26)   Andersen, H. C. *J. Chem. Phys.* **1980**, *72* (4), 2384–2393.

(27)   E, W.; Li, D. *Commun. Pure Appl. Math.* **2008**, *61* (1), 96–136.

(28)   Nosé, S. *Mol. Phys.* **1984**, *52* (2), 255–268.

(29)   Hoover, W. G. *Phys. Rev. A* **1985**, *31* (3), 1695–1697.

(30)   Parrinello, M.; Rahman, A. *J. Appl. Phys.* **1981**, *52* (12), 7182–7190.

(31)   Sugita, Y.; Okamoto, Y. *Chem. Phys. Lett.* **1999**, *314* (1–2), 141–151.

(32)   Hukushima, K.; Nemoto, K. *J. Phys. Soc. Japan* **1996**, *65* (6), 1604–1608.

(33)   Young, M. R.; Pande, V. S. *Biophys. J.* **2003**, *84* (2 I), 775–786.

(34)   Hess, B.; Kutzner, C.; Van Der Spoel, D.; Lindahl, E. *J. Chem. Theory Comput.* **2008**, *4* (3), 435–447.

(35)   Hansen, J. P.; McDonald, I. R. *Theory of Simple Liquids: With Applications to Soft Matter: Fourth Edition*; Elsevier Ltd, 2013.

(36)   Abascal, J. L. F.; Vega, C. *J. Chem. Phys.* **2005**, *123* (23), 234505.

(37)   Errington, J. R.; Debenedetti, P. G. *Nature* **2001**, *409* (6818), 318–321.

Chapter 3: Size Dependent Order-Disorder Transition in Hydration Layer of Hydrophobic Solutes: Analogy with Temperature Dependence in Bulk Water

3.1 Introduction

If life can be considered as a massive self-assembly process, water seems to be a major driving force behind it. Hydrophobic interactions play a major role in many of such processes, including protein folding, denaturation, molecular recognition, self-assembly of amphiphilic molecules into bilayers, vesicles and so on.[1–7] Despite enormous efforts combining both experimental[8–11] and theoretical[5,12–19] tools, the precise molecular nature of hydrophobic interactions has remained elusive and debates continue.[1,19,20] The primary reason behind the complexity of a *simple* solvent like water seems to be the strong context dependence of the water mediated interactions, e.g. properties of bulk water vs. surface water vs. water in a confined medium, or water near a hydrophobic vs. hydrophilic molecule/surface and so on.

In particular, it has been theoretically predicted by Chandler and coworkers[7,12] and later validated by a multitude of computer simulation studies that the molecular nature of hydrophobic interactions undergoes a qualitative change with the size of the hydrophobic solutes.[15,16,21] When the hydrophobic solutes are smaller than a nanometer, water molecules can still maintain the bulk-like hydrogen bonded network around the solute since the local density fluctuations in water can create large enough cavities to accommodate such solutes. In this scenario water maximizes the enthalpic stabilization (by maintaining the bulk-like number of hydrogen bonds) at the cost of loss of entropy of the hydration shell water molecules due to the excluded volume of the solute.[22,23] On the other hand, if the solute becomes much larger than a nanometer in size (much larger compared to the cavity size distribution in bulk water), water molecules are unable to maintain the bulk-like hydrogen bond network. However, water can still lower the surface free energy by introducing a vapor-like interface characterized by higher entropy of the hydration layer.[24]

Although the above theoretical arguments sound quite reasonable and many computer simulation studies have validated different aspects of this prediction,[15,16,21,24] a direct experimental proof of this length-scale dependent order-disorder transition at the nanometer length-scale has

remained somewhat elusive.[1] Most of the earlier attempts to observe the clathrate-like "more ordered" structures of water molecules around sub-nanometer hydrophobic solutes that would be characterized by "lower entropy" compared to bulk water have not been successful.[10,20,25] Experimental observation of the large scale interfacial density fluctuations around larger hydrophobic surfaces has remained elusive as well. Only recently Ben-Amotz and coworkers have used the novel solute correlated Raman spectroscopy technique to demonstrate a similar length-scale dependence of the hydration layer water structure for *n*-alkanols of varying length of the hydrophobic chain (upto *n*-heptanol).[8] They have demonstrated an interesting correlation between the temperature dependence of the OH stretch band of the hydration layer water molecules with their dependence on the size of the hydrophobic tail. They have hypothesized that the blue shift of the OH stretch band for larger solutes originate from the lowering of local tetrahedral order of the water molecules and weakening of the H-bonded interactions. On the other hand, another recent X-ray Raman Scattering (XRS) study by Mikko and coworkers[10] does not find any dependence of the hydration layer water structure on the chain length of the hydrophobic alcohols.

Motivated by the continuing debate on this subject,[8,10,20,26] we have used a fully atomistic extensive molecular dynamics (MD) to understand the molecular nature of the structural order of the water molecules in the hydration layer of model spherical hydrophobic solute systems with varying size, and shape (spherical and planar). We have used both local water density and local tetrahedral order parameter to characterize the position dependent and angle dependent structural order of the water molecules. We investigate the dependence of the structural order of the hydration shell on the size for model spherical hydrophobic solute systems. We also explore whether any correlation might exist between the size-dependence of spherical hydrophobic solutes and temperature dependence in bulk water in the context of structural order parameters and vibrational dynamics of the water molecules.

3.2 Methodology

3.2.1 Simulation details

All molecular dynamics simulations reported in this work have been performed using the GROMACS (version 4.6.5) software.[27] Two types of water models were used. Flexible TIP4P/2005f[28] water model is used to study the vibrational power spectrum of water molecules

and rigid TIP4P/2005[29] water model is used to look into the structural properties of water. We have chosen the TIP4P/2005 water model, since it provides one of the best available description for the liquid water.[29] In order to study the length-scale dependence in spherical solutes, we have used two different types of models (Figure 3.1), namely single uncharged Lennard-Jones (LJ) particles with varying size (σ), and spherically shaped HCP crystal of multiple methane-like particles. Further details about these models have been provided in the following section. The simulations of hydrophobic solutes in water was performed at temperature 300K and the bulk water simulations were performed at temperatures ranging from 273K to 373K with an increment of 10K.

We have followed the following standard protocol for performing the simulations: (i) energy minimization using steepest-descent algorithm, (ii) equilibration for 1 ns at NVT ensemble (300K) using the v-rescale thermostat,[30] (iii) equilibration for 5 ns at NPT ensemble[31] (1 bar and 300K) using the Berendsen barostat. During the NVT and NPT equilibration, we have restrained the positions of the solute atoms. Periodic boundary conditions have been used in all directions. We have used the Parrinello-Rahman barostat[32] in the production runs. In all simulations, the long range electrostatic interactions have been described by the particle mesh Ewald[33] method with 0.16 nm grid spacing. Newton's equation of motion has been solved using the leap-frog integrator. In case of rigid water model, we have used an integration time step of 2 fs and the trajectory frames have been saved at every 1 ps for 50 ns production run. Whereas in case of flexible water model, to capture the vibrational dynamics an integration time step of 0.1 fs and data saving frequency of 1 fs have been used for the run duration of 1 ns. In the special cases where a cluster of solute particles has been kept frozen, we have excluded any non-bonded interactions between these atoms for numerical efficiency.
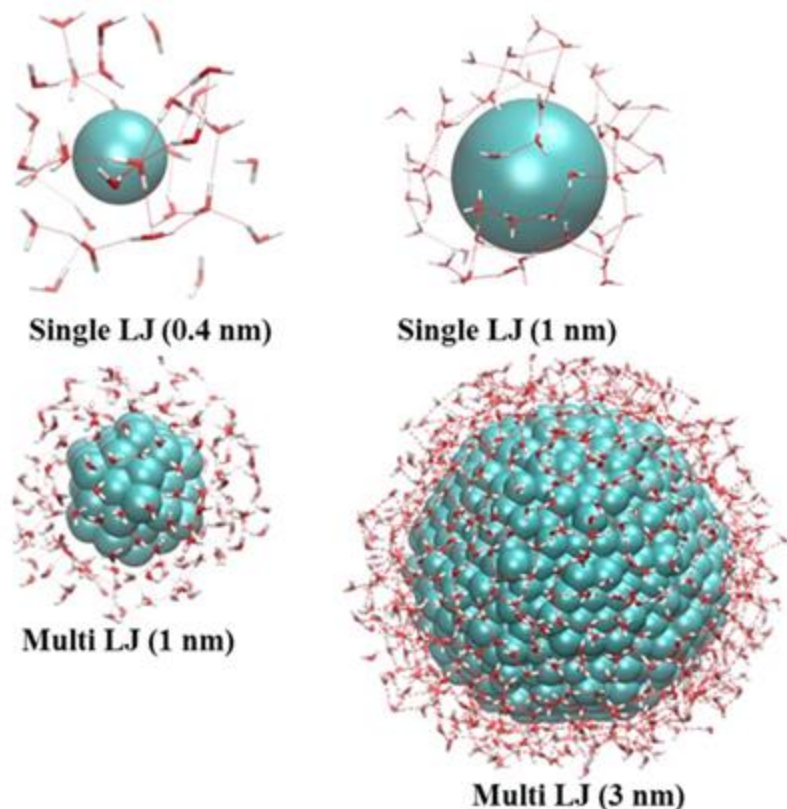
Figure 3.1: Visualization of the different models of hydrophobic solutes used in this work: Spherical solutes: "Single LJ" signifies a single uncharged solute particle, and "Multi LJ" signifies a spherical shaped HCP crystal consisting of multiple methane-like particles. Representative snapshots of the hydration layer have been shown for each case.

3.3 Results and discussion

3.3.1 Tetrahedral order of water molecules and number of hydrogen bonds:

The structural order parameters are calculated using tetrahedral order parameter (Q) as given in Eq. 2.30 and number of hydrogen bond (N_{HB}) using the criterion given in Chapter 2 in subsection 2.6.1.3. The original definition of Q used in bulk water does not involve any cut-off distance for neighborhood criteria, since it requires the four nearest neighbors irrespective of their distances. But in the hydration layer of a hydrophobic surface some of the nearest neighbors of a surface water molecule may appear at very large distances due to lower density of the hydration layer leading to unphysical estimation. In order to avoid this problem, we have introduced a large

cut-off distance of 0.63 nm to check whether a certain water molecule has the four nearest neighbors within this distance. We have ignored any water molecule that does not satisfy this criterion in our calculation of distribution of Q values. We have validated that this definition does not significantly alter the results reported here.

In order to choose the appropriate water model for our study of water structure near hydrophobic solutes, we have performed a benchmark analysis of the probability distribution of the tetrahedral order parameter ($P(Q)$) for different water models (SPC/E, TIP3P, TIP4P, TIP4P/2005 and TIP5P) at 300K temperature and 1 bar pressure (Figure 3.2). It is quite evident that the extent of the tetrahedral structure is quite sensitive to the choice of the water model. In particular, it is quite surprising that the TIP3P water model, which is quite popular in biomolecular simulations, exhibits remarkably less tetrahedral order compared to other models including the other 3-site SPC/E model. For the current work, we have relied on the extensive benchmark studies by Vega and coworkers[29] to choose the relatively recent TIP4P/2005 model,[34] since this model has been found to capture the physical properties of water and ice reasonably well, including various anomalous trends.
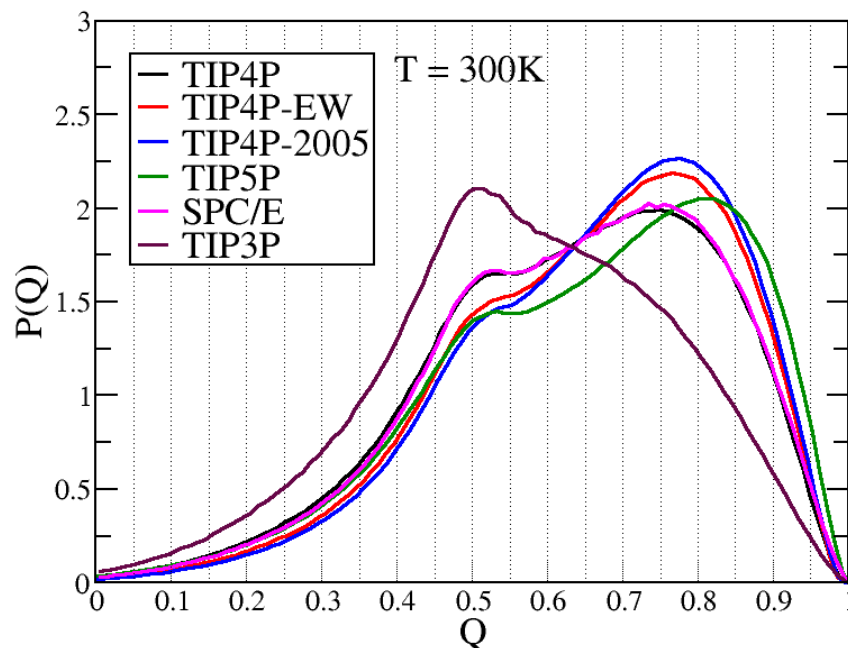
Figure 3.2: The probability distribution of tetrahedral order parameter (P(Q)) for different water models at 300K temperature and 1 bar pressure.

3.3.2 Length-scale dependence of P(Q) in spherical hydrophobic solutes

The main objective of this work is to understand the effect of the size (and shape) of arbitrary hydrophobic solutes on the hydration shell water structure. Before exploring more complex systems, we have first explored the length-scale dependence in model hydrophobic solutes with spherical shape. We have built two different kinds of prototype model systems for this purpose (Figure 3.1): **(i) single LJ:** A single uncharged Lennard-Jones (LJ) sphere immersed in the box of water molecules, where only the size (σ) of the LJ particle has been varied from 0.4nm to 1nm. Please note that for the OPLS-AA united atom model σ=0.373nm for a methane molecule. **(ii) multi LJ:** Since a single LJ sphere of very large size is a rather unphysical model of realistic hydrophobic solutes with large size, we have built spherical models of hydrophobic crystals consisting of multiple LJ spheres with HCP structure. The effective diameter of such spherical crystals has been varied from 1 nm to 4 nm. In the case of the multi LJ model, we have kept all the solute particles frozen and all non-bonded interactions between the solute particles have been turned off.

It must be clarified at this point that we have made a rather unconventional choice of including the solute atom in the calculation of the tetrahedral order parameter while looking for the nearest neighbors of the hydration water molecules. To justify this choice, let us consider a single water molecule (can be considered an arbitrary solute) in the bulk water. While calculating Q for the water molecules in its hydration shell, if we exclude the central "solute" water molecule, we shall obtain a very low Q value, since the central water molecule directly participates in forming the tetrahedral network. This point is demonstrated in Figure 3.3, where we show the sensitivity of the distribution $P(Q)$ of water molecules in the hydration shell of various types of solutes including a single water molecule. While our definition tends to provide slightly higher value of Q for larger solutes, we find it important to stick to a general definition of Q, which should be independent of the solute molecule under consideration (e.g. non-polar/polar/charged/water itself).
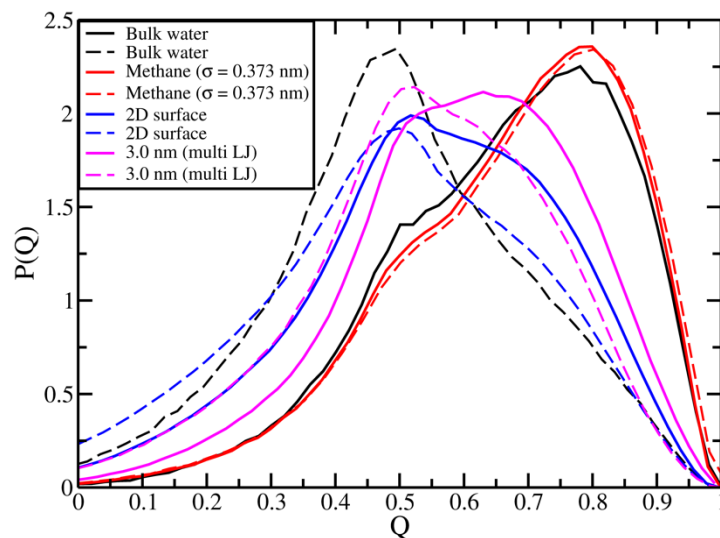
Figure 3.3: The effect of the chosen definition of *Q* value on the *P(Q)* for bulk water, methane, 3 nm sphere and planar surface. The solid lines indicate cases where the solute was included in the neighbor list while calculating *Q*, where the dashed lines indicate where the solute was *not* included. Note the drastic change in the case of water, where excluding the solute leads to complete transformation to a distribution corresponding to a disordered state. Thus, a completely general definition which should be agnostic of the solute under consideration should include the solute in the *Q* calculation as well.

We have calculated the probability distribution of the tetrahedral order parameter (Q) and the number of hydrogen bonds (N_{HB}) formed by the water molecules in the first hydration shell for all of these model hydrophobic solute systems across the size range of 0.4 nm to 3 nm. The results have been summarized in Figure 3.4 (a and b). It is quite evident that both the distributions P(Q) and P(N_{HB}) exhibit a length-scale dependent order-disorder transition around the nanometer length-scale, i.e. the solutes with smaller sizes almost maintain the bulk-like structural order, whereas the larger sizes of the hydrophobic solutes induce structural disorder in its hydration shell. It is quite interesting that both P(Q) and P(N_{HB}) exhibit a distinct bimodal-like distribution between the higher Q (~0.8) and lower Q (~0.5) regions that resembles a weakly first order transition induced by the size of the solute. We have noticed that our "multi LJ" model with 1 nm diameter shows a reduction in structural order compared to the "single LJ" analogue with the same diameter. Of course, presence of multiple LJ particles at the surface creates a different effective interaction as compared to a simple Lennard Jones particle. Irrespective of this dependence on the chosen

model, the qualitative trend of reduction in both Q and N_{HB} with increasing solute size is quite clear.
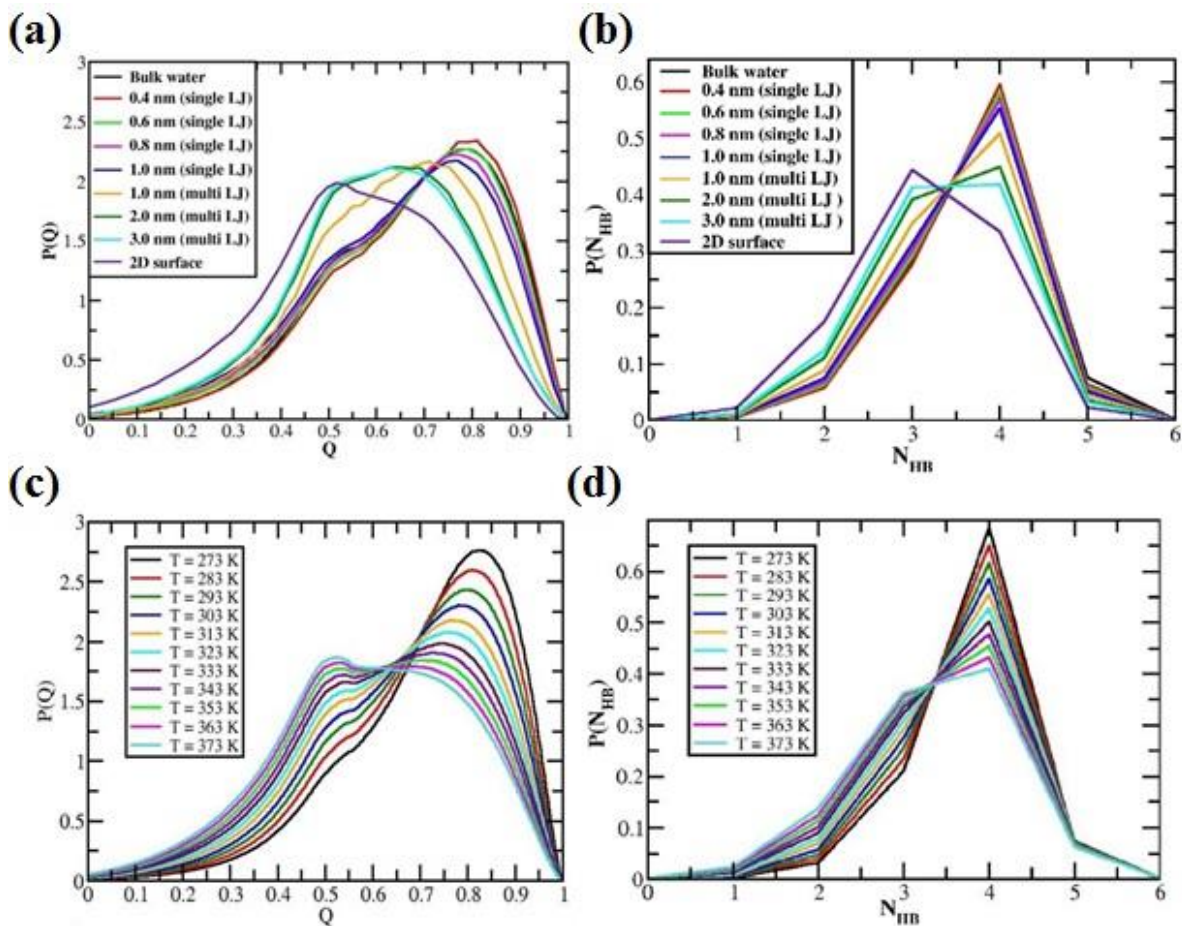
Figure 3.4: Distribution of tetrahedral order parameter **(Q)** and number of hydrogen bonds **(N_{HB})** : **(**a and b**)** first hydration shell water around the hydrophobic molecules for single and multi LJ models with size ranging from 0**.**4 nm to 3 nm, for 2D surface of hydrophobic molecule and bulk water at 300K and **(**c and d**)** bulk water with temperature variation from 273 to 373K.

Similar to the findings of Galamba[26] using a polarizable Amoeba water model, we have also observed that for very small solutes like methane (~0.4 nm) the fraction of water molecules with higher Q values slightly increases as compared to the bulk water. Although it is tempting to correlate this slight enhancement of tetrahedrality to the "iceberg model" of Frank and Evans,[35] it has been clarified that such a small increase in tetrahedrality (if at all) may not be enough to explain the large decrease in water entropy on hydration of small hydrophobic solutes.[36] The origin of the

entropy reduction has been attributed to the excluded volume effect, and the slight enhancement of tetrahedrality might be a curious side effect of that constraint imposed by the solute molecules.

3.3.3 Analogous behavior of hydration shell water around hydrophobes of varying size and bulk water with varying temperature

The seminal work by Ben-Amotz and coworkers[8] have suggested based on their vibrational spectroscopy data that water around smaller solutes may behave as cold temperature water due to enhanced ordering, whereas water around larger solutes resemble higher temperatures. Hence, we explore here the analogy between temperature dependence in bulk water with respect to size-dependence for water around spherical hydrophobic solutes. Figure 3.4 presents the comparison between both kind of dependence for distributions of tetrahedral order parameter and number of hydrogen bonds. The results for bulk water indicate that as the temperature increases, the population of four hydrogen bonds decreases gradually and those of lower number of hydrogen bonds increases. A similar trend in the distribution can be seen for the hydration shell water around hydrophobic solutes of varying size. Thus, we can conclude that water around hydrophobic solutes with increasing size has resemblance to higher temperature bulk water with increased disorder and lower number of hydrogen bonds, i.e. higher entropy and lower enthalpy.
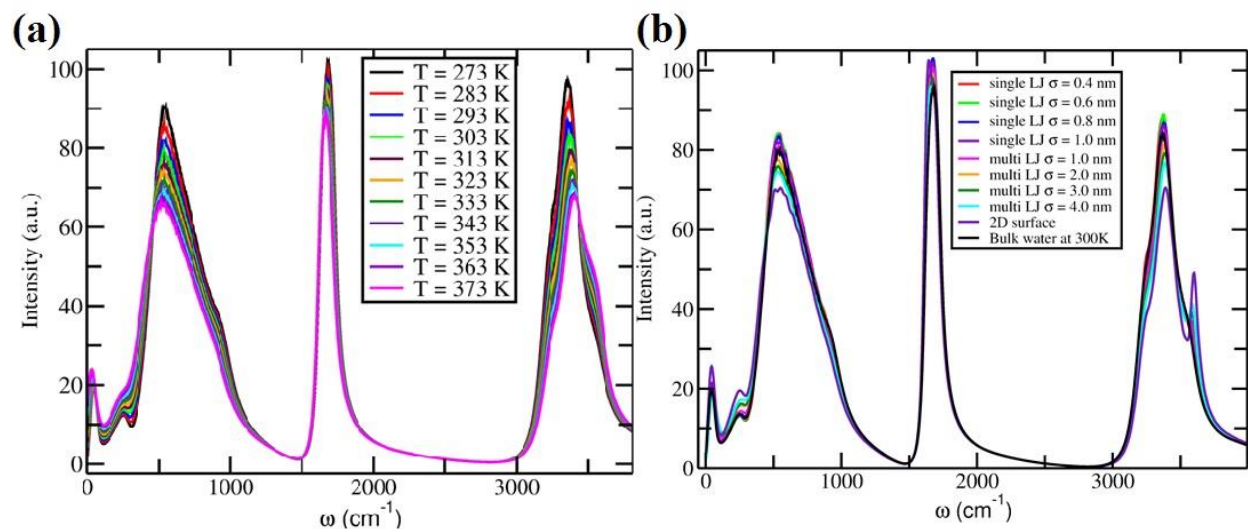
Figure 3.5: Full power spectra of (a) bulk water at temperatures ranging from 273 to 373K with an increment of 10K and (b) hydration shell water around the hydrophobic molecules for single

and multi LJ models with size ranging from 0.4 nm to 4 nm, for 2D surface of hydrophobic molecule and Bulk water at 300K.

Further, we have calculated the vibrational power spectrum of water by using a method based on the computation of the density of states.[37] This involves the Fourier transform of the velocity autocorrelation function (VAC) given as:[37]

$$I(\omega) \propto \int_0^\infty dt \exp(-i\omega t)\langle \vec{v}(0).\vec{v}(t)\rangle \tag{3.1}$$

where, I, ω, v and t are the intensity, frequency, velocity and time respectively. $\langle \vec{v}(0).\vec{v}(t)\rangle$ is the velocity autocorrelation function. Figure 3.6 shows the full power spectrum for (a) bulk water with temperature variation and (b) hydration shell water around hydrophobic solutes with varying size. The observed trend of bulk water matches very well with the existing results from classical simulation of flexible water molecules.[28,37] The vibrational band for the frequency range 3100 to 3800 cm^{-1} of the power spectra is shown in Figure 3.7 (a and b) for bulk and hydration shell water, separately. The intensity of O-H bond stretching band around ~3400 cm^{-1} decreases with increase in temperature whereas the intensity of dangling OH bonds or the percentage of non-hydrogen bonded water increases in the range of 3550 to 3600 cm^{-1} as expected. Similarly, intensities of O-H stretching band of hydration shell water get reduced with an increase in the size of solutes and concurrently, the intensity of the non-hydrogen bonded water molecules is increasing around 3550 to 3600 cm^{-1}. A noticeable increase in this peak intensity can be seen at and beyond hydrophobic solute size of 1nm where the water order-disorder transition takes places as reported previously. A very prominent peak around ~3600cm^{-1} for the extreme case of lowest curvature of the hydrophobic solute (planar 2D surface) shows that the population of non-hydrogen bonded water is maximum. Thus, all of these results support our hypothesis that increasing temperature in bulk water is analogous to the properties of hydration shell water with increasing size of hydrophobes.
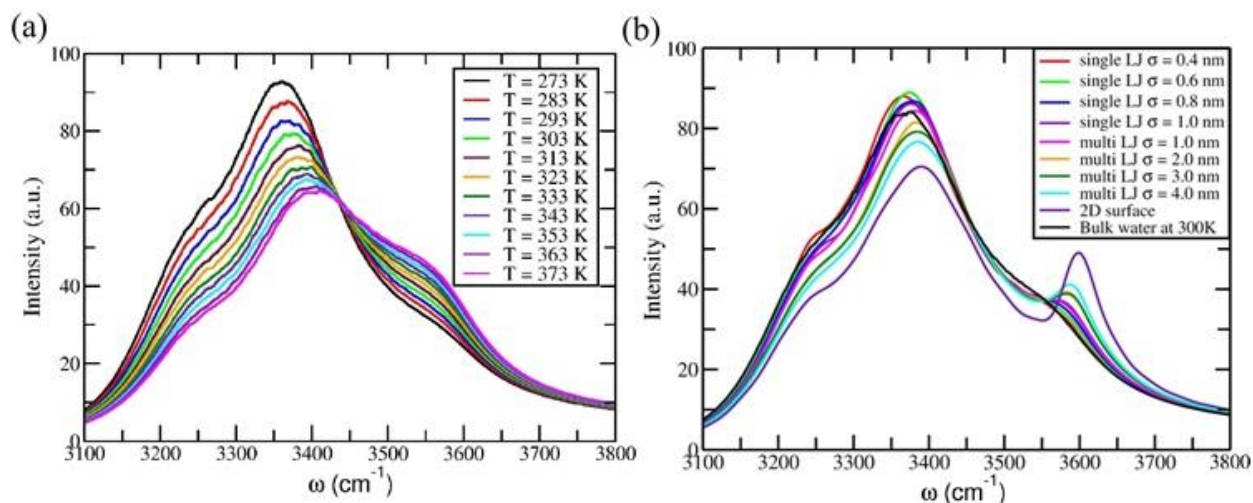
Figure 3.6: Vibrational spectra of OH bond for **(**a**)** bulk water with temperature variation from 273 to 373K and **(**b**)** first hydration shell water around the hydrophobic molecules for single and multi-LJ models with size ranging from 0**.**4 nm to 4 nm, for 2D surface of hydrophobic molecules and bulk water at 300K.

3.4 Conclusion

We have demonstrated the nature of solute size dependent order-disorder transition in the hydration layer of spherical hydrophobic solutes by using the tetrahedral order parameter and number of hydrogen bonds. For small solutes comparable to methane, there is a rather subtle increase in structural ordering in hydration shell, whereas above the nanometer lengthscale the increase in disorder and decrease in number of hydrogen bonds is significant. In addition, we have demonstrated an interesting analogy that variation in structural and dynamical properties of hydration shell water around hydrophobic solutes with increasing size has quite similar behavior as temperature increase in bulk water**.** Hence, hydration shell water around larger sizes behave similar to higher temperature bulk water with higher disorder and lower number of hydrogen bonds associated with an entropy**-**enthalpy compensation effect**.**

3.5 References

 (1)   Ball, P. *Chem. Rev.* **2008**, *108* (1), 74–108.

(2)   W. Kauzmann. *Adv. Protein Chem.* **1959**, *14*, 1–63.

(3)   Tanford, C. *Science* **1978**, *200* (4345), 1012–1018.

(4)   Berne, B. J.; Weeks, J. D.; Zhou, R. *Annu. Rev. Phys. Chem.* **2009**, *60* (1), 85–103.

(5)   Godawat, R.; Jamadagni, S. N.; Garde, S. *Proc. Natl. Acad. Sci. U. S. A.* **2009**, *106* (36), 15119–15124.

(6)   Levy, Y.; Onuchic, J. N. *Proceedings of the National Academy of Sciences of the United States of America*. National Academy of Sciences March 9, 2004, pp 3325–3326.

(7)   Chandler, D. *Nature* **2005**, *437* (7059), 640–647.

(8)   Davis, J. G.; Gierszal, K. P.; Wang, P.; Ben-Amotz, D. *Nature* **2012**, *491* (7425), 582–585.

(9)   Davis, J. G.; Rankin, B. M.; Gierszal, K. P.; Ben-Amotz, D. *Nat. Chem.* **2013**, *5* (9), 796–802.

(10)   Juurinen, I.; Pylkkänen, T.; Sahle, C. J.; Simonelli, L.; Hämäläinen, K.; Huotari, S.; Hakala, M. *J. Phys. Chem. B* **2014**, *118* (29), 8750–8755.

(11)   Stirnemann, G.; Rossky, P. J.; Hynes, J. T.; Laage, D. *Faraday Discuss.* **2010**, *146*, 263–281.

(12)   Lum, K.; Chandler, D.; Weeks, J. D. *J. Phys. Chem. B* **1999**, *103* (22), 4570–4577.

(13)   Kotlarchyk, M.; Chen, S. H.; Huang, J. S. *J. Phys. Chem.* **1982**, *86* (17), 3273–3276.

(14)   ten Wolde, P. R.; Chandler, D. *Proc. Natl. Acad. Sci. U. S. A.* **2002**, *99* (10), 6539–6543.

(15)   Rajamani, S.; Truskett, T. M.; Garde, S. *Proc. Natl. Acad. Sci. U. S. A.* **2005**, *102* (27), 9475–9480.

(16)   Athawale, M. V; Goel, G.; Ghosh, T.; Truskett, T. M.; Garde, S. *Proc. Natl. Acad. Sci. U. S. A.* **2007**, *104* (3), 733–738.

(17)   Xi, E.; Patel, A. J. *Proc. Natl. Acad. Sci. U. S. A.* **2016**, *113* (17), 4549–4551.

(18)   Ashbaugh, H. S.; Truskett, T. M.; Debenedetti, P. G. *J. Chem. Phys.* **2002**, *116* (7), 2907–

2921.

(19)   Banerjee, S.; Singh, R. S.; Bagchi, B. *J. Chem. Phys.* **2015**, *142* (13).

(20)   Blokzijl, W.; Engberts, J. B. F. N. *Angew. Chemie Int. Ed. English* **1993**, *32* (11), 1545–1579.

(21)   Patel, A. J.; Garde, S. *J. Phys. Chem. B* **2014**, *118* (6), 1564–1573.

(22)   Laage, D.; Stirnemann, G.; Hynes, J. T. *J. Phys. Chem. B* **2009**, *113* (8), 2428–2435.

(23)   Sasikala, W. D.; Mukherjee, A. *J. Phys. Chem. B* **2014**, *118* (36), 10553–10564.

(24)   Willard, A. P.; Chandler, D. *J. Chem. Phys.* **2014**, *141* (18), 18C519.

(25)   Pohorille, A.; Pratt, L. R. *J . Am. Chem. SOC* **1990**, *112*, 5066–5074.

(26)   Galamba, N. *J. Phys. Chem. B* **2013**, *117* (7), 2153–2159.

(27)   Hess, B.; Kutzner, C.; Van Der Spoel, D.; Lindahl, E. *J. Chem. Theory Comput.* **2008**, *4* (3), 435–447.

(28)   González, M. A.; Abascal, J. L. F. *J. Chem. Phys.* **2011**, *135* (22).

(29)   Abascal, J. L. F.; Vega, C. *J. Chem. Phys.* **2005**, *123* (23), 234505.

(30)   Bussi, G.; Donadio, D.; Parrinello, M. *J. Chem. Phys.* **2007**, *126* (1).

(31)   Berendsen, H. J. C.; Postma, J. P. M.; Van Gunsteren, W. F.; Dinola, A.; Haak, J. R. *J. Chem. Phys.* **1984**, *81* (8), 3684–3690.

(32)   Parrinello, M.; Rahman, A. *J. Appl. Phys.* **1981**, *52* (12), 7182–7190.

(33)   Essmann, U.; Perera, L.; Berkowitz, M. L.; Darden, T.; Lee, H.; Pedersen, L. G. *J. Chem. Phys.* **1995**, *103* (19), 8577–8593.

(34)   Vega, C.; Abascal, J. L. F. *Physical Chemistry Chemical Physics*. November 28, 2011, pp 19663–19688.

(35)   Frank, H. S.; Evans, M. W. *J. Chem. Phys.* **1945**, *13* (11), 507–532.

(36)   Graziano, G. *J. Phys. Chem. B* **2014**, *118* (9), 2598–2599.

(37)   Liu, H.; Wang, Y.; Bowman, J. M. *J. Chem. Phys.* **2015**, *142* (19).

Chapter 4: Dynamic length-scale and solute-solvent coupling in hydration of flexible hydrophobic polymers

4.1 Introduction

It has been well established that hydrophobic effects encourage a wide range of molecular phenomena in aqueous solutions such as protein folding, membrane formation, micelle formation, and so on.[1–6] As predicted by the Chandler[7], water structural order-disorder transition will takes place on a nanometer length-scale around hydrophobic solutes. Hydrophobic hydration depends on the geometry of the solute surface.[8,9] For the planar interfaces such as air-water interface, surface water sacrifice one hydrogen bond.[10] For the linear rod like geometries such as hydrophobic polymers immersed in water, the hydration shell water preserves almost similar structure to methane hydration shell.[11] The drying transition between the two hydrophobic plates immersed parallel in water will occur below the critical distance of their separation (D_c).[3,12] Additionally, the chemistry of the surface also plays a role in structural modification of hydration shell water.[13] Recently in an experimental study, it has been shown that the OH group attached to methyl group in methanol reduces the tetrahedrality and fragility of the first hydration shell compared to methane.[14] Water structural crossover length-scale is temperature dependent as well, it decreases with increase in temperature.[15,16]

Since, hydrophobic collapse is a vital step in the mechanism of protein folding,[17,18] water expels out after the formation of intermediate partially hydrated protein hydrophobic core.[19] Starting from the extended conformational state, polymers as well as proteins undergo entropic coiling.[20] Recently in MD study, temperature dependent coil-to-globule transition of hydrophobic polymer in water has been shown.[21] The dynamic folding and unfolding of hydrophobic polymer forms a loop-like structures locally which generates the heterogeneous curvatures on the different domains of the polymeric surface. However, shorter polymeric chain would be preferably stays in extended state while longer chains attains globular/rodlike collapsed structure.[22] It has been shown earlier that the solubility and conformation of *n*-alkanes in water has a length dependence,[23,24] and the relative stability of the extended and the collapsed states of these chains in water undergoes a length dependent crossover around the range of C20-C30 depending on the model chosen.[22] Very

long alkanes (e.g. C100) would spontaneously collapse into a "dewetted" conformational state characterized by much smaller radius of gyration (R_g) of the polymer chain.[20] The flexible hydrophobic surface having the patches of higher and lower curvature may induce the structural heterogeneity in the hydration shell. It is quite expected that the hydrophobic collapse into a spherical droplet would be associated with an increase in the effective size of the solute (or solvent excluded region).

Recently, Ben-Amotz and co-workers[25] experimentally found that water structural transformation takes place at ~1 nm for the increasing hydrophobic chain length of alcohol. On the other hand, In XRS study of linear chain alcohols, authors found no changes in the tetrahedrality of the first hydration-shell upto propanol.[26] Therefore, it seems that there is an experimental problem of choosing the suitable model of hydrophobic surface for the study of hydrophobic interaction. Another experimental problem can be the possibility of the clustering of amphiphilic molecules which cannot rule out when used for such studies.[26,27]

In this chapter, we have used a combination of fully atomistic extensive molecular dynamics (MD) and replica exchange molecular dynamics (REMD) studies[28] (a technique to enhance the sampling of configurational space) to understand the molecular nature of the structural order of the water molecules in the hydration layer of model hydrophobic polymeric solute systems (flexible and rigid linear) with varying local topology. We have used both local water density and local tetrahedral order parameter to characterize the position dependent and angle-dependent structural order of the water molecules. Although the length-scale dependence of hydrophobic hydration has been well-studied using molecular dynamics simulations, a systematic study of the effect of size/shape/dimensionality in the case of a complex molecule which can undergo dynamic changes in the local topology has been missing. Further, we have characterized the dependence of the tetrahedral order parameter distribution on the size for model polymeric solute systems. We have explored the presence of length-dependent crossover in linear polymeric systems. Finally, we have taken up the system of a flexible hydrophobic homopolymer (n-alkane) in water that can undergo conformational changes between an extended coil and globular or rodlike collapsed states. We have explored the coupling between the local length-scale of such topologically heterogeneous systems and the local structural properties of the water molecules. We also comment on the relative importance of the fluctuations in position-dependent (density) and orientation-dependent

(tetrahedral order) structural order in controlling the hydrophobicity-induced conformational changes in the polymer. In addition, in the last section, we attempt to envisage the water order-disorder transition for the experimentally used alcohol chain lengths and concentrations.

4.2 Methodology

4.2.1   Simulation details

In order to study the length-scale dependence in hydrophobic homopolymers, we have used n-alkanes with varying number of carbon atoms such as 10, 40, 60, 80 and 100. In the following sections we shall denote these systems by C10, C40 and so on. The representative snapshots of model polymeric systems have been shown in Figure 4.1 (a-c). In all of our simulations, the polymers and alcohols have been modeled using the all-atom OPLS-AA[29] force field. We have also used a slightly modified version of the TraPPE-UA[30] force field in the case of C100 in order to check the dependence of the nature of the hydrophobic collapse on the polymer model. Two types of water models have been used. Flexible TIP4P/2005f[31] water model have been used to study the vibrational power spectrum of water molecules and rigid TIP4P/2005[32] water model have been used to look into the structural properties of water. In addition, we have also simulated only one monomer of alcohol in water with concentrations as listed in Table 4.1. The concentration of alcohol has been kept 0.5M for methanol, 1-propanol (as used by Davis et al.[25] and Perera et al.[27]) and 1-heptanol.

We have followed the following standard protocol for performing the simulations: (i) energy minimization using steepest-descent algorithm, (ii) equilibration for 1ns at NVT ensemble (300K) using the v-rescale thermostat,[33] (iii) equilibration for 5ns at NPT ensemble (1 bar and 300K) using the Berendsen barostat.[34] During the NVT and NPT equilibration, we have restrained the positions of the solute atoms. Periodic boundary conditions have been used in all directions. We have used the Parrinello-Rahman barostat[35] in the production runs. These runs have been continued for 5 ns to 50 ns depending on the system under consideration. In all simulations, the long range electrostatic interactions have been described by the particle mesh Ewald method with 0.16 nm grid spacing.[36] Newton's equation of motion has been solved using the leap-frog integrator. In case of rigid water model, we have used an integration time step of 2 fs and the trajectory frames have been saved at every 1 ps for 50 ns production run. Whereas in case of

flexible water model, to capture the vibrational dynamics an integration time step of 0.1 fs and data saving frequency of 1 fs have been used for the run duration of 1 ns. In the cases where the polymers have been kept frozen, we have excluded any non-bonded interactions between these atoms for numerical efficiency.

Further, we have employed the replica exchange molecular dynamics (REMD)[2] method to enhance the conformational sampling while dealing with the flexible C40, C60 and C80 polymers, since the exchange equilibrium between the extended and collapsed states are too slow for obtaining the correct population distribution using normal MD runs for longer chains. The selected temperature range has been 273K to 373K and 60-70 replicas have been used depending on the system. Each replica has been equilibrated using the protocol mentioned above. During the production run of 100ns, the exchanges between two consecutive replicas have been attempted at every 2ps with an average exchange probability of ~20%. We have reported the population distribution obtained from the replica at 300K only.

C40 (rigid)   C100 (extended)   C100 (collapsed)
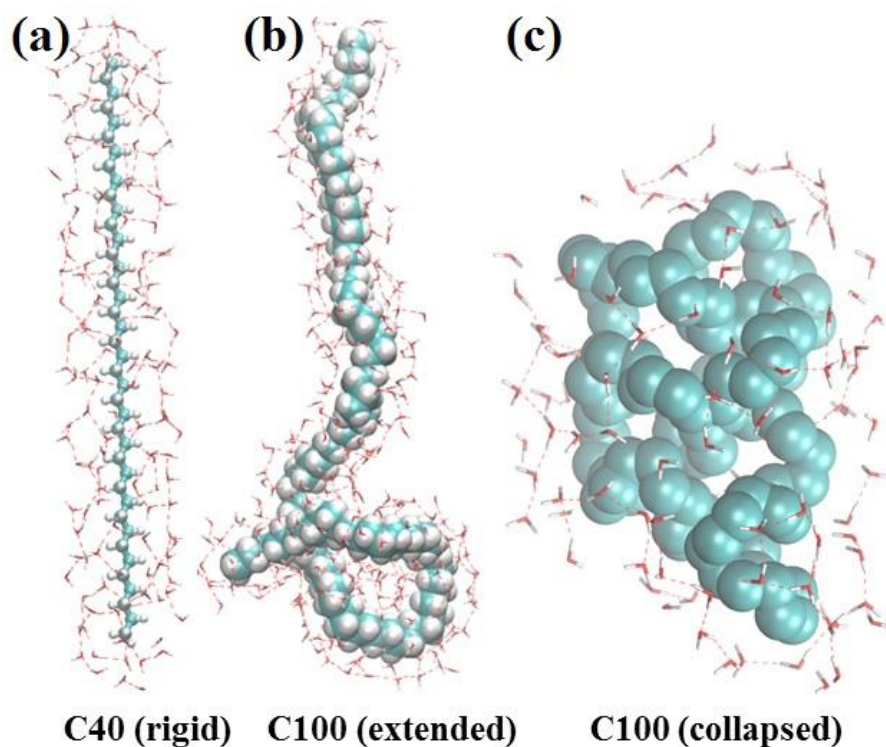
Figure 4.1: Representative snapshots of model hydrophobic polymer systems, (a) C40, a rigid polymer chain (b) C100 extended flexible polymer chain and (c) C100 collapsed flexible polymer chain.

Table 4.1: Concentration of monomeric alcohols in water

System	Concentration (M)
Methanol	0.145
1-propanol	0.106
1-pentanol	0.075
1-heptanol	0.062
1-nonanol	0.046
1-undecanol	0.039

4.3 Results and discussion

4.3.1 Length-scale dependence in linear rigid hydrophobic chains

We have explored whether a nanometer scale order-disorder transition observed for spherical hydrophobic solutes (as discussed in the Chapter 3) would exist for a purely linear system, e.g. a linear *n*-alkane chain with increasing chain length. To address this question from a purely academic point of view, we have first simulated perfectly linear (all-trans) and rigid *n*-alkane chains in water. As discussed briefly in Chapter 3, similar tetrahedral order parameter *(Q)* and number of hydrogen bonds *(N_{HB})* are calculated for the current systems as well. The calculated *P(Q)* for various chain lengths (C1 to C80) have been summarized in Figure 4.2 (a and b). Remarkably, we find that while moving from shorter linear chains (C10) to much longer linear chains (C80) the tetrahedral order does not decrease appreciably. There is only slight decrease in the position of the maximum in *P(Q)* in going from methane (C1) to C10.
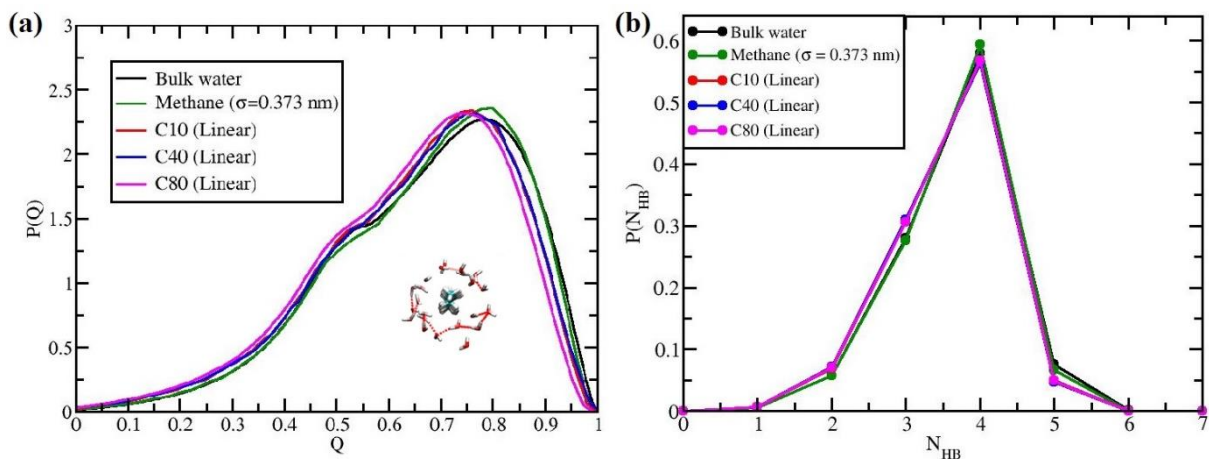
Figure 4.2: Distribution of tetrahedral order parameter *(P(Q))* **(**a**)** and distribution of number of H-bonds *(N$_{HB}$)* **(**b**)** for the water molecules in the first solvation shell of linear **(**all-trans**)** and frozen n-alkane chains with sizes C1 **(**methane**)**, C10, C40 and C80**.** The inset figure shows a representative snapshot of a cross**-**sectional slice, where the water molecules are seamlessly forming hydrogen bonds by wrapping around the very long linear polymer chains**.**

The reason behind this somewhat counter-intuitive phenomenon is rather simple. The all-trans fully linear alkane chain has a cylindrical symmetry. There are two length-scales associated with this cylinder: (i) along the principal axis (axial direction), which is proportional to the length of the chain, and (ii) perpendicular to the principal axis (diameter of the cylinder), which is independent of the length of the chain. This point has been graphically illustrated in the inset of Figure 4.2 (a), where if we look along the principal axis of the linear chain, we get a disk-like view corresponding to the cross-section. The diameter of this cross-section is sub-nanometer (~0.39nm, which is the diameter of a CH_2 group in the OPLS/AA united atom model), and it is independent of the length of the linear alkane chain. Thus, the water molecules can wrap around the cylinder to maintain the hydrogen-bonded network almost as good as any smaller size of the chain. This demonstrates the remarkably adaptive nature of water as a solvent, which can find the dimension with the highest curvature (smaller length-scale) in a complex solute molecule in order to maximize the number of hydrogen bonds and hence minimize the enthalpy. The structural disorder in the hydration layer would not appear unless the shortest length-scale available on the solute surface becomes more than the nanometer length scale.

4.3.2 Length-scale dependence in linear flexible hydrophobic chains

In reality, the chains would undergo folding and unfolding, result in the either the globular collapsed state or extended state. This will result in the decrease in the tetrahedral order (Q) of the water molecules around it. Thus, it would be interesting to explore how the water structure in the hydration shell of these flexible molecules would change as the polymer undergoes hydrophobic collapse, or whether the local water structure is dynamically coupled to the local conformational state of the polymer.

We have studied this aspect of the coupling between the conformational state of the polymer and the local water structure for the n-alkanes with various lengths: C10, C40, C60, C80 and C100. We have started with the all-trans (linear) conformation of the polymer in water, and allowed the system to evolve following the natural dynamics. We have used various structural parameters to characterize the conformational state of the polymer, and the associated change in the solvation shell. We have used the number of intra-molecular contacts ($N_{contacts}$) between the polymer atoms normalized by the chain length in order to describe the conformational state of the polymer. Higher values of $N_{contacts}$ would signify a more compact collapsed state, whereas lower values would indicate extended state (Figure 4.3 (a)). We have defined two atoms to be in contact if they are separated by at least 5 bonds ($|\,i - j\,| > 3$ for the i-th and j-th atoms) and the distance between them is below 0.5 nm. In order to characterize the solvent exposure, we have computed the number of water molecules within a cut-off distance of 0.585 nm (N_{waters}). Since N_{waters} would trivially increase with the chain length, we have decided to scale this with the computed solvent accessible surface area (SASA) to obtain the surface water density (Figure 4.3(b)). While the number of intra-molecular contacts should increase upon the collapse, the surface water density should decrease, if there is any partial dewetting involved with the hydrophobic collapse. In Figure 4.3, we have demonstrated the time evolution of $N_{contacts}$, N_{waters} and $<Q>$ for alkane chains of various lengths (C10 to C100), where each simulation starts with the fully linear conformation. Clearly, C10 remains in the extended state, whereas C40 visits both the extended and collapsed states within 30 ns signifying a comparable stability of these conformational states. The system undergoes an irreversible collapse for C60 onwards and remains in the collapsed state. A direct correlation between the conformational changes of the polymer from extended to collapsed state and associated decrease in both the N_{waters}/SASA and $\langle Q \rangle$ value is quite clear. The decrease in the surface water density associated with the increase in $N_{contacts}$ is a signature of partial dewetting of

the solvent exposed surface, and interestingly the collapsed states in all of these systems exhibit comparable surface water density. To further illustrate the direct correlation between the conformational state of the polymer and the structural properties of the hydration layer, we have computed various cross-correlation functions (CCF) defined as in Eq. 2.32. In Figure 4.4, we have demonstrated the CCFs for each pair of quantities described above, namely (i) Total $N_{contacts}$/Chain length, (ii) N_{waters}/SASA, and (iii) $<Q>$ of hydration layer. We have presented the CCFs for C40 only, since only in this system we observe a dynamic equilibrium between the extended and collapsed states within our observation time scales (see Figure 4.3). CCFs of both water properties (N_{waters}/SASA and $<Q>$) with the polymer property ($N_{contacts}$/Chain length) exhibit an anti-correlation characterized by the negative values of the CCFs, whereas the cross-correlation between water density and tetrahedral order has positive cross-correlation as expected. The anti-correlation is also visible in the Figure 4.3, where the both the water density and tetrahedral order decrease with the increase in $N_{contacts}$ and vice versa. Although the anti- correlation between these global variables is significant only for C40, we shall show later that such anti-correlation exists even in the collapsed state if we consider the fluctuations of the local variables, i.e. $N_{contacts}$, N_{waters} and $<Q>$ around individual polymer atoms.

Surprisingly, the decrease in the average tetrahedral order ($\langle Q \rangle$) upon hydrophobic collapse is not quite dramatic even in the cases of hydrophobic collapse in C80 or C100 (Figure 4.3 (c)). To emphasize this point, we have shown both the $P(Q)$ and $P(N_{HB})$ for the same systems using equilibrium MD and REMD simulations in Figure 4.5. If we compare these distributions with the corresponding spherical systems (see Figure 3.4 (a and b) in Chapter 3), we can easily conclude that the tetrahedral order around the collapsed state of even the largest polymer (C100) is higher than or comparable to our "multi LJ" model with 1 nm diameter, which is essentially the effective diameter of the collapsed states in C100.

We find it quite interesting that even for a very large hydrophobic polymer (up to C100), the local tetrahedral order and hydrogen bond distribution undergoes very little change upon collapse or other conformational changes. Thus, it may not be surprising that it has been virtually impossible to detect such small changes experimentally in the cases of amphiphilic molecules with rather short hydrophobic tails. We do not even expect such changes to be important for chain

lengths shorter than 30, since the population of the collapsed state (larger length-scale) is likely to be negligible for smaller systems.
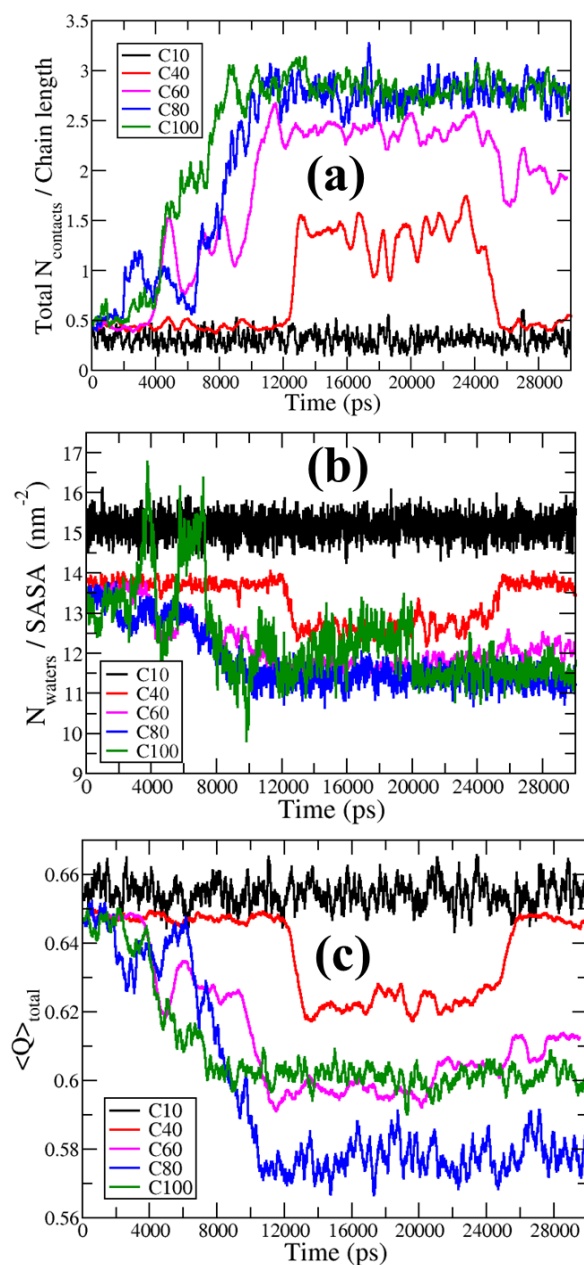
Figure 4.3: Time evolution of **(a)** total number of polymer-polymer contacts / chain length, **(b)** total number of water molecules in the hydration layer per unit area of the solvent accessible surface area **(SASA)**, and **(c)** average tetrahedral order parameter *(<Q>)* of the water molecules in the hydration layer for flexible *n*-alkanes with varying length **(**C10 to C100**)** starting with the all-trans linear conformation**.** The hydrophobic collapse is characterized by the increase in the

number of polymer-polymer contact density and decrease in the surface water density due to partial dewetting. The hydrophobic collapse also correlates with decrease in the $<Q>$ value.
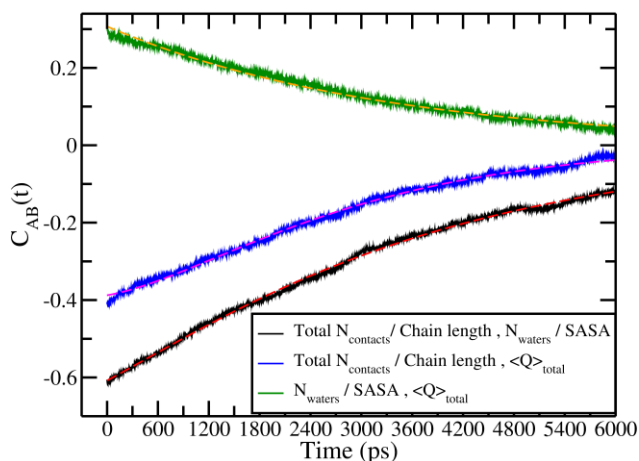
Figure 4.4: Cross-correlation function $(C_{AB}(t))$ for three pairs of quantities (A,B) for C40 from the Figure 4.3, namely (i) Total $N_{contacts}$ / Chain length and N_{waters}/SASA (black line), (ii) Total $N_{contacts}$ / Chain length and $<Q>_{total}$ (blue line), and (iii) N_{waters}/SASA and $<Q>_{total}$ (green line). The first two quantities depict the cross-correlation between the polymer collapse coordinate and the water density/structure coordinates. Both of them show negative values signifying anti-correlation, whereas the cross-correlation between water density and tetrahedral order has positive cross-correlation as expected.
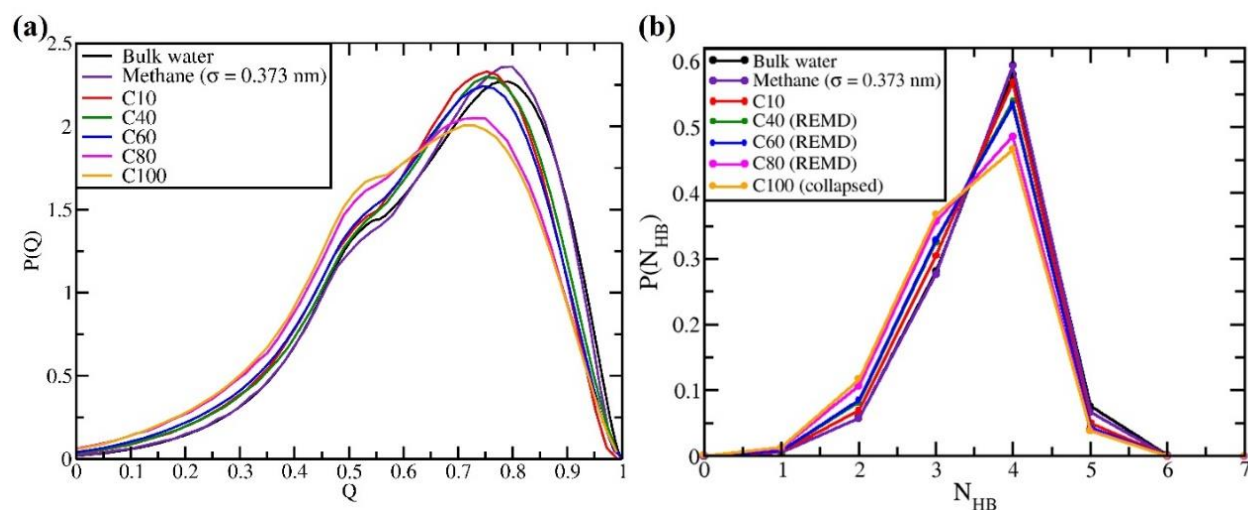
Figure 4.5: Distribution of tetrahedral order parameter *(P(Q))* (a) and distribution of number of H-bonds *(P(N_{HB}))* (b) for the water molecules in the first solvation shell of flexible *n*-alkane chains

with sizes C1 (methane), C10, C40, C60 and C80 and C100. We have used distributions obtained from REMD calculations for intermediate chain lengths C40, C60 and C80. The C100 data has been obtained from the fully collapsed state to avoid any contribution from the unstable extended state. The trends demonstrate that there exist reasonably high Q values and almost bulk-like H-bond distribution up to C60, whereas C80 and C100 shows only minor decrease.

4.3.3   Local structure, density fluctuations and dynamic length-scale

As of now we have been looking at the overall conformational state of the polymer (characterized by the total number contacts, radius of gyration etc.) and the overall water structure over the whole solvent accessible surface of the polymer. But it may so happen that even in the random coil state of the polymer a loop-like structure (higher number of contacts) might have formed locally, and the nearby water molecules must dynamically adjust to these local fluctuations in the solute length-scale, or more precisely, the local curvature. Similarly, even in the collapsed state (analogous to the folded state of a protein) there can be instances of local unfolding ("cracking") or instances of large scale conformational changes in local domains. Thus, it would be interesting to look for signatures of such locally "dynamic length-scales" and their coupling to the local water structure.

As a test case, we have taken the 50th atom in the C100 chain, and followed its local microscopic properties (both intra-molecular and solvation coordinates) during the global hydrophobic collapse of the whole polymer chain. We have considered three properties: (i) number of intra-molecular contacts formed by this single atom, which is an indirect measure of the extent of local hydrophobic collapse, (ii) the number of water molecules in hydration shell of this atom, and (iii) <Q> of this local hydration shell. The time evolution of these properties has been demonstrated in Figure 4.6. We find that even though the global collapse coordinate (total number of contacts, Figure 4.3) shows a monotonous collapse process, the local probe shows signatures of large fluctuations around 5 ns (marked by a blue ellipse in Figure 4.6). More interestingly, the rapid increase in local number of contacts is clearly anti-correlated with the rapid decrease in the number of water molecules, and the average local Q value. Such local fluctuations and signatures of anti-correlation remain even in the collapsed state (after 10 ns), although the fluctuations in Q become much less pronounced due to the inherent limited range of the Q values. A few representative structures have been shown (Figure 4.6, left) to illustrate how the local

conformational changes can directly affect the solvent exposure and structure of the hydration layer.

A closer look at the collapsed structures will tell us that different regions on the polymer surface have large variations in the local curvature and solvent accessibility. Figure 4.7 demonstrates this spatial heterogeneity of the local length scale and its effect on the local water structure. Here all the local parameters ($N_{contacts}$, N_{waters} and $<Q>$) have been calculated along the polymer chain. The oscillatory pattern in Figure 4.7 originates because of the rod-like structure of the collapsed state. All carbon atoms near the two ends of the cylindrical structures have lower $N_{contacts}$ and higher N_{waters}, whereas the atoms near the middle region has the reverse trend. We have also shown the cross-correlation functions (CCF) between these local parameters in Figure 4.8. Interestingly, even in the collapsed state of C100, the fluctuations of the local variables follow the anti-correlation (negative CCF) between the polymer coordinate and the water structure coordinates. Moreover, the timescale of relaxation seems to be dependent on the local length scale as demonstrated by the dependence of CCF on the local $N_{contacts}$. Thus, our results suggest that for any (bio)polymeric system the local water structure should be dynamically coupled to the local fluctuations in the solute coordinate, and both the spatial and temporal heterogeneity (and associated timescale) of the solute molecule would strongly influence the solvation properties.

We have attempted to further analyze this coupling between the local solute length-scale and the local solvation properties in terms of joint probability distributions (Figures 4.9-4.10). Figure 4.9 captures the coupling between (i) the global solute and solvent coordinates (top panels), i.e. average Q of the whole hydration layer and the scaled total number of intra-molecular contacts, and (ii) the local solute and solvent coordinates (bottom panels), i.e. the average Q and the number of intra-molecular contacts due to individual polymer atoms. In the global coordinates, higher $<Q>$ and lower $N_{contacts}$ are associated with the extended state, whereas the opposite can be associated with the collapsed state. We observe a bimodal distribution in C80, which primarily exists in the collapsed state with partial contributions from the extended state. In the global coordinate, the fluctuations along the solute coordinate seems to be more pronounced than the solvent coordinate, whereas the reverse is true in case of the local coordinates. In the bottom panels of Figure 4.9, particularly for C40, we clearly see that for smaller $N_{contacts}$ values (locally extended states), the fluctuations along the $<Q>$ coordinate is much more pronounced, whereas the bimodal-like

distribution is lost in the case of C80. It seems the local $<Q>$ is rather less sensitive toward the global conformational changes. Figure 4.9 (d) shows a single minimum corresponding to a distribution dominated by the extended statelike features, and the locally collapsed regions do not contribute in a significant manner.
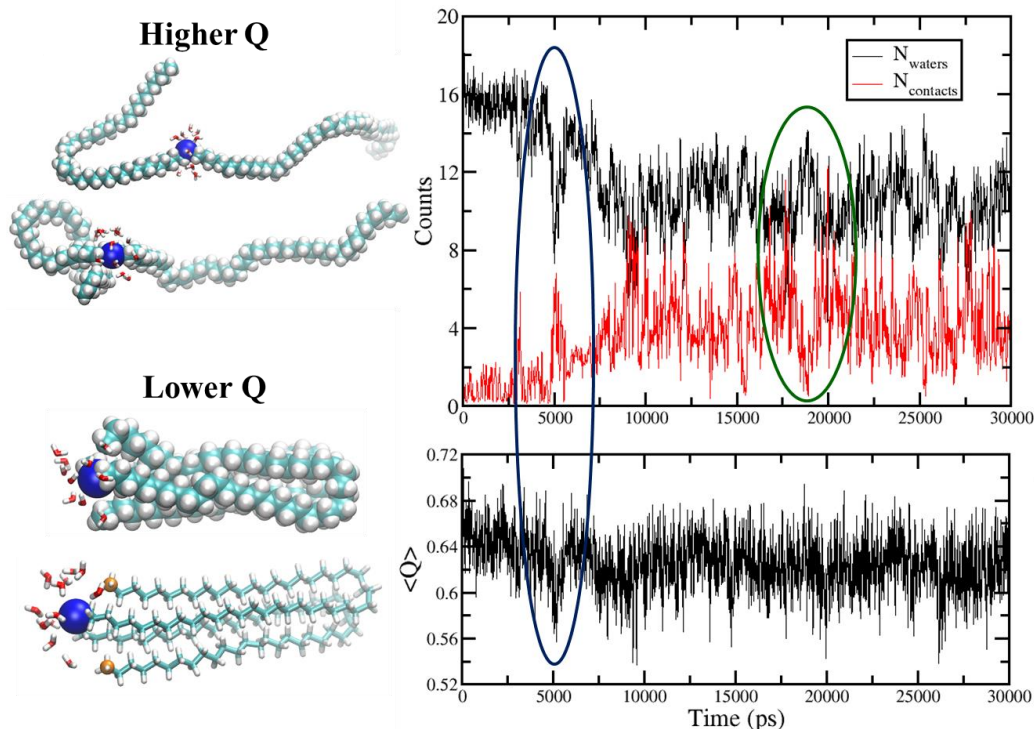
Figure 4.6: Time evolution of the number of contacts formed by the middle **(50th)** carbon with other polymer atoms **(right-top, red)**, and number of water molecules in its hydration shell **(right-top, black)**. We also show the time evolution of the average Q value around that particular carbon atom **(right-bottom)**. This captures the coupling between three different parameters**: (i)** polymer-polymer contacts, which captures the local length-scale, **(ii)** local water density, and **(iii)** local tetrahedral order**.** The distinct anti-correlation between number of local contacts and the local water density as well as Q value has been marked**.** The snapshots on the left show a few representative snapshots where the water molecules around the 50th atom have different Q values depending on the local structure and solvent exposure**.**
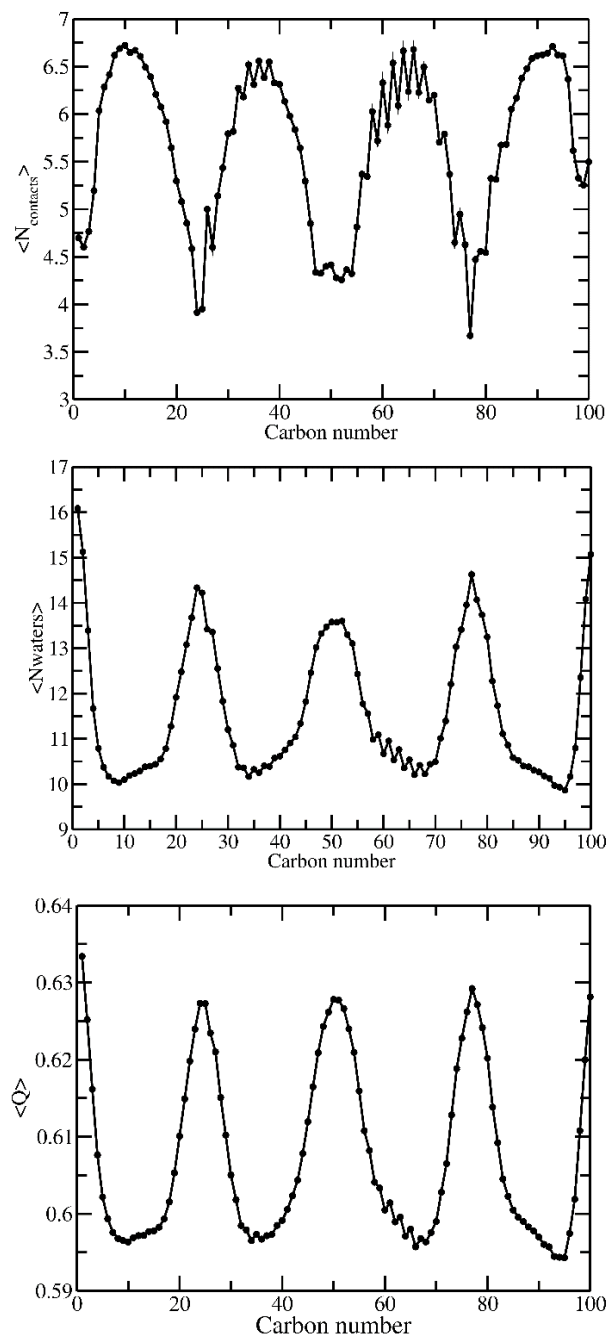
Figure 4.7: The average number of polymer-polymer contacts **(**top**)**, the average number of water molecules in the hydration layer **(**middle**)**, and the average tetrahedral order parameter of the hydration layer **(**bottom**)** for each atom along the chain for the collapsed state of C100 **(**see left panel of Figure 4.6 for a representative snapshot**)**. Because of the rod-like **(**cylindrical**)** nature of the collapsed state the properties vary along the chain length in an oscillatory manner**.** This also

demonstrates the extent of spatial heterogeneity of the local structural order and density depending on the local curvature (and solvent exposure) of the polymer chain.
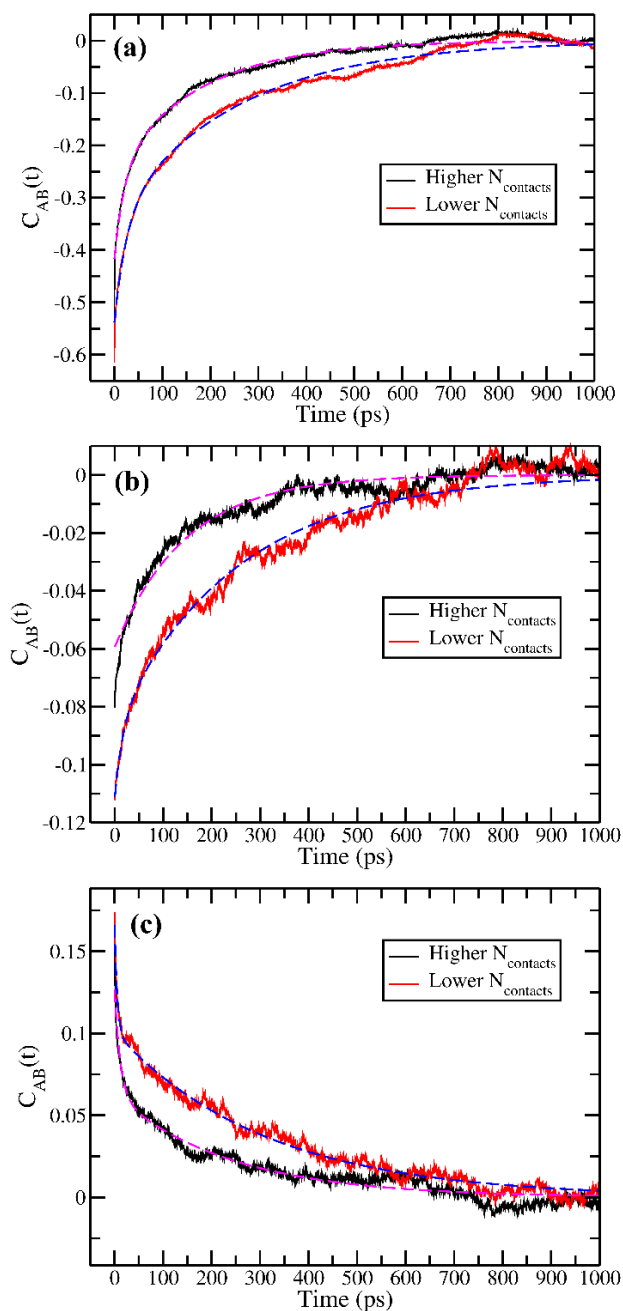
Figure 4.8: The cross-correlation functions ($C_{AB}(t)$) between three pairs of quantities (A,B), namely (a) local number of contacts ($N_{contacts}$) and local number of water molecules (N_{waters}), (b) local number of contacts ($N_{contacts}$) and local average tetrahedral order parameter ($<Q>$), and (c) local N_{waters} and local $<Q>$. Large negative values for $C_{AB}(t)$ involving polymer and water

coordinates **((a)** and **(b))** clearly demonstrates the anti-correlation between them, whereas the local density and local $<Q>$ of hydration layer remains positively correlated as expected**.** We have separately averaged $C_{AB}(t)$ for carbon atoms with high **(**black line**)** and low **(**red line**)** $N_{contacts}$ values to demonstrate the dynamic heterogeneity of the hydration layer depending on the local curvature**.**
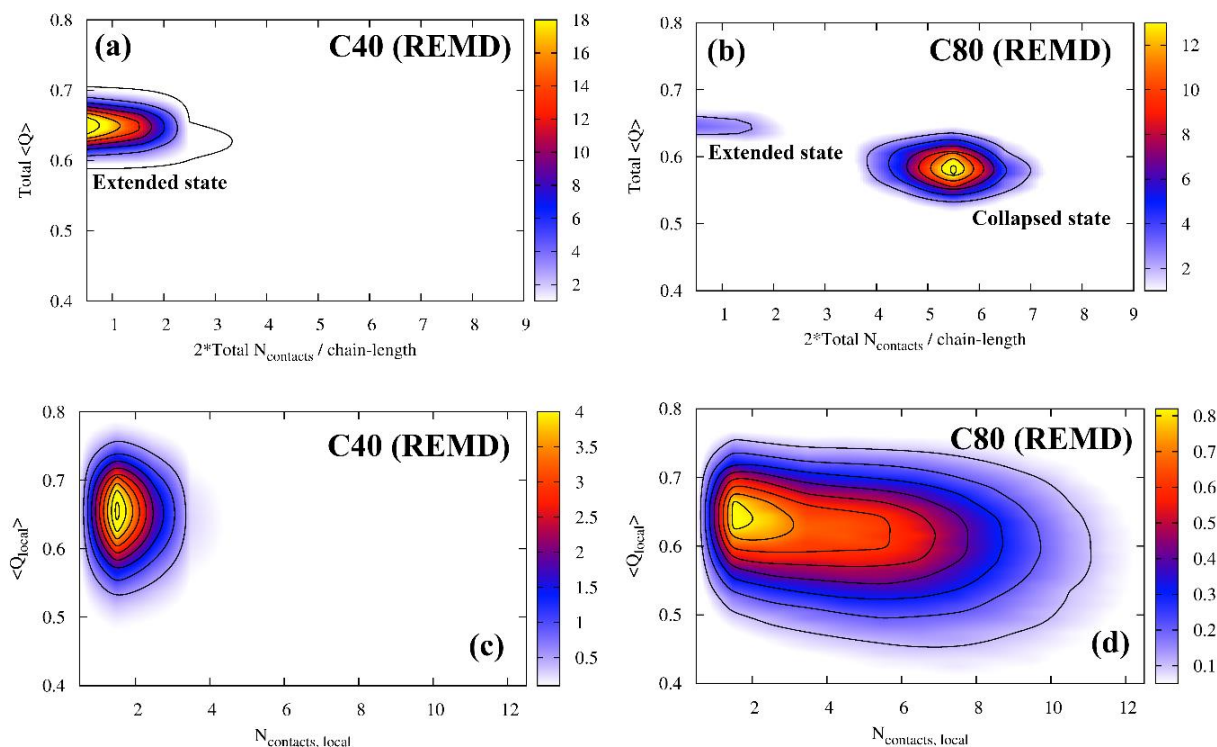
Figure 4.9: (top panels) Joint probability distribution of the global variables, namely the average tetrahedral order parameter of all surface water molecules (Total $<Q>$) and the scaled total number of polymer-polymer contacts (2*Total $N_{contacts}$ / chain-length). (bottom panels) Joint probability distribution of the same quantities calculated over individual polymer atoms (local variables). We have shown the 2D histograms for the C40 (primarily extended) and C80 (primarily collapsed) systems only. The distribution of the local variables captures the microscopic heterogeneity in the polymer topology and the associated changes in the local water structure as it undergoes conformational fluctuations.

A significantly stronger coupling has been observed between the local density coordinate of the solvent (N_{waters}) and $N_{contacts}$ (Figure 4.10). We can clearly see that for smaller lengths of the polymer (C40), there exists a large scale local density fluctuation of the water (vertical direction),

and these fluctuations are practically independent of the solute coordinate. But beyond certain length-scales (for C80 and C100), we can observe an interesting crossover regime. For the smaller $N_{contact}$ values, which signify a locally unfolded state, the water density fluctuations are still prominent and independent of the solute coordinate. Interestingly, the increase in the local $N_{contact}$ (initiation of hydrophobic collapse) is prompted by a major decrease in the local water density. Thus, the initial stages of hydrophobic collapse involve large scale density fluctuations of water, partial local dewetting followed by further collapse along the polymer coordinate. Beyond the initial dewetting phase, the solvent coordinate seems to be more strongly coupled to the solute coordinate, which is expected since the increase in the number of intra-molecular contacts would inevitably decrease the solvent exposure. While this phenomenon has been predicted earlier using a coarse grained model of water,[37,38] our fully atomistic simulation study provides a more direct evidence and molecular representation.
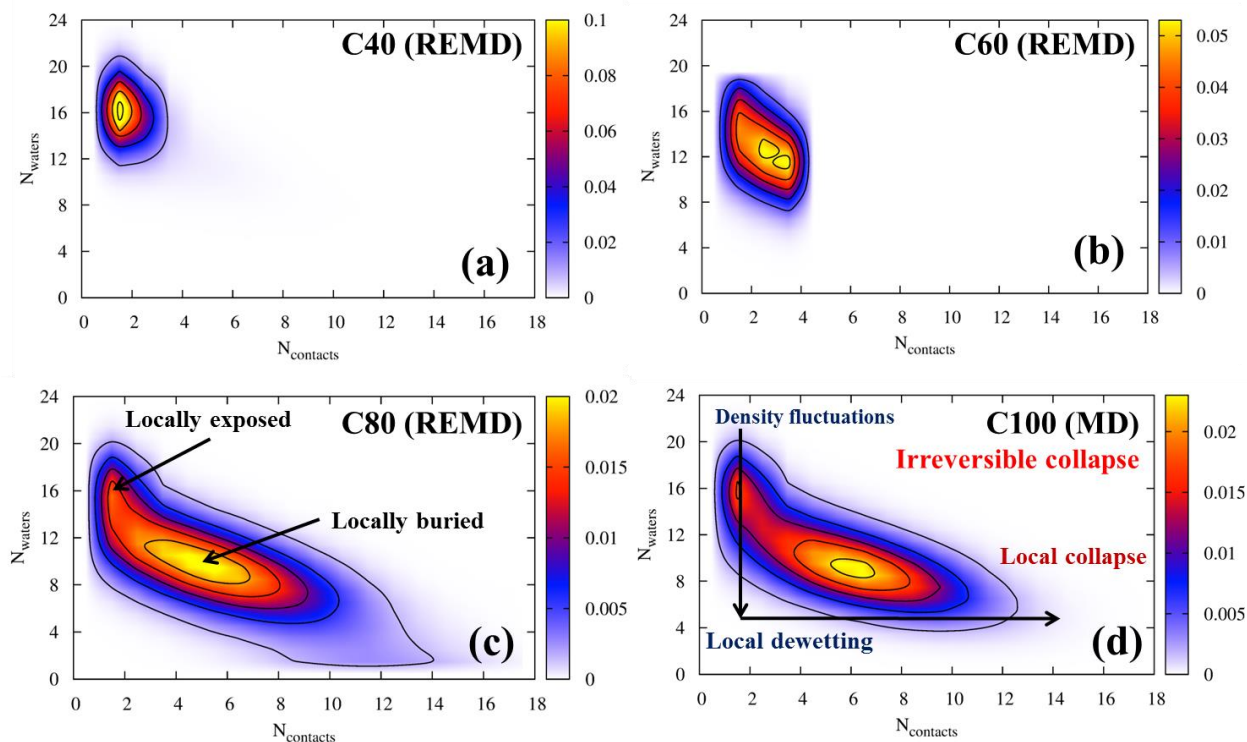
Figure 4.10: Joint probability distribution of the number of water molecules around each polymer atom **(N_{waters})** and the number of polymer-polymer contacts **($N_{contacts}$)** formed by that particular atom for different polymer lengths **(C40 to C100).** Note that the histograms for C40 to C80 have been constructed from equilibrium REMD simulations, whereas for C100 we are following the

pathway for irreversible hydrophobic collapse as seen from regular MD simulation. The vertical direction signifies the local density fluctuations of the water molecules, whereas the horizontal direction depicts the polymer collapse coordinate. It's quite clear that for the extended states (lower number of local contacts) there exists a pronounced local water density fluctuation, and the hydrophobic collapse is prompted by a reduction in local water density (dewetting). At smaller lengthscales (lower number of local contacts), water density fluctuations seem to be almost independent of the polymer structure, whereas they are more strongly coupled at larger lengthscales (higher number of local contacts).

4.3.4 Alcohols

In this section, we have focused on the spectral and structural properties of hydration shell water present within 0.585 nm of distance around hydrophobic part of alcohols. The list of alcohols studied here is provided in Table 4.1 along with concentration of single molecule of alcohol in water. Other than this concentration, we have also simulated 0.5M of methanol, 1-propanol, 1-heptanol similar to the experimental study of Davis et al.[25] and Perera et al.[27].

4.3.4.1 Local hydration shell water structure around alcohols

We further attempt to prove that no such order-disorder cross-over of water molecules exists with only increasing hydrophobic length upto 11 carbon atoms in one dimension. Using an advantage of MD study of directly deducing the water structure on a molecular level, we looked at the water tetrahedrality and number of hydrogen bonds.

For alcohols, the hydration shell of only carbon atoms (hydrophobic part of alcohol) has been considered. In the calculation of Q of hydration shell water, we considered the carbon and/or oxygen of alcohol if they are among the nearest four neighbors of that hydration shell water molecule. The distribution of Q is demonstrated in Figure 4.11 (a) for the monomer and 0.5M concentrations of alcohols, in addition bulk water at 300K is shown as a reference. For the monomers as well as for the higher concentrations of alcohols, the distribution of Q appears to be more or less similar to bulk water except for the monomer of methanol. For monomer of methanol, the population of Q at ~0.8 is decreased considerably, which clearly supports the experimental observation that water around methanol has decreased tetrahedrality compared to hydration shell water of methane.[39] Though methanol is small in size but it is not a non-polar solute as methane and therefore, we cannot expect it to cause the enhancement in the hydration shell water. Although,

Davis et al.1 reported that increase in temperature as well as in the hydrophobic chain length more than 1nm lowers the water structure, we do not observe any lowering of water structure on increasing the chain length of alcohols from 1 to 11 (and so the hydrophobicity of chains is increasing). They have used the alcohols from methanol to n-heptanol, which certainly does not include the hydrophobic chain of length more than 1 nm. In addition, it should be noted here that, the length of alkane hydrophobic chain is not the origin for the decrease in water structure. In fact, the size and curvature of the molecular surface are the determining factors for the water structure to change. Chandler[40] as shown that the order-disorder transition of water takes place when the size of spherical solute exceeds 1 nm. However, increasing the length of the hydrophobic chain in one dimension may not necessarily change the water structure around it since water has the ability to find highest curvature/lowest dimension to wrap around to maintain its hydrogen bonded network as demonstrated in above section 4.3.1. When the chain undergoes collapse, if water finds it difficult to accommodate the new geometry of size exceeding ~1 nm, it undergoes structural transformation. Similar to bulk water with increase in temperature, the water around hydrophobic solutes can be expected to lose its hydrogen bonds as well as tetrahedrality. But in the case of alcohols of shorter chain length, we do not find a totally collapsed structure that would exceed the size of ~1 nm. As reported previously the hydrophobic chain of length less than or equal to 10 carbon atoms, remains preferably in the extended state.[22,26] Hence, it is impossible for water to change its structure around them so drastically, in case of alcohols of lengths smaller than 10 carbons.
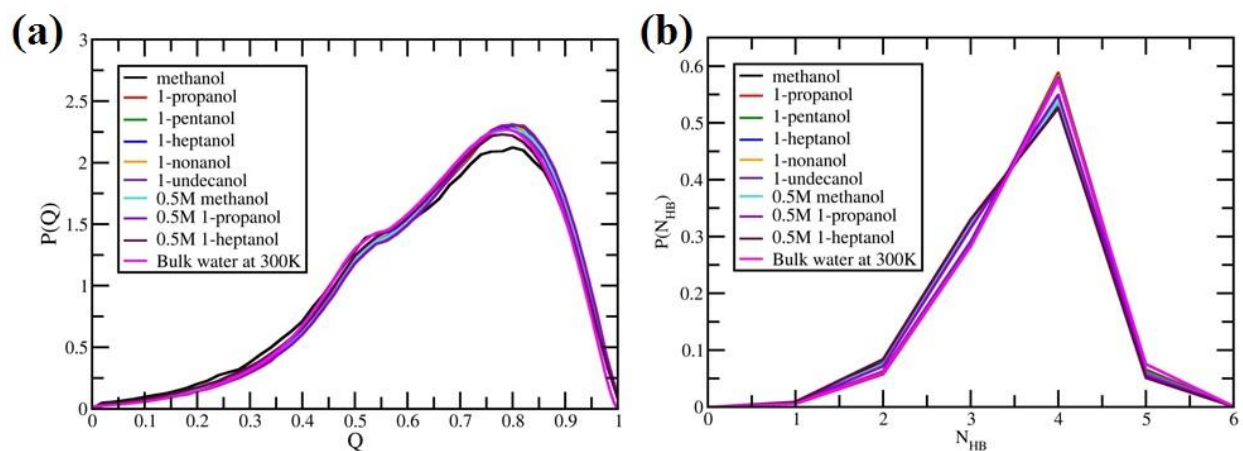
Figure 4.11: Distributions of **(a)** tetrahedral order parameter *(Q)* and **(b)** number of Hydrogen bonds *(N_{HB})* in hydration shell water around alcohols for monomers and for 0**.**5M concentrations**.**

The solute **(**Carbon and Oxygen of alcohol**)** is included in the neighbor list of oxygen of tagged water in the calculation of *Q* as mentioned in the text**.** In the calculation of N_{HB}, OH group of corresponding alcohol is considered if it is making hydrogen bond with the tagged water molecule**.**

We also attempt to calculate number of hydrogen bonds formed by individual hydration shell water molecules using the same condition mentioned above. It should be noted that in the case of alcohols, we have additionally counted the hydrogen bonds if made between hydration shell water and OH group of alcohols. The distribution of number of hydrogen bonds is shown in Figure 4.11 (b). The distribution of monomeric alcohols overlaps with bulk water except methanol while higher concentration of alcohols and methanol has little decrease in the population of four hydrogen bonds. Overall, the hydrogen bond distribution shows similar trend to the water tetrahedrality and thus increasing of hydrophobic chain length upto 11 carbon atoms does not have any effect on the water hydrogen bonding. This again confirms that the water tetrahedrality as well as hydrogen bonding does not get affected by the increase in the hydrophobic chain length.

4.3.4.2 Vibrational dynamics of local hydration shell water around alcohols

Using the same definition of vibrational power spectrum as given in Chapter 3 section 3.3.3, the power spectrum of hydration shell around alcohols have been calculated, the full spectrum is shown in Figure 4.12 and the vibrational band of spectrum is shown in Figure 4.13. The intensities of the spectrum almost overlap with each other irrespective of the increase in
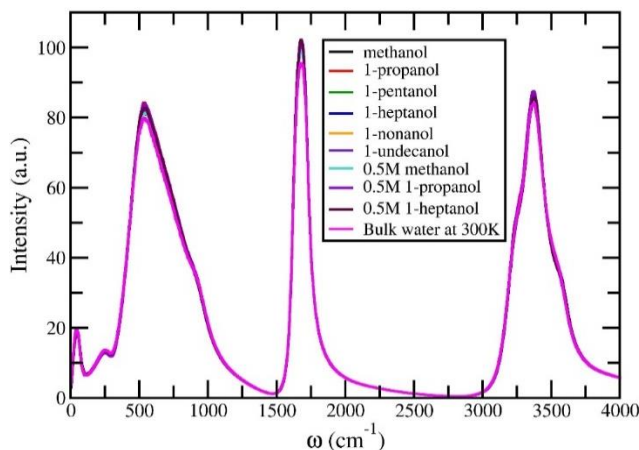
Figure 4.12: Full power spectra of first hydration shell water around the alcohols; for monomers ranging from methanol to undecanol and for 0.5M concentration of methanol, 1-propanol and 1-heptanol as well as for Bulk water at 300K.
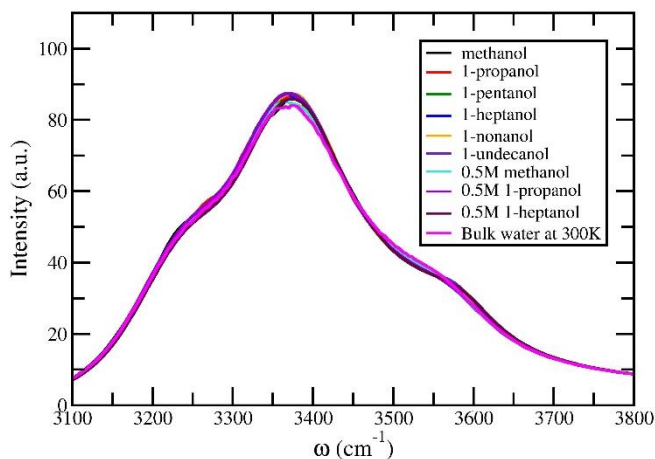
Figure 4.13: Vibrational spectra of first hydration shell water around the alcohols ranging from methanol to undecanol, and bulk water at 300K.

hydrophobic chain length up to 11 carbon atoms for the alcohols. Thus, percentage of water dangling OH bonds (the frequency range of 3550-3660 cm^{-1}) does not seem to depend on the variation of hydrophobic chain length in one dimension as long as the chain is in extended state or is not in the collapsed state of size of more than 1 nm. In both the experimental studies, authors used a concentration much less than required for the aggregation of alcohols and thus claim that they observe the spectrum around monomers of alcohols and not around the cluster. Hence for the proper comparison of our results with experimental results we did simulations of monomers of alcohols in addition to experimentally used concentration. Also they confirm that the obtained solute correlated Raman spectrum is purely from the hydrophobic part of the alcohol molecules and does not include the OH group of alcohol in it. The results from these studies indicate that with length scale variation, the percentage of dangling OH bonds increases and tetrahedral ordering of hydration shell water decreases. But, previously reported critical size of hydrophobic solute for the order-disorder cross-over of water molecules as well as our current results do not agree these experimental observations on a molecular scale.

4.4 Conclusion

We have extensively studied the effect of local topological heterogeneity (both spatial and temporal) of hydrophobic polymeric solutes on the structure of water molecules in the hydration layer. We have used the tetrahedral order parameter of water and number of hydrogen bonds to demonstrate the order-disorder transition. We have shown that length-scale dependent crossover does not exist in the linear hydrophobic chains due to presence of a sub-nanometer cross-sectional length scale. Water molecules can adaptively maintain the almost bulk-like hydrogen bonded network by wrapping around the cylindrical polymer chain.

We have demonstrated that the hydrophobic collapse or conformational fluctuations of the flexible hydrophobic chains have strong effect on the surface water density and tetrahedral order in the hydration layer. Although, we find that the local water density is more strongly sensitive to the local changes in the polymer topology as compared to the tetrahedral order. The order-disorder transition probed by the tetrahedral order parameter does not become noticeable up to C40 (quantitatively this might be dependent on the chosen polymer model). Thus, it is likely that it would be very difficult to observe the length-scale dependent structural changes experimentally using smaller hydrophobic molecules as probe such as alcohols.

We have also shown that the microscopic local solvation properties would be dynamically coupled to the local topology of the complex molecules. Even when the whole molecule may exist in a globally defined conformational state (extended/collapsed), the local fluctuations can induce appreciable changes in the local solvation properties. Thus, it is extremely important to understand the spatial and temporal heterogeneity of both structural and dynamical properties of the hydration layer in the context of this coupling. Finally, using the joint probability distributions of the solvent and solute structural coordinates we have demonstrated that there exists a pronounced local density fluctuation in the hydration layer at smaller length-scales (locally), which is practically independent of the size of the solutes. A local "partial dewetting" triggered by such density fluctuations prompts further collapse in agreement to existing theories.[37,38]

In addition, we have simulated the experimentally studied alcohols with varying hydropobic chain-length and found that structural as well as vibrational dynamical properties do not vary with the variation of chain length. The contradictory results of computer simulation than experimental study could be because non-accountability of the polarizability of the

alcohol/water.[41] Therefore, to reproduce the experimental results an *ab-initio* molecular dynamics study or use of polarizable water force-field would be helpful.

4.5 References

(1)   Ball, P. *Chem. Rev.* **2008**, *108* (1), 74–108.

(2)   Sugita, Y.; Okamoto, Y. *Chem. Phys. Lett.* **1999**, *314* (1–2), 141–151.

(3)   Meyer, E. E.; Rosenberg, K. J.; Israelachvili, J. *Proc. Natl. Acad. Sci. U. S. A.* **2006**, *103* (43), 15739–15746.

(4)   Ball, P. *Proc. Natl. Acad. Sci. U. S. A.* **2017**, *114* (51), 13327–13335.

(5)   Walde, P.; Giuliani, A. M.; Boicelli, C. A.; Luisi, P. L. *Chemistry and Physics of Lipids*. 1990, pp 265–288.

(6)   Maibaum, L.; Aaron R. Dinner, A.; Chandler, D. *J. Phys. Chem. B* **2004**, *108* (21), 6778–6781.

(7)   Lum, K.; Chandler, D.; Weeks, J. D. *J. Phys. Chem. B* **1999**, *103* (22), 4570–4577.

(8)   Hillyer, M. B.; Gibb, B. C. *Annu. Rev. Phys. Chem.* **2016**, *67* (1), 307–329.

(9)   Giovambattista, N.; Lopez, C. F.; Rossky, P. J.; Debenedetti, P. G. *Proc. Natl. Acad. Sci. U. S. A.* **2008**, *105* (7), 2274–2279.

(10)   Dill, K. A.; Truskett, T. M.; Vlachy, V.; Hribar-Lee, B. *Annu. Rev. Biophys. Biomol. Struct.* **2005**, *34* (1), 173–199.

(11)   Mountain, R. D.; Thirumalai, D. *Proc. Natl. Acad. Sci.* **1998**, *95* (15).

(12)   Bratko, D.; Curtis, R. A.; Blanch, H. W.; Prausnitz, J. M. *J. Chem. Phys.* **2001**, *115* (8), 3873–3877.

(13)   Harris, R. C.; Pettitt, B. M.; Debenedetti, P. G. *Proc. Natl. Acad. Sci. U. S. A* **2014**, *111* (41), 14681–14686.

(14)   Wu, X.; Lu, W.; Streacker, L. M.; Ashbaugh, H. S.; Ben-Amotz, D. *Angew. Chemie Int. Ed.* **2018**, *57* (46), 15133–15137.

(15)   Huang, D. M.; Chandler, D. *Proc. Natl. Acad. Sci.* **2000**, *97* (15), 8324–8327.

(16)   Wu, X.; Lu, W.; Streacker, L. M.; Ashbaugh, H. S.; Ben-Amotz, D. *J. Phys. Chem. Lett.* **2018**, *9*

(5), 1012–1017.

(17)   Sadqi, M.; Lapidus, L. J.; Muñoz, V. *Proc. Natl. Acad. Sci. U. S. A.* **2003**, *100* (21), 12117–12122.

(18)   Brylinski, M.; Konieczny, L.; Roterman, I. *Comput. Biol. Chem.* **2006**, *30* (4), 255–267.

(19)   Cheung, M. S.; García, A. E.; Onuchic, J. N. *Proc. Natl. Acad. Sci. U. S. A.* **2002**, *99* (2), 685–690.

(20)   Li, I. T. S.; Walker, G. C. *Proc. Natl. Acad. Sci. U. S. A.* **2011**, *108* (40), 16527–16532.

(21)   Hatano, I.; Mochizuki, K.; Sumi, T.; Koga, K. *J. Phys. Chem. B* **2016**, *120* (47), 12127–12134.

(22)   Chakrabarty, S.; Bagchi, B. *J. Phys. Chem. B* **2009**, *113* (25), 8446–8448.

(23)   Ferguson, A. L.; Debenedetti, P. G.; Panagiotopoulos, A. Z. *J. Phys. Chem. B* **2009**, *113* (18), 6405–6414.

(24)   Graziano, G. *Chem. Phys. Lett.* **2011**, *511* (4–6), 262–265.

(25)   Davis, J. G.; Gierszal, K. P.; Wang, P.; Ben-Amotz, D. *Nature* **2012**, *491* (7425), 582–585.

(26)   Juurinen, I.; Pylkkänen, T.; Sahle, C. J.; Simonelli, L.; Hämäläinen, K.; Huotari, S.; Hakala, M. *J. Phys. Chem. B* **2014**, *118* (29), 8750–8755.

(27)   Perera, P. N.; Fega, K. R.; Lawrence, C.; Sundstrom, E. J.; Tomlinson-Phillips, J.; Ben-Amotz, D. *Proc. Natl. Acad. Sci. U. S. A.* **2009**, *106* (30), 12230–12234.

(28)   Sugita, Y.; letters, Y. O.-C. physics; 1999, undefined. *Elsevier.*

(29)   Jorgensen, W. L.; Maxwell, D. S.; Tirado-Rives, J. *J. Am. Chem. Soc.* **1996**, *118* (45), 11225–11236.

(30)   Marcus G.M. and; Siepmann, J. I. **1998**.

(31)   González, M. A.; Abascal, J. L. F. *J. Chem. Phys.* **2011**, *135* (22).

(32)   Abascal, J. L. F.; Vega, C. *J. Chem. Phys.* **2005**, *123* (23), 234505.

(33)   Bussi, G.; Donadio, D.; Parrinello, M. *J. Chem. Phys.* **2007**, *126* (1).

(34)   Berendsen, H. J. C.; Postma, J. P. M.; van Gunsteren, W. F.; DiNola, A.; Haak, J. R. *J. Chem. Phys.* **1984**, *81* (8), 3684–3690.

(35)   Parrinello, M.; Rahman, A. *J. Appl. Phys.* **1981**, *52* (12), 7182–7190.

(36)   Essmann, U.; Perera, L.; Berkowitz, M. L.; Darden, T.; Lee, H.; Pedersen, L. G. *J. Chem. Phys.*

1995, *103* (19), 8577–8593.

(37)   ten Wolde, P. R.; Chandler, D. *Proc. Natl. Acad. Sci. U. S. A.* **2002**, *99* (10), 6539–6543.

(38)   Miller, T. F.; Vanden-Eijnden, E.; Chandler, D. *Proc. Natl. Acad. Sci. U. S. A.* **2007**, *104* (37), 14559–14564.

(39)   Wu, X.; Lu, W.; Streacker, L. M.; Ashbaugh, H. S.; Ben-Amotz, D. *Angew. Chemie Int. Ed.* **2018**, *57* (46), 15133–15137.

(40)   Chandler, D. *Nature* **2005**, *437* (7059), 640–647.

(41)   Kim, J. S.; Wu, Z.; Morrow, A. R.; Yethiraj, A.; Yethiraj, A. *J. Phys. Chem. B* **2012**, *116* (39), 12007–12013.

Chapter 5 : Water under Confinement: Factors Responsible for Departure from Bulk Behaviour

5.1 Introduction

Despite being a deceptively small molecule water remains an enigma to the scientific community.[1,2] Not only does it have a wide array of anomalous bulk properties,[3] "water under confinement" and "interfacial water" have turned into active areas of research due to the staggering diversity of the context dependent properties of water.[4–13] Most of the functional roles of water in both biological and materials science contexts originate due to the unique properties of interfacial and/or confined water, e.g. cellular water exists in a highly crowded and confined medium, surface water molecules dictate the phenomena like hydrophobic collapse and self-assembly, and water may experience extreme confinement in clays, minerals as well as deep interiors of functional sites in biomolecules.

Reverse micelles (RMs) and water-in-oil microemulsions (W/O) have been popular choices as model systems to study the physicochemical properties of water under confinement and in a crowded environment, as well as various chemical and biomolecular processes under confinement, e.g. protein folding, enzyme catalysis, light induced charge separation, proton transfer and so on.[4,5,11,14–19] Sodium bis(2-ethylhexyl) sulfosuccinate (AOT) is one of the most commonly used surfactants with anionic head groups to study reverse micelles.[4,8,20–22] In the last few decades, the shape, size and composition of RMs as well as the structural and dynamical properties of the water molecules confined in these RMs have been studied extensively using a wide range of experimental techniques like NMR, small angle X-ray scattering (SAXS), dynamic light scattering (DLS), quasielastic neutron scattering (QENS), vibrational spectroscopy and spectral diffusion, dielectric relaxation, solvation dynamics studies and so on.[4,7,9,15,17,20,21,23–28] The experimental studies have often been motivated and complemented by an impressive amount of theoretical and computational studies that have built the foundation of our current understanding of the unique properties of water under confinement and interfacial water.[6,8,11,18,19,29–37]

Through the extensive body of research developed over the last few decades it has been well established that the water under confinement may exhibit drastically different

physicochemical properties as compared to bulk water. Confined water may have reduced polarity (dielectric constant), a perturbed hydrogen bonded network, and structural ordering at the interfacial region among many others.[32,36,38–40] The dynamical properties of water are highly affected by the confinement as well, e.g. both orientational dynamics and translation mobility along with dielectric relaxation of water slow down considerably for interfacial water.[18,20,25,30,37,40–43]

Spatial confinement is only one of the factors that might affect the properties of water in RMs. Since the interior surface in RMs is most commonly charged or polar depending on the surfactant composition, the water molecules can have a strong binding affinity to the interior surface. Thus, the slower exchange between the "bound" interfacial water and "free" core water leads to the observed slow dynamics near the surface region.[11,18] A core–shell type of model has often been invoked where the shell consisting of the interfacial water would have drastically different properties than bulk water, and the water molecules further away from the interface (core water) would gradually recover the bulk-like characteristics as the distance from the interface increases for larger RMs. This hypothesis has been examined both experimentally and by simulation studies by varying the size of the RMs, since it can be expected that if the size of the water pool gets bigger, the relative ratio of "bulk-like" core water molecules should increase.[27,41] The effective size of RMs and hence the size of the confined water pool is usually controlled by the water loading ratio given by $w_0 = [H2O]/[AOT]$. Multiple studies have suggested that the water dynamics in the core region of the RMs for larger RMs ($w_0 > 10$) gradually recovers the bulk-like characteristics.[20,27,30,37,41,44]

Using theoretical vibrational spectroscopy and simulation studies, Skinner and coworkers have nicely demonstrated that the distance dependence of the water dynamics from the interface as well as the length scale over which the bulk properties would be recovered, are dependent on the RM size due to the curvature induced effects, which is in clear contradiction to a simple core–shell type model of water dynamics in RMs.[6] They have also shown that the rotational anisotropy dynamics reaches bulk-like characteristics beyond 0.8 nm distance from the interface for $w_0 = 7.5$. On the other hand, it has been speculated in different contexts that water mediated interactions induced by dipolar correlations between

large polar (and even non-polar) interfaces might extend across several nanometers.[45,46] Thus, one may not rule out that the length-scale over which the properties of water may vary as a function of distance from the interface might depend on the properties of water that are being probed, namely local spatial order, translational order versus global dipolar orientation/correlation. Bagchi and coworkers[47] have put forward a somewhat similar argument in the context of the water interface with hydrophobic surfaces. They have suggested that the spatial (translational) structural ordering may not be as long range as the orientational (or tetrahedral) structural ordering of water, where the orientational order may sustain longer range correlations. Thus, the length-scale of water structure being perturbed by an external interface may depend on whether we are investigating the translational order versus orientational order.

Fayer and coworkers[27] have also suggested that a simple distinction between interfacial and bulk-like core water may not be possible depending on the properties of water that are being investigated. In particular, they found that the size dependence of the hydroxyl stretch absorption spectra and vibrational population relaxation times can be well described by an appropriately weighted average between the bulk water and small RMs ($w_0 = 2$; all water molecules are assumed to be interfacial), whereas the same model does not perform well for spectral diffusion and orientational relaxation due to long range coupling between the interfacial and core regions. Thus, depending on the sensitivity of the properties/phenomena of interest to the perturbations induced by the environment, we may observe different behaviors.

In an attempt to dissect the relative role of spatial confinement versus the specific interactions with the RM interior surface, several studies have compared the water dynamics inside charged and neutral RM systems.[23,48,49] Surprisingly, water dynamics near both charged and neutral hydrophilic interfaces has been found to be comparable and slower compared to bulk water. Thus, it has been concluded from these studies that the overall hydrophilic nature of the interface and the spatial confinement effects lead to the slow dynamics of interfacial water, whereas the specific chemical composition of the interface plays only a secondary role. On the other hand, the simulation studies by Laage and Thompson on the water dynamics in hydrophilic and hydrophobic nanoporous media clearly

demonstrate that slowing down of water dynamics is only modest in the case of hydrophobic cavities.[50] Thus, the spatial confinement effects may not contribute to the slower orientational dynamics observed in a hydrophilic confinement (either neutral or charged), which should be due to the favorable hydrogen bonding interactions between the surface and interfacial water molecules.

The above discussion clearly highlights the need for a systematic investigation of the various types of structural and dynamical properties of water in both hydrophilic and hydrophobic confinements as a function of the size of the confinement as well as the distance dependence of the properties from the interface as they approach bulk-like characteristics. In this work, we investigate three different types of structural order parameters, namely (i) local density (spatial order), (ii) local tetrahedral order and hydrogen bond distribution (local orientational order) and (iii) average dipolar orientation (global orientational order). We have also investigated the orientational and translational (diffusion) dynamics of the water molecules in a layer-wise fashion. The effect of confinement size has been studied using three different sizes of AOT RMs (w_0 = 10, 15 and 20), which are relatively larger in size as compared to prior MD simulation studies enabling us to actually observe the bulk-like characteristics instead of using extrapolation techniques. Our results clearly demonstrate that whether the water present inside a RM is bulk-like or not the effective size of the bulk-like core water region would strongly depend on the choice of order parameter (i.e. translational versus orientational).

Moreover, in order to clearly distinguish between the effects of "confinement" versus the proximity to a "hydrophilic" surface. on the properties of water, we have systematically compared the behavior of water in RMs with the control systems of water-in-oil (isooctane) nanodroplets with the identical number of water molecules as the respective RM systems. The water-in-oil (W/O) systems would allow us to separately understand the effect of confinement on the water in the absence of the AOT surfactants (negatively charged interface). Of course, the structure and dynamics of water molecules at the water–oil interface have been actively studied through decades.[12,13,51–58] In the limited scope of our work, we present a systematic size dependent comparison of the water structure and

dynamics in both the RM and W/O systems to highlight the key factors that lead to the unique behavior of water inside RMs.

5.2 Computational details

We have used three different sizes of the reverse micelle (RM) systems corresponding to the molar ratio $[H_2O]/[AOT] = w_0 = 10$, 15 and 20 in the increasing order of size. The corresponding three water-in-oil nanodroplet systems (W/O) have been prepared by keeping the number of water molecules the same as the $w_0 = 10$, 15 and 20 RM systems, where the water pools have been surrounded by the isooctane molecules. For the AOT RM systems we have added the same number of Na^+ counter-ions as AOT molecules in order to charge neutralize the whole system and the ions have been added at close proximity to the AOT head groups as clarified in Table 5.1. The number of water molecules, AOT, Na^+ ions and isooctane molecules used for preparing the above six systems are shown in Table 5.2. During the subsequent discussions, we shall refer to the RM systems by $w_0 = 10$, 15 and 20, whereas the water-in-oil systems will be referred as W/O = 10, 15 and 20, respectively.

Table 5.1: The initial packing radii (in nm) supplied to the Packmol software for preparation of the initial structures of the RM systems. The radii of the outermost layer for packing the following species are shown in the increasing order: water, Na^+ ions, sulfur (S) atoms of the AOT head groups, and C9 atoms (terminal carbon atoms of the AOT monomer). The minimum inter-atomic distance while packing these molecules has been set to 0.2nm to avoid overlap.

For example, for RM $w_0 = 20$: The water molecules have been put inside a sphere of radius 3.7 nm centered at the origin. Na^+ ions have been constrained to be at a distance of 3.75 nm (just outside water sphere, but within the AOT head group layer), and the sulfur (S) atoms of polar head groups have been constrained inside the sphere of radius 3.9 nm, and finally C9 atoms (terminal carbon of tail groups) have been constrained to be outside the sphere of radius 5.0 nm. The input structure of AOT monomer contains the Na^+ ion proximally placed to the head group.

Identical protocol has been used for preparing the W/O systems, where only the water sphere has been prepared using Packmol with identical number of water molecules as the respective RM systems and solvated with isooctane subsequently.

Please note that these spherical distance constraints are used to prepare the initial structures only. No position or distance constraint has been used during the MD simulation, which would allow sufficient equilibration of the internal structure.

System/Residue	Water (in nm)	Na^+ (in nm)	S (in nm)	C9 (in nm)
RM $w_0 = 20$	3.7	3.75	3.9	5.0
RM $w_0 = 15$	3.0	3.05	3.2	4.3
RM $w_0 = 10$	2.1	2.15	2.3	3.4

Table 5.2: The number of different species used to simulate the RM and W/O systems. nH_2O, nAOT, nNa^+ and nISO are the number of water, AOT, Na^+ counter-ion and isooctane molecules used to build the initial configurations of RMs and W/O systems. The production run lengths for all systems have been shown in the last column

System	nH2O	nAOT	nNa^+	nISO	Production run length (ns)
Bulk water	4125	—	—	—	20
RM $w_0 = 20$	6040	302	302	23 474	100
RM $w_0 = 15$	2835	189	189	33 830	100
RM $w_0 = 10$	980	98	98	10 111	100
W/O = 20	6040	—	—	5572	20
W/O = 15	2835	—	—	2274	20
W/O = 10	980	—	—	724	20

The number of AOT and water molecules, and the packing radii for the different water loading of RM systems have been taken from existing NMR data,[26] which has been subsequently used in other simulation studies as well.[14,59] These structural parameters are in agreement with the aggregation number and radii derived using other experimental techniques.[27,44,60] The initial structures for the RM and W/O systems have been created using the Packmol[44] software, where each molecular species has been packed within a certain spherical cut-off radius as used by Abel et al.[14] The chosen packing radii for the inner water

pool, counter-ions and the outer sphere of the AOT monolayer have been provided in Table 5.2 for every system studied here.

The AOT surfactant and isooctane molecules have been modeled using the CHARMM27 all-atom force-field following the protocol used by Abel et al.[14] Although the TIP3P water model is commonly used with the CHARMM force field, we have shown earlier that this water model does not capture the tetrahedral ordering of water molecules correctly.[61] Thus we have used the more recent TIP4P/2005 water model, which has been shown to perform quite well in reproducing a wide range of bulk water properties.[62,63] Since our primary goal is to investigate the structural and dynamical properties of water, we feel that choice of a better water model is very important

We have used the GROMACS (version 5.0.7) software suite[64] for the molecular dynamics simulations reported here. Periodic boundary conditions have been applied in all directions. In every case the simulation box dimension has been chosen such that the distance between the surface of the AOT RM or the water pool in the W/O system and the box boundary is at least 1 nm to avoid any short range interaction between the periodic images. All bonds have been constrained to their equilibrium bond lengths. We have used a cutoff of 1.0 nm for both short- range coulomb and van der Waals interactions. The long-range electrostatic interactions have been treated with the particle mesh Ewald method with a grid spacing of 0.16 nm. Before starting the molecular dynamics simulations, we have performed energy minimization using the steepest-descent algorithm in order to remove any clashes between the molecules. Afterwards NVT equilibration has been performed for 2 ns at 300 K temperature using the V-rescale thermostat[65] and NPT equilibration has been performed at 1 bar pressure and 300 K temperature using the Berendsen barostat[66] for the duration of 2 ns for W/O systems and 20 ns for RM systems. We have used the Parrinello– Rahman barostat[67] during the production runs with a 2 fs integration time step, and the trajectory frames have been saved every 1 ps for subsequent analysis. The total production run lengths for various systems are provided in Table 5.2. Additionally, we have performed simulations for bulk water as the reference system for comparison with various confined water systems. In this case, the NVT and NPT equilibration run lengths are 1 ns each with all other details remaining the same as described above.

5.3 Results and discussion

5.3.1 Nature of the confinement: reverse micelles vs. water-in-oil nanodroplets

The structure and dynamics of water under confinement have been well studied using a wide variety of surfactant molecules including cationic/anionic/neutral.[24,48,49,68] All of these systems are characterized by a hydrophilic interior surface, where water can preferentially bind. Although the strength of the interaction between interfacial water and the RM interior wall may depend on the charge distribution of the surface, it is expected that the favorable interactions would lead to a slower exchange between the interfacial and core water molecules leading to the traditionally observed slower dynamics in these systems. Thus, in addition to the confinement effect (size of the water pool), the reverse micelles also provide an additional perturbation of a strongly hydrophilic interface due to the favorable electrostatic interaction with the interface.

In order to dissect the relative role of size induced "confinement" versus the charged surface induced "binding/ordering" at the interface, we have taken up the reference systems of water-in-oil nanodroplets, where we keep the identical number of water molecules (as compared to the RM systems of w_0 = 10, 15 and in a hydrophobic isooctane background. In the absence of any AOT surfactant molecules, these systems would allow us to investigate the purely confinement size induced perturbations in the water nanodroplets in the absence of any hydrophilic interfaces. Our molecular dynamics trajectories show quite stable quasi-spherical water pools in both RM (3 sizes) and W/O (3 sizes) systems. Representative snapshots from the MD trajectory are shown in Figure 5.1 for the w_0 = 10, 15, 20 and W/O = 20 systems. On the left panels we include the surrounding isooctane medium, whereas the right panel zooms into the RM and W/O interior. The AOT head groups and counter-ions have been clearly identified as visual guidelines to the interfacial regions. We have observed considerable shape fluctuations (deviations from spherical shape) in the AOT RM systems. Similar observations have been made before using both dynamic light scattering experiments and MD simulations of RMs by Straub and coworkers.[8,21,69] The shape fluctuations seem to be particularly pronounced in smaller RMs.[21] We have shown the time evolution of the radius of gyration (indicator of size) and the anisotropy shape parameter (ratio of smallest and largest principal components of the gyration tensor, which would be 1 for a perfect
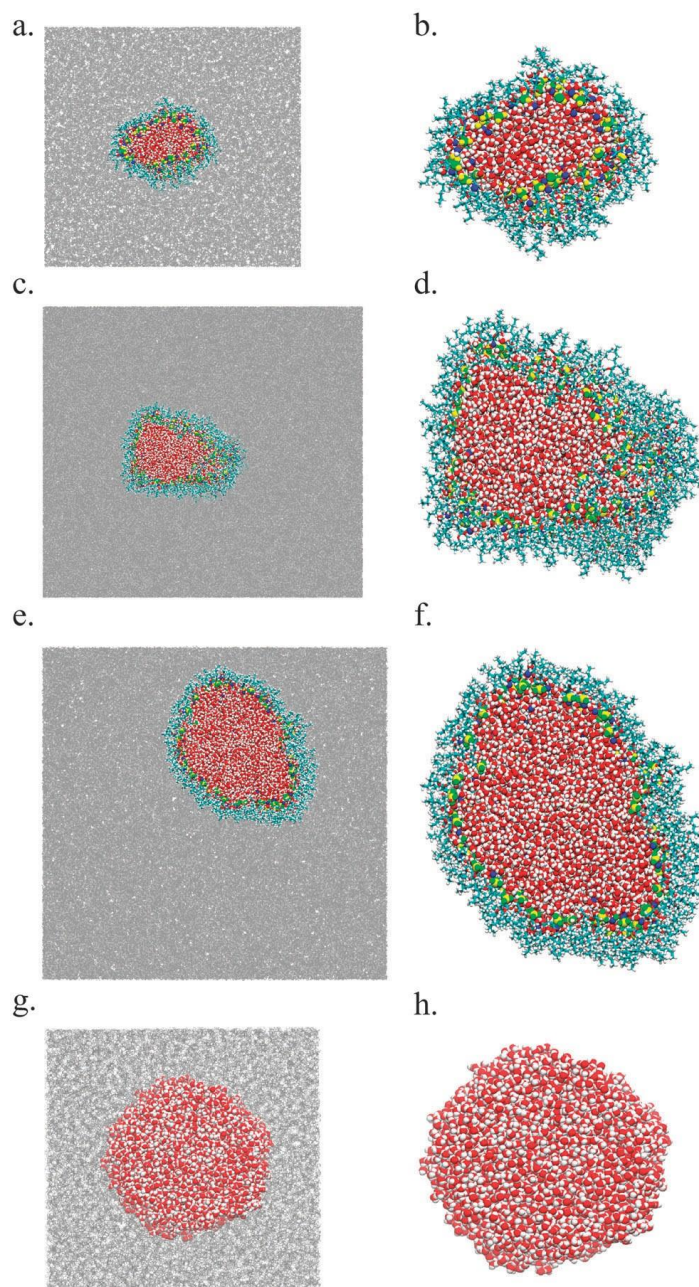
Figure 5.1: Representative snapshots from the MD simulation trajectories for (a and b) $w_0 =$ 10, (c and d) $w_0 = 15$, (e and f) $w_0 = 20$ and (g and h) W/O $= 20$. The left panel figures show the snapshots with the background isooctane medium included, whereas the right panel figures focus on either the AOT RM system or the water pool in the W/O system for clarity. The following color scheme has been adopted for various molecular species: isooctane (gray), hydrogen atoms of AOT and water (white), oxygen atoms of the AOT head group

(green), sulfur (yellow), Na$^+$ (blue) and remaining oxygen atoms of AOT and water (red).
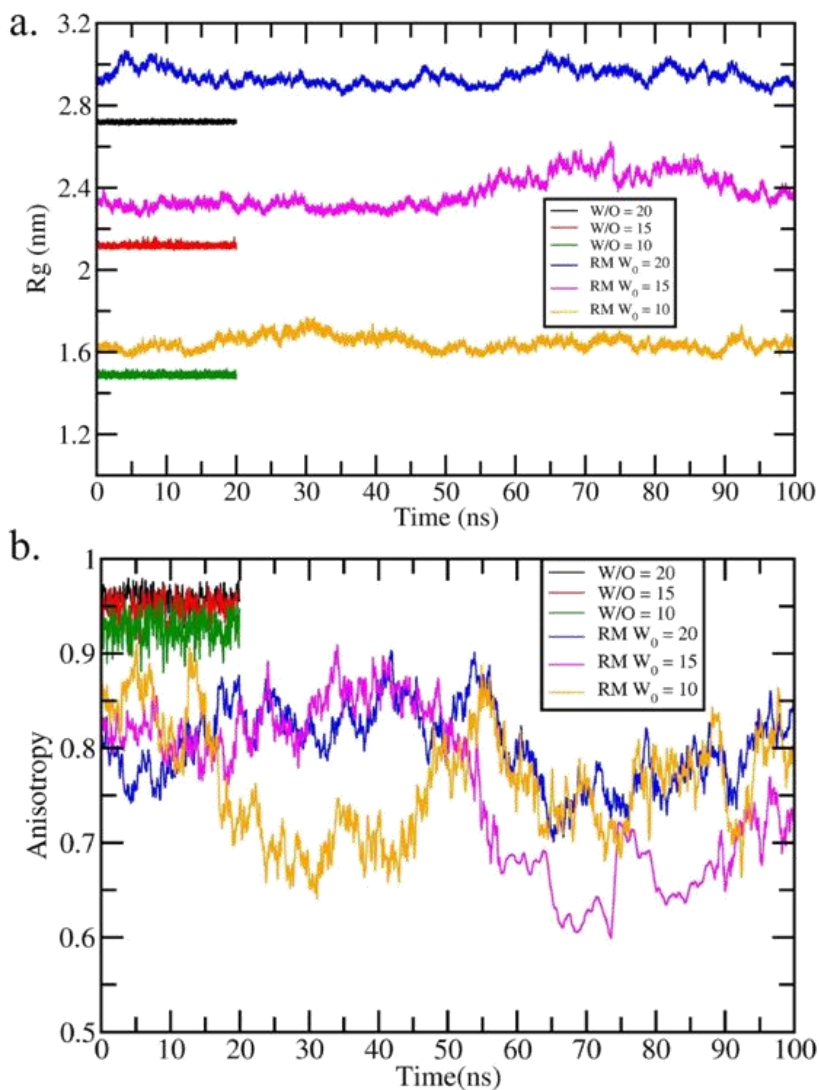
Figure 5.2: Time evolution of (a) radius of gyration (Rg) and (b) anisotropy parameter defined as ratio of smallest to largest principal components of Rg for all the systems studied in this work.

sphere) in Figure 5.2. The time evolution of the radius of gyration shows that both the RM and W/O systems maintain a relatively compact structure with considerably higher fluctuations for the RM system. But the RM structures remain stable and intact throughout the 100 ns trajectory for each system. Whereas the shape anisotropy parameter indicates that the deviations from spherical symmetry is remarkably higher in the RM systems as reported

earlier by Straub and coworkers,[8] whereas the W/O systems seem to retain a much higher degree of spherical nature. In the subsequent sections we shall demonstrate that both the structural and dynamical properties of water between these two systems are drastically different. Despite being a confined system, the water molecules in a W/O nanodroplet show remarkable similarity to bulk water even for the smallest size (W/O = 10) for most of the properties studied in this work. The deviations from bulk-like properties are not significant as compared to the RM systems even for the interfacial water (except for a few properties) in these systems as will be demonstrated below.

5.3.2 Choice of the structural order parameters

We have used three classes of structural order parameters in order to probe both the translational and orientational ordering of the water molecules under confinement of RM and W/O systems. The chosen order parameters are:

5.3.2.1 Number density *(ρ)*

The number of water molecules present per unit volume for different probe regions. This quantity would capture the local translational ordering (density) of the water molecules as compared to the bulk water density.

5.3.2.2 Tetrahedral order parameter *(Q) and the number of hydrogen bonds (N$_{HB}$):*

Tetrahedral order parameter is calculated using Eq. 2.30. Whereas to calculate a hydrogen bond the criterion given in the subsection 2.6.1.3 of Chapter 2 is used. For both the tetrahedral order parameter and hydrogen bond calculations we have included the O atoms of the AOT head groups among the possible neighbors (for Q) and hydrogen bond acceptors (for N_{HB}) for the water molecules, since the interfacial water molecules preferentially form hydrogen bonds with the AOT head groups at the expense of losing water–water hydrogen bonds.[34]

Interestingly, for all subsequent analyses we find that the variation in the average and probability distribution of the tetrahedral order parameter follows an identical trend as the number of hydrogen bonds, since both of these quantities capture the local tetrahedral order and hydrogen bonding pattern of the water molecules. Thus, we report only the data for the

tetrahedral order parameter here, since it shows slightly higher sensitivity to environmental changes due to the inherent discrete nature of the number of hydrogen bonds.

5.3.2.3 Dipolar orientation relative to the radial vector *(P):*

Being an isotropic medium there is no net dipolar orientation in bulk water, whereas near a charged interface the water dipoles are likely to have a preferred direction of orientation. We have quantified the dipolar orientation (P) as

$$P = \frac{\vec{\mu} \cdot \vec{r}}{|\vec{\mu}| \cdot |\vec{r}|} = \cos\theta \tag{5.1}$$

where $\vec{r}$ is the radial vector from the oxygen atom of a water molecule to the center of mass (COM) of the water pool, $\vec{\mu}$ is the dipole moment vector of that water molecule. The angle between these vectors (θ) would be zero if the water dipole is pointed towards the COM. We have used the cosine of the angle ($\cos\theta$) for describing the orientational polarization of the water molecules.

5.3.3 Radial profiles of the structural order parameters

It has been well established that the interfacial water in reverse micelles have distinctive structural and dynamical properties as compared to bulk water. Thus, we expect that the water molecules further away from the interfacial region should gradually recover their bulk-like characteristics. In other words, the central core region of the confined water pool is likely to have closer resemblance to the bulk water. Moreover, the effective size of this bulk-like core water region is expected to increase with the overall size of the water pool.

In order to investigate the above hypotheses, we have first calculated the radial profiles of the three structural order parameters described above for both the RM and W/O systems for all three sizes. The comparison between these radial profiles has been shown in Figure 5.3 (a–c). Here we have constructed spherical shells (with increasing radius in the range of 0.3 nm to 5 nm) around the center of mass (COM) of the water pool with the thickness of each shell being 0.1 nm. All the radial profiles have been obtained by averaging the corresponding properties for all water molecules lying within the radial shells. Thus, the

radial profiles describe the average structural order parameters as a function of distance from the COM of the water pool towards the interfacial region. We expect the bulk-like behavior at a smaller radius (nearer to the COM) and the deviation from the corresponding bulk properties (shown as a black line in each case) would signify the boundary of a spherical bulk-like core region.

Figure 5.3 (a) summarizes the radial number density profiles in both RM (3 sizes) and W/O (3 sizes) systems. We observe that all the systems demonstrate a flat region (constant value) near the COM signifying a core region where the water density is uniform and almost identical to the bulk water value (33.2 nm^{-3}). The number density slightly increases for smaller systems, since the higher curvature of the interfaces in smaller confined systems would induce a higher internal pressure on the internal water. Interestingly, the W/O systems demonstrate a much sharper drop in the density profile as compared to the RM systems, since they retain a higher degree of spherical nature as compared to the RM systems. Thus, the drop in the number density coincides with a well-defined radius of the water pool. In contrast, the RM systems undergo substantial shape fluctuations and a radial average over these fluctuations giving rise to a slower fall in the density profile. Nevertheless, the radii of the core regions with bulk-like water density for the RM systems are approximately 1 nm, 1.8 nm and 2.5 nm for w_0 = 10, 15 and 20, respectively. For W/O systems these regions are larger by ~0.7 nm in each case. The effective radii of each studied system can be directly deduced from the interfacial sharp drop in the radial profile. The effective radii of the water pool for the RM and W/O systems are consistent with the previous small angle X-ray scattering measurements[70] and viscosity measurements.[71]

The radial profiles of the tetrahedral order parameter have been compared in Figure 5.3(b). The profiles follow similar qualitative trends as the number density profiles, i.e. there is a core region with a bulk-like value and the tetrahedral order gradually decreases to zero across the interfacial region. Interestingly, we notice that the radii of the spherical regions with a bulk-like value (~0.67 for the TIP4P/2005 water model) have become smaller by 0.3 nm as compared to the corresponding density profiles. Thus, the tetrahedrality or orientational order of the water molecules is perturbed to a slightly larger length scale by the interface as compared to the number density. Moreover, the difference between the RM and

W/O systems has become more pronounced in the tetrahedral ordering. While for the W/O systems the radial profile drops almost as sharply as the number density profiles, it changes much more slowly for the RM systems. This evidently points towards the fact that the negatively charged interface in the AOT RM system affects the tetrahedral order of the water molecules due to the long range electrostatic interactions, which can be either directly perturbed or gradually propagated through the structural changes of intermediate water molecules.
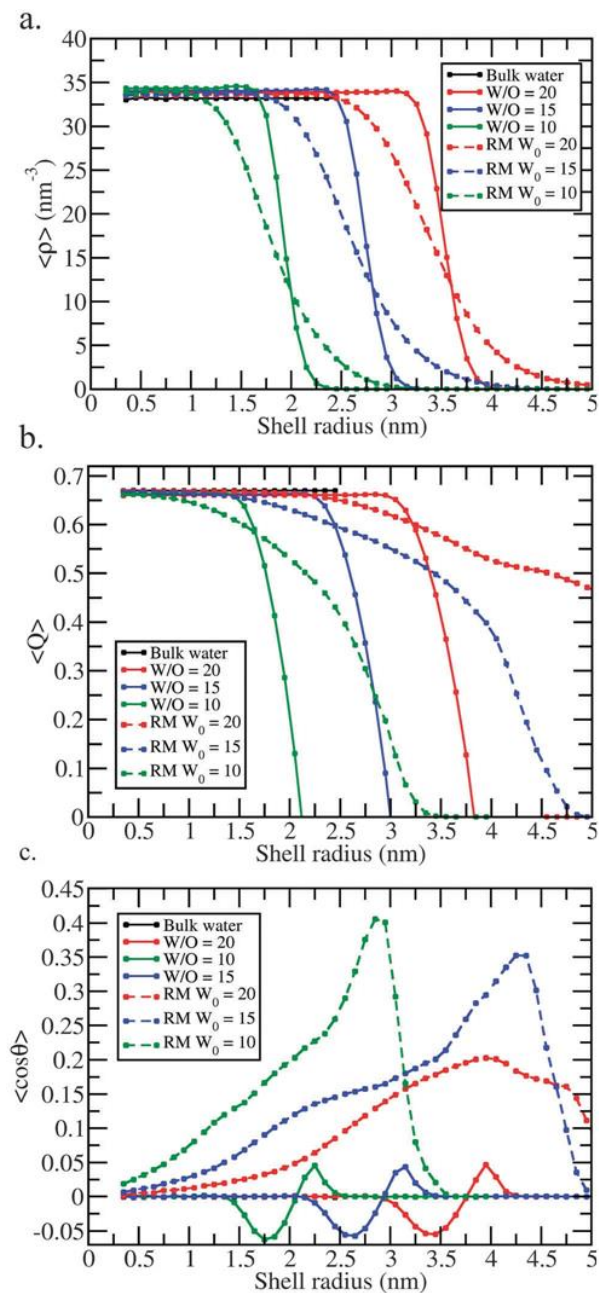
Figure 5.3: Radial profile of shell-wise **(a)** average number density (ρ), **(b)** average tetrahedral order parameter **(Q)**, and **(c)** average dipolar orientation of water molecules with respect to the radial vector as described by $\langle \cos\theta \rangle = \langle P \rangle$. All distances are measured from the center of mass of the water pool in respective cases. The dashed and solid lines correspond to the reverse micelle **(RM)** and water-in-oil **(W/O)** systems, respectively. The green, blue and red lines represent systems with w_0 or W/O = 10, 15 and 20, respectively.

Finally, we compare the dipolar orientation of the water molecules with respect to the radial vector in Figure 5.3(c). Remarkably, the radial profiles of $\langle cos\theta \rangle$ for the RM and W/O systems show a huge difference. In bulk water, the dipole vectors of the water molecules should not have any preferential orientation since the medium is fully isotropic. Thus, the reference calculation performed in bulk water (black line) shows a constant value of zero. Similarly, for all the W/O systems the core water region is devoid of any orientational preference. Only near the interface of these systems we observe an oscillatory behavior around zero due to a certain orientational constraint imposed on the water molecules at the interface. But for all of the RM systems the radial profile remains non-zero ($\langle \cos\theta \rangle > 0$) for almost the whole water pool. Even for the largest RM system ($w_0 = 20$), the approach towards $\langle \cos\theta \rangle \rightarrow 0$ is very slow as we approach from the interfacial region to the deeper core of the water pool. The predominantly positive values of $\langle \cos\theta \rangle$ at all radial shells would signify that the electrostatic field due the negatively charged interior surface would orient the dipole vector of the water molecules away from it, thus creating a substantial preferential orientation of the water molecules towards the COM of the water pool.

The overall physical picture obtained from the above analyses has been schematically described in Figure 5.4. Here we have identified two regions in the water pool based on the distance from the interface, namely "interfacial water" (<1.1 nm from the S atoms of the AOT head groups) and "core water". The concentric circles in the "core water" region clearly delineate the zones resembling the bulk-like characteristics based on the properties of water that are being investigated. While the number density becomes bulk-like much closer to the interface, the tetrahedral ordering of water (and hydrogen bonding pattern) is affected to a

longer distance. The dipolar orientation is affected the most in a RM system (>3 nm from the interface).
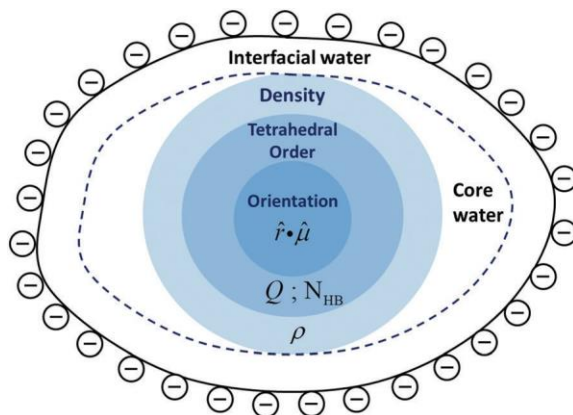
Figure 5.4: Schematic representation of different regions inside the reverse micelle. The negative charges around the outermost layer depict the head- groups of the AOT surfactant molecules. We consider water molecules within 1.1 nm of the charged surface to be the "interfacial water" layer, where water molecules are expected to have distinct properties as compared to bulk water. The rest of the water molecules in the interior of the water pool are considered "core water" (inside the dashed line), which may or may not resemble "bulk water" depending on the properties of interest as shown in Figure 5.3. The spherical regions provide a visual representation of the size of regions where bulk-like behavior is recovered for various properties. The effective size of the bulk-like water pool decreases in the order of number density, tetrahedral order parameter (and number of hydrogen bond), and average dipolar orientation of water molecules.

5.3.4   Distribution of the structural order parameters: core versus interface

The radial profiles shown in Figure 5.3 clearly distinguish the bulk-like behavior (or lack thereof) of the core water region using various structural order parameters. But, due to the substantial shape fluctuations (deviations from the spherical shape), the spherical symmetry is lost, particularly in the RM systems.[8,21] Thus, the radial profiles are not sufficient to study the characteristics of the interfacial regions, since the spherical shells might be averaging over both the interfacial and core water molecules depending on the radius of the shell and shape of the RM. The schematic picture shown in Figure 5.4 clarifies this issue due to spherical asymmetry. The deviations from spherical structure in the RM

systems have been highlighted through the shape anisotropy parameter, which is the ratio of the smallest to the largest component of the gyration tensor, as shown in Figure 5.2. The anisotropy parameter values for the W/O systems remain above 0.9, whereas for the RM systems they undergo huge fluctuations over a broad range of 0.6–0.9.

In order to clearly delineate between core and interfacial water molecules, we have used a different protocol of dividing the water molecules based on the distance from the interface. Based on the radial distribution function of water from the interface (data not shown) and earlier simulation studies where a distance cut-off ≤ 1 nm had been used,[34] we have decided to use a comfortable margin of 1.1 nm to define the "interfacial water" so that the "core water" remains far away from the interface. Subsequently, we compute the probability distributions of the structural order parameters separately for the "core water" and "interfacial water" molecules in order to investigate their possible deviations from bulk properties.

We have outlined the distribution of number density (ρ) separately for core and interfacial water in Figure 5.5 (a and b), respectively. The core water in the RM systems shows almost identical density distribution as bulk water. However, the smaller W/O systems (W/O = 10 and 15) demonstrate lowering of population at bulk-water density and develops a tail distribution at lower density. In the interfacial region, this variation is even more pronounced (Figure 5.5(b)). We must clarify here that a subpopulation of the interfacial water molecules exactly at the boundary of the interface would not have enough number of nearest neighbors to satisfy the bulk-like number density, thus the local average coordination number (density) is expected to be lower than the bulk value for interfacial water. So we expect a tail distribution at lower density values as compared to bulk water for interfacial water in both RM and W/O systems. Interestingly, we observe that while the density distribution in the RM systems shows the peak at the same position as bulk water, for the W/O systems it drastically shifts to much lower values. Of course, there exists a shoulder-like tail at lower densities for the RM systems as expected. The lowering of surface density near an extended hydrophobic surface has been well documented before and it has been suggested that the local water density undergoes large scale density fluctuations near extended hydrophobic surfaces.[56,57,61] We feel that similar factors are leading to the large deviations in the local

density distribution for the interfacial water in W/O systems. In contrast, the hydrophilic anionic interface in the RM systems reinstates the water density leading to a discernable population of water molecules with a bulk-like coordination number.
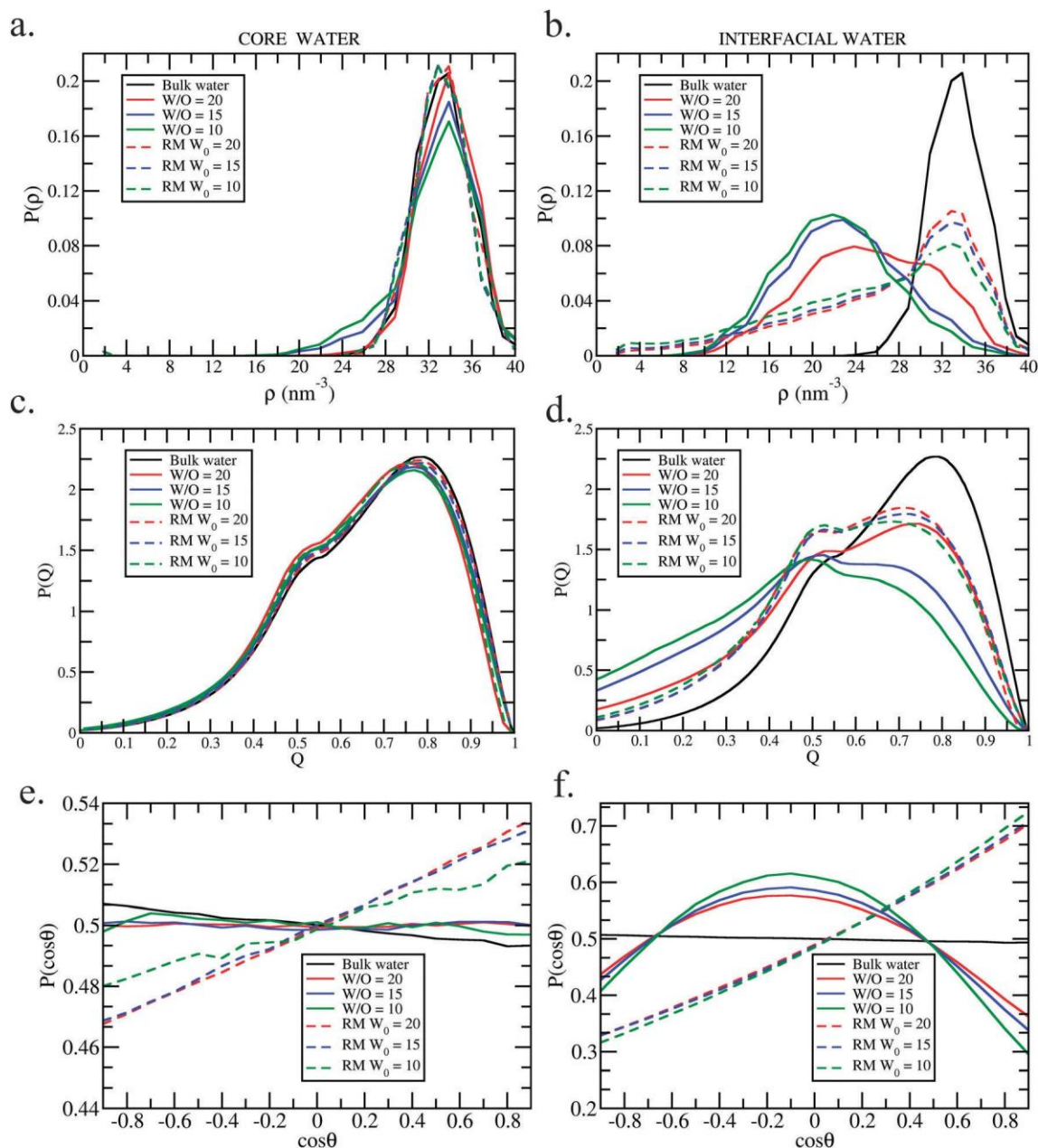
Figure 5.5: Distribution of the structural properties of water for **"core water"** (left panels) and **"interfacial water"** (right panels). The top panels (a and b), middle panels (c and d) and bottom panels (e and f) depict the distribution of local number density (ρ), tetrahedral order parameter (Q) and dipolar orientation relative to the radial vector ($\cos\theta$). Here we have

combined results for both RM and water-in-oil systems for w_0 = 10, 15 and 20 and compared with bulk water.

Figure 5.5 (c and d) show similar distributions for the tetrahedral order parameter. The tetrahedrality displays bulk-like characteristics (with very minor decrease) across the systems for the core water molecules. On the other hand, for the interfacial water there is a distinct decrease in the tetrahedral ordering. Interestingly, the W/O systems demonstrate lower tetrahedral order than the RM systems in the interfacial region. While the hydrophobic interface in the W/O systems induces large perturbation on the hydrogen bonded network of the interfacial water, the negatively charged interface reinforce this due to preferential hydrogen bonding between water and the AOT head groups. While the interfacial water molecules may lose certain amount of water–water hydrogen bonds, this is counter- balanced by the preferential hydrogen bonding between the AOT head groups and the interfacial water molecules.[34] Thus, the overall tetrahedral order or hydrogen bonding pattern is preserved to some extent in the RM systems. We have also compared the hydrogen bond distributions between these regions, but the data have not been shown here since the trends are almost identical to the tetrahedral order parameter distributions.

The distributions of the dipolar orientation ($\cos\theta$) in the core and interfacial region have been shown in Figure 5.5 (e and f). As discussed in the radial profiles of the same properties (Figure 5.3), in an isotropic bulk liquid all possible orientations are equally likely. Thus, P($\cos\theta$) remains constant for bulk water. The same scenario holds for the core water in the W/O systems, where there is no long range electrostatic perturbation from the interface. Of course the interfacial water shows a non-uniform distribution even for the W/O systems due to the preferential orientation of the water dipoles to remain parallel to the interface. On the other hand, for the RM systems not only the interfacial water, but even the core region demonstrates a preference towards an orientation towards the COM of the water pool as discussed earlier in the context of the radial profiles.

5.3.5 Orientational relaxation dynamics: core versus interface

The dynamics of the water molecules in the reverse micelles has been studied extensively in the past.[8,9,29,72–74] But how do the orientational and translational dynamics compare between the RM and W/O systems? We have addressed this question by studying

the orientational relaxation of the water molecules separately in the core and interfacial regions, by using the similar functional form given in Eq. 2.31 to calculate orientational time autocorrelation function (OTCF):

$$C_\mu(t) = \frac{\langle \vec{\mu_i}(t) \cdot \vec{\mu_i}(0) \rangle}{\langle \vec{\mu_i}(0) \cdot \vec{\mu_i}(0) \rangle} \tag{5.2}$$

Where $\vec{\mu_i}(t)$ is the dipole vector of the ith water molecule at time t. The averaging is performed over the water molecule which stays continuously in the selected region for the time interval of 0 to t in order to avoid the mixing of dynamics when a water molecule is exchanged between the interfacial and core regions. Depending on the size of the RM system and associated heterogeneity in the time scales present in the system, the OTCF can be fit well by either single exponential or multi-exponential or stretched exponential or power law functions as reported in earlier studies.[8,27,50] In our work, we have used a tri-exponential fit of the OTCF to compare the time scales observed across all of the seven systems (including bulk water). The time scales and their relative contributions have been reported in Table 5.3 for core and interfacial regions across all the systems. For the shorter survival time of ~50 ps of water molecules in the respective region, OTCFs fit well to the tri-exponential fitting function. For the long-lived tails of correlation functions, both fitting functions fail to catch the decay times as reported earlier.[8]
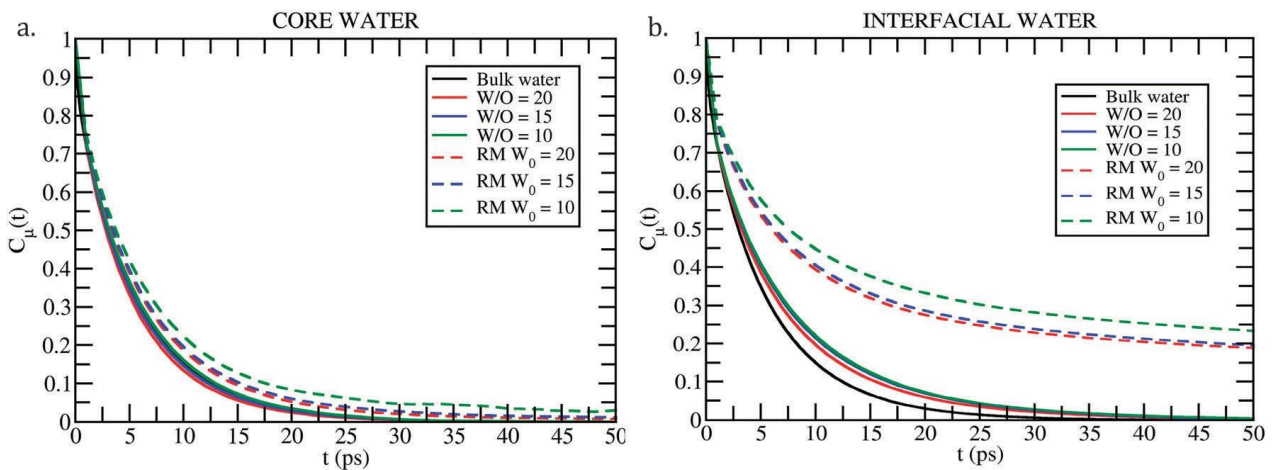
Figure 5.6: Orientational time correlation function **(OTCF)** of **(a)** core water and **(b)** interfacial water**.** We compare the OTCF for w0 = 10, 15 and 20 in both RM and water-in-oil systems**.** The OTCF for bulk water is shown as reference**.** The OTCF is calculated for the

water molecules which continuously stay in the respective regions at least for 50 ps.

Figure 5.6 (a and b) show the comparison of OTCF across all systems for the core and interfacial water, respectively. A visual inspection of the figures clearly shows that for the W/O systems the orientational dynamics is almost identical to the bulk water, while the time scales are slightly higher for the inter- facial water. In contrast, for the RM systems the interfacial water undergoes a dramatic slowdown (more than an order of magnitude) as demonstrated through a multitude of prior experimental and simulation studies. We observe that the slowest component of the OTCF in the interfacial region of RMs fall in the range of ~100 ps (Table 5.3), which is in very good agreement with prior simulation studies.[31] Interestingly, the increase in the slowest time component in the interfacial water of the W/O systems is very small (~10 ps) as compared to bulk water (~6 ps). This clearly confirms the role of the hydrophilic interface in the RM systems towards the observed slow dynamics. Since the free energy of binding of water to the RM surface is much stronger compared to the W/O systems, the exchange rate of the bound water molecules is likely to be much smaller as well.

Interestingly, even for the core water in the RM systems a slight slowdown is visible. The comparison of the time scales observed for the core water (Table 5.3) clearly shows that for RM systems the slowdown remains to a certain extent even beyond 1.1 nm distance from the interface. The time scales are ~45 ps, ~27 ps and ~24 ps for w_0 = 10, 15 and 20, respectively. This long-range slowdown is likely to originate from the long range electrostatic interactions with the charged interface, since such slowdown is completely absent in the core water for W/O systems. Moreover, the dependence of the water dynamics on the distance from the interface might be slower compared to our chosen distance cut-off of 1.1 nm to distinguish between the interfacial and core water. Thus, a core–shell model with clear demarcation between "interfacial" and "core" water might be too simplistic as indicated by prior experimental studies.[9,20,27] For example, according to the simulation studies by Skinner and coworkers[9] the rotational anisotropy reaches the bulk value at a distance of 0.8 nm from the interface for w_0= 7.5, whereas this distance dependence is much slower for smaller RMs due to curvature induced effects. On the other hand, simulation studies of water dynamics around micelles[37] indicate that interfacial effects may sustain up

to 2 nm distance from the charged interface of the micelle. Our observations regarding the long- range perturbations on the global dipolar orientations that might extend up to 3 nm from the RM interface also suggests the possibility that certain water properties might be more sensitive with longer length-scale of perturbation. Thus, a more detailed layer-wise decomposition of various types of water dynamics (vibrational, rotational, collective modes, dielectric relaxation etc.) as a function of distance from the interface would be necessary to shed light on the length scale of such interfacial perturbations.[29,73] Although we can safely conclude that bulk-like dynamics can be observed in reverse micelles with a water pool diameter larger than 4 nm ($w_0 > 20$) as confirmed by Fayer and coworkers.[20,27]

Table 5.3: Tri-exponential fitting of orientational time correlation function **(OTCF)** of water molecules in the **(I)** core region and **(II)** interfacial region of water pools for RM $w_0 = 20$, 15, 10 and W/O= 20, 15, 10 as well as for bulk water**.** The fitting function is $C_\mu(t) = \sum_{i=1}^{3} f_i \exp(\frac{t}{\tau_i})$ where f_i is the fraction of the ith component with the timescale being τ_i**.** The correlation coefficients for the fitting are greater than 0**.**99 in all cases

System	%f_1	τ_1 (ps)	%f_2	τ_2 (ps)	%f_3	τ_3 (ps)
(I) For core water						
Bulk water	75	6.16	13	2.26	12	0.14
RM $w_0 = 20$	6	23.84	79	6.04	15	0.47
RM $w_0 = 15$	7	26.56	78	6.03	15	0.46
RM $w_0 = 10$	8	44.82	77	6.25	15	0.40
W/O = 20	59	6.16	27	3.60	14	0.36
W/O = 15	46	6.88	40	4.27	14	0.37
W/O = 10	59	6.84	27	4.10	14	0.37
(II) For interfacial water						
RM w0 = 20	30	99.62	55	6.44	15	0.017
RM $w_0 = 15$	32	97.25	53	6.49	15	0.017
RM $w_0 = 10$	37	104.49	48	6.75	15	0.017
W/O = 20	51	9.25	34	3.74	15	0.017

| W/O = 15 | 55 | 9.64 | 30 | 3.62 | 15 | 0.017 |
| W/O = 10 | 52 | 10.07 | 32 | 4.03 | 16 | 0.017 |

Previous experimental studies have shown that the hydrogen bond orientational relaxation timescale is almost similar for the neutral and ionic interfaces concluding that the hydrophilic interface and confinement play a dominant role, while the specific chemical nature of the interface plays a secondary role.[24,49,50] We argue that the comparison between neutral and charged RM systems does not separately investigate the effect due to the purely spatial confinement in a clean way, since both systems have hydrophilic interfaces that strongly interact with the water molecules leading to the observed slow dynamics. In the present study, we have dissected the effect of confinement versus the presence of a hydrophilic interface to conclude that the spatial confinement does not affect the orientational dynamics of the interfacial water molecules. Our results are in good agreement with the work of Laage and Thompson[50] showing that the OH reorientation in water is significantly slower in hydrophilic confinement compared to the bulk water, whereas the dynamics of water in the hydrophobic pores are more modestly affected.

5.3.6 Diffusion of water: core versus interface

Next we compare the translational mobility of the core and interfacial water in the RM and W/O systems by monitoring the respective mean square displacement (MSD) versus time using Eq. 2.33 (Fig. 5.7 (a and b)). Since the water molecules are likely to be exchanged between the core and interfacial regions, we have restricted the averaging of MSD for those fragments of the trajectory where a water molecule stays continuously for the chosen time interval of 0 to t ps. Here we have focused on the short time dynamics (~200 ps), since the MSD reaches a plateau beyond a certain time scale due to the spatial confinement. There is a characteristic timescale for each system beyond which the water molecules reach the limits of the confinement size and hence MSD cannot grow any further. Moreover, for this reason we do not include the data for the smallest water pool systems (w_0 = 10 and W/O = 10) for MSD analysis, since we have been unable to generate statistically significant data due to relatively small residence time in the interfacial/core regions in these cases. As we compare the MSD curves of all the systems, we find that the core water

molecules in W/O systems are consistently faster than the RMs (Figure 5.7(a)), and they are much closer to the bulk-like behavior. The translational mobility monotonically increases
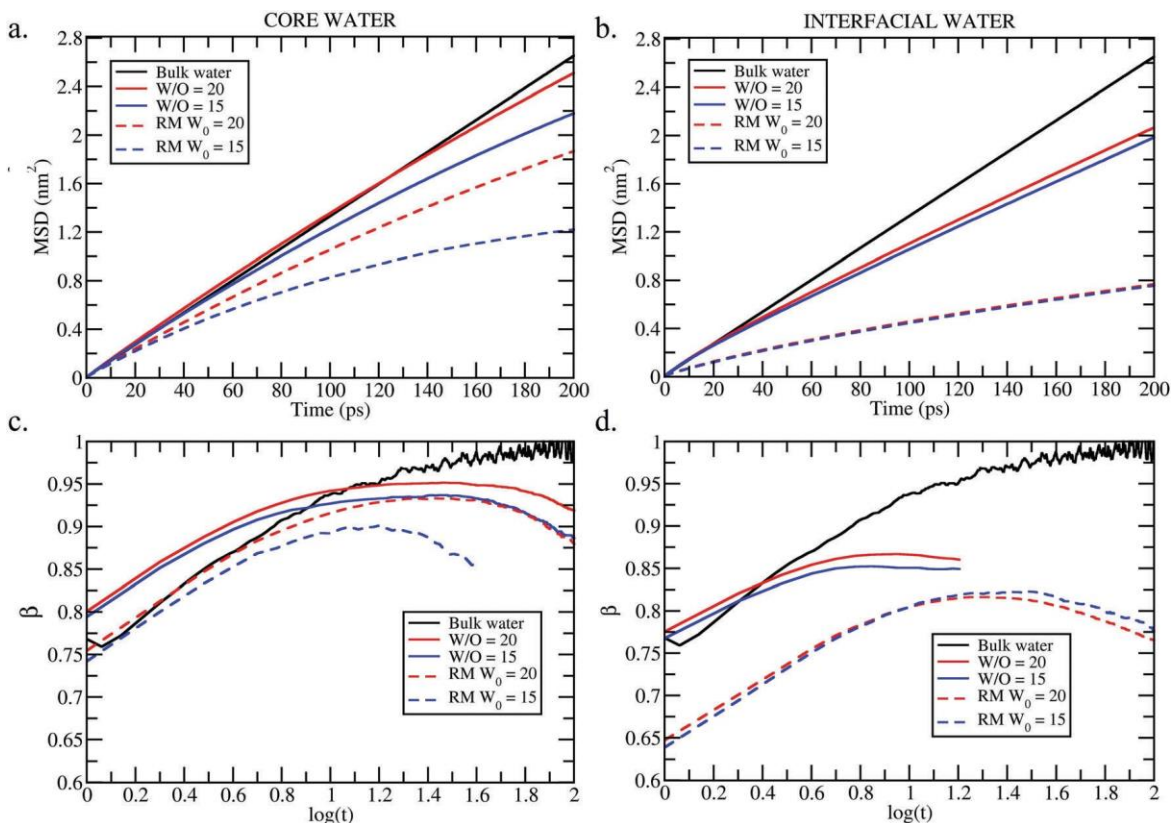
Figure 5.7: **(**top panel**)** Mean square displacement **(**MSD**)** versus time for the oxygen atoms of **(a)** core water and **(b)** interfacial water molecules**. (**bottom panel**)** The slope of the log**(**MSD**)** versus log**(**t**)** for **(c)** core water and **(d)** interfacial water molecules, depicting the β exponent, where MSD $r(t) \propto t^\beta$**.** For a diffusive process, $\beta = 1$, whereas for the sub-diffusive process, $\beta < 1$, which seems to be the case for all confined systems studied here**.** We show the comparison for both RM and water-in-oil systems for $w_0 = 15$ and 20, and compare with the bulk water**.** MSD is calculated for the water molecules which continuously stay in the respective regions at least for 200 ps**.**

with the size of the water pool in each system. Interestingly, for the W/O systems there exists a short-to-intermediate time scale (~50 ps) where the MSD goes slightly above the bulk MSD (possibly due to the absence of long-range electrostatic interactions and lower polarity of the W/O water pool as compared to bulk), but subsequently they start to grow much slower than the bulk water as expected. The difference in mobility between RM and W/O systems

becomes particularly pronounced for the interfacial water, where the water in RM systems shows ~4 times slower diffusion as compared to the W/O systems. For the interfacial water, we find a much weaker size dependence in the RM systems. This indicates the fact that there exists a characteristic timescale of "interfacial water" that can be independent of the size of the "core water" pool. The slower translational dynamics of the interfacial water molecules have the same molecular origin as the corresponding orientational dynamics. The strong electrostatic and hydrogen bonding interactions between the interfacial water and the charged AOT head groups would considerably increase both the residence time and the hydrogen bond lifetime in this region.[69] However, in W/O systems, such strong perturbation is absent leading to bulk-like diffusivity even for the interfacial water.

Finally, we characterize whether the translational motion of the water molecules is diffusive or sub-diffusive in nature. For this purpose, we evaluate the linearity of the time dependence of MSD, i.e. for $\langle \Delta r \rangle 2(t) \propto t^{\beta}$, where $\beta = 1$ and $\beta < 1$ would signify diffusive and sub-diffusive motions, respectively.[29] We compute the exponent β as the slope of the log–log plot of MSD as shown in Figure 5.7 (c and d) for core and interfacial water, respectively. Our results clearly indicate that water under confinement remains sub-diffusive ($\beta < 1$) consistently across all systems and sizes. Of course, the time scale at which the bulk water attains the perfect diffusive regime ($\beta = 1$) is slightly larger than the time scale at which we have managed to gather sufficient statistics for confined water due to the limitations of residence time. Nevertheless, we can qualitatively conclude that the W/O systems display a higher degree of similarity to the bulk water as compared to the RM systems. As usual, for the interfacial water this difference is remarkably pronounced and sub-diffusive dynamics persists for both RM and W/O systems.

5.4 Conclusion

We have presented a systematic investigation of three different kinds of structural order parameters, and translational and rotational dynamics of water molecules in the confinement of AOT RMs and W/O nanodroplets as a function of their sizes in the quest for characterizing the deviations from bulk-like behavior in these confined systems. We demonstrated that the characterization of confined water as "bulk-like" water would strongly depend on which properties of water we are looking at. While the translational order

parameters tend to be less perturbed by the interface, the tetrahedral and orientational order parameters have long range perturbations due to the presence of the charged/hydrophilic interface in the AOT RMs. Moreover, we show that the global orientational ordering of the water molecules may persist to a much larger length-scale (~3 nm) from the charged interface, as compared to the local orientational ordering due to a hydrogen-bonded network. Interestingly, previous simulation studies in reverse micelles have shown that the rotational anisotropy time-scale may reach bulk behavior beyond a distance of 0.8 nm from the interface for $w_0 = 7.5$.[6] This wide mismatch between the length-scales leads to a very significant conclusion that the local orientational dynamics might be dictated by the local environment and local hydrogen bonded network of the probe water molecules, whereas the overall global dipolar orientational ordering may sustain much longer length-scales near charged interfaces. This observation might have significant implications towards earlier suggestions that long range dipolar correlations might lead to attractive interaction between polar (and even non-polar) interfaces over a length-scale of several nanometers.[46]

We have further dissected the relative effect of the size induced confinement versus the perturbation due to the charged interface by comparing all properties with respect to the model control systems of W/O nanodroplets with the same size as the corresponding RM systems. We clearly demonstrate that the effect of confinement in the W/O systems is almost negligible as compared to the pronounced effect on the water structure and dynamics in the RM systems. Previously, the observation of similar interfacial water dynamics in neutral and charged RM systems has led to the conclusion that either the spatial confinement or hydrophilic interface causes the slowdown, and the specific chemical nature of the interface has only a secondary role. We argue that while the local orientational order and dynamics might remain similar between the neutral and charged interfaces due to the hydrophilic nature of the interfaces, (i) the long range orientational order would be substantially different between these systems, and (ii) in the absence of a hydrophilic interface the slowdown becomes negligible, thus ruling out the possible role of spatial confinement effects. Thus, our results clearly delineate the major role of long range electrostatic interactions and the high binding affinity of the water molecules for the hydrophilic RM interior surface in contrast to the spatial confinement effects.

Interestingly, we find that the dynamical properties of water have a higher degree of sensitivity to the environmental perturbations as compared to the structural order parameters. The translational dynamics shows substantial sub-diffusive behavior in both RM and W/O systems. Thus, this is the only water property where both RM and W/O systems show a significant deviation from bulk behavior. Thus, we may also conclude that the translational dynamics can be significantly affected by the pure spatial confinement effect, whereas all other structural order parameters and orientational dynamics are only perturbed by the electrostatic interactions in the RM systems.

5.5 References

(1)   Bagchi, B. *Water in Biological and Chemical Processes: From Structure and Dynamics to Function*; Cambridge University Press, 2011.

(2)   Ball, P. *Chem. Rev.* **2008**, *108* (1), 74–108.

(3)   Errington, J. R.; Debenedetti, P. G. *Nature* **2001**, *409* (6818), 318–321.

(4)   Levinger, N. E.; Swafford, L. A. *Annu. Rev. Phys. Chem.* **2009**, *60* (1), 385–406.

(5)   Fayer, M. D.; Levinger, N. E. *Annu. Rev. Anal. Chem.* **2010**, *3* (1), 89–107.

(6)   Pieniazek, P. A.; Lin, Y.-S.; Chowdhary, J.; Ladanyi, B. M.; Skinner, J. L. *J. Phys. Chem. B* **2009**, *113* (45), 15017–15028.

(7)   Harpham, M. R.; Ladanyi, B. M.; Levinger, N. E.; Herwig, K. W. *J. Chem. Phys.* **2004**, *121* (16), 7855–7868.

(8)   Martinez, A. V.; Dominguez, L.; Małolepsza, E.; Moser, A.; Ziegler, Z.; Straub, J. E. *J. Phys. Chem. B* **2013**, *117* (24), 7345–7351.

(9)   Skinner, J. L.; Pieniazek, P. A.; Gruenbaum, S. M. *Acc. Chem. Res.* **2012**, *45* (1), 93–100.

(10)   Levinger, N. E. *Science*. November 29, 2002, pp 1722–1723.

(11)   Nandi, N.; Bhattacharyya, K.; Bagchi, B. *Chem. Rev.* **2000**, *100* (6), 2013–2046.

(12)   Romero-Vargas Castrillón, S.; Giovambattista, N.; Aksay, I. A.; Debenedetti, P. G. *J.*

Phys. Chem. B **2009**, *113* (5), 1438–1446.

(13)   Koga, K.; Gao, G. T.; Tanaka, H.; Zeng, X. C. *Nature* **2001**, *412* (6849), 802–805.

(14)   Abel, S.; Sterpone, F.; Bandyopadhyay, S.; Marchi, M. *J. Phys. Chem. B* **2004**, *108* (50), 19458–19466.

(15)   Bhattacharyya, K. *Acc. Chem. Res.* **2003**, *36* (2), 95–101.

(16)   Hauser, H.; Haering, G.; Pande, A.; Luisi, P. L. *J. Phys. Chem.* **1989**, *93* (23), 7869–7876.

(17)   Klíčová, L.; Muchová, E.; Šebej, P.; Slavíček, P.; Klán, P. *Langmuir* **2015**, *31* (30), 8284–8293.

(18)   Nandi, N.; Bagchi, B. *J. Phys. Chem. B* **1997**, *101* (50), 10954–10961.

(19)   Biswas, R.; Rohman, N.; Pradhan, T.; Buchner, R. *J. Phys. Chem. B* **2008**, *112* (31), 9379–9388.

(20)   Moilanen, D. E.; Fenn, E. E.; Wong, D.; Fayer, M. D. *J. Phys. Chem. B* **2009**, *113* (25), 8560–8568.

(21)   Vasquez, V. R.; Williams, B. C.; Graeve, O. A. *J. Phys. Chem. B* **2011**, *115* (12), 2979–2987.

(22)   De, T. K.; Maitra, A. *Adv. Colloid Interface Sci.* **1995**, *59* (C), 95–193.

(23)   Patra, A.; Luong, T. Q.; Mitra, R. K.; Havenith, M. *Phys. Chem. Chem. Phys.* **2013**, *15* (3), 930–939.

(24)   Patra, A.; Luong, T. Q.; Mitra, R. K.; Havenith, M. *Phys. Chem. Chem. Phys.* **2014**, *16* (25), 12875–12883.

(25)   Bakulin, A. A.; Cringus, D.; Pieniazek, P. A.; Skinner, J. L.; Jansen, T. L. C.; Pshenichnikov, M. S. *J. Phys. Chem. B* **2013**, *117* (49), 15545–15558.

(26)   Maitra, A. *J. Phys. Chem.* **1984**, *88* (21), 5122–5125.

(27)   Piletic, I. R.; Moilanen, D. E.; Spry, D. B.; Levinger, N. E.; Fayer, M. D. *J. Phys. Chem.*

A **2006**, *110* (15), 4985–4999.

(28)   Sarkar, N.; Das, K.; Datta, A.; Das, S.; Bhattacharyya, K. *Solvation Dynamics of Coumarin 480 in Reverse Micelles. Slow Relaxation of Water Molecules*; 1996.

(29)   Biswas, R.; Furtado, J.; Bagchi, B. *J. Chem. Phys.* **2013**, *139* (14).

(30)   Chowdhary, J.; Ladanyi, B. M. *J. Phys. Chem. A* **2011**, *115* (23), 6306–6316.

(31)   Faeder, J.; Ladanyi, B. M. *J. Phys. Chem. B* **2000**, *104* (5), 1033–1046.

(32)   Harpham, M. R.; Ladanyi, B. M.; Levinger, N. E. *J. Phys. Chem. B* **2005**, *109* (35), 16891–16900.

(33)   Bagchi, B. **2005**.

(34)   Senapati, S.; Berkowitz, M. L. *J. Chem. Phys.* **2003**, *118* (4), 1937–1944.

(35)   Bruce, C. D.; Berkowitz, M. L.; Perera, L.; Forbes, M. D. E. *J. Phys. Chem. B* **2002**, *106* (15), 3788–3793.

(36)   Senapati, S.; Chandra, A. *J. Phys. Chem. B* **2001**, *105* (22), 5106–5109.

(37)   S. Balasubramanian, A.; Bagchi, B. **2001**.

(38)   Costard, R.; Levinger, N. E.; Nibbering, E. T. J.; Elsaesser, T. *J. Phys. Chem. B* **2012**, *116* (19), 5752–5759.

(39)   Pang, Y. **2007**.

(40)   Bhattacharyya, K.; Bagchi, B. *J. Phys. Chem. A* **2000**, *104* (46), 10603–10613.

(41)   Moilanen, D. E.; Fenn, E. E.; Wong, D.; Fayer, M. D. *J. Chem. Phys.* **2009**, *131* (1).

(42)   Van Der Loop, T. H.; Ottosson, N.; Lotze, S.; Kentzinger, E.; Vad, T.; Sager, W. F. C.; Bakker, H. J.; Woutersen, S. *J. Chem. Phys.* **2014**, *141* (18).

(43)   Verma, P. K.; Saha, R.; Mitra, R. K.; Pal, S. K. *Soft Matter* **2010**, *6* (23), 5971–5979.

(44)   Martínez, L.; Andrade, R.; Birgin, E. G.; Martínez, J. M. *J. Comput. Chem.* **2009**, *30* (13), 2157–2164.

(45) Pashley, R. M.; Mcguiggan, P. M.; Ninham, B. W.; Evans, D. F. *Science (80-.).* **1985**, *229* (4718), 1088–1089.

(46) Despa, F.; Berry, R. S. *Biophys. J.* **2007**, *92* (2), 373–378.

(47) Banerjee, S.; Singh, R. S.; Bagchi, B. *J. Chem. Phys.* **2015**, *142* (13), 134505.

(48) Fenn, E. E.; Wong, D. B.; Fayer, M. D. *Proc. Natl. Acad. Sci. U. S. A.* **2009**, *106* (36), 15243–15248.

(49) Moilanen, D. E.; Levinger, N. E.; Spry, D. B.; Fayer, M. D. *J. Am. Chem. Soc.* **2007**, *129* (46), 14311–14318.

(50) Laage, D.; Thompson, W. H. *J. Chem. Phys.* **2012**, *136* (4), 044513.

(51) Moore, F. G.; Richmond, G. L. *Acc. Chem. Res.* **2008**, *41* (6), 739–748.

(52) Jinesh, K. B.; Frenken, J. W. M. *Phys. Rev. Lett.* **2008**, *101* (3).

(53) Gragson, D. E.; Richmond, G. L. *J. Phys. Chem. B* **1998**, *102* (3), 569–576.

(54) Stirnemann, G.; Rossky, P. J.; Hynes, J. T.; Laage, D. *Faraday Discuss.* **2010**, *146*, 263–281; discussion 283-98, 395–401.

(55) Davis, J. G.; Gierszal, K. P.; Wang, P.; Ben-Amotz, D. *Nature* **2012**, *491* (7425), 582–585.

(56) Lum, K.; Chandler, D.; Weeks, J. D. *J. Phys. Chem. B* **1999**, *103* (22), 4570–4577.

(57) Chandler, D. *Nature* **2005**, *437* (7059), 640–647.

(58) Tian, C. S.; Shen, Y. R. *Proc. Natl. Acad. Sci. U. S. A.* **2009**, *106* (36), 15148–15153.

(59) Abel, S.; Waks, M.; Marchi, M. *Eur. Phys. J. E* **2010**, *32* (4), 399–409.

(60) Zulauf, M.; Eicke, H. F. *J. Phys. Chem.* **1979**, *83* (4), 480–486.

(61) Hande, V. R.; Chakrabarty, S. *J. Phys. Chem. B* **2015**, *119* (34), 11346–11357.

(62) Abascal, J. L. F.; Vega, C. *J. Chem. Phys.* **2005**, *123* (23), 234505.

(63) Vega, C.; Abascal, J. L. F. *Physical Chemistry Chemical Physics*. November 28, 2011,

pp 19663–19688.

(64)   Hess, B.; Kutzner, C.; Van Der Spoel, D.; Lindahl, E. *J. Chem. Theory Comput.* **2008**, *4* (3), 435–447.

(65)   Bussi, G.; Donadio, D.; Parrinello, M. *J. Chem. Phys.* **2007**, *126* (1), 014101.

(66)   Berendsen, H. J. C.; Postma, J. P. M.; Van Gunsteren, W. F.; Dinola, A.; Haak, J. R. *J. Chem. Phys.* **1984**, *81* (8), 3684–3690.

(67)   Parrinello, M.; Rahman, A. *J. Appl. Phys.* **1981**, *52* (12), 7182–7190.

(68)   Guchhait, B.; Biswas, R.; Ghorai, P. K. *J. Phys. Chem. B* **2013**, *117* (12), 3345–3361.

(69)   Pomata, M. H. H.; Laria, D.; Skaf, M. S.; Elola, M. D. *J. Chem. Phys.* **2008**, *129* (24).

(70)   Valdez, D.; Le Huérou, J. Y.; Gindre, M.; Urbach, W.; Waks, M. *Biophys. J.* **2001**, *80* (6), 2751–2760.

(71)   Kinugasa, T.; Kondo, A.; Nishimura, S.; Miyauchi, Y.; Nishii, Y.; Watanabe, K.; Takeuchi, H. *Colloids Surfaces A Physicochem. Eng. Asp.* **2002**, *204* (1–3), 193–199.

(72)   Laage, D.; Thompson, W. H. *J. Chem. Phys.* **2012**, *136* (4).

(73)   Biswas, R.; Chakraborti, T.; Bagchi, B.; Ayappa, K. G. *J. Chem. Phys.* **2012**, *137* (1).

(74)   Marchi, M.; Sterpone, F.; Ceccarelli, M. *J. Am. Chem. Soc.* **2002**, *124* (23), 6787–6791.

Chapter 6: Water Around Planar Surfaces: Effect of Surface Charges, Specific Interactions and Coupling to Surface Fluctuations

6.1 Introduction

The interfacial water is known to control and determine the structural and dynamical features of bio-membranes as it regulates the membrane-membrane and membrane-protein interactions.[1] The properties of interfacial water molecules also deviate remarkably from homogeneous bulk water due to different types of interactions with the membrane surfaces.[2] The chemical heterogeneity and electrostatic field due the surface induce energetic perturbation in the interfacial water molecules.[3] However, the length scale over which this structural and dynamical perturbation of water may be sustained has been extensively debated with varying conclusions.[4,5] The situation becomes even more complicated when the interface contains heterogeneity in chemical composition and charge distribution.[2]

Recent experimental and computational studies have contributed to the understanding of the length-scale of water perturbation.[5–8] However, the agreement between these studies is poor.[3,4,8] Therefore, it is imperative to undertake a systematic investigation of interfacial water near different types of surfaces, namely hydrophobic, charged and polar neutral (zwitterionic). The length-scale of perturbation is expected to vary across different systems depending upon the geometry as well as the chemical environment around it.[3,9,10] In Chapter 5, we have demonstrated that the water perturbation length-scale in the confined environment of AOT reverse micelle is strongly dependent on the property under consideration.[11] We have elucidated that electrostatic interaction plays the primary role in controlling the water structure and orientational dynamics, whereas confinement only affects the translational dynamics of water.

Therefore, using MD simulation, we aim to study the structure and dynamics of interfacial water near the anionic/zwitterionic(neutral-polar)/hydrophobic bilayer surfaces to decipher the effect of surface charges, specific interactions and its coupling to surface fluctuations in a distance-dependent manner. We also attempt to deduce the water perturbation length scale from these surfaces and how this length scale varies depending on the nature of the interface.

6.2 System setup and computational details

We have performed atomistic MD simulations of three different types of membrane bilayers: (1) anionic; AOT ($C_{20}H_{37}NaO_7S$, Dioctyl sodium sulfosuccinate) (2) zwitterionic (neutral-polar) POPC ($C_{42}H_{82}NO_8P$, 1-palmitoyl-2-oleoyl-sn-glycero-3-phosphocholine) (3) Hydrophobic ISO (C_8H_{18}, Isooctane). All the molecular dynamics simulations have been performed using GROMACS version 5.0.7[12] with CHARMM36[13] force field and the TIP4P-2005[14] water model. The equilibrated POPC bilayer structure has been taken from the site: https://terpconnect.umd.edu/~jbklauda/research/download.html. The AOT and ISO layers have been constructed using the Gromacs utility genconf to multiplicate molecules across X and Y directions and bilayer have been created along Z direction. The equilibrated box of water has been attached on both sides of them so that the final system will become water-surfactant-water layers as shown in Figure 6.1. We have simulated around 72 molecules of AOT and POPC, 36 molecules on each leaflet. The AOT bilayer system have been neutralized by adding counter ions, Na^+. The hydrophobic surface has been constructed using 886 ISO molecules. The number of water molecules used is 9830, 16860 and 19256 in bilayers of AOT, POPC and ISO respectively. For the purpose of finding out the length-scale of water perturbation as well as to ensure that water near bilayer interface is not interacting with the mirror image, a larger water slab of dimension [5.0X5.6X13.0 (AOT), 6.5X 6.5X19 (POPC) and 9.1X6.8X13.6 (ISO)] has been taken for the simulation.

The bilayers have been initially subjected to energy minimization using steepest-descent algorithm to eliminate any clashes of atoms. Afterwards, NVT equilibration has been carried out for 2 ns at 300 K temperature using the V-rescale thermostat.[15] Semiisotropic pressure coupling method has been used during the NPT equilibration of 30 ns at 1 bar pressure using the Berendsen barostat.[16] This is followed by the production run of 100 ns by means of Parrinello–Rahman barostat[17] with a 2 fs integration time step. The trajectory frames have been saved every 1 ps and 0.1 ps for subsequent analysis of structural and dynamical quantities of water, respectively. The simulations have been performed using periodic boundary conditions and long-range electrostatic interactions have been treated using particle mesh Ewald method.[18] The cut-off distance for short-range electrostatic and van der Waals interactions has been set to 1.0 nm. The bonds have been constrained with LINCS algorithm.[19] The equilibrated structures of the three bilayer systems are shown in Figure 6.1 (a-c) and molecules used to construct this bilayer are shown in Figure 6.1 (d).
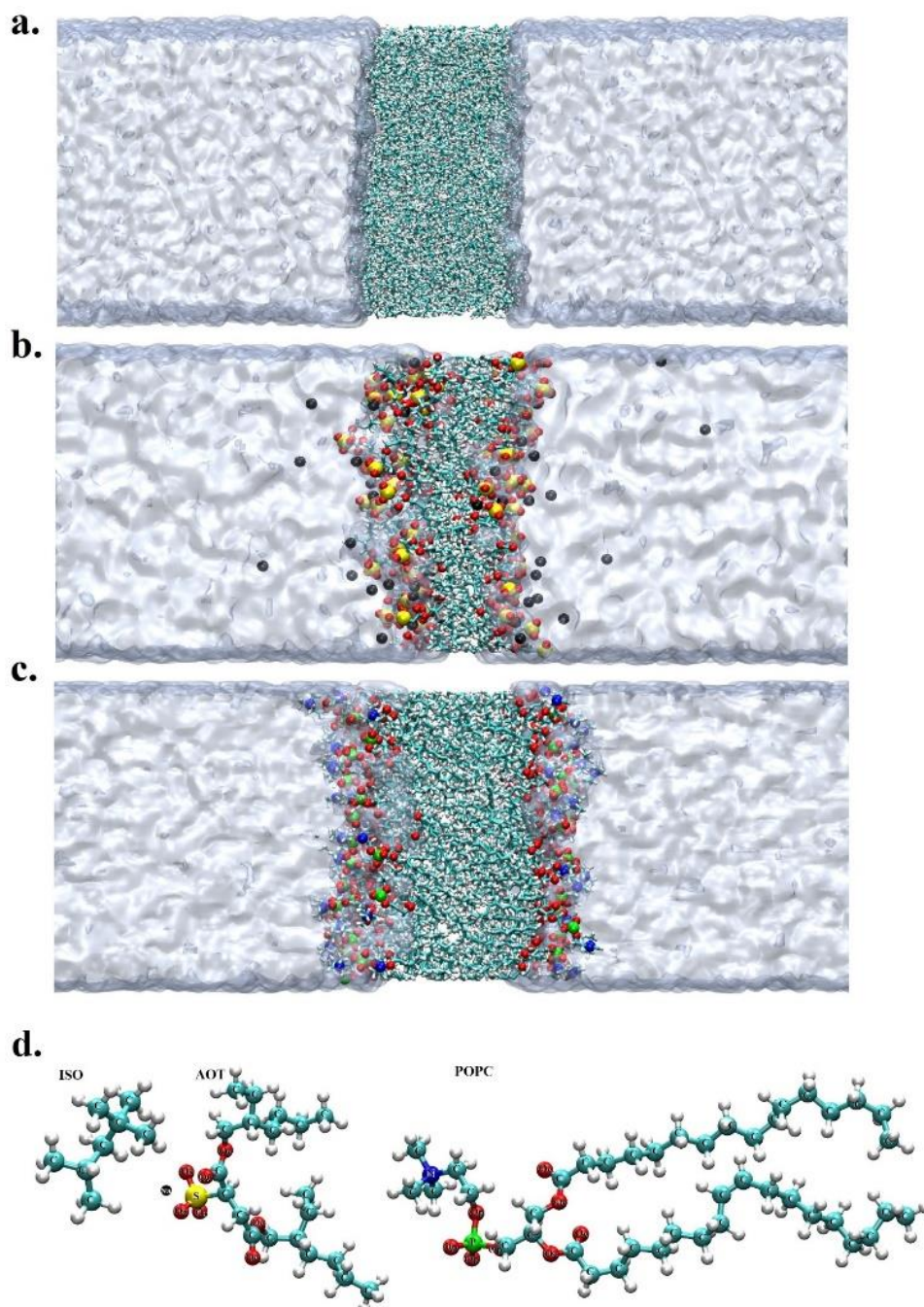
Figure 6.**1**: Representative snapshots of equilibrated bilayers of a**.** ISO, b**.** AOT, c**.** POPC, and d**.** molecular structures of them with atomic labels**.** The transparent surface illustrates the water phase**.**

6.3 Results and discussion

6.3.1 Choice of structural order parameters

We have chosen four order parameters to investigate the length scale of perturbation in water structure due to the presence of differently charged surfaces; negative, zwitterionic, and neutral (hydrophobic). The structural order parameters used here are namely, number density (ρ), tetrahedral order parameter (Q) as given in Eq. 2.30, number of hydrogen bond (N_{HB}) calculated using the criterion given in Chapter 2 in subsection 2.6.1.3, and average dipolar orientation with respect to bilayer normal (P). In the calculation of Q, we have included the oxygen atoms of head groups of surfactant molecules as well, if they are among the first four nearest neighbors of the ith water molecule or if they satisfy hydrogen bonding criterion in the calculation of N_{HB}, which is highly possible for the water molecules that bind to the bilayer interface.

1. **Number density**

This is defined as the number of water molecules present per unit sliced volume of the box. The thin slices are created along the Z-axis with same cross-sectional area in the XY plane. This quantity captures how the local density of water molecules would vary from the interface to further away from it.

2. **Dipolar orientation relative to the bilayer normal (P)**

Dipolar orientation (P) of the water molecule with respect to bilayer normal is quantified as

$$P = \frac{\vec{\mu} \cdot \vec{r}}{\left|\vec{\mu}\right| \cdot \left|\vec{r}\right|} = \cos\theta \tag{6.1}$$

where, $\vec{r}$ is the bilayer normal vector and $\vec{\mu}$ is the dipole vector of the water molecule. The angle between these vectors (θ) is zero if the dipole vector is oriented towards the bilayer.

6.3.2 Partial density profiles

The equilibrated density profiles of various elements of the bilayers ISO, AOT and POPC are represented in Figure 6.2a, b, and c. In all cases the midpoint of the density profile is shifted to z=0 for easier comparison across various systems. It is important to note that the AOT bilayer is more flexible and fluctuates more compared to the other two systems, resulting in the asymmetric shape of the interface although it never breaks or forms spherical micelles. Therefore, the bilayer

remains intact throughout the simulation trajectory. The hydrophobic part of the bilayer is the innermost layer and the hydrophilic components of the bilayers are pointing towards the water phase as expected. The equilibrated bilayers, bilayer constituents and their atomic labels are shown in Figure 6.1.
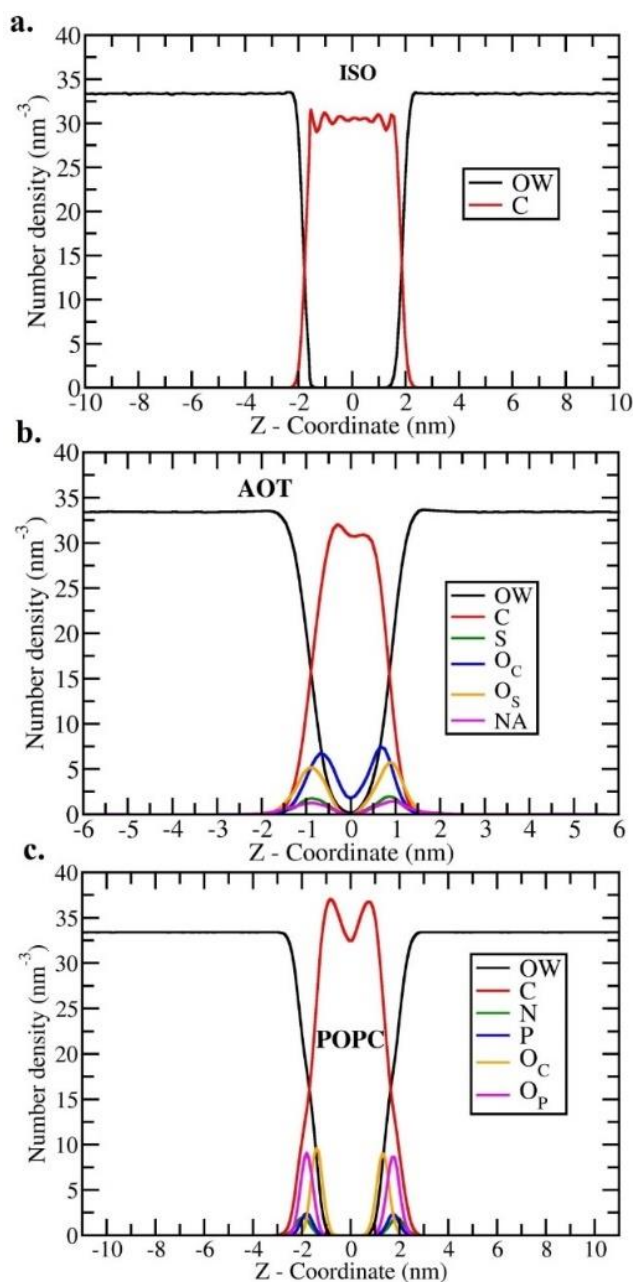
Figure 6.2: Partial density profiles of various species in the bilayer of a. ISO b. AOT c. POPC. O_S, O_C, and O_P refer to partial densities of oxygen atoms bonded to S, C and P, respectively as defined in Figure 6.1 (d).

6.3.3 Distance dependence of structural order parameters

Various structural order parameters are examined within thin slabs of width 0.1nm along the bilayer normal to elucidate the distance dependence from the interface. All the profiles are obtained by averaging over all the water molecules present in that slab and by the total number of time frames. Thus, they represent the average structural order parameters as a function of distance from the interface (located at $z=z_0$). The interface location along Z-axis (z_0) is determined from the maximum in the first derivative of partial density profiles of surface atoms C, S, and N for ISO, AOT and POPC. The values of z_0 are accordingly 3.45, 7.25 and 13.0 nm for ISO, AOT and POPC. Thus, the difference $\Delta z = (z - z_0)$ is the distance of a water molecule from the interface, where z is the z-coordinate of O atom of the water molecule.
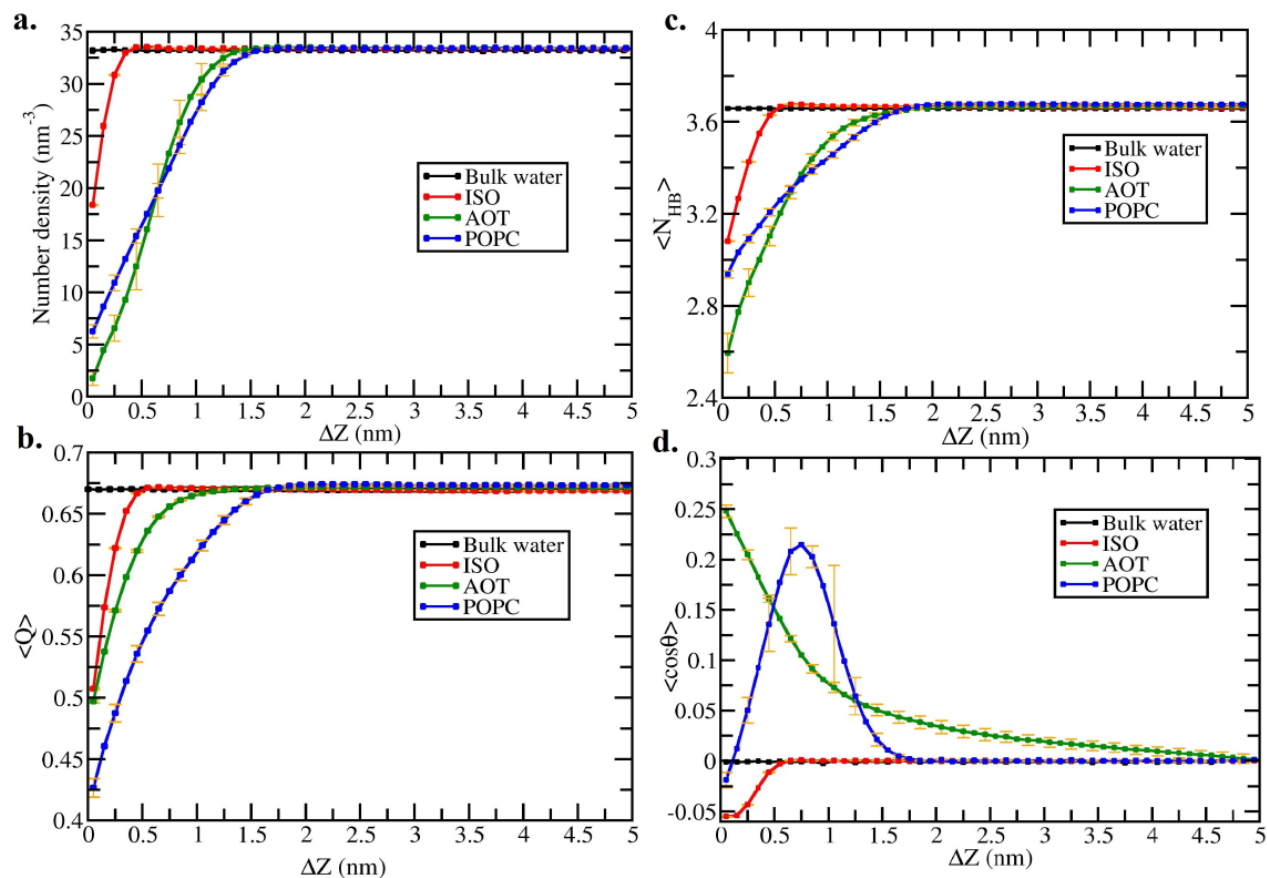
Figure 6.3: Average properties with error bars (in yellow color) along the bilayer normal: a. number density b. tetrahedral order parameter (Q), c. number of hydrogen bonds (N_{HB}) and d. dipolar orientation of water w.r.t. bilayer normal (P or cosθ);. The reference line for bulk water is shown in black color.

Figure 6.3 (a to c) represents the local structural order profiles such as number density, tetrahedral order parameter (Q), and number of hydrogen bonds (N_{HB}) of water molecules. In all the profiles, bulk water (in black color) is shown for a reference. Figure 6.3(a) shows that density has reached to bulk value around 0.5 nm from the hydrophobic ISO surface and 1.5 nm from the AOT and POPC bilayer. The tetrahedrality of water reaches to the bulk value at different lengths for all of these systems. As Figure 6.3(b) depicts that tetrahedral order parameter (Q) reaches bulk value at distances ~0.5 nm, ~1.0 nm and ~1.5 nm for ISO, AOT and POPC, respectively. These length-scales are quite comparable with number density only the length-scale for AOT is lower by ~0.5 nm. In case of ISO and POPC, the length scale of average number of hydrogen bonds is similar to number density and tetrahedrality. However, AOT has length-scale of ~1.5 nm from $\langle N_{HB} \rangle$ profile same as $\langle \rho \rangle$ but increased by 0.5 nm as compared $\langle Q \rangle$. The difference in length-scale between Q and N_{HB} can be attributed to their definitions. In definition of Q, nearest four neighbors are taken for the calculation while in hydrogen bond calculation, we look for the water molecules which satisfy distance as well as angle criterion and we note that these neighbors can be different in calculation of Q and N_{HB}.

Figure 6.3(d) shows the global orientational order of water i.e. the average dipolar orientation of water with respect to bilayer normal. ISO and POPC preserve their perturbation length-scale to 0.5 and 1.5 nm; however, AOT has a much longer length-scale of ~4.5 nm. This suggests that negative interface perturbs water to higher length-scale globally than a neutral polar or non-polar interface. Also, the length-scale of water perturbation is different depending upon parameter under consideration. Interestingly, POPC shows a non-monotonic distance dependence in cosθ with a maximum at intermediate value. The inner side of POPC bilayer has phosphate and ester groups that are negatively charged, therefore the water has an increase in positive $\cos\theta$, while the water facing alkyl ammonium cationic head groups cannot form hydrogen bonds with water and have significant hydrophobic characteristics.[20] The non-monotonic distance dependence occurs due to the differential competing interactions with the phosphate and ammonium groups present near the interface.
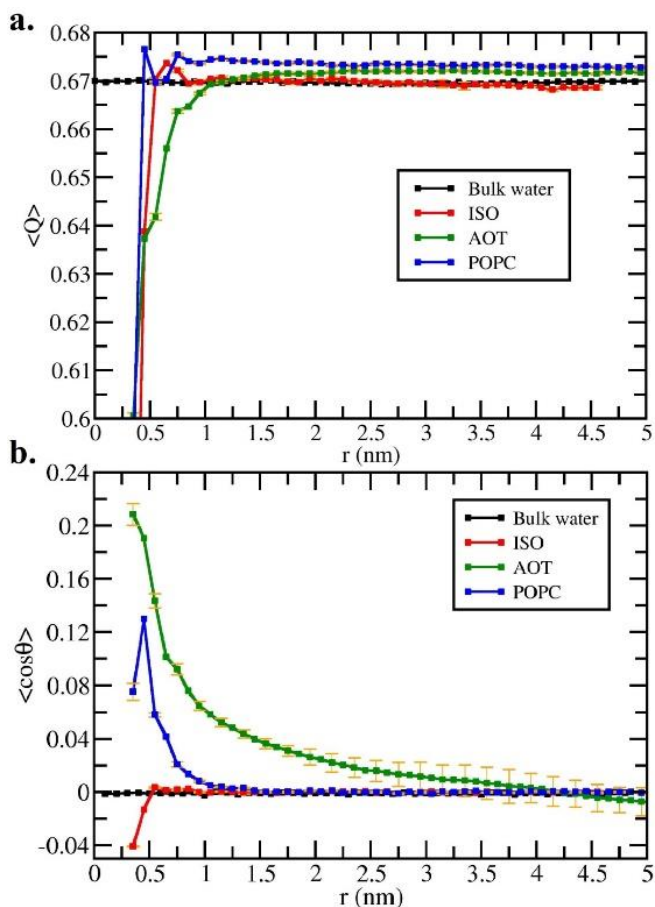
Figure 6.4: Average properties from the reference surfaces of S, N of AOT and POPC respectively; a**.** average tetrahedral order, b**.** average cosθ**.** Due to undulating reference surfaces **(**as shown in Figure 6**.**1b and 1c**)** of especially AOT and POPC bilayers, we considered water slab according to the definition that targeted OW of water should be present towards the water phase from its closest reference atom of surfactant**.** In this case, we do not allow this water to be in bilayer phase since it could be trapped in surfactant phase**.** Therefore, in this case we can see the length of water perturbation strictly because of the presence of adjacent bilayer**.**

Since the bilayer fluctuations result in an undulating interface and therefore to minimize such effect of undulating surface on the water perturbation length-scale, parallel undulating water slabs are constructed based on the minimum distance from the nearest surface atom. In this case, only the water molecules present towards water phase into surfactant phase are considered for the calculation of local and global orientational order parameters i.e. tetrahedral order parameter and dipolar orientation order as shown in Figure 6.4a and b, respectively. This definition does take into account the embedded water molecules in the surfactant phase. The reference surface atoms are C,

S and N from the ISO, AOT and POPC, respectively. The new definition provides us an estimate of water perturbation due to presence of the different kinds of surfaces. The length-scale of perturbation near ISO shows the little enhancement in the tetrahedrality; well-known for the hydrophobic surfaces.[21] In case of AOT this length-scale is 1.0 nm from the surface of S atoms. AOT has an undulating surface to a considerable extent, that may cause the same length-scale in this case also. In case of POPC, this length-scale has been decreased by 1 nm. The global average dipolar orientation order or the $\cos\theta$ is in Figure 6.4b. The order is always towards the positive values of $\cos\theta$ implies that the water dipole vectors are oriented away from the surface. The length-scales of water perturbation have been decreased by around 0.5 nm and this is purely due to the presence of charged surfaces nearby. The length-scales are in this case are ~1 nm and 4 nm for POPC and AOT, respectively; although it is the same for ISO as previous case. Interestingly, the orientation of water around ammonium group is still similar to AOT with negative surfaces. The terminal nitrogen atoms of POPC are acting as the hydrophobic surface and therefore the dipolar orientation of the water molecules has not been affected much because of the cancellation of interactions with the positive and negative functional groups.

6.3.4   Layer-wise translational dynamics of water

In addition to structural perturbation of water, we also shed the light on the dynamics of water namely the translational and orientational dynamics of the water in a layer-wise manner. As discussed earlier, to make the slabs from the reference position; Z_0, which is maximum in the first derivative of number density of surface atoms. The surface atoms are C, S, and N are chosen accordingly in case of ISO, AOT and POPC bilayer systems. The layers or slabs of width 0.4 nm are made along the bilayer normal to dissect the length-scale of perturbation in water dynamics. Both the translational and rotational dynamics are calculated for the water which continuously stays in the given slab. Water near the head-group area or embedded in the surfactant phase has more residence time of ~500ps than the far-away water or the bulk water which resides for ~50ps in the given slab. In Figure 6.5, translational dynamics is measured using mean squared displacement (MSD) of water in slab-wise manner using equation 2.33. We have studied the dynamics in two different ways: (i) along the Z-axis, i.e. perpendicular to the interface using the
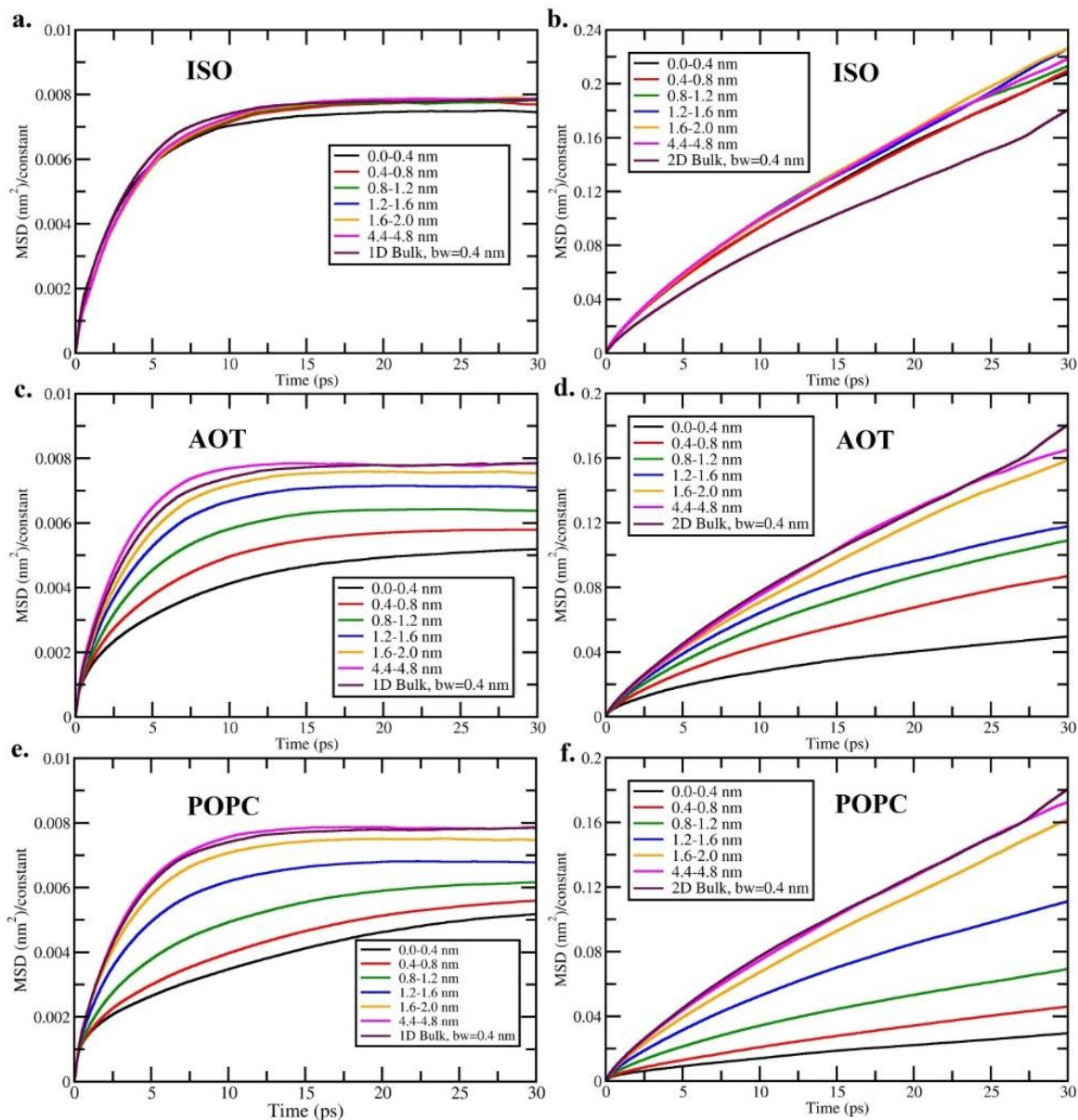
Figure 6.5: MSD; left panel is 1D MSD and the right panel is 2D MSD of oxygen atoms of water. The top panel (a and b), middle panel (c and d) and bottom panel (e and f) are of ISO, AOT and POPC, respectively. The constants are 2 and 4, in case of 1D and 2D MSDs, respectively. MSDs are calculated for those water molecules which continuously stay in the selected slab of width 0.4 nm. We avoided the water molecule which satisfies the minimum image criterion.

1D MSD as shown in Figure 6.5 (a, c, and e; left panel) and (ii) parallel to the interface along the XY plane using 2D MSD as shown in Figure 6.5 (b, d, and f; right panel) for ISO, AOT and POPC

interfaces, respectively. To calculate these MSDs, the trajectories where the water molecule does not jump abruptly along the edges of the simulation box are considered to avoid the sudden rise in the MSDs. MSDs are plotted only up to 30ps, since we are limited by the residence time of the water in the given slab. 1D MSDs normalized by constant 2 reaches to the plateau region in about 10ps. This is due to the slab-width of the slab and it shows the behavior same as the confined water. We observed that 2D MSD normalized by constant 4 is faster compared to 1D MSDs and also the motion is sub-diffusive near the surface. Figure 6.5(a) indicates that the water around hydrophobic surface of ISO is behaving similarly as bulk water. In Figure 6.5(c), the water around negative surface of AOT has quite slow translational motion which indicates the strong binding of water to the surface. Water recovers its bulk like behavior only beyond ~2 nm from the surface. The water around zwitterionic surface of POPC shows a similar behavior as near AOT surface (Figure 6.5(e)).

In Figure 6.5(b) 2D MSD of ISO is plotted, where water dynamics is faster compared to bulk water. Almost all MSDs are overlapping on each other, suggesting that they are of the same type near the surface as well far away from it. In Figure 6.5(d), the 2D MSD of AOT is monotonically increasing as the slab is farther away from the surface of AOT. The translational dynamics of water continues to be perturbed till 2nm. The bulk-like behavior is recovered at much larger distance of ~4.5 nm. Since the surfactant layer undergoes significant amount of fluctuations and undulations, the dynamics of trapped water in the surfactant layer is coupled to the surface fluctuations. 2D MSD of water near POPC bilayer is shown in Figure 6.5(f). The behavior of water near POPC is reasonably comparable to AOT and the length-scale of water perturbation is also 2 nm.

6.3.5 Layer-wise re-orientational dynamics of water

It is expected that along with the translational dynamics, re-orientational dynamics of water would get affected by the presence of charged/polar surfaces. We have calculated the orientational time autocorrelation function (OTCF) of water as a function of distance from the surface in a layer-wise fashion to understand the distance dependence of rotational dynamics.
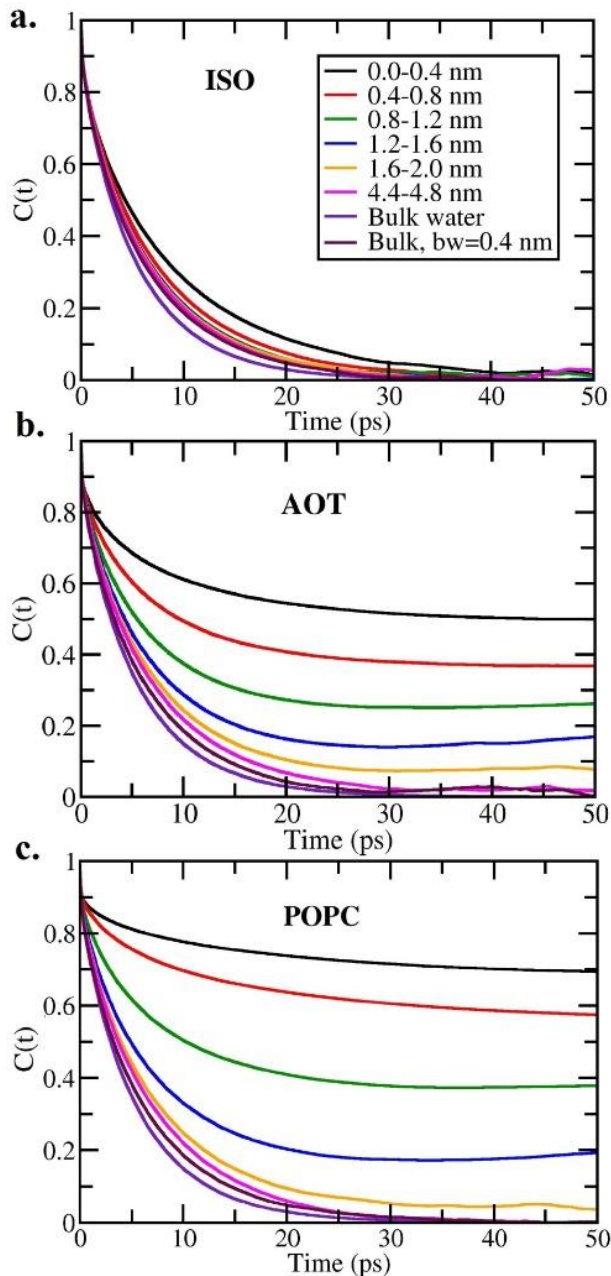
Figure 6.**6**: OTCF of water molecules in a layer-wsie manner for the bilayer of a**.** ISO, b**.** AOT and c**.** POPC**.** OTCFs are calculated for those water molecules which continuously stay in the selected slab of width 0**.**4 nm**.**

Orientational time autocorrelation function (OTCF) by using the functional form given in equation 2.31can be written,

$$C(t) = \langle \frac{\vec{\mu}_i(t).\vec{\mu}_i(0)}{\vec{\mu}_i(0).\vec{\mu}_i(0)} \rangle \tag{6.2}$$

where, $\vec{\mu}_i(t)$ is the dipole vector of the ith water molecule at time t. The averaging is performed for the time interval of 0 to t over the water molecules which stay continuously in the selected slab in order to avoid the mixing of dynamics when a water molecule is exchanged between the neighboring slabs.

The layer-wise OTCF for the three bilayers is shown in Figure 6.6 with slab width 0.4 nm for 50ps data length. Figure 6.6(a) represents the layer-wise OTCFs of ISO bilayer. Only the first slab near to surface shows slightly slower dynamics, whereas otherwise it remains mostly bulk-like water. However, in the case of AOT and POPC bilayers as shown in Figure 6.6(b) and (c), the decay is very slow and has a long-lived tail to OTCF for the slabs exists nearby to surface. This indicates that interfacial water molecule has strong binding to the head group of AOT because of the electrostatic interactions and hydrogen-bonding with the interface. The electrostatic effect continues to influence the water up to 2 nm from the interface. Long-lived tails of OTCF also suggests that the water is trapped orientationally. Another possibility could be that water motion is coupled with the surface fluctuations of bilayer. We also investigated this and discussed in the next section.

These OTCF curves are fitted to bi-exponential function up to the initial 20 ps using and the time-scales of relaxations are listed in Tabel 6.1 for the three bilayers (A) ISO (B) AOT and (C) POPC. The water has slow timescale of relaxation in first slab otherwise, bulk-like timescales are almost achieved in the subsequent slabs towards water phase in ISO bilayer system. Near AOT surface, the slabs up to 2 nm have slower water present. The first slab

Table 6.1: OTCF**:** planar fitting parameters (fitting upto 20 ps length)

A. ISO

Bin (nm)	a0	a1(ps)	a2	a3(ps)
0.0-0.4	0.23	2.23	0.67	11.52
0.4-0.8	0.18	1.45	0.75	8.69
0.8-1.2	0.18	1.42	0.75	7.95
1.2-1.6	0.15	0.79	0.80	7.49
1.6-2.0	0.16	0.88	0.79	7.47
4.4-4.8	0.15	0.68	0.81	7.17

| Bulk water, 0.4 nm | 0.18 | 0.54 | 0.80 | 6.90 |
| Bulk water | 0.16 | 0.29 | 0.84 | 5.80 |

B. AOT

Bin (nm)	a0	a1(ps)	a2	a3(ps)
0.0-0.4	0.22	2.61	0.69	79.59
0.4-0.8	0.33	3.34	0.57	55.13
0.8-1.2	0.45	3.72	0.45	36.40
1.2-1.6	0.46	3.55	0.45	18.48
1.6-2.0	0.31	2.60	0.61	10.75
4.4-4.8	0.16	0.90	0.79	7.82
Bulk water , 0.4nm	0.18	0.54	0.80	6.90
Bulk water	0.16	0.29	0.84	5.80

C. POPC

Bin (nm)	a0	a1(ps)	a2	a3(ps)
0.0-0.4	0.10	1.45	0.83	157.87
0.4-0.8	0.16	2.50	0.77	102.52
0.8-1.2	0.32	3.42	0.59	51.18
1.2-1.6	0.42	3.49	0.49	21.42
1.6-2.0	0.20	1.60	0.73	9.38
4.4-4.8	0.14	0.56	0.82	7.61
Bulk water , 0.4nm	0.18	0.54	0.80	6.90
Bulk water	0.16	0.29	0.84	5.80

contains the slowest water molecules having a timescale of relaxation ~80 ps. While for the later on slabs these length-scale decreases and eventually attains the bulk value. In POPC surface, the relaxation times are slowest. Near the surface or for the water present in the surfactant phase the water reorientation is slowed down to a considerable extent. This effect is pronounced up to the fourth slab i.e. till 1.6 nm. After that it is gradually attaining the bulk behavior. The sharp drop in the initial slabs may be attributed to the local densities of the positive and negative charges present in zwitterionic surfactant. We have seen that water which is involved in hydrogen bonding with

ester and phosphate groups are arrested their orientational as well as translational motions. However, water that presents near to the tertiary ammonium group is not making any hydrogen bonds with it and more mobile comparatively. For these water relaxation time-scales are not decreased to a greater magnitude.

6.3.6 Length-scale of perturbation of water from re-orientational dynamics

Based on relaxation time-scale data from the re-orientational dynamics of water near the surface, we plotted the distance dependence of it along the bilayer normal. The normalization of the timescales is performed as the following,

$$C(\Delta z) = \frac{\tau(\Delta z) - \tau(\infty)}{\tau(0) - \tau(\infty)} \tag{6.3}$$

Where, $\tau(\Delta z)$ is slowest relaxation timescale at the length-scale (Δz) nm, $\tau(\infty)$ is the timescale of relaxation at the longer length when water attains its bulk-like behavior and $\tau(0)$ is the
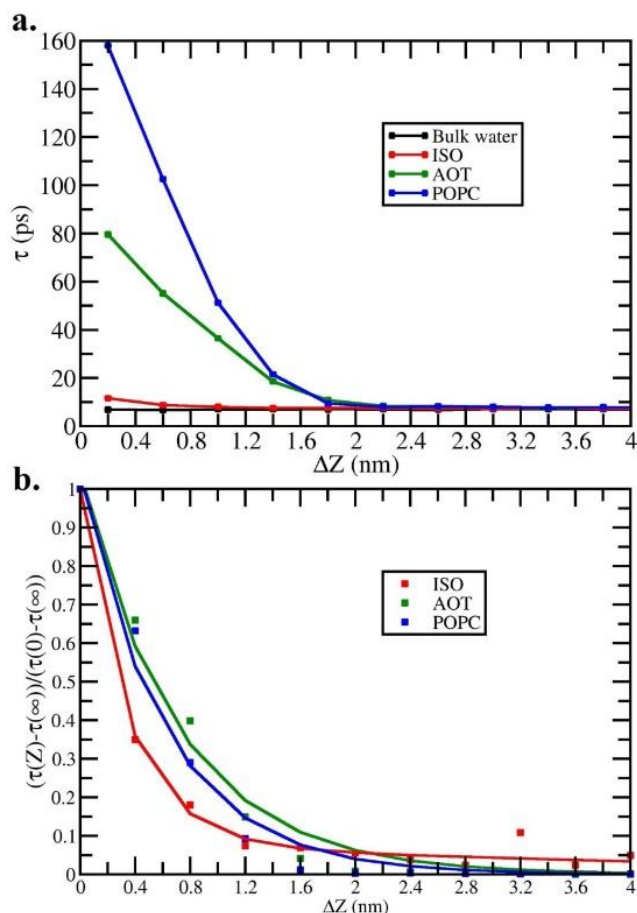

Figure 6.7: Slowest relaxation time along the bilayer normal for ISO, AOT, and POPC; a. unnormalized b. normalized. Data is obtained from the 20 ps OTCF (of planar slab definitions) data biexponential fitting.

slowest time scale near the surface (in the first slab 0.0-0.4 nm). Figure 6.7 (a) and (b) show the magnitude of the slowest timescale and normalized timescale. It shows that the magnitude differs but the length-scale of water perturbation is similar for both the charged/polar surfaces (AOT and POPC) which is ~2 nm from the surface from Figure 6.7(a). Later on time-scales overlap to the bulk values. In case of ISO this match is found at ~0.6 nm similar to length-scales obtained from Figure 6.3 (average structural properties along bilayer normal).

6.3.7 Layer-wise re-orientational dynamics of water based on the proximity to the surface

As mentioned earlier bilayer fluctuates and hence the surface atoms too, therefore we decided to analyze re-orientational dynamics using another definition and compare the differences between the definitions. The definition is based on the proximity of water to the surface atoms, where we select the water present towards the water phase only from the nearest surface atom. To compare time-scales properly we used the average Z ($<Z>$ along the bilayer normal) position of the surface atoms and calculated OTCF from this $<Z>$. The surface atoms are S and N in case of AOT and POPC, respectively. We did not calculate OTCF for the ISO bilayer to avoid computationally expensive and heavy calculations. Since it has a thick layer of carbon atoms, therefore, calculating average Z and proximal water from carbon is difficult and also this layer does not fluctuate and has less perturbed water. Moreover, to select the proximal distance, radial distribution function (RDF) is calculated from the selected surface atoms with water and taken the first minimum as first shell from the surface which is shown in Figure 6.8.

The results of OTCF are shown in Figure 6.9(a) and (b) for AOT and POPC for the 50 ps data length. In case of AOT, the decay from $<Z>$ and from the first slab 0.30-0.55 nm from surface atoms are almost similar. Both of them have a long-lived tail as observed earlier. While for the second slab $<Z>$ is decaying slower than the slab of 0.55-0.90 nm from the surface. A similar observation can be made from the third slab. Moreover, the $<Z>$ has slower decay comparatively than the proximal distance criterion definition. the same can be concluded from the timescales of relaxations are shown in Table 6.1. However, if these results are compared to earlier definition of Z_0 then these timescales are sooner relatively. The second slab of Z_0 is matching somewhat to the first slab in this case and so on. While in Figure 6.9(b) for the POPC, the $<Z>$ has in the first slab has very slow decay than that of 0.32-0.62 slab of proximal distance.
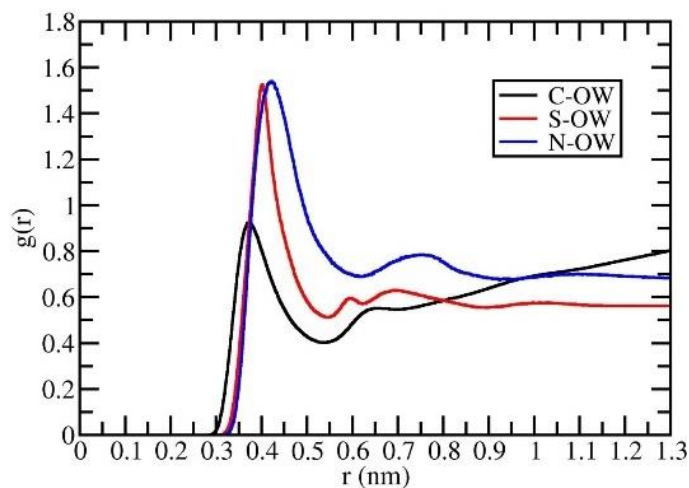
Figure 6.8: RDF between reference atom and OW of water. Reference atoms are C, S, and N for ISO, AOT and POPC bilayer systems, respectively.
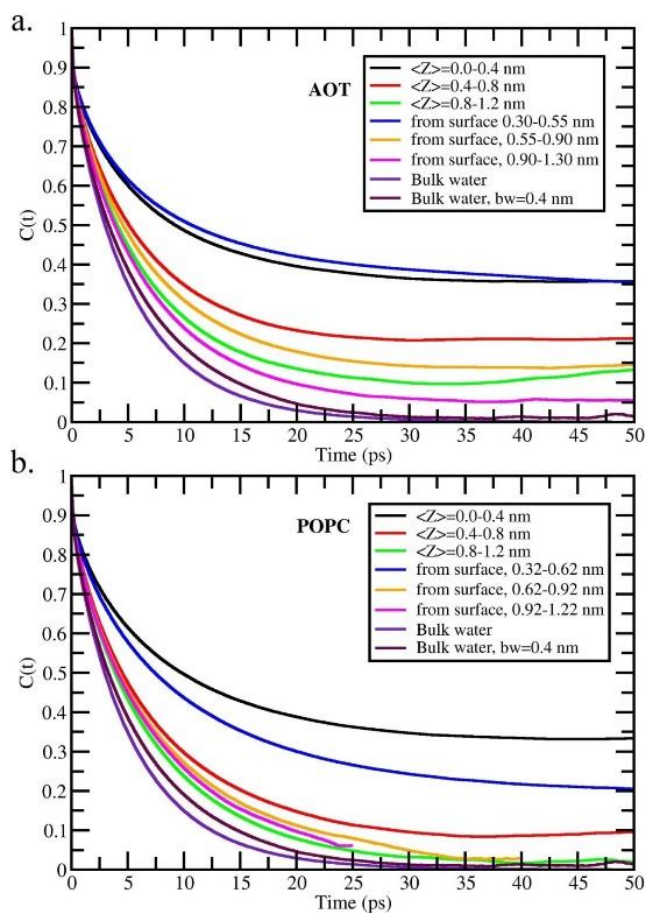
Figure 6.9: Comparison of OTCFs of water using two definitions; a. AOT and b. POPC. from the surface and from the average Z positions, of the reference surfactant atoms, S and N. Here, from

surface definition is where we considered water slab according to the definition that targeted OW of water should be present towards the water phase from its closest reference atom of surfactant. In this case we do not allow this water to be in bilayer phase since it could be trapped in surfactant phase. And, in the second definition of the average Z position, we defined it as the center of mass of the S or N atoms of one leaflet of bilayer.

Table 6.2: Comparison of definitions (fitting upto 20 ps length)

A. AOT

Bin (nm)	a0	a1(ps)	a2	a3(ps)
$<Z>$=0.0-0.4 nm	0.33	3.39	0.57	51.27
$<Z>$=0.4-0.8 nm	0.44	3.63	0.47	27.12
$<Z>$=0.8-1.2 nm	0.43	3.40	0.48	15.03
From S, 0.30-0.55 nm	0.31	3.13	0.60	53.09
From S, 0.55-0.90 nm	0.41	3.33	0.50	18.47
From S, 0.90-1.30 nm	0.26	2.25	0.66	9.96
Bulk water, 0.4 nm	0.18	0.54	0.80	6.90
Bulk water	0.16	0.29	0.84	5.80

B. POPC

Bin (nm)	a0	a1(ps)	a2	a3(ps)
$<Z>$=0.0-0.4 nm	0.30	3.23	0.62	41.05
$<Z>$=0.4-0.8 nm	0.30	2.61	0.61	13.58
$<Z>$=0.8-1.2 nm	0.16	1.00	0.78	8.47
From N, 0.32-0.62 nm	0.28	2.96	0.63	25.96
From N, 0.62-0.92 nm	0.21	1.59	0.72	10.38
From N, 0.92-1.22 nm	0.18	1.17	0.76	9.39
Bulk water, 0.4 nm	0.18	0.54	0.80	6.90
Bulk water	0.16	0.29	0.84	5.80

Afterward they in fact match quite well, the results of the time-scales of relaxation is shown in Table 6.2. Among these two bilayers, AOT shows slower relaxation than the POPC. The result for

the comparison of the three bilayer systems using the proximal distance criterion is shown in Figure 6.10 for the 100ps; from where the same observation can be made. The bi-exponential fitting data of relaxation timescales are listed in Table 6.3 only for the first shell. AOT and POPC show almost same results and are much slower than the bulk water. While in ISO it is comparable to bulk water. We also note that the fitting parameters of OTCFs are dependent on the data length up to which the decay function is fitted if the long-lived tail involved, the timescales of relaxations increase to a significant extent.
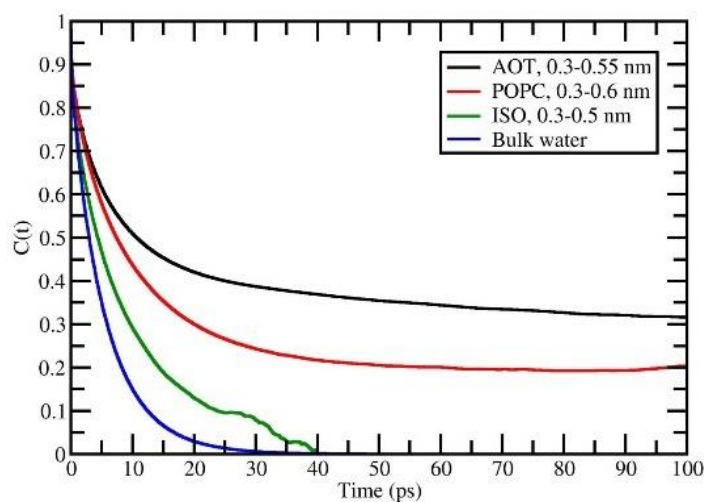
Figure 6.**10**: Comparison of OTCFs of surface water among three bilayer systems**.** Only the first hydration shell of surface atoms is considered during OTCF calculation**.** Further, it is calculated only for the water molecules which are continuously staying in the first hydration shell**.**

Table 6.**3**: OTCF from the surface, first shell

System	a0	a1(ps)	a2	a3(ps)
AOT (0.3-0.55nm)	0.43	280.29	0.45	6.35
POPC (0.32-0.62nm)	0.25	286.06	0.62	8.80
ISO (0.3-0.5nm)	0.68	12.03	0.23	1.84
Bulk water	0.84	5.8	0.16	0.29

6.3.8 Region-wise OTCF

Further, we also looked at the water in the different locations, one is towards the water phase and another one towards the surfactant phase or embedded in there. The third one will be combined first and second regions. Such a comparison between AOT and POPC bilayers are presented in
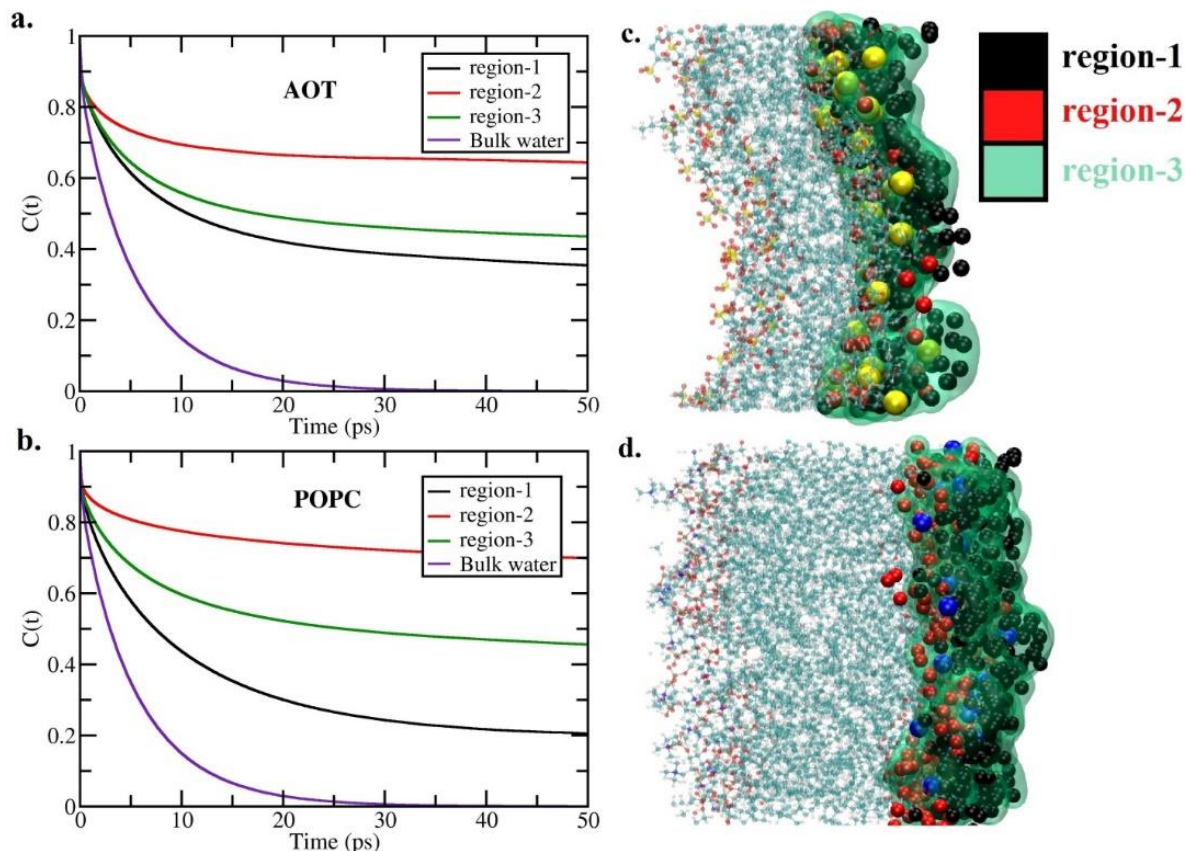
Figure 6.**11**: OTCF of the water molecules around the interface of a**.** AOT and b**.** POPC; surface water molecules for which $Z_{OW} > Z_S$ or Z_N are denoted by region 1**(**black**)** where, Z_{OW} is the Z coordinate of oxygen of water and Z_S or Z_N is the Z coordinate of closest S or N atoms of AOT or POPC to that water molecule, similarly trapped water molecules in surfactant layer for which $Z_{OW} < Z_S$ or Z_N is denoted as region 2 **(**red**)** and water molecules within 0**.**6 nm of S or N atoms are denoted as region 3 **(**green transparent surface**).** region 3 contains both the surface as well as trapped water molecules**.**

Table 6.**4**: Region**-**wise OTCF (fitting upto 20 ps length)

A. AOT

Region	a0	a1(ps)	a2	a3(ps)

region-1	0.31	3.13	0.60	53.09
region-2	0.17	1.82	0.74	173.53
region-3	0.28	2.89	0.63	73.32
Bulk water	0.16	0.29	0.84	5.78

B. POPC

Region	a0	a1(ps)	a2	a3(ps)
region-1	0.28	2.96	0.63	25.96
region-2	0.11	1.52	0.82	178.73
region-3	0.24	2.90	0.68	73.90
Bulk water	0.16	0.29	0.84	5.78

Figure 6.11(a) and (b), whereas Figure 6.11(c) and (d) show the locations of the water molecules, the color used is explained in the figure captions. The regions are defined from the Z position of water molecules (Z_{OW}) and surface atoms (Z_S and Z_N) where, S and N are selected as surface atoms. These OTCF calculations are not done for the ISO bilayer. The region 1 is defined as Z_{OW} is greater than Z_S and towards the water phase, while region 2 is where Z_s is greater than Z_{OW} and towards the surfactant phase. And, region 3 is the water within 0.6 nm of the selected

Figure 6.12: OTCF of S→O (of AOT) and P→N (of POPC) headgroup vectors relaxation
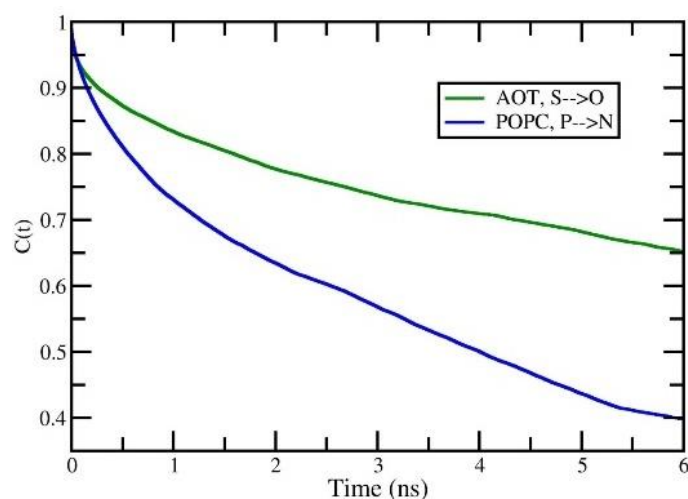
Table 6.5: OTCF of headgroup relaxation

Bilayer	a0	a1(ns)	a2	a3(ns)
AOT	0.12	0.98	0.82	27.28
POPC	0.16	0.38	0.81	8.18

surface atoms. For region 1 and region 2 the distance cutoff is 0.6 nm as well. Therefore, region 3 is combination of region1 and region 2 which includes surface as well as embedded water molecules. As can be seen in the Figure 6.11(a), region 2 has a very slowest decay among them although region 1 has fastest decay and region 3 has decay in between them. This implies that embedded water molecules are arrested dynamically as well as structurally. In Figure 6.11(b), the three regions are very clearly separated, region1 has very slow decay while region 2 has fastest decay and region 3 has in between them. Water is more restricted in region 2 structurally as well as dynamically compared to region 1. The timescales of relaxations are shown in Table 6.4(A) and (B) for AOT and POPC using bi-exponential fitting function. From both the tables it can be understood that region 2 has relaxation timescales of ~170-180 ps. In case of AOT region 1 has slowest water than POPC; however, region 3 is showing almost similar relaxation timescales. Since this slowing down can be due to the bilayer fluctuations, therefore head group vectors S→O and P→N relaxations are studied in case of AOT and POPC as shown in Figure 6.12. AOT has slower decay function than POPC and their timescales of relaxations are shown in Table 6.5. AOT head group has ~27 ns relaxation time-scale while POPC has ~8 ns. This is also because of the hydrogen bonding and electrostatic interaction between water and head group atoms. Thus, this is also a reason for the existence of slower water in case of AOT than POPC.

6.4 Conclusion

We have studied the structure and dynamics of interfacial water molecules near planar surfaces using molecular dynamics simulations. We systematically investigate perturbation length-scale of interfacial water next to three different charged surfaces such as zwitterionic (neutral polar); POPC lipid, anionic(polar); AOT surfactant and hydrophobic (nonpolar); Isooctane bilayers. We demonstrate that translational and local orientational order parameters are perturbed less than the global orientational ordering of interfacial water. This suggests that water perturbation length-scale is highly property dependent. The negative AOT surface perturbs water to highest length (~4.5

nm) than neutral polar POPC surface (~1.5 nm). The embedded water molecules in the head group region are mostly frustrated water molecules having lesser number of hydrogen bonds. They can be hydrogen-bonded to surface as well as to nearby water molecules. The dipolar orientation of water in AOT surface is towards the water phase. However, near the POPC surface the net direction of the dipole depends on the charge density of negative carbonate and phosphate moieties as well as positive choline group. Therefore, the global orientation order shows shorter length-scale near POPC bilayer. The diffusion of water molecules along normal is dissected in two components (i) 1D MSD along Z direction and (ii) 2D MSD across XY plane as function of distance from the bilayer. 1D MSD reaches plateau in shorter time than 2D MSD. Nevertheless, near both the polar surfaces, translational dynamics is slowed down compared to the bulk water as well as to hydrophobic surface. The structure and dynamics of interfacial water is perturbed least near hydrophobic surface. Finally, the re-orientational dynamics of water is investigated using different definitions since surface fluctuations result in an undulating bilayer surface. AOT surface fluctuates more than POPC surface. We observed the noticeable slowed down of embedded water molecules in the surface. This penetration of water in the head group areas of the bilayer results in the orientationally trapping of it. We also demonstrate that water dynamics is coupled to surface fluctuations.

6.5 References

(1)   Tanford, C. *Science* **1978**, *200* (4345), 1012–1018.

(2)   Róg, T.; Murzyn, K.; Pasenkiewicz-Gierula, M. *Chem. Phys. Lett.* **2002**, *352* (5–6), 323–327.

(3)   Zhang, Z.; Berkowitz, M. L. *J. Phys. Chem. B* **2009**, *113* (21), 7676–7680.

(4)   Dewan, S.; Carnevale, V.; Bankura, A.; Eftekhari-Bafrooei, A.; Fiorin, G.; Klein, M. L.; Borguet, E. **2014**, *30*, 8065.

(5)   Marry, V.; Rotenberg, B.; Turq, P. *Phys. Chem. Chem. Phys.* **2008**, *10* (32), 4802.

(6)   Cyran, J. D.; Backus, E. H. G.; Nagata, Y.; Bonn, M. **2018**.

(7)   Murzyn, K.; Zhao, W.; Karttunen, M.; Kurdziel, M.; Róg, T. *Biointerphases* **2006**, *1* (3), 98–105.

(8)   Zhao, W.; Moilanen, D. E.; Fenn, E. E.; Fayer, M. D. *J. Am. Chem. Soc.* **2008**, *130* (42), 13927–13937.

(9)   Harris, R. C.; Pettitt, B. M.; Debenedetti, P. G. *Proc. Natl. Acad. Sci. U. S. A* **2014**, *111*

(41), 14681–14686.

(10)   Moilanen, D. E.; Fenn, E. E.; Wong, D.; Fayer, M. D. *J. Phys. Chem. B* **2009**, *113* (25), 8560–8568.

(11)   Hande, V. R.; Chakrabarty, S. *Phys. Chem. Chem. Phys.* **2016**, *18* (31), 21767–21779.

(12)   Hess, B.; Kutzner, C.; Van Der Spoel, D.; Lindahl, E. *J. Chem. Theory Comput.* **2008**, *4* (3), 435–447.

(13)   Klauda, J. B.; Venable, R. M.; Freites, J. A.; O'Connor, J. W.; Tobias, D. J.; Mondragon-Ramirez, C.; Vorobyov, I.; MacKerell, A. D.; Pastor, R. W. *J. Phys. Chem. B* **2010**, *114* (23), 7830–7843.

(14)   Abascal, J. L.; Vega, C. *J. Chem. Phys.* **2005**, *234505* (23), 0–12.

(15)   Bussi, G.; Donadio, D.; Parrinello, M. *J. Chem. Phys.* **2007**, *126* (1), 014101.

(16)   Berendsen, H. J. C.; Postma, J. P. M.; Van Gunsteren, W. F.; Dinola, A.; Haak, J. R. *J. Chem. Phys.* **1984**, *81* (8), 3684–3690.

(17)   Parrinello, M.; Rahman, A. *J. Appl. Phys.* **1981**, *52* (12), 7182–7190.

(18)   Essmann, U.; Perera, L.; Berkowitz, M. L.; Darden, T.; Lee, H.; Pedersen, L. G. *J. Chem. Phys.* **1995**, *103* (19), 8577–8593.

(19)   Hess, B.; Bekker, H.; Berendsen, H. J. C.; Fraaije, J. G. E. M. *J. Comput. Chem.* **1997**, *18* (12), 1463–1472.

(20)   Srivastava, A.; Debnath, A. *J. Chem. Phys.* **2018**, *148* (9), 094901.

(21)   Hande, V. R.; Chakrabarty, S. *J. Phys. Chem. B* **2015**, *119* (34), 11346–11357.

Chapter 7: Structure and Conformational Dynamics of N-Terminal Domain of CXCR1 in Confinement of AOT Reverse Micelle: Effect of the Size of Water Nanopool

7.1 Introduction

Confinement and crowded cellular environment significantly affect the protein structure and dynamics.[1] Therefore, understanding of the protein folding in such cellular environment requires understanding the protein organization and dynamics under confinement.[2] The reverse micelles are commonly used model for such confinement studies.[3] CTAB and LDAO are known to stabilize the protein in reverse micelle.[4,5] AOT is known for the alteration in structure of most of the proteins.[2,6,7] Local chemistry of the headgroup of surfactants is important for the protein stability in the RM confinement.[2]

The N-terminal domain of CXC chemokine receptors 1 (CXCR1) becomes more ordered when present near membranes. Recent experimental study by Chattopadhyay and coworkers[8] has revealed that the β sheet structure is adopted by the CXCR1 N-terminal domain and is critically dependent on hydration size in reverse micelle. The tryptophan residues experience motional restriction inside AOT reverse micelle as well as near DOPC bilayer.[8,9] Previous MD simulation study has investigated the dynamics of the CXCR1 N-terminal domain in the presence of POPC membrane bilayers and report significant β-sheet formation near bilayers.[10] They used the sequence: MEVNVWNMTDLWTWFEDEFANATGMPPVEKDYSP for the N-terminal domain CXCR1.[10] Whereas the scrambled sequence of this peptide does not show any secondary structure formation. Therefore, this suggests the role of sequence-dependent electrostatic interactions modulated by the membrane.[10]

In this chapter, using atomistic MD simulations we have studied the structure and dynamics of the N-terminal domain of CXCR1 in the AOT reverse micelle confinement. For the purpose of comparison, we have simulated peptide near the planar AOT/water monolayer/interface. We aim to decipher the role of confinement/hydration size on the structure and conformational dynamics of peptide. In this view, we provide insights into the surface seeking tendency of the peptide, which may help in understanding the ligand binding specificity as well as affinity of this peptide.

7.2 System setup and computational details

The sequence of the rabbit CXCR1 N-terminal 34-mer peptide is taken from the experimental work of Chattopadhyay and coworkers as follows: LWTWFEDEFANATGMPPVEKDYSPSLVVTQTLNK.[9] An extended 3D conformation of the peptide is built using Avogadro software.[11] The peptide is first simulated in a bulk water by addition of three sodium ions to neutralize the net charge of protein. A representative compact structure with low Rg (0.95 nm) is then selected to prepare RM systems by placing the peptide in the middle of the water nanopool. A sphere of water around center of mass (COM) of peptide containing approximately the same number of water molecules as given in Table 7.2 is cut according to the given size of water nanopool of reverse micelle (RM) (as given in Table 7.1). Four different sizes of the reverse micelle (RM) systems are prepared corresponding to the molar ratio [H2O]/[AOT] = w_0 = 5, 10, 15 and 20 in the increasing order of size. The net charge on AOT molecules in RM systems is neutralized by adding the same number of Na^+ counter-ions and the sodium ions have been placed at the distance near to the AOT head groups as mentioned in Table 7.1. The number of AOT and water molecules, and the packing radii for the different water loading of RM systems have been taken from existing NMR data,[12] which has been subsequently used in other simulation studies as well.[3,13] The initial structures for the RM systems have been generated by means of the Packmol[14] software. The selected packing radii of the water nanopool, sodium ions and the outer sphere of the AOT monolayer have been provided in Table 5.1. CHARMM36[15] all-atom force-field is used to model AOT surfactant and isooctane molecules following the protocol used by Abel et al.[3] We have used TIP3P[16] water model which is generally used with the CHARMM force field. On other hand, the peptide is placed at the AOT/water planar interface to simulate the extreme case of lowest curvature. To make a stable planar monolayer of AOT, an isooctane interface is attached towards the hydrophobic phase of AOT monolayer. This system is referred as "AOT/water interface". The initial prepared structures for the simulations is shown in Figure 7.1 (left panel).

We have used the GROMACS (version 5.0.7) software[17] to perform all the MD simulations presented here. Periodic boundary conditions have been applied in all directions. All bonds have been constrained to their equilibrium bond lengths. Distance between the AOT

RM surface and the simulation box edge is kept at least 1 nm to avoid interactions between the periodic images. We have used a cutoff of 1.0 nm for both short- range coulomb and van der Waals interactions. The long-range electrostatic interactions have been treated using PME method with a grid spacing of 0.16 nm.[18] Energy minimization of all the systems have been performed by using the steepest-descent algorithm to remove any clashes between the molecules. Subsequently, NVT equilibration has been done for 2 ns at 300 K temperature using the V-rescale thermostat[19] followed by NPT equilibration of 20 ns at 1 bar pressure using the Berendsen barostat[20]. During production runs, Parrinello– Rahman barostat[21] is used with a integration time step of 2 fs, and the trajectory is saved at every 10 ps and 1 ps for structural and dynamical analysis of peptide, respectively. The total production run length is 500 ns.

Table 7.1: The initial packing radii **(**in nm**)** supplied to the Packmol software for preparation of the initial structures of the RM systems**.** The radii of the outermost layer for packing the following species are shown in the increasing order**:** water, Na^+ ions, sulfur **(S)** atoms of the AOT head groups, and C_9 atoms **(**terminal carbon atoms of the AOT monomer**).**

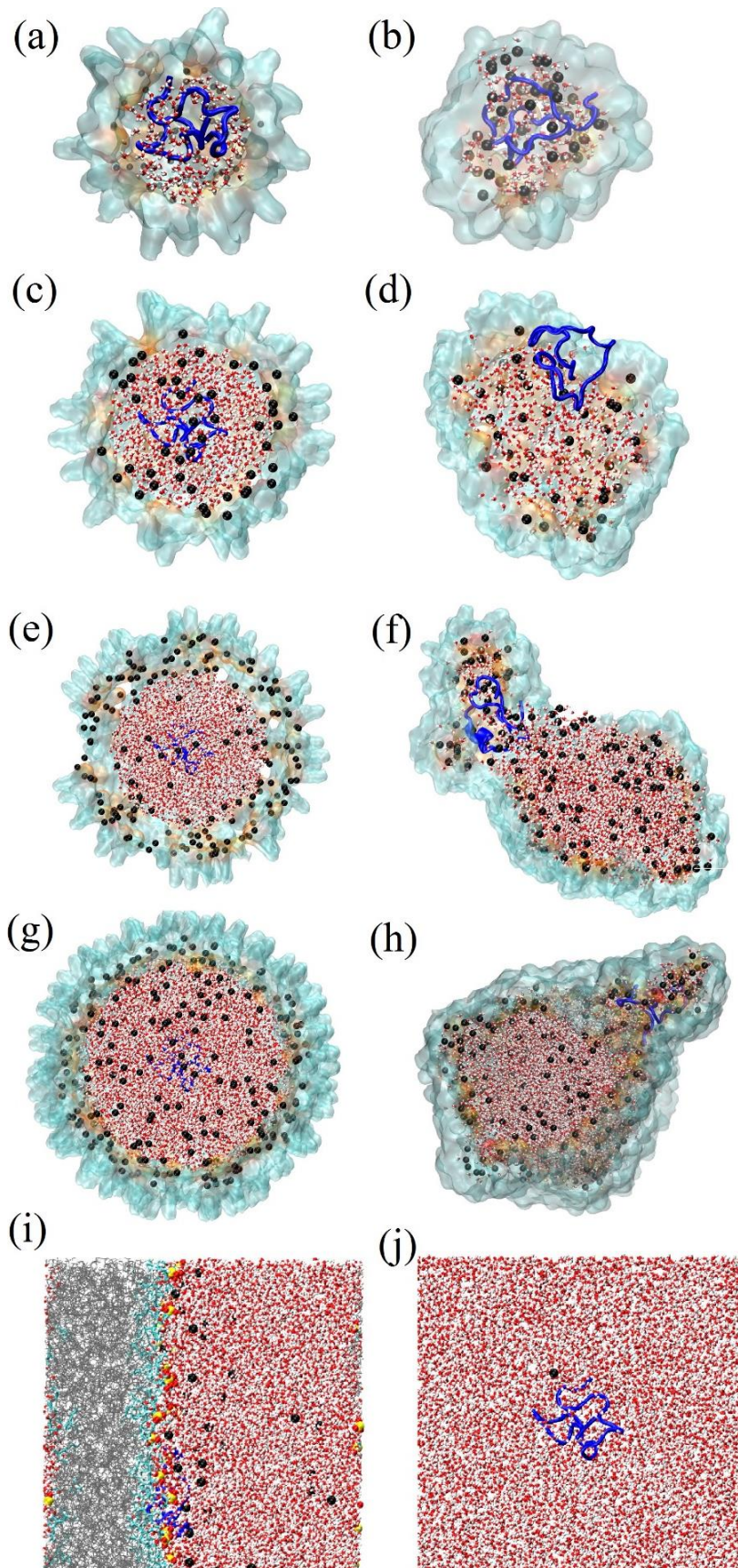| System/Residue	Water (in nm)	Na^+ (in nm)	S (in nm)	C9 (in nm)
RM $w_0 = 20$	3.70	3.75	3.90	5.00
RM $w_0 = 15$	3.00	3.05	3.20	4.30
RM $w_0 = 10$	2.10	2.15	2.30	3.40
RM $w_0 = 5$	1.25	1.30	1.45	2.55

Figure 7.1: Snapshots of the initial **(**Left panel; a, c, e, g**)** and equilibrated structures **(**right panel; b, d, f, h**)** of N-domain CXCR1 peptide in the RM systems; **(**a and b**)** RM w_0=5, **(**c and d**)** RM w_0=10, **(**e and f**)** RM w_0=15, **(**g and h**)** RM w_0=20. Equilibrated structure of N-domain CXCR1 peptide in **(**i**)** AOT/water interface **(**j**)** bulk water. The color scheme used is as following; blue**:** peptide, cyan**:** AOT hydrophobic part **(**transparent surface and licorice presentation **(**in **(**i**)))**, black**:**Na$^+$ ions, red**:**oxygen, white**:** hydrogen, yellow**:**sulfur.

Table 7.2: The number of different species used to simulate the RM systems. nH$_2$O, nAOT, nNa$^+$ and nISO are the number of water, AOT, Na$^+$ counter-ion and isooctane molecules used to build the initial configurations of RMs.

System	nH$_2$O	nAOT	nNa$^+$	nISO
Bulk water	15448	—	—	—
RM w_0 = 20	6027	302	302	3888
RM w_0 = 15	2827	189	189	3006
RM w_0 = 10	971	98	98	2001
RM w_0 = 5	200	42	42	1000

7.3 Results and discussion

We have carried out atomistic molecular dynamics simulations to investigate the structural and dynamical aspects of the N-terminal domain of CXCR1. The truncated N-terminal region of the CXCR1 have been prepared in an extended conformation and simulated in bulk water to obtain lowest Rg structure. This structure is simulated in the confinement of pre-formed AOT reverse micelle (RM) as well as near the AOT/water planar interface. The initial prepared systems of RM are shown in the left panel of Figure 7.1, while the equilibrated structures are shown in the right panel of Figure 7.1. Bottom figures shows the equilibrated structures of CXCR1 near planar interface and bulk water. As seen in Chapter 5, RM fluctuates substantially resulting in the distortion from the spherical shape as evident from the right panel of RMs of the Figure 7.1.

7.3.1 Secondary structure analysis

Experimental study of Chattopadhyay and coworkers[8] observed a membrane induced β sheet formation in the AOT RM confinement and is critically dependent on the hydration size. The analysis of secondary structural elements per residue from the 500 ns MD simulation is shown in Figure 7.2. We do not observe the significant formation of β sheet in any system. There is only an intermittent β sheet formation in RM w_0=10, whereas a stable α helix formation is observed in RM w_0=15. Signatures of β bridge formation can be observed in the RM w_0=10, AOT/water interface and bulk water. Whereas the formation of 3_{10} helices is also seen in some of the systems. Several β turns and bends are observed predominantly. The representative most populated clusters structures are shown in Figure 7.3.

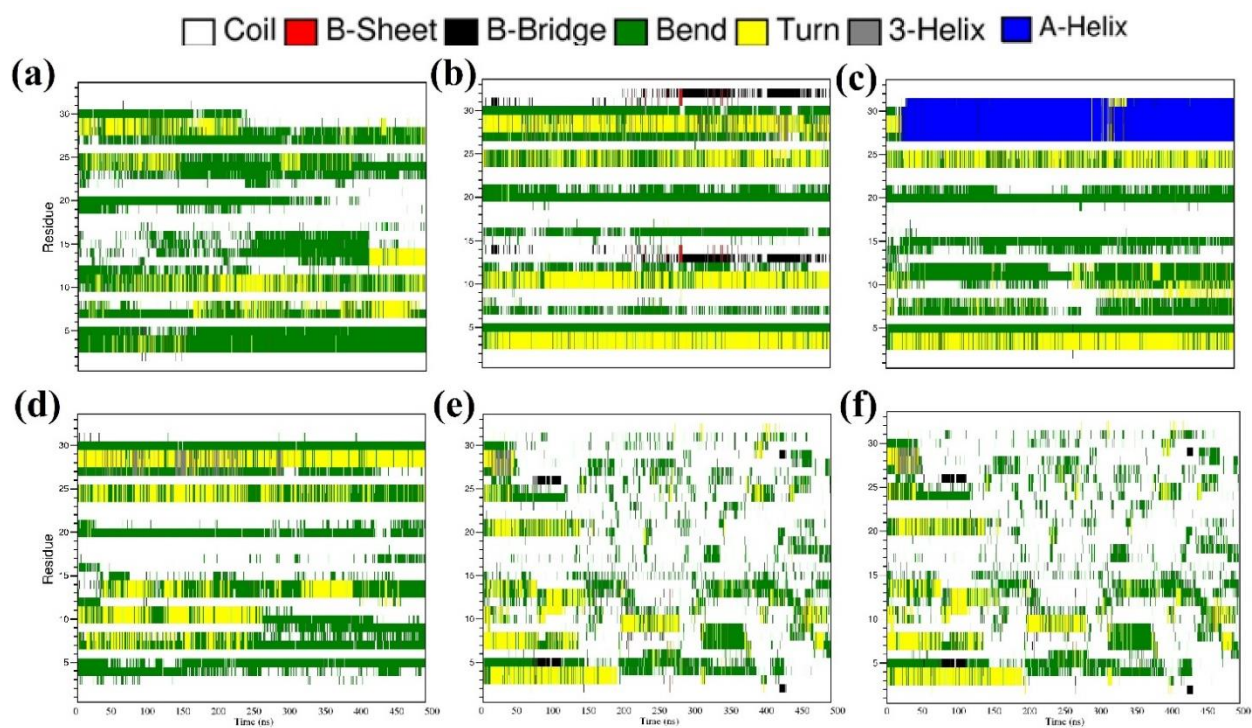
Figure 7.2: Secondary structural elements per residue of the N-terminal domain of CXCR1 peptide in confinement of RMs with **(a)** w_0=5 **(b)** w_0=10 **(c)** w_0=15, **(d)** w_0=20, **(e)** AOT/water **(planar)** interface and **(f)** bulk water**.** Secondary structures have been calculated as per the DSSP nomenclature**.** The color scheme is shown on the top of the figure**.**
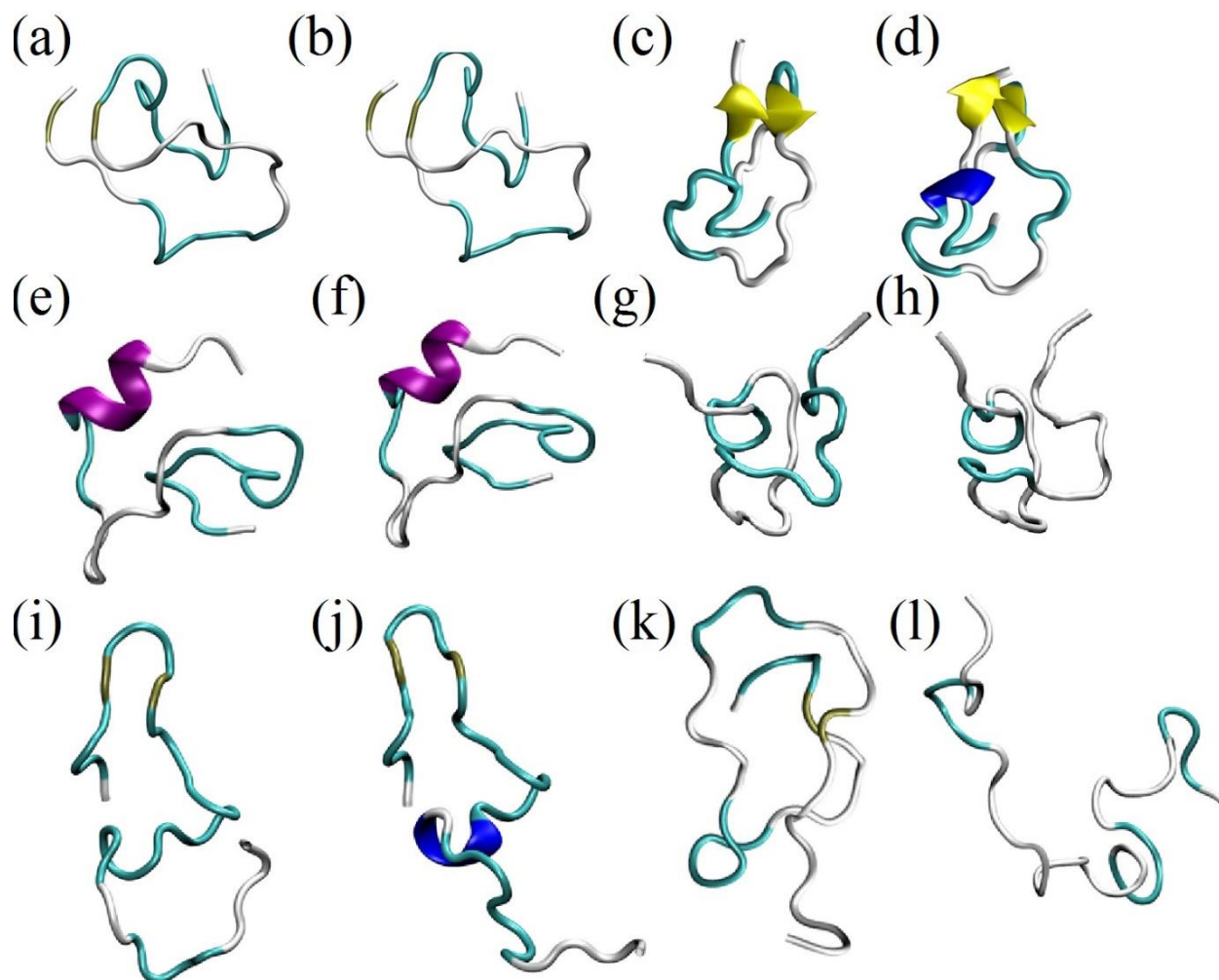
Figure 7.3: Representative most populated cluster structures of CXCR1 N-terminal peptide from **(**a and b**)** RM w_0=5 **(**c and d**)** RM w_0=10 **(**e and f**)** RM w_0=15 **(**g and h**)** RM w_0=20 **(**i and j**)** AOT/water **(**planar**)** interface and **(**k and l**)** bulk water**.**

7.3.2 Compactness of N-terminal domain of CXCR1 structure

To examine structural aspects of N-domain CXCR1 in the confinement, we have done RMSD and radius of gyration (Rg) investigation in confinement as shown in Figure 7.4. It has been observed that Rg as well as RMSD changes with increasing hydration size of RM confinement. However, CXCR1 in bulk water explores the wide range of Rg and RMSD. At AOT/water planar interface, a limited and more compact structure of CXCR1 is formed. A motional restriction has been noted in RM confinement. Although no specific trend has been detected in RMs as a function of size due to insufficient statistical sampling within the simulation time.
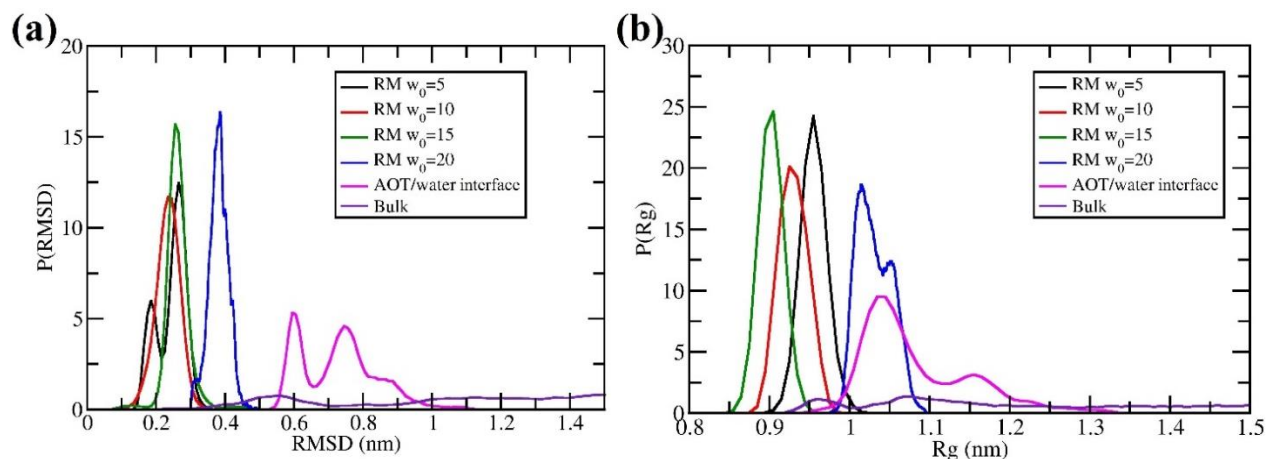
Figure 7.4: Distribution of **(**a**)** RMSD of the backbone and **(**b**)** Rg of CXCR1 N-terminal peptide

7.3.3 Interaction of N-terminal domain of CXCR1 with AOT and water in confinement

It would be interesting to know whether in confinement CXCR1 has more affinity towards water or AOT, i.e. whether the peptide remains in the water phase or binds to the interface. Therefore, the distribution of number of water and AOT around N-terminal domain of CXCR1 are plotted in Figure 7.5 (a and b). In the starting of simulation, CXCR1 is only surrounded by the water molecules, however, over the time, CXCR1 moves towards to the AOT/water surface of RM. Although, number of water molecules are higher than AOT around peptide; a clear surface seeking tendency of peptide is evident from these profiles. Moreover, the number of water molecules around peptide increases with the increase in size of water nanopool. On the other hand, the number of AOT molecules decreases around the peptide as the confinement size increases. Further, we have investigated the hydrogen bonding interaction between the N-terminal domain of CXCR1 and water/AOT using the criteria given in section 2.6.1.3. Distribution among them is depicted in Figure 7.5 (c and d). The number of hydrogen bonds between peptide and water increases with an increase in the hydration size of the RM, while the trend is reverse in case of peptide and AOT.
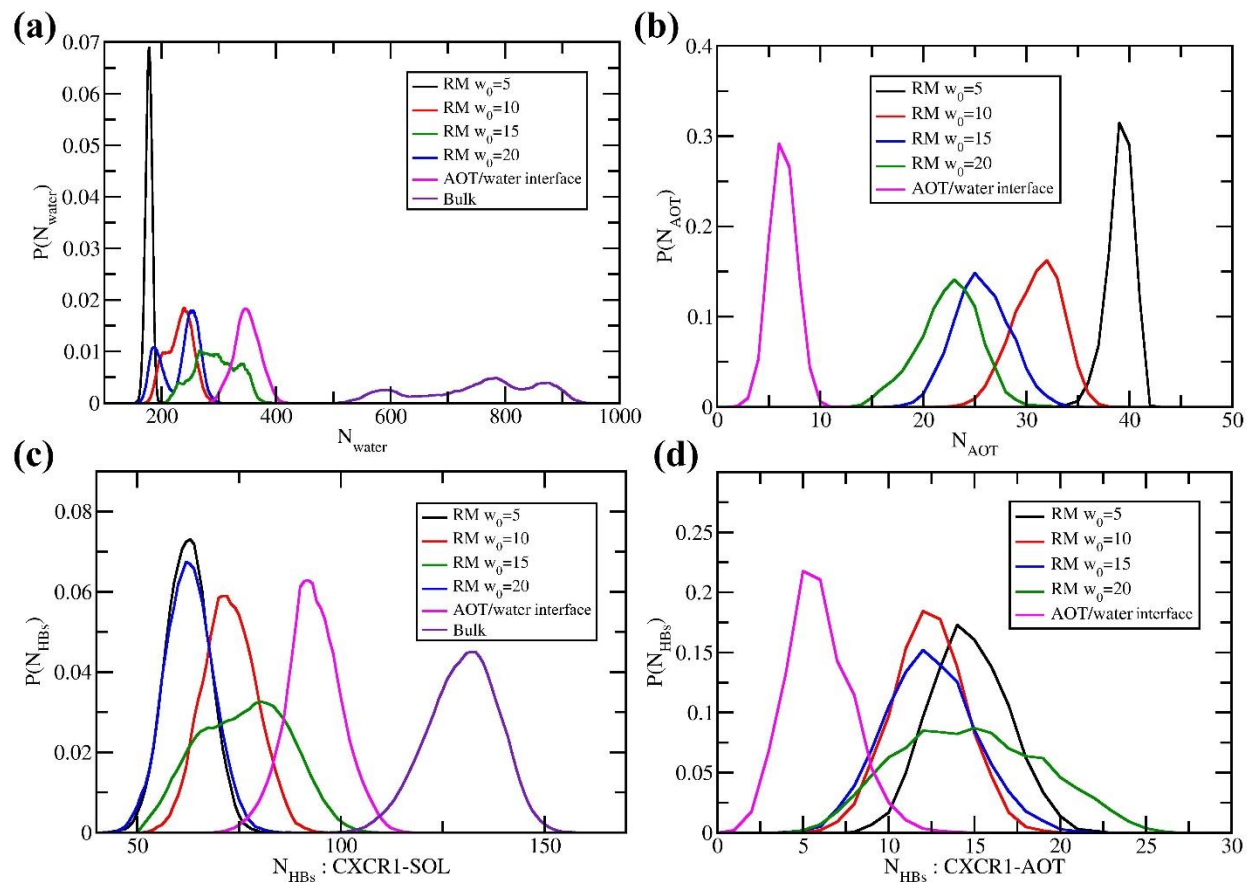
Figure 7.5: Distribution of **(a)** N_{water} and **(b)** N_{AOT} around N-terminal domain of CXCR1 peptide; number of hydrogen bonds **(**N_{HB}**)** between N-terminal domain of CXCR1 and **(c)** water **(d)** AOT headgroup**.**

Since, a residue-wise analysis is also important to identify the key residues interacting with water and AOT. The profiles of number of water and AOT interacting with peptide as well as hydrogen bonding among them is shown in Figure 7.6 (a to d). It has been reported experimentally that tryptophan residue has motional restriction.[8] Our analysis of water around peptide (Figure 7.6 (a)) reveals that number of water are almost constant around this residue which is at second and fourth position in the sequence of 34mer N-terminal domain of CXCR1. However, no clear trend among residues can be established from the profiles of number of water and AOT (Figure 7.6 (a and b)). Interestingly, it can be noted here from Figure 7.6 (b) that, number of AOT around residues of CXCR1 is lowest near AOT/water planar interface. From the hydrogen bonding profiles (Figure 7.6 (c and d)) also, no clear trend can be recognized.
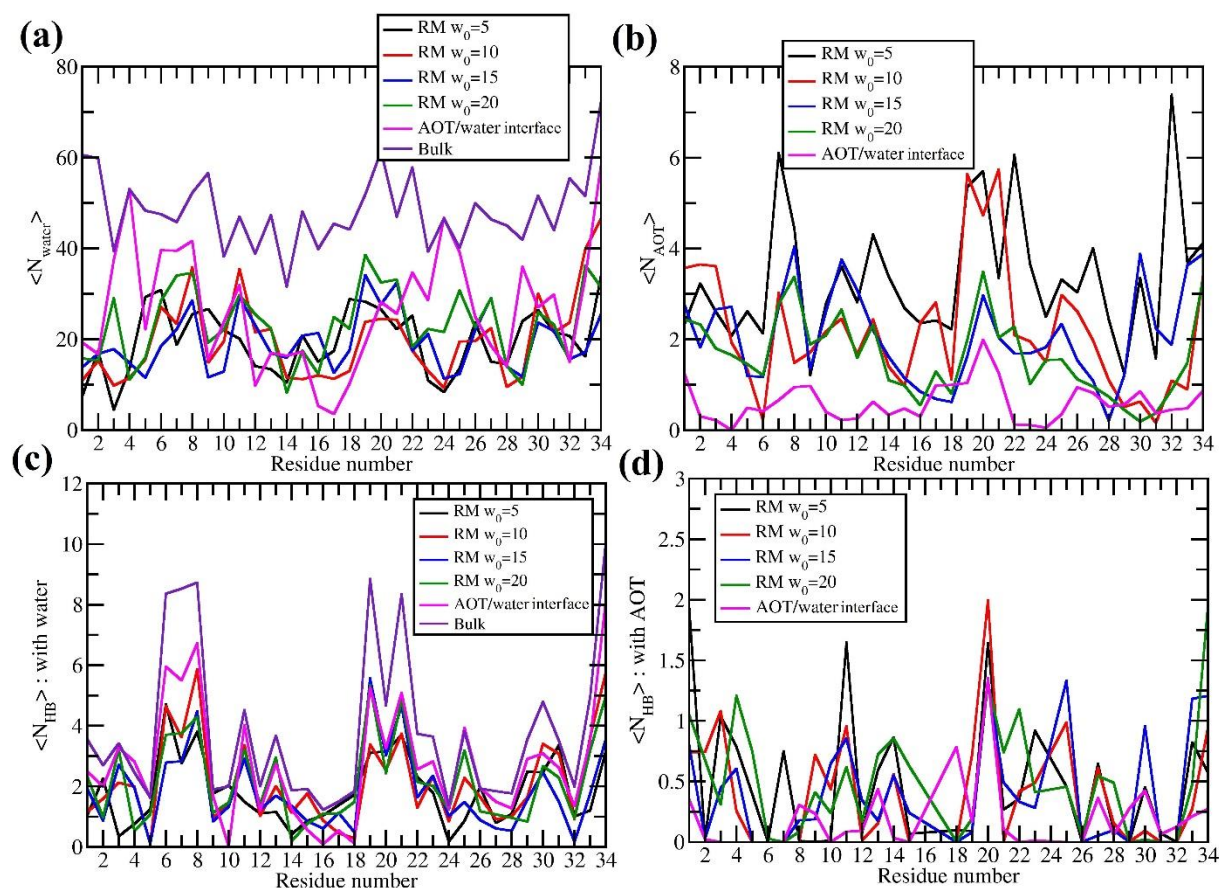
Figure 7.6: Residue-wise distribution of **(a)** N_{water} and **(b)** N_{AOT} around N-terminal domain of CXCR1 peptide; number of hydrogen bonds **(N_{HB})** between N-terminal domain of CXCR1 residues and **(c)** water and **(d)** and AOT headgroup**.**

7.3.4 Distance Distribution: Location of CXCR1 in RM

It has been understood from the above analysis that N-terminal domain of CXCR1 moves towards the AOT. Therefore, it would be worthy to identify the location of the peptide in the RM confinement. Figure 7.7 displays the distance distribution between center of mass (COM) of peptide and COM of whole RM as well as between COM of the whole RM and sulfur (S) atom of the headgroup. This indicate the confinement boundary of water as well size of confinement. Clearly, in all the sizes of RMs, CXCR1 resides at the boundary interacting well with AOT headgroup as seen in above section as well. As expected, an increase in the wider distribution of COM of CXCR1 w.r.t. COM of RM shows that as the hydration size increase peptide explores

more space in the confinement. However, in case of RM w_0=5, being smallest size of confinement; peptide would occupy almost all the confinement space, therefore location of peptide appears near the COM of RM. Also, the deviation from the spherical shape of RM can also be noted from the broader distance distribution of COM of RM w.r.t. S. Shape fluctuation of RM increases with increase in the confinement size.
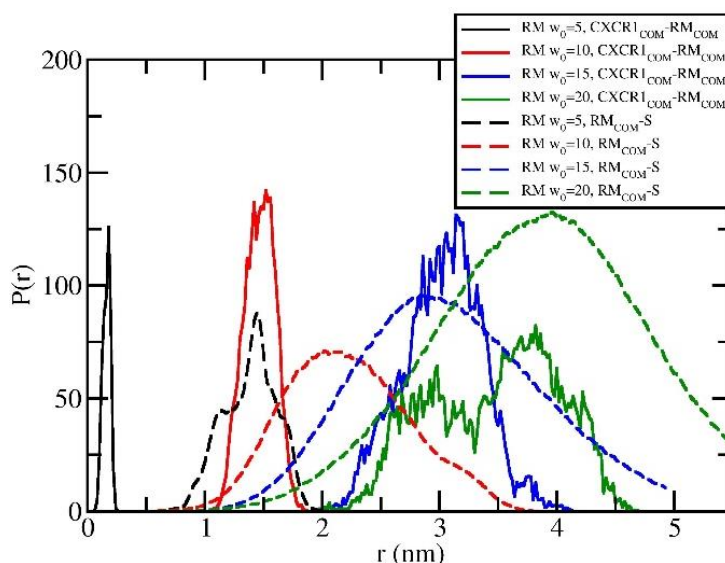
Figure 7.7: Distance distribution to identify the location of the N-terminal of CXCR1 in the RM region. CXCR1$_{COM}$-RM$_{COM}$ indicates the position of COM of peptide w.r.t. COM of whole RM, signifies how far CXCR1 have been travelled from the initial (middle of the RM) position of it. RM$_{COM}$-S indicates the confinement boundary of the water in RM and confinement size of RM.

7.3.5 Translational dynamics of COM of CXCR1 after removal of COM motion of whole RM

We also explore the translational dynamical behavior of the peptide using the MSD (Eq. 2.33). The translational dynamics of COM of CXCR1 after subtracting COM motion of the whole RM is shown in Figure 7.8. Since, in RM w_0=5, the space for the movement of peptide is almost negligible, this is well reflected in the MSD of COM of CXCR1, which is almost zero. Otherwise, MSD increases monotonically with hydration size for all other system. As expected, MSD is maximum for Bulk water. For the AOT/water planar interface, we have plotted the 1D and 2D MSDs along Z and XY direction separately. 1D MSD is perpendicular to the interface while 2D is

parallel to the interface. 1D MSD is slower than 2D MSD of peptide. 1D MSD appears to be sub-diffusive in motion than 2D MSD.
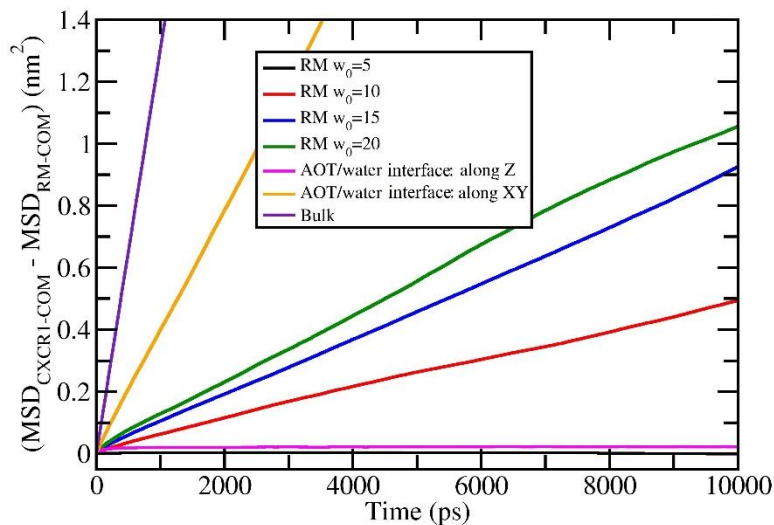
Figure 7.8: MSD of COM of N-terminal domain of CXCR1 peptide after removal COM motion of whole RM.

7.4 Conclusion

In this chapter, we have investigated the structure and conformational dynamics of the N-terminal domain of CXCR1 peptide in AOT reverse micelle confinement, sizes ranging from w_0=5, 10, 15 and 20. In addition, peptide is also simulated near the extreme case of lower curvature of planar AOT/water interface. We report no significant probability of formation of secondary structure with increasing the hydration size. CXCR1 adopts more compact structure near interfaces and demonstrates marked surface seeking tendency, i.e. preferentially binds to the AOT surface. N_{water} and hydrogen bonds between peptide and water increases proportionally with the hydration size as expected. On other hand, N_{AOT} around the peptide and hydrogen bonds between peptide and AOT decreases with increase in hydration size. Finally, we report the MSD of COM of CXCR1 after removal of COM motion of whole RM. It increases with increase in hydration size of confinement. The motion is almost entirely suppressed for the smallest RM with $w_0 = 5$.

7.5 References

(1)   Zhou, H. X. *Archives of Biochemistry and Biophysics*. January 1, 2008, pp 76–82.

(2)   Senske, M.; Xu, Y.; Bäumer, A.; Schäfer, S.; Wirtz, H.; Savolainen, J.; Weingärtner, H.; Havenith, M. *Phys. Chem. Chem. Phys.* **2018**, *20* (13), 8515–8522.

(3)   Abel, S.; Sterpone, F.; Bandyopadhyay, S.; Marchi, M. *J. Phys. Chem. B* **2004**, *108* (50), 19458–19466.

(4)   Senske, M.; Smith, A. E.; Pielak, G. J. *Angew. Chemie* **2016**, *128* (11), 3650–3653.

(5)   Tauber, M. J.; Mathies, R. A. *J. Am. Chem. Soc.* **2003**, *125* (5), 1394–1402.

(6)   Peterson, R. W.; Pometun, M. S.; Shi, Z.; Wand, A. J. *Protein Sci.* **2005**, *14* (11), 2919–2921.

(7)   Nucci, N. V.; Valentine, K. G.; Wand, A. J. *J. Magn. Reson.* **2014**, *241* (1), 137–147.

(8)   Chaudhuri, A.; Basu, P.; Haldar, S.; Kombrabail, M.; Krishnamoorthy, G.; Rajarathnam, K.; Chattopadhyay, A. *J. Phys. Chem. B* **2013**, *117* (5), 1225–1233.

(9)   Haldar, S.; Raghuraman, H.; Namani, T.; Rajarathnam, K.; Chattopadhyay, A. *Biochim. Biophys. Acta - Biomembr.* **2010**, *1798* (6), 1056–1061.

(10)   Kharche, S.; Joshi, M.; Sengupta, D.; Chattopadhyay, A. *Chem. Phys. Lipids* **2018**, *210*, 142–148.

(11)   Hanwell, M. D.; Curtis, D. E.; Lonie, D. C.; Vandermeerschd, T.; Zurek, E.; Hutchison, G. R. *J. Cheminform.* **2012**, *4* (8), 17.

(12)   Maitra, A. *J. Phys. Chem.* **1984**, *88* (21), 5122–5125.

(13)   Abel, S.; Waks, M.; Marchi, M. *Eur. Phys. J. E* **2010**, *32* (4), 399–409.

(14)   Martínez, L.; Andrade, R.; Birgin, E. G.; Martínez, J. M. *J. Comput. Chem.* **2009**, *30* (13), 2157–2164.

(15)   Huang, J.; Mackerell, A. D. *J. Comput. Chem.* **2013**, *34* (25), 2135–2145.

(16)   Mark, P.; Nilsson, L. *J. Phys. Chem. A* **2001**, *105* (43), 9954–9960.

(17)   Hess, B.; Kutzner, C.; Van Der Spoel, D.; Lindahl, E. *J. Chem. Theory Comput.* **2008**, *4*

(3), 435–447.

(18) Essmann, U.; Perera, L.; Berkowitz, M. L.; Darden, T.; Lee, H.; Pedersen, L. G. *J. Chem. Phys.* **1995**, *103* (19), 8577–8593.

(19) Bussi, G.; Donadio, D.; Parrinello, M. *J. Chem. Phys.* **2007**, *126* (1), 014101.

(20) Berendsen, H. J. C.; Postma, J. P. M.; Van Gunsteren, W. F.; Dinola, A.; Haak, J. R. *J. Chem. Phys.* **1984**, *81* (8), 3684–3690.

(21) Parrinello, M.; Rahman, A. *J. Appl. Phys.* **1981**, *52* (12), 7182–7190.

Chapter 8: Morphology and Dynamics of Self-Assembled Structures in Mixed Surfactant Systems (SDS+CAPB) in the Context of Methane Absorption

8.1 Introduction

Self-assembly of surfactant molecules is known to exhibit morphological diversity on the microscopic scale. They tend to aggregate in aqueous medium to form numerous kinds of structures with different shapes and orientations such as spherical, cylindrical micelles, bilayers, and many other multilayer structures.[1] Their self-assembly can also be tuned by other factors like temperature, mixing salts, other co-surfactants etc.[2] A zwitterionic co-surfactant such as Cocamidopropylbetaine (CAPB; {[3-(Dodecanoylamino)propyl](dimethyl)ammonio}acetate, $C_{19}H_{38}N_2O_3$) helps to increase the size and induce efficient packing of micelles formed by other surfactants like SDS (Sodium dodecyl sulfate, $NaC_{12}H_{25}SO_4$).[3] CAPB consists of a quaternary ammonium cation as polar head group and a long hydrophobic tail. The mixed-surfactant micelles are formed by the electrostatic attraction (and favorable solvation) between the hydrophilic part of the cationic fragment of the zwitterionic surfactant and the anionic fragment of the dodecyl sulfate ion of SDS surfactant.[3,4]

Kinetics of hydrate growth is typically measured by gas uptake rate, presence of SDS in aqueous phase has shown to promote gas hydrate growth.[5] It has been reported that SDS provides early nucleation which results in a reduction in its induction time.[2,6–9] Further, it has been shown that in presence of surfactants methane solubility in aqueous phase is higher. Thus, the questions arise (i) why does the gas uptake increase during gas hydrate formation in the presence of SDS? (ii) does SDS form micelle at typical gas hydrate forming conditions (275K and 50 bar) and (iii) is it possible to induce micelle formation by doping a co-surfactant which in turn may promote hydrate nucleation by providing a nucleating site to growing crystals.[2,10,11] Some earlier experimental studies have shown that SDS micelle formation does not occur under hydrate forming conditions.[2,10,11] Whereas some other studies have reported contradictory results regarding formation of micelles.[12,13] However, the formation of SDS micelle at low SDS concentration and at such a low temperature would be counter-intuitive, since it is known that micelle formation occurs only at and above the critical micelle concentration (CMC) and Krafft temperature.

Presence of long tail co-surfactants is known to decrease CMC and Krafft temperature of mixed surfactant systems.[14] In this regard, Prajapati et al[15,16] have measured CMC and Krafft temperature of the mixed surfactant (SDS+CAPB) system and showed that the Krafft temperature drops significantly below 273 K and CMC below ~100 mol.kg^{-1} in presence of 0.01 mol.kg^{-1} NaCl salt. Recently, Bhattacharjee et al.[11] have revealed that SDS:CAPB in the ratio of 7:3 mixture forms micelle at 275K and 50 bar as confirmed by the measurement of hydrodynamic radii of the micelle using dynamic light scattering (DLS) experiment. However, DLS is unable to distinguish between morphologies with different orientational ordering, e.g. liquid crystalline ordering versus spherical micellar forms. Molecular dynamics (MD) simulation is a powerful tool that can shed light on the molecular mechanism, structure and kinetics of self-assembly and aggregate formation.[5]

Therefore, in this Chapter, we aim to elucidate the morphology and dynamics of the self-assembly processes in the pure (SDS) as well as mixed surfactant systems (SDS+CAPB) in water at room temperature (298K) and at hydrate forming temperature and pressure (275K and 50 bar). Since formation of hydrates involve presence of the guest gas molecules along with the surfactant mixture, we also systematically investigate how presence of methane may alter the morphology and kinetics of the self-assembly processes.

8.2 Computational details

We have studied various combinations of the surfactant systems as summarized in Table 8.1. In the first system (SDS), 77 SDS molecules are distributed uniformly in water, corresponding to 9.4wt% SDS solutions (approximately 317 millimolar SDS solution). The second system (mixed surfactant system (SDS+CAPB)) consists of 40 SDS and 37 CAPB molecules in water that is 4.9wt% of SDS and 5.3wt% of CAPB in solution (approximately 164 millimolar SDS in solution). The third system (SDS-methane system (SDS+MET)) consists of 77 SDS molecules (9.4wt% of SDS (same as first system)) and 350 methane molecules were uniformly dispersed in the water. In the fourth system (mixed surfactant–methane (SDS+CAPB+MET)), 40 SDS molecules (4.9wt%), 37 CAPB molecules (5.3wt%) and 350 methane molecules were uniformly dispersed in water. The representative snapshots of the systems are shown in Figure 8.1. The aggregate formation in SDS and SDS+CAPB systems are studied both at temperature 275K (below Krafft temperature of SDS) and 298K (above Krafft temperature of SDS) at 50bar pressure. SDS+MET and

SDS+CAPB+MET systems are used to study aggregation in the presence of methane. These systems were simulated only at hydrate forming conditions (at 275K and 50bar pressure). The CMC of SDS is 8 millimolar at atmospheric pressure and room temperature, therefore the selected concentration of SDS is well above this CMC value. In experiments, surfactant concentration was below 1 wt%, slightly higher SDS concentration used in this work is expected to reduce the computational time by accelerating the aggregation of surfactant. Similar hydrate forming temperature and pressure were used in the current work.[17]

All the simulations have been performed using GROMACS (5.0.7 version) package.[18] The AMBER forcefield was used for modeling SDS and CAPB surfactants.[19] The parameters were generated using online software RED SERVER.[20] SDS is an anionic surfactant and therefore, the negatively charged head group of all SDS molecules were neutralized by the same number of sodium ions. On the other hand, CAPB does not require neutralization as it is zwitterionic surfactant. Water is modeled through TIP4P/ice model, suitable for gas hydrate simulations.[21] Methane is modeled using OPLS-UA force field.[22]

The initial structures of all the systems have been energy minimized using the steepest-descent algorithm.[23] These energy minimized structures have been subjected to NVT equilibration for 2ns using V-rescale thermostat at either 275K or 298K depending upon the system under consideration.[24] When the systems achieved the required temperature, NPT equilibration was done for further 2ns using Berendsen barostat at 50bar.[25] After the temperature and pressure equilibration, production run of 3 microseconds was done using Parrinello-Rahman barostat with integration time step of 2fs.[26] Periodic boundary conditions were applied in all the directions. All bonds were constrained to their equilibrium bond lengths. We have used a cutoff of 1.0nm for both the short-range Coulomb and van der Waals interactions. The long-range interactions have been treated with particle mesh Ewald method having a grid spacing of 0.16 nm.[27]
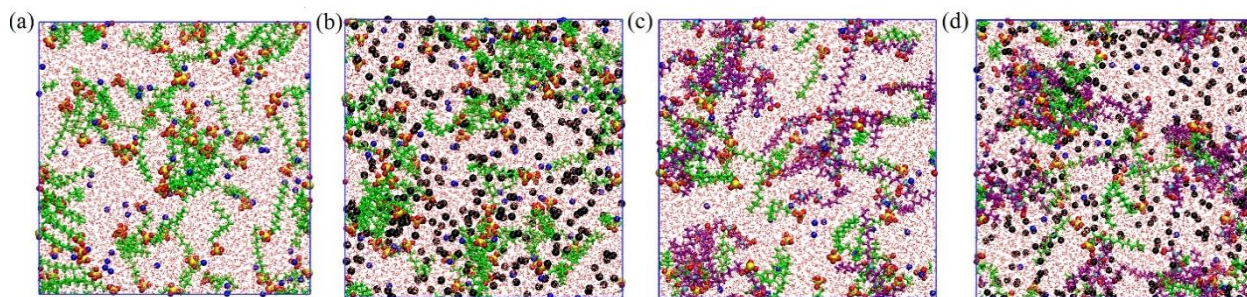
Figure 8.**1**: Representative snapshots of the simulated systems **(a)** SDS **(b)** SDS+MET **(c)** SDS+CAPB and **(d)** SDS+CAPB+MET at ~35ns**.** The colour representation is as following; green**:** hydrophobic tail of SDS and purple**:** hydrophobic tail of CAPB, red**:** water, black**:** methane, blue**:** sodium ions, cyan**:** nitrogen, red**:** oxygen, yellow**:** sulfur.

Table 8.**1**: Composition of all systems at pressure 50 bar**.** Number of SDS, CAPB, sodium, methane and water are named as N_{SDS}, N_{CAPB}, N_{NA}, N_{MET}, and N_{water} respectively**.**

Systems	N_{SDS}	N_{CAPB}	N_{NA}	N_{MET}	N_{water}	Temperature in K
SDS	77	0	77	0	11852	275 and 298
SDS+MET	77	0	77	350	11852	275
SDS+CAPB	40	37	40	0	11654	275 and 298
SDS+CAPB+MET	40	37	40	350	11654	275

8.3 Results and discussion

8.3.1 Structural order parameter calculation

We have used several parameters to examine the shape of aggregates, organization of surfactants inside them as well as number density of surfactants inside aggregates. They are defined as following,

1. **Shape parameters: morphology of aggregates**

We have investigated the shapes of the aggregates, using two different shape descriptors: asphericity (b) and acylindricity (c) as given below,[28]

$$b = S_1 - \frac{1}{2}(S_2 + S_3) \tag{8.1}$$

$$c = S_2 - S_3 \tag{8.2}$$

where, S_i are the eigenvalues of the gyration tensor, asphericity *b* measures the deviation from the spherical symmetry (b=0; for perfect sphere) and acylindricity *c* measures the deviation from the cylindrical symmetry (c=0; for perfect cylinder).

2. **Organization of surfactant molecules in aggregates**

To investigate the orientational ordering of the surfactants with respect to each other in the aggregates, the following order parameter is used: [29]

$$\Omega = \langle P_2(\cos\theta) \rangle = \langle \tfrac{3}{2}\cos^2\theta - \tfrac{1}{2} \rangle \tag{8.3}$$

Where, Ω is the order parameter and has second order Legendre polynomial functional form ($P_2(\cos\theta)$). Here, θ is the angle between end to end vectors of hydrophobic part of the surfactant molecules belonging to the same cluster and is calculated for every possible pair of surfactants in the same cluster (as shown in the inset Figure 8.6 (c)). The angular bracket denotes an average over the total number of pairs of surfactants in the given cluster at a given time. The range of Ω is from 0 to 1, where 0 represents an isotropic liquid with completely random arrangement of the molecules, while 1 represents perfectly aligned molecules with respect to each other.

3. Number density of aggregates

The number density of the aggregates is calculated using following form,

$$\rho = \frac{N_S}{R_g{}^3} \tag{8.4}$$

where, ρ is the number density, N_S is the aggregation size of the given aggregate and R_g is the radius of gyration of the aggregate. R_g is used as an approximate radii of the aggregates. This parameter shows positional (or translational) ordering of the surfactant.

8.3.2 Cluster formation in the (mixed) surfactant systems

Initially, all surfactant molecules were uniformly distributed in the entire simulation box. As simulation proceeds, the surfactant molecules came close to each other and started aggregating. We calculated the number of clusters and their sizes using the definition that if any atom of SDS or CAPB molecules falls within a distance of 0.3 nm of any atom of another SDS or CAPB molecule, they are considered to be a part of the same cluster. This cutoff was chosen after careful experimentation and visualization of the configurations to ensure accurate cluster size. The analysis of number of clusters (N$_{clusters}$), their size distribution and the growth of largest cluster were performed for each system as shown in Figure 8.2. The reduction in number of cluster signifies the merging of clusters into aggregates of higher size as shown in Figure 8.3. In the end of production run, multiple clusters of different size was depicted as shown in Figure 8.2 (a). The clustering at lower temperature is slower than higher temperature as expected. In spite of lower temperature, the presence of co-surfactant and methane enhances the rate of aggregation to a considerable extent as discussed in next sections. The sizes of largest clusters at the end of 3

microseconds production run as shown in Figure 8.2 (b) are 21 and 33 in SDS system at 275K and 298K, respectively. In presence of CAPB at both the temperatures, the SDS+CAPB system show comparable size of largest cluster 43 and 42 at 275K and 298K, respectively. In presence of methane at 275K, in SDS+MET and SDS+CAPB+MET systems, the sizes of largest clusters are 25 and 63, respectively. We note that the SDS+CAPB+MET system have the largest cluster size among all the systems. It is remarkable that in presence of methane the aggregation is significantly promoted, and the cluster sizes are much larger in presence of methane. This result is in agreement with the previous reports that long hydrophobic tail co-surfactants increase the size of aggregation/micellization.[3] Hereafter, we have used this largest grown and stable aggregates for the further analysis.
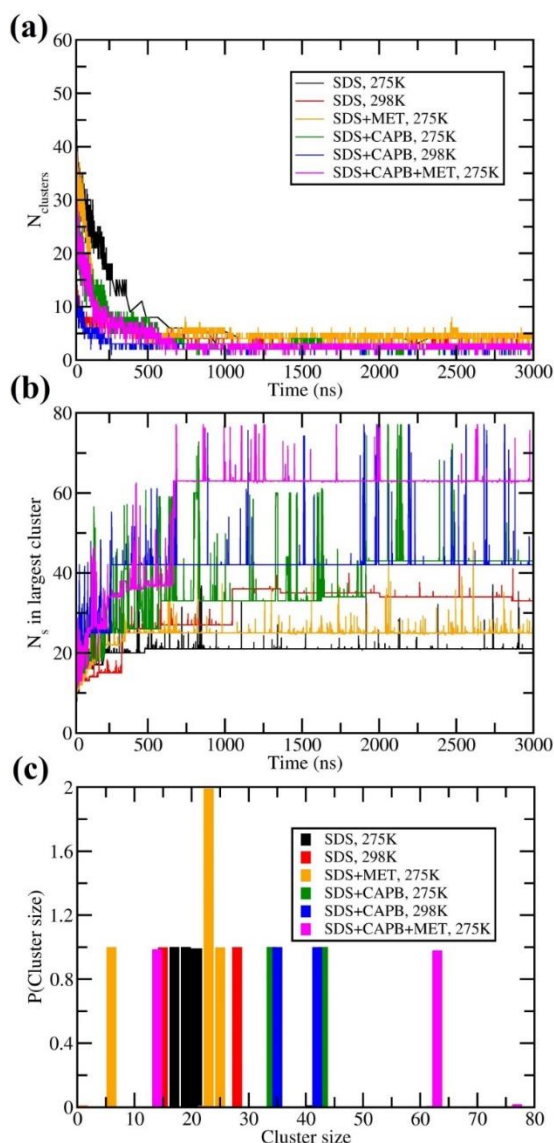
Figure 8.2: Time evolution of (a) total number of clusters ($N_{clusters}$) (b) number of surfactant molecules (N_s) in largest cluster (c) distribution in aggregation number of different clusters formed. The distribution is calculated from the last 200ns of the trajectory. The cutoff distance of the neighbor searching for cluster calculation is kept as 0.3nm.
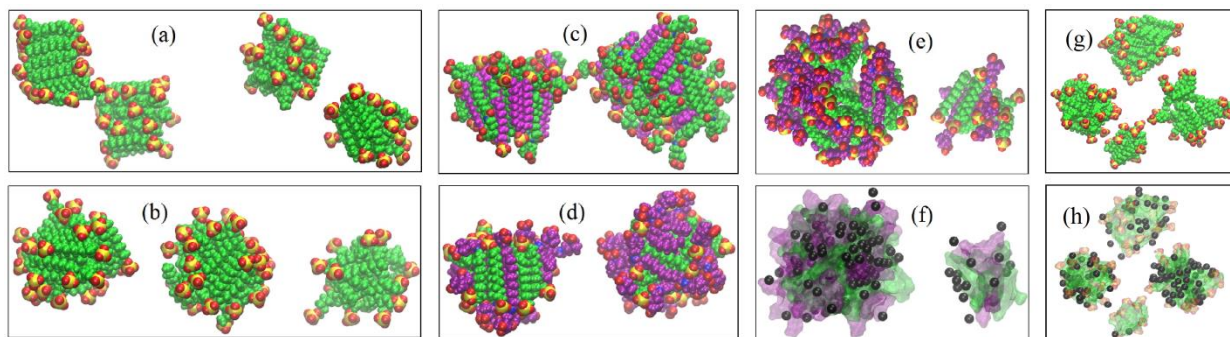

Figure 8.3: Aggregate structures for SDS at (a) 275K and (b) 298K, SDS+CAPB at (c) 275K and (d) 298K, SDS+CAPB+MET at (e & f) 275K and SDS+MET at (g & h) 275K. Methane in structures (e) & (g) is not shown for clarity. The color representation is as following; green: SDS hydrophobic tail including carbon and hydrogen, magenta: hydrophobic part of CAPB including carbon and hydrogen, yellow: sulfur, red: oxygen, blue: nitrogen, and black: methane. The sodium of SDS and water is omitted for clarity. In the surface representation (e), SDS is in green while CAPB is in magenta color. Black border does not represent the simulation box.

8.3.3 Role of methane and water in aggregation process

In presence of methane, as the aggregation of surfactants takes place, the number of water molecules decreases while population of methane molecules increases gradually. During aggregation, water has to move out and methane adheres to surfactant molecules via favorable hydrophobic interactions. This observation is in accordance with the phenomenon of dewetting during aggregation of hydrophobic molecules.[30,31] Figure 8.4 outlines the number of methane and water molecules present within 0.35 nm of the surfactant of largest cluster and is normalized by the aggregation size. Methane goes inside the aggregates resulting in enhanced gas uptake or increased mole fraction of methane in solution, as observed experimentally; in experiments, enhanced consumption of methane from the gas phase has been inferred as high conversion of water-to-hydrate.[32] However, as seen in this study water prefers to stay only at the hydrophilic surface of the cluster and never goes inside the cluster.[33,34]
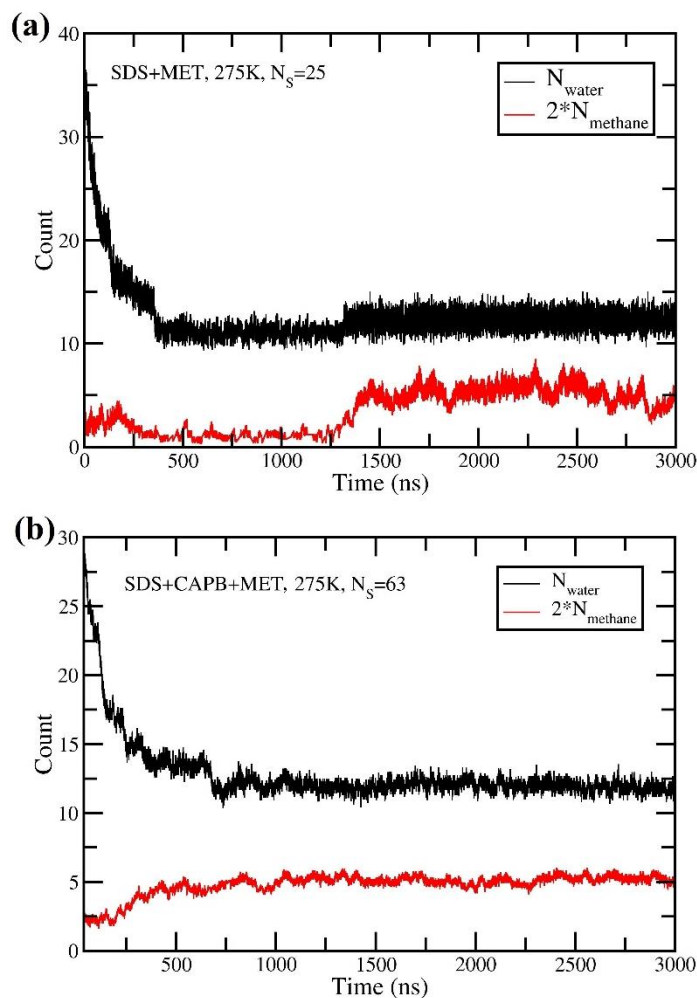
Figure 8. 4: Number of methane ($N_{methane}$) and water (N_{water}) around 0.35 nm of surfactants belongs to the aggregates of size (a) 25 in SDS+MET and (b) 63 in SDS+CAPB+MET systems and are normalized by the aggregation size.

Merging of isolated clusters during aggregation is apparent but its visualization gives meaningful insight. Hence, Figure 8.5 reveals the fusion of the smaller clusters into bigger ones for SDS+CAPB+MET system. At ~ 650 ns, total three clusters of the sizes 14, 26 and 37 were present. Out of them, clusters of sizes 26 and 37 merge and forms single cluster of size 63. Finally, only two clusters of sizes 63 and 14 were present in the system and the structural arrangement of these two clusters were quite different. Cluster of size 14 is quite rigid, compact, crystalline in nature and lacks methane inside it. Interestingly, this cluster comes in contact with other clusters but never merges or exchanges its surfactant molecules with them. Its size was found to be constant after its formation within the simulation time. On other hand, cluster of size 63 has methane inside

hydrophobic core (as marked by the red dotted circle in Figure 8.5 (d)). Before merging, the other two clusters (of sizes 26 and 37) come in contact with each other and linked through the CAPB molecule (as marked by the red dotted circle in Figure 8.5 (b)). The possible reason of the linkage of head group of CAPB with both the clusters can be its ability to form H-bonds with hydrophilic head-groups of SDS as well as other CAPB molecules.[4,35] This hydrogen bonding network propagates through other CAPB and SDS molecules, and simultaneously the methane molecules in the middle of these two individual cluster shifts towards the middle of newly formed super cluster. Rapid re-arrangement of the surfactant molecules took place to occupy minimum surface area which ultimately resulted in a cluster of size 63.
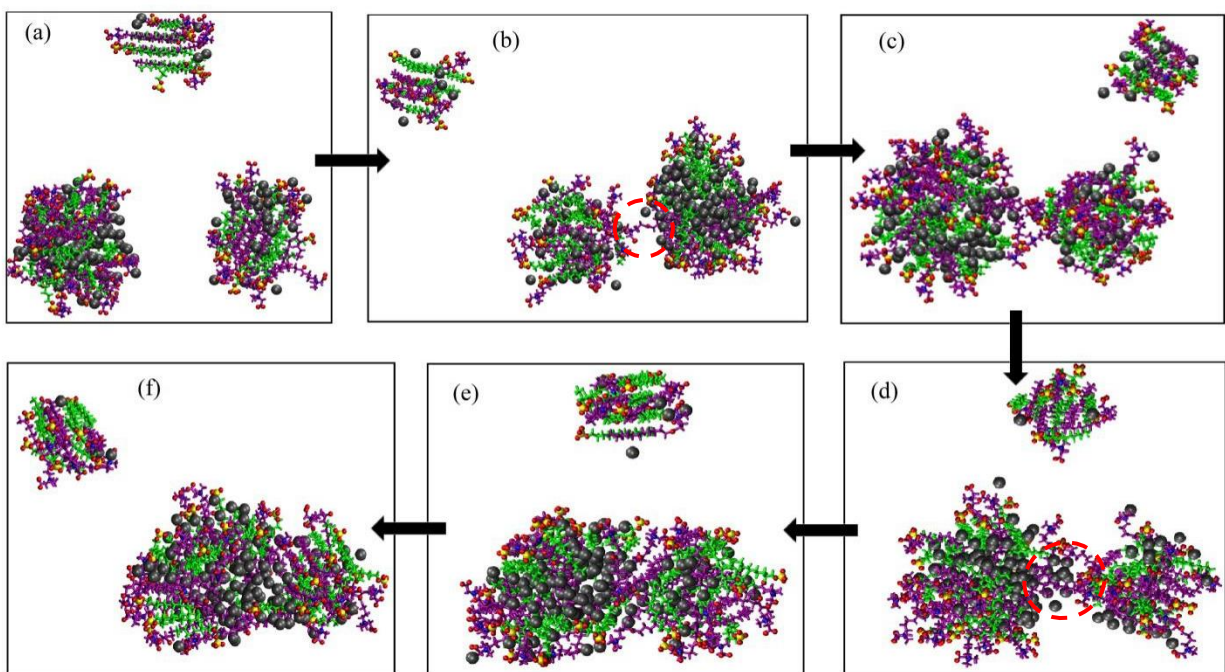
Figure 8.5: Snapshots showing fusion of two clusters of sizes 26 and 35 into cluster of size 63 from SDS+CAPB+MET system. The color representation is same as Figure 8.4. The exchange of CAPB and methane between the aggregates is marked by red dotted circle.

8.3.4 Morphology of aggregates and structural organization of surfactants

The morphology of aggregates is determined by using the parameters; asphericity and acylindricity. The analysis is done for the part trajectory from where the size N_s of largest cluster is achieved and stable. The calculations are performed for the single stable sized cluster which is largest in size from the last 100ns of the part of the trajectory. Figure 8.6 (a) and (b) shows

normalized distribution of asphericity and acylindricity of the most stable and largest aggregate, respectively. Maximum deviation from the spherical as well as cylindrical shape is observed for the SDS+CAPB+MET aggregate and minimum deviation for the SDS+CAPB at 298K. Whereas SDS and SDS+MET systems peak around the similar values for both asphericity and acylindricity. Figure 8.7 (a) and (b), shows the normalized distribution of asphericity and acylindricity of the individual surfactant molecules from the same stable and largest aggregate, respectively. Both the distributions are broader for CAPB and narrower for the SDS. In the distribution of asphericity, two distinct peaks appear for the SDS surfactant. From the distribution of acylindricity, we can conclude that the SDS aggregates both in presence and absence of CAPB have predominantly cylindrical shape, while CAPB molecules may exist in somewhat bent form within the aggregates.
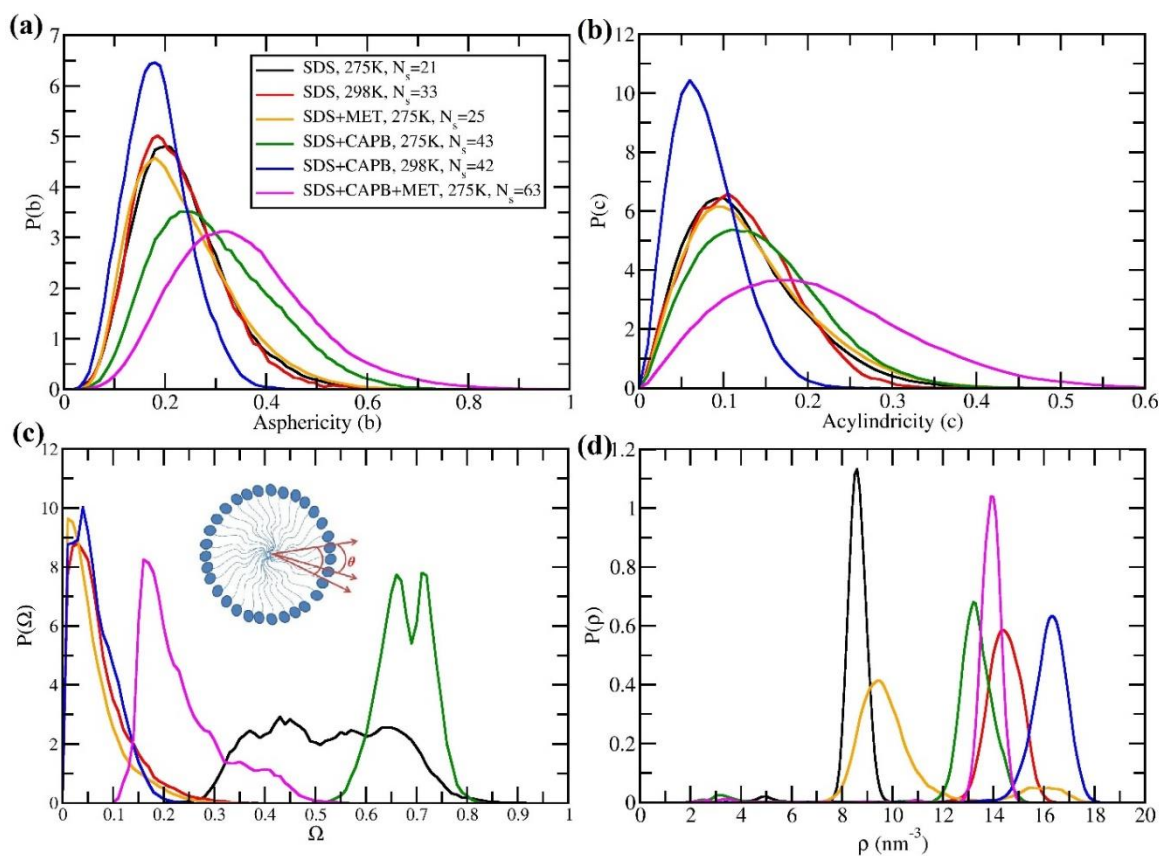

Figure 8.6: Distribution of (a) asphericity and (b) acylindricity (c) order parameter (Ω), and (d) density (ρ) of single largest aggregates. Inset figure shows the calculation of the angles between different surfactant pairs in single aggregate in calculation of Ω.
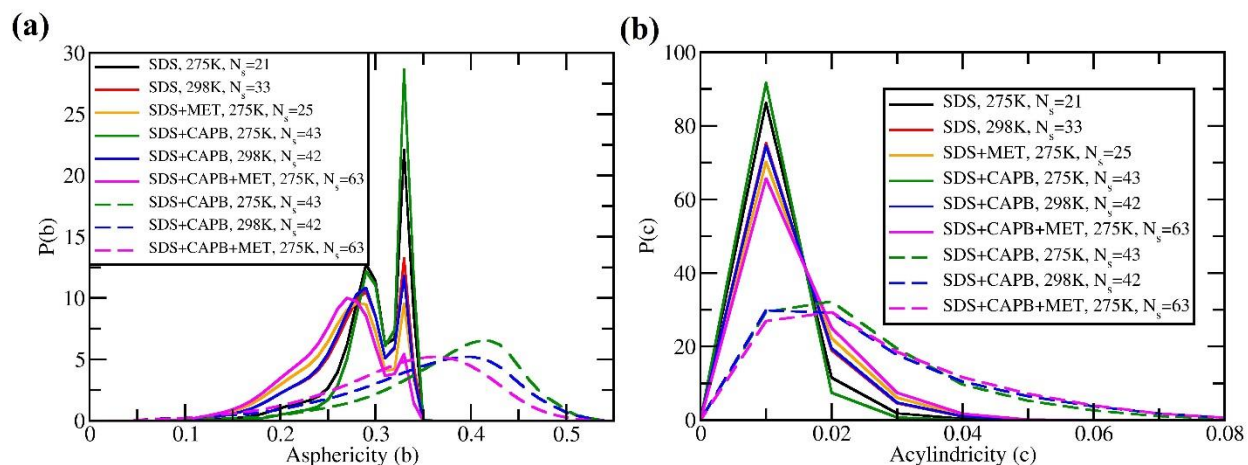
(a)

(b)

Figure 8.7: Distribution of structural order parameters of the individual molecules from largest cluster (a) asphericity and (b) acylindricity. The analysis is done for the part trajectory from where the size N_s of largest cluster is achieved and stable. Solid lines represent SDS molecules and dashed lines represent CAPB molecules.

The structural arrangement of the surfactant with respect to each other inside the aggregates for the last 100ns of the trajectory is shown in Figure 8.6 (c) using the structural order parameter, Ω. For the SDS system at 275K and 50 bar (hydrate forming conditions) Ω falls between 0.3 and 0.8 values. This cluster has reasonable orientational ordering even though positional ordering is not very well defined. This result agrees well with the phase diagram which suggests that below Krafft temperature surfactant will be in crystalline aggregates if taken in higher concentrations.[36] Whereas, same SDS system at 298K and 50 bar, Ω is highly populated towards 0 which clearly shows that at this pressure, SDS aggregates are liquid in nature.[13] Interestingly, in presence of methane (SDS+MET system) at hydrate forming conditions (275K and 50 bar), Ω is falling towards 0 which is a transition to the liquid phase completely from the liquid crystalline phase. Thus, it confirms that SDS can form soluble liquid aggregate in the water in presence of methane at hydrate forming conditions. Nevertheless, this is only possible when hydrophobic molecules such as methane are present in the hydrophobic interior of the cluster and due to favorable interactions between hydrophobic moieties, the interior becomes liquid in nature. This is evident from Figure 8.5 and are in agreement with the experimental observation of Peng et al.[13] that SDS can form micelle and methane can be soluble in that micelle at hydrate forming conditions. SDS micellization occurs at hydrate forming conditions (274.2K and 27.2 bar) and CMC decreases to

2.772 mmol/L.[13] Nishikido et al.[37] reported that with an increase in pressure, the Krafft temperature increases for SDS as shown using electroconductivity method. However, Zhang et al.[10] reported that at the hydrate forming conditions, the range of Krafft temperature for SDS remains similar to atmospheric pressure and SDS micelle formation does not occur at all concentration of methane. Our result shows that in presence of methane, aggregation of SDS happens by incorporating methane in its structure. Further due to such structure, methane solubility in the aqueous phase increases.

Further, for the mixed surfactant system SDS+CAPB at 275K as shown in Figure 8.6 (c), Ω falls in the range 0.55 to 0.8 indicating that the given aggregate can be liquid crystal. For this system, the experimental work of Prajapati et al.[15,16] and Bhattacharjee et al.[11] reports that micellization occurs for the SDS+CAPB system at hydrate forming conditions. Prajapati et al.[15,16] have performed their (SDS+CAPB) experiments in presence of sodium chloride which have the effect of lowering Krafft temperature and CMC as shown by Tsujii et al.[38] Bhattacharjee et al.[11] measured the hydrodynamic radii of the formed aggregates using a dynamic light scattering experiment which may not be distinguishing between micelle and liquid crystal. On the other hand, Ω populates near to 0 at 298K, confirms that it is fluid in nature. Furthermore, in presence of methane, in the mixed surfactant system (SDS+CAPB+MET) at hydrate forming conditions, distribution of Ω shows a peak around 0.2, indicating reduction in orientational ordering in presence of methane. Thus, methane promotes liquid-like disorder in the otherwise ordered surfactant structure at low temperature. The number density of the surfactants as shown in Figure 8.6 (d) is lower for the small aggregates, and comparatively higher for the larger cluster.

In addition, we also attempt to shed light on radial distribution of surfactants with each other in the clusters. The radial distribution function (RDF) of center of mass (COM) of reference surfactant with the COMs of rest of the surfactants in same aggregate were analyzed for the last 100ns of the trajectory. Figure 8.8 (a) shows the RDF between centers of mass of SDS. RDF peaks for SDS and SDS+CAPB systems at 275K are sharper; indicating crystalline nature compared to the same systems at 298K which are in liquid form. While, for SDS+MET and SDS+CAPB+MET systems at 275K, the broader distribution of peaks again confirms the possibility of their fluid nature. Similarly, Figure 8.8 (b) shows the RDF of CAPB COM with CAPB COM. It shows that SDS+CAPB system at 275K has significant structural ordering, whereas SDS+CAPB system at 298K and SDS+CAPB+MET system at 275K system have broader radial distribution signifying

liquid-like disordered nature of clusters. In conclusion, adsorption methane renders structural fluidity to the aggregates even at the hydrate forming conditions.
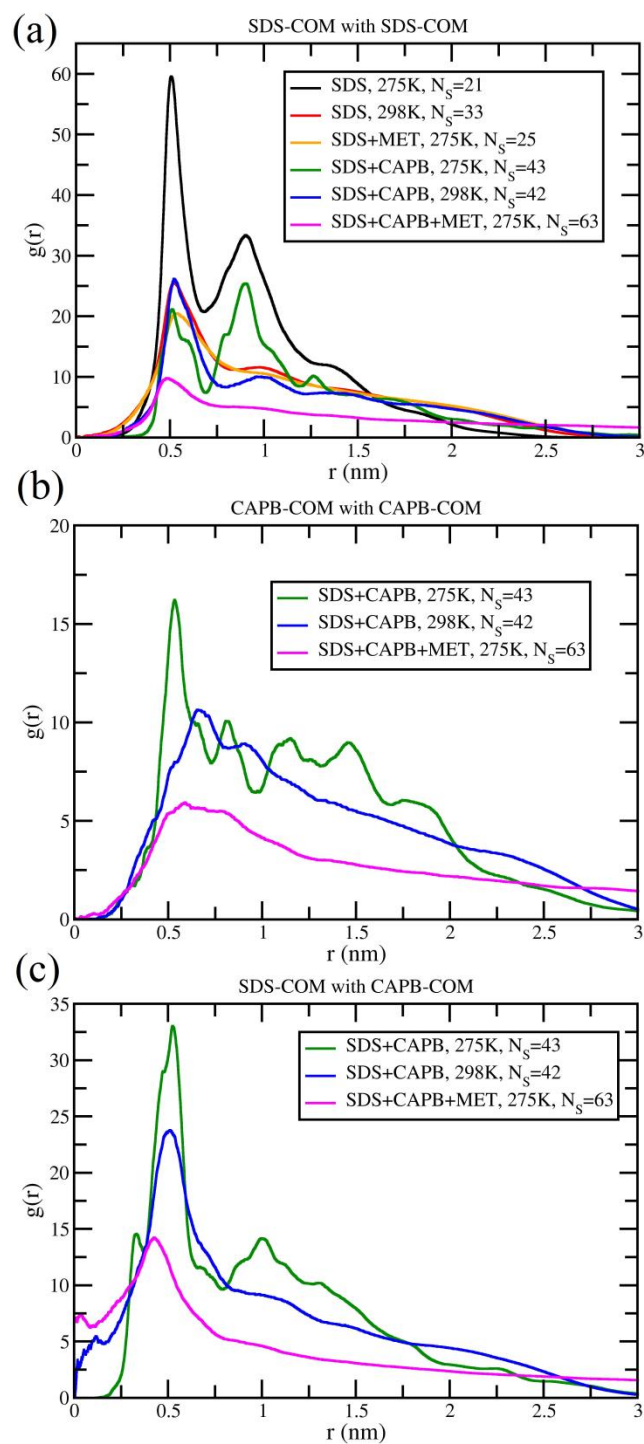
Figure 8.8: Radial distribution function g(r) of (a) SDS-COM with SDS-COM (b) CAPB-COM with CAPB-COM (c) SDS-COM with CAPB-COM. This is done for single clusters which is stable for sufficient time. Center of mass is abbreviated as COM.

8.3.5   Radius of gyration (R_g) and dynamics of surfactants and aggregates

The flexibility of the surfactants in the aggregates is obtained with the help of radius of gyration (R_g) parameter. The distribution of R_g of individual surfactant belonging to the same stable sized aggregate is shown in Figure 8.9. R_g of SDS is lower than that of CAPB if both are fully extended. In the SDS system, at 275K, SDS aggregates are crystalline in nature and has larger R_g, compared to SDS aggregate at 298K which is in fluid form. Similarly, for SDS+MET system, at 275K the population is shifted towards lower R_g in comparison at 298K. In presence of CAPB (SDS+CAPB system), R_g of SDS and CAPB at both the temperatures are comparable however, they are liquid crystal and fluid at 275K and 298K, respectively. In presence of methane (SDS+CAPB+MET system) at hydrate forming conditions (275K and 50 bar), R_g of both the surfactants decreased, hence, methane might be providing an extra flexibility to surfactants and possibly converts the cluster into micelle.

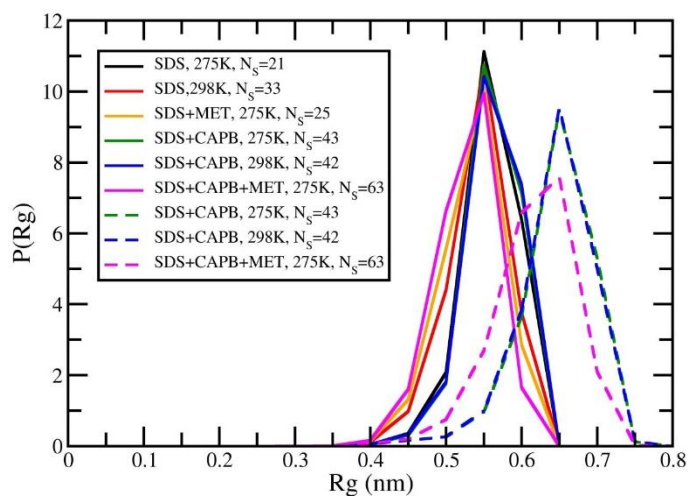**Figure 8.9**: Distribution in radius of gyration (Rg) from the single stable sized cluster. The Rg is calculated for individual surfactant in the cluster. Solid lines represent SDS surfactants and dashed lines represent CAPB surfactants.

To determine the timescale of fluctuations of radius of gyration of both the SDS and CAPB surfactants in the selected aggregates as well as the shape anisotropy of those aggregates, we

considered the time autocorrelations of them using the equation 2.31 given in Chapter 2. Shape anisotropy is calculated from the principle components of radius of gyration for the whole aggregate. The following equation is used to get shape anisotropy of aggregate,

$$\text{Shape anisotropy} = \frac{\text{smallest component of radius of gyration}}{\text{largest component of radius of gyration}} \tag{8.5}$$

The autocorrelation of shape anisotropy for the single cluster is shown in Figure 8.10 (a). Among the two temperatures of SDS system, C(t) at 275K is relaxing slowly than at 298K while the trend is reverse for SDS+CAPB system at those two temperatures. However, the systems in which methane is present such as SDS+MET and SDS+CAPB+MET, the shape fluctuations of clusters are comparatively more than without methane systems. This implies that the presence of methane is contributing to the shape fluctuations of the cluster. In Table 8.2(I), the timescale of fluctuations of shape anisotropy from the triexponential fitting of 10ns data length is given. The slowest component of the order of 3-8 nanoseconds exists for SDS systems while for the SDS+CAPB systems, because of the tight packing of surfactants it is of the order of 100 nanoseconds. While in presence of methane for both systems, timescale of fluctuations is considerably decreased. In addition, the individual contribution of Rg of surfactant inside the aggregate is plotted in Figure 8.10 (b) and (c) for SDS and CAPB surfactants, respectively. In Table 8.2 (II and III), the timescale of fluctuations of Rg of SDS and CAPB surfactants from the triexponential fitting of 2ns data length is presented. The correlation coefficient of these curves is almost ~ 0.99. Three timescales of relaxations exist for both the autocorrelations. Due to the long-lived tail, SDS in presence of methane shows timescale of relaxation more than SDS at 298K system. While, in SDS+CAPB system, it decreases with increase in temperature and in presence of methane it is lowest. On the other hand, CAPB relaxes at the similar timescale for both the systems without methane, while in presence of methane this timescale is drastically lowered to ~2ns.
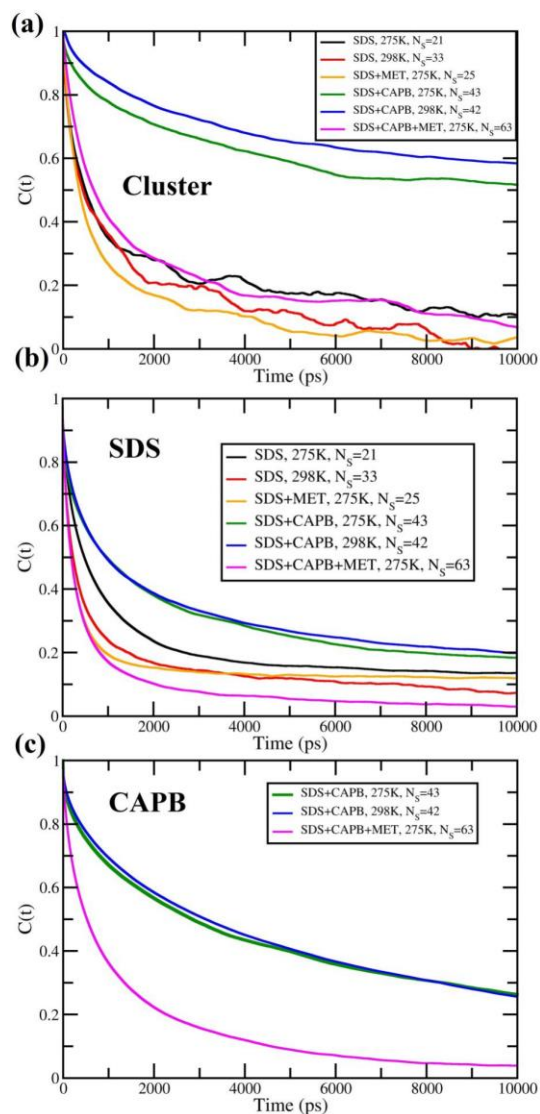
Figure 8.10: Autocorrelations of **(a)** Shape anisotropy of single clusters of aggregation size, Ns **(b)** radius of gyration of SDS in those selected clusters from each system and **(c)** radius of gyration of CAPB in those selected clusters from each system.

Table 8.2: Triexponential fitting of the autocorrelation function of shape anisotropy of single cluster and radius of gyration of SDS and CAPB separately belonging to that single cluster. The fitting function is $C(t) = f_1.e^{\frac{-t}{\tau_1}} + f_2.e^{\frac{-t}{\tau_2}} + f_3.e^{\frac{-t}{\tau_3}}$ where, f_i is the fraction of radius of gyration or shape anisotropy of cluster relaxing with timescale τ_i in autocorrelations.

I. Shape anisotropy of cluster (10ns)

System	f_1	τ_1(ps)	f_2	τ_2 (ps)	f_3	τ_3 (ps)
SDS, 275K	0.13	59	0.52	491	0.32	8711
SDS, 298K	0.19	76	0.40	475	0.39	3729
SDS+MET, 275K	0.18	155	0.51	439	0.28	3645
SDS+CAPB, 275K	0.10	218	0.38	3551	0.5	1.28×10^6
SDS+CAPB, 298K	0.07	220	0.30	2761	0.64	97779
SDS+CAPB+MET, 275K	0.26	252	0.44	986	0.28	9036

II. Radius of gyration of SDS (2ns)

System	f_1	τ_1(ps)	f_2	τ_2 (ps)	f_3	τ_3 (ps)
SDS, 275K	0.20	123	0.52	848	0.20	31309
SDS, 298K	0.17	45	0.48	289	0.30	3297
SDS+MET, 275K	0.22	73	0.53	317	0.20	7648
SDS+CAPB, 275K	0.09	38	0.21	368	0.61	4180
SDS+CAPB, 298K	0.10	65	0.31	509	0.53	6133
SDS+CAPB+MET, 275K	0.19	61	0.52	294	0.24	2375

III. Radius of gyration of CAPB (2ns)

System	f_1	τ_1(ps)	f_2	τ_2 (ps)	f_3	τ_3 (ps)
SDS+CAPB, 275K	0.07	0.02	0.14	285	0.79	5884
SDS+CAPB, 298K	0.06	0.02	0.12	277	0.82	5758
SDS+CAPB+MET, 275K	0.08	0.02	0.33	244	0.599	1995

8.4 Conclusion

Using extensive molecular dynamic simulations, we have investigated the SDS aggregation in presence/absence of CAPB (co-surfactant) as well as methane at room temperature (298 K) and at hydrate forming temperature and pressure (275 K & 50bar). Aggregation occur in all the systems

during 3 microseconds run at both the temperatures. We have shown the time evolution of the total number of aggregates formed, growth of largest aggregate as well as distribution of the aggregation sizes. In absence of methane, at 275K, clusters in SDS and SDS+CAPB systems are more rigid with higher liquid crystalline orientational ordering of hydrophobic tails, while they are more fluidic in nature at room temperature (298K). For the SDS+MET and SDS+CAPB+MET systems, we observed significant amount of methane enters into the hydrophobic core of aggregate and gives it an extra flexibility. The aggregation size in the SDS+CAPB+MET system is greater than the SDS+MET system. This significant absorption of methane by the surfactant aggregates is consistent with the experimental observation of enhanced methane gas uptake during the hydrate formation in presence of surfactants.[11]

The morphology of the aggregates is quantified using shape descriptors: asphericity (b) and acylindricity (c). We have shown that aggregates are neither in spherical nor in cylindrical shape. We further used order parameter (Ω) to predict the crystalline/liquid nature of aggregates. Contradictory to the experimental observation that at hydrate forming conditions micelles are formed in SDS+CAPB system, we observed liquid crystalline orientational ordering in this system at these conditions.[11,15,16] However, we have successfully shown that at room temperature the clusters are primarily in liquid form. In presence of methane, aggregation of surfactants takes place in both the system SDS+MET and SDS+CAPB+MET at hydrate forming conditions. This result supports experimental observation of Peng et al.[13] that SDS micellization does occur and methane goes inside the cluster and gets solubilized inside the hydrophobic core of micelle.

We have shown the fusion process of clusters in the SDS+CAPB+MET system happening via linkage of two clusters primarily through CAPB molecule. The CAPB molecule facilitates the formation of hydrogen bonding with itself and anionic SDS surfactant which supports quite well to the earlier observation of the Iwasaki et al.[4] Additionally, we looked at the timescales of fluctuations of the shape anisotropy of the clusters as well as the radius of gyration of individual surfactants belonging to those clusters. We found that both of these timescales are different and are not correlated. In SDS+CAPB+MET system, the cluster with methane inside is fluctuating more than any other cluster for both the properties. Shape anisotropy parameter relaxes slowly compared to the individual radii of gyrations.

8.5 References

(1)   Chen, J.; Hao, J. *Phys. Chem. Chem. Phys.* **2013**, *15* (15), 5563–5571.

(2)   Kumar, A.; Bhattacharjee, G.; Kulkarni, B. D.; Kumar, R. *Ind. Eng. Chem. Res.* **2015**, *54* (49), 12217–12232.

(3)   Baruah, A.; Chauhan, G.; Ojha, K.; Pathak, A. K. *Ind. Eng. Chem. Res.* **2014**, *53* (51), 19765–19774.

(4)   Iwasaki, T.; Ogawa, M.; Esumi, K.; Meguro, K. *Langmuir* **1991**, *7* (1), 30–35.

(5)   Choudhary, N.; Kushwaha, O. S.; Bhattacharjee, G.; Chakrabarty, S.; Kumar, R. *Energy Procedia* **2017**, *105*, 5026–5033.

(6)   Lee, S. Y.; Kim, H. C.; Lee, J. D. *J. Cryst. Growth* **2014**, *402*, 249–259.

(7)   Chua, P. C.; Kelland, M. A. *Energy & Fuels* **2013**, *27* (3), 1285–1292.

(8)   Bhattacharjee, G.; Choudhary, N.; Kumar, A.; Chakrabarty, S.; Kumar, R. *J. Nat. Gas Sci. Eng.* **2016**, *35*, 1453–1462.

(9)   Kumar, A.; Bhattacharjee, G.; Barmecha, V.; Diwan, S.; Kushwaha, O. S. *J. Environ. Chem. Eng.* **2016**, *4* (2), 1955–1961.

(10)   Zhang, J. S.; Lee, S.; Lee, J. W. *J. Colloid Interface Sci.* **2007**, *315* (1), 313–318.

(11)   Bhattacharjee, G.; Kushwaha, O. S.; Kumar, A.; Khan, M. Y.; Patel, J. N.; Kumar, R. *Ind. Eng. Chem. Res.* **2017**, *56* (13), 3687–3698.

(12)   Luo, H.; Sun, C.-Y.; Peng, B.-Z.; Chen, G.-J. *J. Colloid Interface Sci.* **2006**, *298* (2), 952–956.

(13)   Peng, B. Z.; Chen, G. J.; Luo, H.; Sun, C. Y. *J. Colloid Interface Sci.* **2006**, *304* (2), 558–561.

(14)   Yu, Z.-J.; Zhang, X.; Xu, G.; Zhao, G.-X. *J. Phys. Chem* **1990**, *94*, 3675–3681.

(15)   Prajapati, R. R.; Bhagwat, S. S. *J. Chem. Eng. Data* **2012**, *57* (12), 3644–3650.

(16)   Prajapati, R. R.; Bhagwat, S. S. *J. Chem. Eng. Data* **2012**, *57* (3), 869–874.

(17)   Choudhary, N.; Hande, V. R.; Roy, S.; Chakrabarty, S.; Kumar, R. *J. Phys. Chem. B* **2018**, *122* (25), 6536–6542.

(18)   M.J. Abraham, D. van der Spoel, E. Lindahl, B. H. *There is no Corresp. Rec. this Ref.* **2015**.

(19)   Wang, J.; Wolf, R. M.; Caldwell, J. W.; Kollman, P. A.; Case, D. A. *J. Comput. Chem.* **2004**, *25* (9), 1157–1174.

(20)   Vanquelef, E.; Simon, S.; Marquant, G.; Garcia, E.; Klimerak, G.; Delepine, J. C.; Cieplak, P.; Dupradeau, F.-Y. *Nucleic Acids Res.* **2011**, *39* (suppl_2), W511–W517.

(21)   Abascal, J. L. F.; Sanz, E.; García Fernández, R.; Vega, C. *J. Chem. Phys.* **2005**, *122* (23), 234511.

(22)   Jorgensen, W. L.; Madura, J. D.; Swenson, C. J. *J. Am. Chem. Soc.* **1984**, *106* (22), 6638–6646.

(23)   Lindahl, E. *Molecular Dynamics Simulations*; Elsevier (formerly published by Academic Press), 2015; Vol. 1215.

(24)   Bussi, G.; Donadio, D.; Parrinello, M. *J. Chem. Phys.* **2007**, *126* (1), 014101.

(25)   Berendsen, H. J. C.; Postma, J. P. M.; van Gunsteren, W. F.; DiNola, A.; Haak, J. R. *J. Chem. Phys.* **1984**, *81* (8), 3684–3690.

(26)   Parrinello, M.; Rahman, A. *J. Appl. Phys.* **1981**, *52* (12), 7182–7190.

(27)   Essmann, U.; Perera, L.; Berkowitz, M. L.; Darden, T.; Lee, H.; Pedersen, L. G. *J. Chem. Phys.* **1995**, *103* (19), 8577–8593.

(28)   Vymětal, J.; Vondrášek, J. *J. Phys. Chem. A* **2011**, *115* (41), 11455–11465.

(29)   Saupe, A. *Angew. Chemie Int. Ed. English* **1968**, *7* (2), 97–112.

(30)   Chandler, D. *Nature* **2005**, *437* (7059), 640–647.

(31)   Hande, V. R.; Chakrabarty, S. *J. Phys. Chem. B* **2015**, *119* (34), 11346–11357.

(32)   Verrett, J.; Posteraro, D.; Servio, P. *Chem. Eng. Sci.* **2012**, *84*, 80–84.

(33)   Yoshii, N.; Okazaki, S. *J. Chem. Phys.* **2007**, *126* (9), 096101.

(34)   Fujimoto, K.; Yoshii, N.; Okazaki, S. *J. Chem. Phys.* **2012**, *136* (1), 014511.

(35)   Maillet, J.-B.; Lachet, V.; Coveney, P. V. *Phys. Chem. Chem. Phys.* **1999**, *1* (23), 5277–5290.

(36)   Smirnova, N. A.; Solutions, M.; Equilibrium, S.; Solubility, S. *Fluid Phase Equilib.* **1995**, *110* (1), 1–15.

(37)   Nishikido, N.; Kobayashi, H.; Tanaka, M. *J. Phys. Chem.* **1982**, *86* (16), 3170–3172.

(38)   Tsujii, K.; Mino, J. *J. Phys. Chem.* **1978**, *82* (14), 1610–1614.

Chapter 9: Conclusion and future outlook

9.1 Summary and conclusion

The long standing mystery of hydrophobic interactions in water is unsolved till date. Previous studies on hydrophobic hydration and interactions report several ways to measure the hydrophobicity, but failed to quantify it exactly. Among the several existing definitions of hydrophobicity, the water structure around hydrophobic groups offers one of the way to define microscopic hydrophobicity. We have therefore focused our study on the water structure and dynamics around chemically and topologically heterogenous molecules and surfaces. Water has an excellent ability to rapidly adjust to any heterogeneity present in the surface for example curvature heterogeneity, charge heterogeneity and geometrical heterogeneity. Water exclusively interacts with the surface by either electrostatic interactions or hydrogen bonding interactions. In this thesis, we have primarily studied the structural, and translational and orientational dynamics of the water. We establish that it is highly dependent on the surface present nearby pointing towards the fact of unique solvation property of water.

According to the size of heterogeneous surface for example near hydrophobic surfaces water undergoes size dependent order-disorder crossover at around 1 nm. We establish a remarkable analogy between the temperature dependence in bulk water and hydration shell water around spherical hydrophobes with size variation. Interestingly, we demonstrate that increasing the hydrophobic length of rigid polymers in one dimension does not affect the hydration shell water structure and is more or less similar to hydration shell of methane. On the other hand, the curvature dependent structural organization of water is observed around flexible polymeric surface. This shows water is efficiently adjusting to the local topological heterogeneity of flexible hydrophobic polymeric surface. In the heterogeneous topological surface, it prefers to find out the higher curvature region to maintain its hydrogen bond integrity to the best. In addition, we demonstrate that the water structural coordinates are coupled to the solute coordinates during conformational fluctuations of a flexible polymer and hydrophobic collapse is driven by local dewetting around the polymer.

Water in spherical confinement of AOT reverse micelles shows significant perturbation in the structural as well as dynamical properties of water. We demonstrate that the changes in water properties are primarily due to the electrostatic interactions between water and surfaces. The orientation dependent properties of water do not get perturbed significantly by hydrophobic confinement. Interestingly, the length scale of water perturbation depends upon property under consideration. Our results reveal that density is much less perturbed than local orientational order (tetrahedral order) which in turn is less perturbed by the global orientational order. Only the translational dynamics of water is affected due to hydrophobic confinement. In addition, near bilayer (roughly planar) surfaces made by three different kinds of charged surfaces namely anionic (AOT surfactant), zwitterionic (POPC lipid molecule) and hydrophobic (isooctane), water structural and dynamical properties have been investigated. We show that the anionic surface perturbs the water to a greater extent as compared to the other surfaces.

We have also investigated the effect of the confinement/hydration size on the structure and conformational dynamics of the N-terminal CXCR1 peptide in AOT reverse micelle confinement. Experimentally, formation of β sheet structure occurs in AOT RM confinement as well as near DOPC bilayer. We have not observed such propensity towards β sheet formation in our simulation, possibly due to limitations in the force fields or lack of sufficient sampling. Nevertheless, our results primarily reveal the surface binding/seeking tendency and motional restriction of this peptide at smaller confinement. Translational dynamics of the center of mass of the peptide after decoupling its motion from the whole RM motion found to increase with the hydration size. Since, water drives the self-assembly of lipids, surfactants etc. In the final study of this thesis, we have investigated upon the morphology and dynamics of the clusters of mixed surfactant system of SDS and CAPB under methane hydrate formation conditions and at room temperature. We have demonstrated that the structure and dynamics of the aggregates are strongly dependent on the thermodynamic condition. In the context of the role of these surfactants in tuning the kinetics of methane hydrate growth, we show that these

aggregates have propensity to absorb methane and they become significantly more dynamic and flexible in this process.

9.2 Future outlook

1. Water is an extremely challenging molecule to model using classical force fields. There exist more than 40 water models, but none of them are able to reproduce all properties of water in a consistent manner. In our study of vibrational spectra of water in the hydration shell of hydrophobic molecules, we were not able to reproduce the experimental observation (Raman spectroscopy) of size-dependent order-disorder crossover near small length alcohols. The origin of this discrepancy may be due to use of classical non-polarizable forcefields. Therefore, systematic investigation using *ab initio* MD simulation or polarizable force-fields (e.g. amoeba) may be utilized to investigate the spectral signatures of structural order-disorder crossover around hydrophobic solutes.

2. We have discussed in Chapter 1 regarding the unusually fast transport of water inside 1D confinement of carbon nanotube. It would be interesting to undertake a systematic comparison of water transport between 1D, 2D and 3D hydrophobic confinements. Model systems of choice could be carbon nanotube for the cylindrical confinement, graphene sheets for the planar confinement and fullerene C60 buckyballs for spherical confinement.

3. N-terminal CXCR1 peptide near bilayers and in reverse micelle confinement adopts more compact structures and has surface seeking tendency. Previous experimental studies indicate that they have propensity of secondary structure formation near negatively charged interfaces. Therefore, it would be interesting to investigate systematically the structural and conformational dynamics of N-terminal CXCR1 peptide inside hydrophobic confinements with varying degree of chemical and topographical heterogeneity. It would also be interesting to study the effect of molecular crowders on the conformational dynamics and structural ensemble of this peptide.

4. Biomimetics: Aquaporin serves as chemically selective gatekeeper with protein walls that allows immensely quick transport of water with high degree of selectivity. MD simulations

of water inside such aquaporins would give molecular insights to explain the origin of selectivity and efficiency of these channels. This knowledge would be helpful towards developing rational design principles of membrane technologies for water filtration and purification process.